



HAL
open science

APPLICATION OF THE COMPRESSIBLE AND LOW-MACH NUMBER APPROACHES TO LARGE-EDDY SIMULATION OF TURBULENT FLOWS IN AERO-ENGINES

Matthias Kraushaar

► **To cite this version:**

Matthias Kraushaar. APPLICATION OF THE COMPRESSIBLE AND LOW-MACH NUMBER APPROACHES TO LARGE-EDDY SIMULATION OF TURBULENT FLOWS IN AERO-ENGINES. Fluids mechanics [physics.class-ph]. Institut National Polytechnique de Toulouse - INPT, 2011. English. NNT: . tel-04240525v1

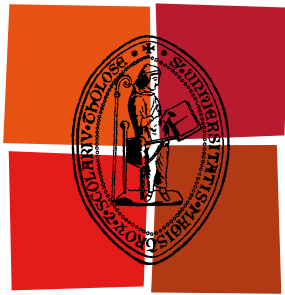
HAL Id: tel-04240525

<https://theses.hal.science/tel-04240525v1>

Submitted on 25 Jun 2012 (v1), last revised 13 Oct 2023 (v2)

HAL is a multi-disciplinary open access archive for the deposit and dissemination of scientific research documents, whether they are published or not. The documents may come from teaching and research institutions in France or abroad, or from public or private research centers.

L'archive ouverte pluridisciplinaire **HAL**, est destinée au dépôt et à la diffusion de documents scientifiques de niveau recherche, publiés ou non, émanant des établissements d'enseignement et de recherche français ou étrangers, des laboratoires publics ou privés.



Université
de Toulouse

THÈSE

En vue de l'obtention du
DOCTORAT DE L'UNIVERSITÉ DE TOULOUSE

Délivré par :

Institut National Polytechnique Toulouse

Discipline ou spécialité :

Dynamique des fluides

Présentée et soutenue par :

Matthias KRAUSHAAR

le : 01 Décembre 2011

Titre :

APPLICATION OF THE COMPRESSIBLE AND LOW-MACH NUMBER
APPROACHES TO LARGE-EDDY SIMULATION OF TURBULENT FLOWS IN
AERO-ENGINES

Ecole doctorale :

Mécanique, Energétique, Génie civil et Procédés

Unité de recherche :

Centre Européen de Recherche et de Formation Avancée en Calcul Scientifique

Directeur(s) de Thèse :

Dr. Laurent GICQUEL
Dr. Vincent MOUREAU

CERFACS Toulouse
CORIA Rouen

Rapporteurs :

Prof. Jens-Dominik MÜLLER
Dr. Eric SERRE

Queen Mary, University London
Université de Marseille

Membre(s) du jury :

Prof. Boniface NKONGA
Prof. Franck NICOUD
Dr. Anthony ROUX
Dr. Sébastien ROUX

Université de Nice
Université de Montpellier II
Turboméca
SNECMA

To my parents

Acknowledgements

[Remerciements/Danksagung]

First, I would like to express my gratitude to my supervisors Laurent Gicquel and Vincent Moureau for their guidance throughout my research work, for their support and encouragement as well as for their patience. I also wish to thank Thierry Poinot for giving me the opportunity to work within the CFD team of CERFACS. Furthermore, I would like to thank Thomas Lederlin and the team of Jean-Philippe Ousty for welcoming me during my secondment at Turboméca.

Likewise, I am grateful to the jury for dedicating their time to read and comment on this manuscript, as well as traveling to Toulouse the day of the defense.

Special thanks go to Antoine Dauplain, Nicolas Lamarque, Olivier Vermorel, Gabriel Staffebach, Eléonore Riber and Bénédicte Cuenot for all the helpful discussions concerning very different areas of expertise, be it spectral analysis, numerics, implementation or portability of codes, preparing courses, etc., and for every time they assisted to 'test run' of all sorts of presentations. I must also thank my collaborators and colleagues, who have contributed to or have given me valuable suggestions about my thesis.

Moreover, I would like to thank a lot my "immigration office" mates Benedetta (just where does all this energy come from???), Marta (always good for some funny office tunes - #1: My planet is your planet :D), Jorge (there are a lot less interesting links in my mailbox now!?) and Geoffroy (même si tu n'étais pas un vrai immigrant ;)), my project mate Patricia (all those meetings wouldn't have been this hilarious without your company!!!), der deutschen Clique bestehend aus Kerstin (für die frühen Kaffeepausen), Basti (für die etwas späteren), Felix (für Aktionen wie das Osterpicknick) und Jean-Matthieu (die personifizierte Europäische Union :)), Elsa (and her daily newflash on Bubu), Camilo (the voice!) and Victor (tu as trouvé un remplacement pour les canneloni?!) for a marvelous time.

And of course I owe a big thank-you to everyone who has made my life as a Ph.D. student at CERFACS and in Toulouse most gemütlich - friends or (former) colleagues, whether by discussing topical issues (or just the daily horoscope) or during French classes, by providing distractions, such as soccer, beach volley or rock climbing, or simply sitting at the Garonne enjoying the good weather...so, THANK YOU :D

Also I would like to thank the Computer Support Group for their assistance in the daily struggle with computers of any size and Michèle Campassens, Chantal Nasri, Marie Labadens and Nicole Boutet for their help with the administration.

Ein ganz herzliches Dankeschön an Sabrina für die schöne Zeit in der Toulouser Wohngemeinschaft (mit all der Kunst und den Kreuzfahrtdokus ;)). Mein größter Dank gilt schließlich meinen Eltern und meiner Familie, die mir, wie schon so oft, auch während dieses Abenteuers vorbehaltlos mit Rat und Tat zur Seite standen. Ohne euren Rückhalt würde ich jetzt nicht hier sitzen und diese Zeilen verfassen!

Abstract Large-Eddy Simulation (LES) becomes a more and more demanded tool to improve the design of aero-engines. The main reason for this request stems from the constraints imposed on the next generation low-emission engines at the industrial development level and the ability for LES to provide information on the instantaneous turbulent flow field which greatly contributes to improving the prediction of mixing and combustion thereby offering an improved prediction of the exhaust emission. The work presented in this thesis discusses two recurring issues of LES. For one, numerical schemes for LES require certain properties, i.e. low-diffusion schemes of high order of accuracy so as not to interfere with the turbulence models. To meet this purpose in the context of fully unstructured solvers, a new family of high-order time-integration schemes is proposed. With this class of schemes, the diffusion implied by the numerical scheme become adjustable and built-in. Second, since fully unsteady by nature, LES is very consuming in terms of CPU time. Even with today's supercomputers complex problems require long simulation times. Due to the low flow velocities often occurring in industrial applications, the use of a low-Mach number solver seems suitable and can lead to large reductions in CPU time if comparable to fully compressible solvers. The impact of the incompressibility assumption and the different nature of the numerical algorithms are rarely discussed. To partly answer the question, detailed comparisons are proposed for an experimental swirled configuration representative of a real burner that is simulated by LES using a fully explicit compressible solver and an incompressible solution developed at CORIA.

Keywords: *Large-Eddy Simulation, compressible, low-Mach number, numerical schemes, time integration schemes, High Performance Computing*

Résumé La Simulation aux Grandes Echelles (SGE) est de plus en plus utilisée dans les processus de développement et la conception des réacteurs aéronautiques industriels. L'une des raisons pour ce besoin résulte dans la capacité de la SGE à fournir des informations instantanées d'un écoulement turbulent augmentant la quantité des prédictions de la composition des gaz d'échappement. Ce manuscrit de thèse aborde deux sujets récurrents de la SGE. D'une part, les schémas numériques pour la SGE nécessitent certaines propriétés, notamment une précision élevée avec une diffusivité faible pour ne pas nuire aux modèles de turbulence. Afin de répondre à ce pré requis, une famille de schémas d'intégration temporelle d'ordre élevée est proposée, permettant de modifier la diffusion numérique du schéma. D'autre part, la SGE étant intrinsèquement instationnaire, elle est très consommatrice en temps CPU. De plus, une géométrie complexe prend beaucoup de temps de simulation même avec les super calculateurs d'aujourd'hui. Dans le cas particulier d'intérêt et souvent rencontré dans les applications industrielles, l'approche bas-Mach est constituée une alternative intéressante permettant de réduire le coût et le temps de retour d'une simulation LES. L'impact et la comparaison des formalismes compressible et incompressible sont toutefois rarement quantifiés, ce qui est proposé dans ce travail pour une configuration représentative d'un brûleur swirlé industriel mesuré au CORIA.

Mot clés: *Simulation aux Grandes Echelles, compressible, approche bas-Mach, schémas numériques, intégration temporelle, High Performance Computing*

Contents

Acknowledgements	i
Abstract	iii
Nomenclature	ix
1 Introduction	1
1.1 General context	1
1.2 Numerical simulation - its development and the example of CFD	3
1.3 Influence of HPC development	5
1.4 Influence of the Mach number on simulations	7
1.5 Outline of the thesis	8
I Different approaches to LES on massively parallel systems	11
2 Mathematical modelling	15
2.1 Basic equations of fluid mechanics	15
2.1.1 Conservation of mass	15
2.1.2 Conservation of momentum	15
2.1.3 Conservation of energy	16
2.1.4 The compressible Navier-Stokes equations	16
2.1.5 The low-Mach number approach	17
2.1.6 Applicability of the different approaches	17
2.2 The fundamentals of LES	18
2.2.1 The LES filtering approach	18
2.2.2 LES equations for the compressible approach	19
2.2.3 The incompressible LES equations	22
2.3 Subgrid-scale modeling	23
2.3.1 Smagorinsky model	23
2.3.2 Dynamic Smagorinsky model	23
2.3.3 Wall-Adapting Local Eddy-viscosity (WALE) model	24
3 Numerics	25
3.1 AVBP	25
3.1.1 Spatial discretization	26
3.1.2 Metrics	27
3.1.3 Weighted cell residual approach	28
3.1.4 Numerical schemes	30
3.1.5 Artificial viscosity	35
3.1.6 Boundary conditions	35

3.1.7	HPC	36
3.2	YALES2	37
3.2.1	Discretization	37
3.2.2	Numerics for the time advancement	43
3.2.3	HPC	45
II	Tunable time integration scheme for the LES	47
4	Numerical schemes for LES	51
4.1	The Two-step Runge-Kutta family of schemes	51
4.2	Development of the TRK schemes	52
4.3	Implementation of the TRK schemes in AVBP	53
4.4	Mathematical properties of the newly developed schemes	55
4.4.1	The second order scheme TRK2	56
4.4.2	The fourth order scheme TRK4	58
4.4.3	Temporal order measurements	62
4.4.4	Scalar step advection	62
4.4.5	Dissipation measurements in a turbulent flow	63
4.5	Application of TRK4 in the cell-vertex formulation to complex test-cases	66
4.5.1	Turbine blade in two dimensions	66
4.5.2	Full 3D LES of turbine blade	68
4.5.3	Full 3D LES of a reactive flow in PRECCINSTA	72
4.6	Conclusions	77
III	Comparison of the compressible and the incompressible approach to LES	79
5	Basic test cases	83
5.1	Convection of a vortex	83
5.1.1	2D vortex	84
5.1.2	3D vortex benchmark	85
6	Application to a realistic configuration	93
6.1	The test case of the KIAI burner	93
6.1.1	Numerical setup	94
6.1.2	General flow characteristics	97
6.1.3	Mean flow quantities analysis	98
6.1.4	Instantaneous results	105
6.1.5	The effect of refining the mesh	122
6.1.6	Performance	131
6.1.7	Conclusions	134

IV	Conclusions and Perspectives	137
7	Conclusion and Perspectives	139
7.1	Conclusions	139
7.2	Perspectives	141
A	Explanations for incompressible flow	143
A.1	Influence of the Mach number on compressibility	143
A.2	Derivation of the incompressible conservation equations	144
B	Application of the TRK4 time integration in AVBP to the KIAI burner	147
	Bibliography	153

Nomenclature

Roman letters

ΔP	Pressure loss	[Pa]
$\Delta x, \Delta y, \Delta z$	Characteristic length of mesh element in cartesian coordinates	[m]
\mathbf{a}^i	Eigenvector of mode i of the POD	[-]
\mathbf{C}	Correlation matrix of the eigenwert problem of the POD	[-]
\mathcal{I}	Identity matrix	[-]
$\mathbf{f}, \mathbf{g}, \mathbf{h}$	Flux vectors in x,y,z - direction	[-]
\mathbf{F}	Flux tensor of the conservative NS-equations	[$\frac{kg}{m^2s^2}$]
\mathbf{F}^I	Inviscid flux tensor of the conservative NS-equations	[$\frac{kg}{m^2s^2}$]
\mathbf{F}^V	Viscous flux tensor of the conservative NS-equations	[$\frac{kg}{m^2s^2}$]
\mathbf{f}_m	mass flux	[$\frac{kg}{m^2s}$]
\mathbf{n}	Surface normal vector	[-]
\mathbf{q}	Heat flux	[$\frac{W}{m^2}$]
\mathbf{s}	Source term vector	[-]
\mathbf{u}	Velocity vector	[$\frac{m}{s}$]
\mathbf{w}	State vector of the conserved variables	[-]
\mathbf{x}	Coordinate vector	[-]
c	Speed of sound	[$\frac{m}{s}$]
C_p	Specific heat capacity at constant pressure	[$\frac{kJ}{kgK}$]
C_{SD}	Parameter of the dynamic Smagorinsky model	[-]
C_S	Parameter of the Smagorinsky model	[-]
C_W	Parameter of the WALE model	[-]
d	Number of dimensions	[-]
D_{ext}	External nozzle diameter	[m]
D_k	Diffusion coefficient for species k	[$\frac{m^2}{s}$]
E	Total energy per unit mass	[$\frac{N}{m^2}$]
e	Total enthalpy per unit mass	[$\frac{N}{m^2}$]
$E(p)$	Efficiency for p processors	[μs]
g_{ij}	Velocity gradients of resolved scales	[$\frac{m}{s^2}$]
h	Mesh size	[m]
$h_{s,k}$	Sensible enthalpy of species k	[$\frac{J}{kg}$]
$J_{i,k}$	Diffusive flux vector component i for species k	[$\frac{mol}{m^2 \cdot s}$]
k	Material conductivity	[$\frac{W}{mK}$]
L	Characteristic length	[m]
N	Number of species of a mixture	[-]
n_v^f	Number of faces connected to node v	[-]
$n_{\Omega_j}^v$	Total number of vertices of a given cell Ω_j	[-]
N_{cell}	Total number of mesh elements within a computational grid	[-]
N_{iter}	Total number of iterations	[-]
N_{node}	Total number of nodes within a computational grid	[-]

N_{sol}	Total numbers of instantaneous solutions	[-]
P	Polygon or polyhedra of the mesh	[-]
p	Number of processors	[-]
P^*	Hydrodynamic pressure	[Pa]
P_{stat}	Static pressure	[Pa]
P_{tot}	Total pressure	[Pa]
Q	Thermal energy	[J]
q_i	Heat flux vector component in i - direction	[$\frac{W}{m^2}$]
R	Radius	[m]
$RE(p)$	Reduced efficiency for p processors	[μs]
$S(p)$	Speedup for p processors	[-]
S_{ij}	Strain rate tensor component (i,j)	[$\frac{1}{s}$]
T	Temperature of the gas	[K]
t	Time	[s]
T_{av}	Time period used to obtain temporal average.	[s]
t_p	Simulation time for p processors	[s]
t_{seq}	Reference simulation time - usually for sequential run	[s]
u, v, w	Components of the velocity vector in x, y, z-direction	[$\frac{m}{s}$]
u_τ	Friction velocity	[$\frac{m}{s}$]
$V_{i,k}$	Component i of the diffusion velocity vector for species k	[$\frac{m}{s}$]
W	Molecular weight of the mixture	[$\frac{kg}{kmol}$]
w_j	Trial function	[-]
W_k	Molecular weight of species k	[$\frac{kg}{kmol}$]
X_k	Mole fraction of species k	[-]
G	Filtering function	[-]
Greek letters		
$\delta\Omega$	Boundary of subdomain of physical space	[-]
Δt_{av}	Sample rate for the computation of the temporal average.	[s]
Δ	Filter width	[m]
ε	Specific energy	[$\frac{J}{kg}$]
ε_k	Orthogonal projection error of the POD	[-]
η^k	Kolmogorov length scale	[m]
Γ	Vortex strength	[$\frac{m^2}{s}$]
$\hat{\Delta}$	Test filter	[m]
λ	Thermal conductivity	[$\frac{W}{mK}$]
λ^i	Eigenvalue of mode i of the POD	[-]
μ	Dynamic viscosity	[$\frac{Ns}{m^2}$]
ν^t	Turbulent kinematic viscosity	[$\frac{m^2}{s}$]
Ω	Subdomain of physical space	[-]
ω	Vorticity distribution of vortex	[$\frac{1}{s}$]
ϕ	Equivalence ratio	[-]
$\phi(\mathbf{x}, t)$	Quantity of the instantaneous field.	[-]
$\phi_i(\mathbf{x})$	Test function of the Galerkin method	[-]

Π_i	Pair of nodes in YALES2	[-]
Ψ	Stream function	[-]
ρ	Mass density	[$\frac{kg}{m^3}$]
σ	Stress tensor	[$\frac{N}{m^2}$]
τ	Shear stress tensor	[$\frac{N}{m^2}$]

Non-dimensional numbers

C	Courant-Friedrichs-Lewy number
Ma	Mach number
Pr	Prandtl-number
Re	Reynolds number
Sc_k	Schmidt-number of the species k
St	Strouhal number

Operators

δ	Kronecker delta
$\langle \cdot \rangle$	Temporal average of a quantity
$\mathcal{C}(\phi^n, t)$	Discretized convection operator in general form
$\mathcal{D}(\phi^n, t)$	Discretized diffusion operator in general form
$\nabla \cdot$	Divergence

Subscripts

0	Initial values
k	k -th species
max	Maximum value of a quantity
subtri	Subtriangle to construct CV in YALES2

Superscripts

*	Non-dimensionalized quantities
+	Wall units
!	Subfilter quantity
-	Resolved part of the filtered quantity
\sim	Favre filtered quantity
t	Turbulent quantities of the SGS

Abbreviations

ACARE	Advisory Council for Aeronautics Research in Europe
ASCAC	Advanced Scientific Computing Advisory Committee
AVBP	A Very Big Problem - in-house code of CERFACS
CERFACS	Centre Européen de Recherche et de Formation en Calcul Scientifique
CFD	Computational fluid dynamics
CFL	Courant-Friedrichs-Lewy
COTS	Components Off-the-shelf
CV	Control volume
DNS	Direct Numerical Simulation
DOE	Department of Energy, United States of America
FFT	Fast Fourier Transformation
GPU	Graphic Processing Unit
HPC	High performance computing

ICAO	International Civil Aviation Organization
KIAI	Knowledge for Ignition, Acoustics and Instabilities
LES	Large-eddy Simulation
LHS	Left hand side
LINPACK	LINear equations solver PACKAge
LW	Lax-Wendroff
PDE	Partial differential equation
PIV	Particle Image Velocimetry
PLIF	Planar Laser Induced Fluorescence
POD	Propper Orthogonal Decomposition
PVC	Precessing vortex core
RAM	Random Access Memory
RANS	Reynolds-averaged Navier-Stokes
RHS	Right hand side
RK	Runge-Kutta
SGS	Subgrid-scale (\equiv Subfilter scale)
WALE	Wall-Adapting Local Eddy-viscosity
YALES2	Y et A nother LES S olver - in-house code of CORIA (Rouen)

Introduction

1.1 General context

In autumn 2010, the subcommittee on Exascale Computing, which is subordinated to the Advanced Scientific Computing Advisory Committee (ASCAC), published its report [Subcommittee on Exascale Computing 2010] on the "Opportunities and Challenges of Exascale Computing". This report is based on materials and reports that have been presented during meetings and workshops of the Department of Energy (DOE) on this topic. The subcommittee was composed of experts in a wide range of fields. The objective of the subcommittee's work was to give an opinion on how to orient the current computing capacities to profit at most of exascale systems, which represent the next generation of High Performance Computing (HPC) architectures. This report clearly shows how numerical simulation has already become an inherent part in today's scientific and industrial context and what can be expected in the near future.

Some disciplines for which numerical simulations are of advantage or even inevitable, are:

Meteorology

Accurate prediction of local as well as global climate changes.

Optimization

First and foremost this is about the optimization of technical procedures or designs. This is particularly interesting in applications, for which experiments are too dangerous or simply impossible, e. g. when working on combustion. A side-effect is that, since parameter of the numerical model studies can be conducted very easily, the optimization enables to reduce the number of experimental test runs, which can be extremely expensive.

Scientific insight

The first large-scale application of numerical simulation is seen in the work performed within the Manhattan Project during World War II to model the process of nuclear detonation. Fortunately, military research did not stay the only application and today, computer simulations also are used, e. g., to study new ways of energy production, medical problems, climate change etc.

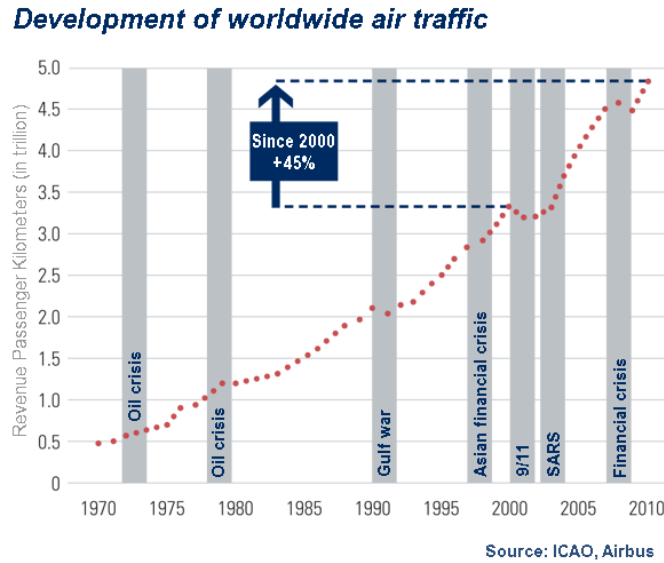


Figure 1.1: *Development of the worldwide transported flight passengers.* Source: ICAO / Airbus

Safety

Other fields of application are related to security matters. An example is the prediction of the safety in case of a fire of industrial facilities or in the case of wild fires.

An interesting application from the field of Computational Fluid Dynamics (CFD) are aircraft engines. New regulations stipulate a reduction of the exhausted greenhouse gases for jet engines, e. g. a reduction of CO_2 by 50% and of NO_x by 80% in 2020 as demanded by the *Advisory Council for Aeronautics Research in Europe* (ACARE). This is mainly due to the continuously growing demand for air travel, be it the transport of people or goods. Figure 1.1 presents the development of the *Revenue Passenger Kilometers* for the last 40 years. Amongst experts it is believed that this tendency will continue. N. Teyssier, e. g., presented during the *37th session of the ICAO assembly (2010)* a forecast, stating a growth of 4.7% for 2030. Although the overall contribution of air traffic to the worldwide emitted greenhouse gases is approximately 2%, their release in high altitudes renders them more harmful.

The growing number of flights generally is dealt with extending the operating hours of airports, which, in addition, are increasingly often situated within urban space. Hence, the topic noise pollution is also becoming more and more important. Taking only these two constraints, the impact on the development of a system such as an aero-engine is very high. At this point it becomes obvious that for such a project all aspects of numerical simulations have to be considered, starting from the development of models up to their application in solvers on super-computers.

1.2 Numerical simulation - its development and the example of CFD

In CFD three main methodologies are known and can be used for the simulation of turbulent flow.

Reynolds-Averaged Navier-Stokes (RANS)

This approach [Launder 1972, Pope 2002] consists in averaging the instantaneous balance equations. In order to be capable of performing the calculations, closure models have to be provided. For turbulent combustion, a turbulence model to capture the flow dynamics is combined with a model for turbulent combustion, which takes into account the chemical species conversion and the heat release. Such a simulation can be interpreted as if the average of different realizations (or cycles for periodic flows) is calculated. The computational cost for this simulation type is rather small.

Direct Numerical Simulation (DNS)

DNS is working without any turbulence or chemical model by solving the full instantaneous Navier-Stokes equations [Leonard 1995]. The complete spectrum of turbulent length scales as well as the reacting zones are resolved. It is the small turbulent and flame structures that require a very fine mesh, which renders DNS not only very accurate but also very costly and thus, DNS remains limited to academic cases. Its advancement was possible mainly due to the development in High Performance Computing (HPC), which will be treated in section 1.3. By this means DNS has provided much insight, e. g. into turbulent combustion flow analysis.

Large-Eddy Simulation (LES)

In LES the large turbulent structures (eddies) are resolved whereas the smaller scales are modeled. In this case the balance equations are obtained by applying a filter to the instantaneous Navier-Stokes equations [Pope 2002, Sagaut 2002]. Equally as for the turbulent structures, the large scale contribution of the flame is captured by the LES equations. A sub-filter model has to be provided to consider the effects of the small scales of turbulence as well as their interaction with the flame front.

Since the very beginning of numerical simulation in the early 1940s, an enormous progress has been made. Regarding the report of the ASCAC, a good example for CFD applications are LES of gas turbines, see Fig. 1.2. In the beginning, the geometries stayed very simple, i. e. academic test burners. With the increase in computing capacities, the complexity started to rise and about 10 years later, the ignition process of a complete combustor composed of 18 sections using two-phase flow simulations could be computed [Boileau 2008]. This simulation, performed on an unstructured mesh of 19 million cells, took 160 execution hours on 700 processors of a CRAY XT2. Nevertheless, this represents just one single component in the complex system of a jet engine.

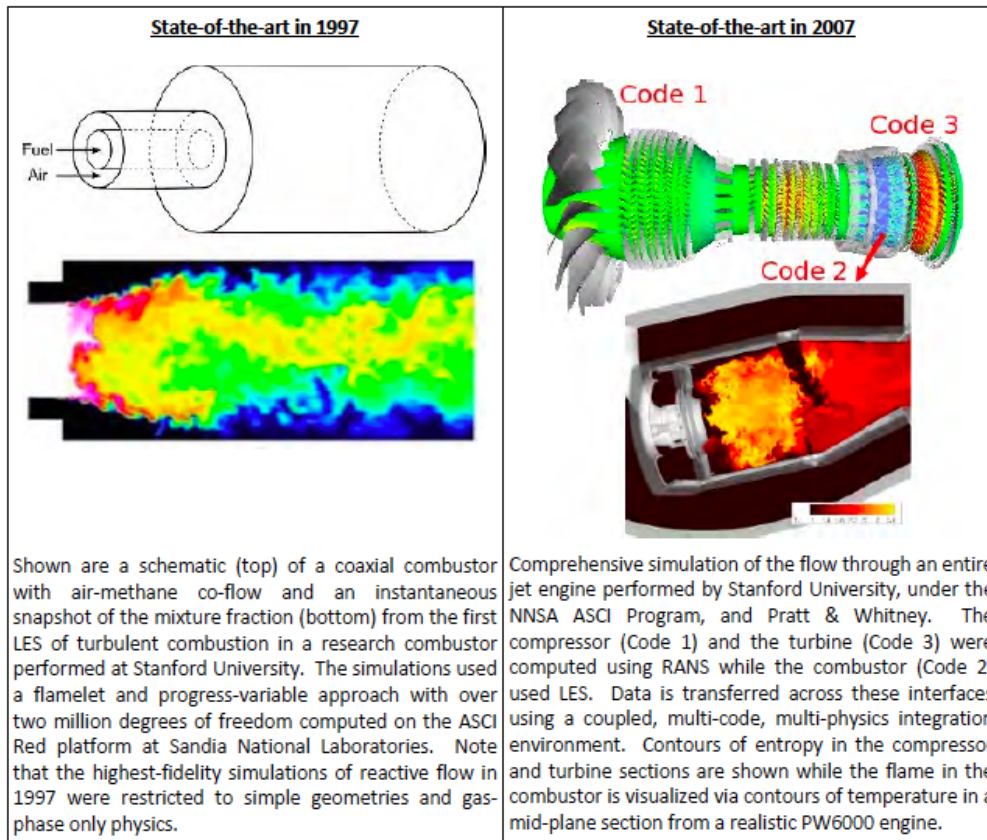


Figure 1.2: Source: *Opportunities and Challenges of Exascale Computing*, report from ASCAC - subcommittee on exascale computing for the Department of Energy (USA), 2010 - [Subcommittee on Exascale Computing 2010]

The need to compute complete systems, brings up a new dimension of complexity. Looking at a complete gas turbine different physical phenomena require different simulation approaches. Today, this can be overcome by coupling different solver types, treating different parts of the application. In [Medic 2006], RANS simulations for the compressor and the turbine have been coupled to LES of the combustion chamber. This choice was taken because RANS has a long history in the prediction of boundary layers needed here for the accurate prediction of the flow around the blades of the compressor and the turbine.

Although these examples are encouraging, a lot has to be improved. Examples are the representation of chemistry in the simulations, in order to predict and optimize the composition of the exhaust gases, the consideration of the impact of heat radiation and heat transfer on the flow [Amaya 2010] or the flame structure and its stability in turbulent combustion [Franzelli 2011], just to name a few.

So far, the advancement of CFD has rather been looked at from a scientific point of view. Of course, numerical simulation has found its way into the daily design process, mainly

due to the advantage of the price-performance ratio. Companies, such as Turboméca, MTU or Rolls Royce, depend on such above mentioned developments. But keeping in mind that the companies are subjected to economic constraints, it is beyond all questions to wait more than over night for simulation results. Furthermore, the computing capacities at hand in the industry are far from being comparable to what is available to research facilities. Hence, most industrial use of CFD concerns the optimization or characterization of single parts.

1.3 Influence of HPC development

As stated in section 1.2, computational power was and still is one of the big influencing factors for numerical simulations, although its development was rather steady. Gordon Moore stated in 1965 that "the complexity for minimum component costs has increased at a rate of roughly a factor of two per year" and that "Over the longer term, the rate of increase is a bit more uncertain, although there is no reason to believe it will not remain nearly constant for at least 10 years" [Moore 1965]. Figure 1.3 reveals that this so-called "Moore's law" turned out to be correct for almost half a century. A quite impressive

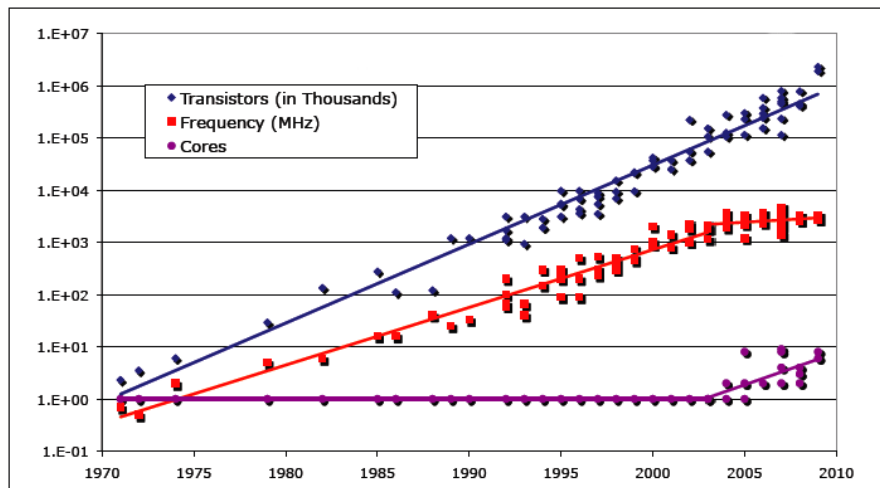


Figure 1.3: Moore's law from 1965 turned out to be very accurate (blue line). Nevertheless, a change occurred passing from high clock speeds for fast sequential processing to an increase of the number of cores per processor.

example of the advancements made so far was demonstrated by Dr. Jack Dongarra (University of Tennessee). His research group implemented the LINPACK computing benchmark [Dongarra 1988] on the Apple's iPad 2. This linear algebra test, evaluating the mathematical capabilities of computers, is also the basis for the *top500* list of supercomputers (www.top500.org). The tablet computer returned a peak performance of 620 Mflop/s using only one of the two cores available. The value itself is not really outstanding compared to today's supercomputers, but when compared to the supercomputers that made an appearance in one of the *top500* lists, see Fig. 1.4, it would

have been the 500th fastest computer in 1994. This result becomes even more significant,

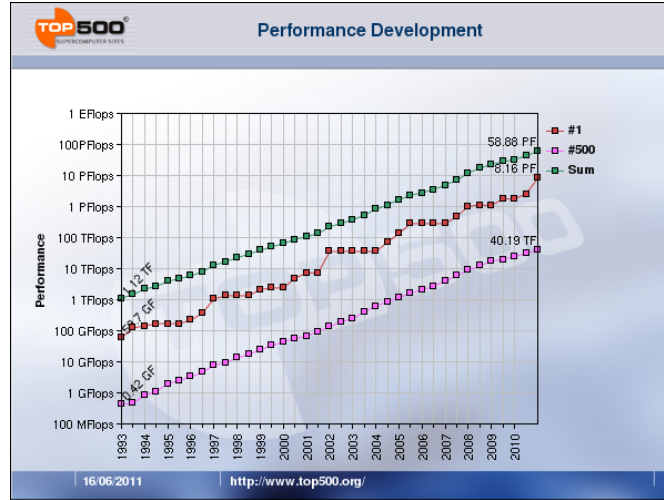


Figure 1.4: Development of computing power - Source: www.top500.org, June 2011

when compared to the vector supercomputer *Cray-2* of 1985, which was still at position 242 of the *top500* list in November 1993. The peak performance of one of its processors is indicated equal to 488 Mflop/s and 4 processors were the maximum configuration. In contrast to the tablet, the *Cray-2* measured 1.35m in height and 1.15m in diameter and weighed about 2.5 tons, of which one third accounted for the cooling liquid needed to keep the computer running.

Coming back to Fig. 1.3, a change occurring around the year 2003 can be noticed. The graph depicts that the clock speed starts attaining an asymptotic value. At the same time as the processor frequency started stagnating, the number of cores per processor increases.

$$\begin{aligned}
 \text{Power} &\propto \text{Voltage}^2 \text{ Frequency} \\
 \text{Frequency} &\propto \text{Voltage} \\
 \Rightarrow \text{Power} &\propto \text{Frequency}^3
 \end{aligned} \tag{1.1}$$

This is simply due to the power consumed by the systems and becomes clear when looking at the relations in Eq. (1.1). Figure 1.5 shows the characteristics of the five fastest computers of the *top500* list, confirming this trend. The (fast) increasing number of cores within a computer system is even more amplified by the introduction of graphic processors (GPU) as computing resources. With this effect a change in responsibilities occurs. While for many years the constraint for simulations, like LES or DNS, was due to the lack of computing power, the task of exploiting massively parallel systems has been shifted and became more and more a software issue. Stated already in 1997 by Keyes in [Keyes 1997], today attention has to be paid at different levels, namely by the software developer at the algorithmic level, the system developer at the compiler and runtime level and, lastly, at the hardware level. Still today, nearly 25 years after this

Rank	Site	Computer/Year Vendor	Cores	R_{\max}	R_{peak}	Power
1	RIKEN Advanced Institute for Computational Science (AICS) Japan	K computer, SPARC64 VIIIx 2.0GHz, Tofu interconnect / 2011 Fujitsu	548352	8162.00	8773.63	9898.56
2	National Supercomputing Center in Tianjin China	Tianhe-1A - NUDT TH MPP, X5670 2.93GHz 6C, NVIDIA GPU, FT-1000 8C / 2010 NUDT	186368	2566.00	4701.00	4040.00
3	DOE/SC/Oak Ridge National Laboratory United States	Jaguar - Cray XT5-HE Opteron 6-core 2.6 GHz / 2009 Cray Inc.	224162	1759.00	2331.00	6950.60
4	National Supercomputing Centre in Shenzhen (NSCS) China	Nebulae - Dawning TC3600 Blade, Intel X5650, NVidia Tesla C2050 GPU / 2010 Dawning	120640	1271.00	2984.30	2580.00
5	GSIC Center, Tokyo Institute of Technology Japan	TSUBAME 2.0 - HP ProLiant SL390s G7 Xeon 6C X5670, Nvidia GPU, Linux/Windows / 2010 NEC/HP	73278	1192.00	2287.63	1398.61

Figure 1.5: *The characteristics of the top five supercomputers of the top500 list - Source: www.top500.org, June 2011*

statement, the number of codes capable of capitalizing on the rapidly growing number of cores is rather small.

Concerning CFD applications, an issue is the augmented use of superscalar cache-based cores following COTS (Components Off-the-shelf). This approach allowed to accelerate the development and reduce the costs by using technology that is found in standard personal computers. It was noted in [Gicquel 2011, Gourdain 2009a, Gourdain 2009b] that these processors are rather inappropriate for these applications (common computing efficiency of CFD codes $< 20\%$). This is mainly due to the fact that for CFD problems large amounts of data are processed and lots of communications between the cache and the cores are required.

1.4 Influence of the Mach number on simulations

Very often the velocities occurring in flows are rather small compared to the speed of sound, e. g. in aero-engine combustors. Mathematically speaking, this is expressed by the Mach number tending towards 0. This dimensionless quantity represents the ratio of the convective velocity u to the speed of sound c :

$$Ma = \frac{u}{c}. \quad (1.2)$$

This is not supposed to mean that the convective velocity $v = 0$, but that $v \ll c$ or $c \rightarrow \infty$ compared to v [Meister 2002], respectively. In terms of physics, this means that in such flows the propagation of small, isentropic disturbances (e. g. pressure waves), which happens at the speed of sound, is much faster than the advection of the flow. Thus, the pressure is leveled out more rapidly throughout the domain of interest. Due to this effect, differences within the velocity field are not able to create pressure fluctuations and, hence, no density fluctuations, too. The flow is considered incompressible. It is shown in appendix A.1 that density variations in low-Mach number flows are small, since they are scaled by the square of the Mach number. To give an example, the change in density of an air flow at ambient temperature and for $Ma = 0.14$ is about 1%. In general, a flow at

a Mach number inferior to 0.3 is considered to be incompressible. The lack of pressure fluctuations prohibits the occurrence of acoustics in the flow field. Consequently, this impacts the time step size of the simulation and hence, the time needed to advance the solution to the final simulation time of interest. This becomes obvious when looking at the Courant-Friedrichs-Lewy (CFL) number, denoted C in the following. It represents a very important quantity in numerics, which basically defines the distance travelled by information during one time step. It thus plays a major role in stability of numerical schemes, which will become obvious in chapter 4. The CFL number is defined as follows

$$C = v \frac{\Delta t}{\Delta x}, \quad (1.3)$$

where v represents a velocity, more precisely the highest velocity at which information is transported within the simulation. In the case of a compressible simulation disturbances are transported at the speed of sound and thus, $v = |u + c|$, with u being the convective velocity of the flow field. For the low-Mach number approach, on the other hand, $v = |u|$ since no acoustics occurs. The relation between the compressible (a.k.a. *acoustic*) and the incompressible (a.k.a. *convective*) CFL number yields:

$$\begin{aligned} C_{acoustic} &= |u + c| \frac{\Delta t}{\Delta x} = \frac{u \Delta t}{\Delta x} \left(1 + \frac{1}{Ma} \right) = C_{convective} \left(1 + \frac{1}{Ma} \right) \\ &\Rightarrow C_{acoustic} \left(\frac{Ma}{Ma + 1} \right) = C_{convective} \end{aligned} \quad (1.4)$$

Considering again the flow at $Ma = 0.14$ from the above example, this means that the acoustic CFL number is only about 12% of the convective one. For a given mesh size Δx in reverse, the time step obtained in the low-Mach number computation is about eight times higher than for the compressible one. This represents a considerable gain in computational time, which still is one of the main issues of LES, even when having access to today's supercomputers.

Nevertheless, this is only one aspect that has to be considered for future codes conceived for HPC. The choice of one approach or another impacts the solver's design down to the algorithmic level. For the low-Mach number approach, e. g., an implicit method is of essence due to the nature of the equations (see section 2.1.5). In the case of a compressible solver this is no real constraint, but more of an option. In general, the question whether future CFD solvers are preferably applying the one or the other is anything but clear from a today's point of view and the present work contributes to this discussion as presented in the outline of the thesis below.

1.5 Outline of the thesis

The contribution of the present work is split into two main parts. The first one is dedicated to LES in order to improve the accuracy and robustness of numerical simulation. Therefore, a newly developed high-order, low-dissipation scheme for time integration was implemented into an already existing unstructured HPC-LES code to the extent of its use to ever-more-complex flow problems.

The second part then takes into account the explanations of this chapter and presents a study comparing two state of the art LES solvers for CFD applications, a compressible and an incompressible one. The objective is to quantify the impact of each approach on LES predictions as well as on the code's performance for HPC applications. The structure of the document is the following:

Part I

A description of the problem in form of the governing equations for LES of the compressible and the incompressible approach is given. The two CFD solvers, used during this dissertation, are then presented in more detail.

Part II

A newly developed time integration family of schemes is introduced. After describing the construction of the second and fourth order method, the particularities for its implementation in the cell-vertex framework of the AVBP code (CERFACS, Toulouse) are specified. Then, the mathematical properties are evaluated and the applicability of the fourth order scheme is presented by means of test cases of different complexity in 2D and 3D.

Part III

Dedicated to the comparison of the compressible and the incompressible approach, different test cases are presented that are computed using the CFD solvers AVBP and YALES2 (CORIA, Rouen). Both codes are designed to work on massively parallel architectures. In order to obtain representative statements for the behavior of both codes regarding realistic applications, the test case studied within the European project *KIAI*¹ is simulated. This combustor uses a one stage swirled injection system that is close to what can be found in industrial applications.

Chapter 5

Representing the last chapter of the dissertation it contains the conclusions that can be drawn from this work. To finish, possible future developments and perspectives are listed.

This dissertation was accomplished within the project *MYPLANET*, which is organized in the *Seventh Framework Program* of the European Commission. A part of the Ph.D. thesis consisted in a secondment to Turboméca (Bordes - FRANCE), which had as objective to evaluate the possibilities of performing massively parallel simulations using the incompressible solver YALES2 in an industrial framework.

¹Knowledge for Ignition, Acoustics and Instabilities - project within *Seventh Framework Program* of the Marie-Curie Actions of the European Commission.

Part I

Different approaches to LES on massively parallel systems

The present work is in the field of LES. But before getting into detail of the time integration scheme and the comparison of the compressible and the low-Mach number approaches, this chapter recalls the fundamentals that lead to LES and their implementation in the state-of-the-art CFD solvers AVBP and YALES2.

Chapter 2 is dedicated to the mathematical basics and the resulting differences for the compressible and the low-Mach number approaches. Following, in Chapter 3 numerical aspects of CFD in general and of LES in particular are outlined, as well as the implementation of the so far presented equations and models in the deployed solvers is covered.

2	Mathematical modelling	15
2.1	Basic equations of fluid mechanics	15
2.1.1	Conservation of mass	15
2.1.2	Conservation of momentum	15
2.1.3	Conservation of energy	16
2.1.4	The compressible Navier-Stokes equations	16
2.1.5	The low-Mach number approach	17
2.1.6	Applicability of the different approaches	17
2.2	The fundamentals of LES	18
2.2.1	The LES filtering approach	18
2.2.2	LES equations for the compressible approach	19
2.2.3	The incompressible LES equations	22
2.3	Subgrid-scale modeling	23
2.3.1	Smagorinsky model	23
2.3.2	Dynamic Smagorinsky model	23
2.3.3	Wall-Adapting Local Eddy-viscosity (WALE) model	24
3	Numerics	25
3.1	AVBP	25
3.1.1	Spatial discretization	26
3.1.2	Metrics	27
3.1.3	Weighted cell residual approach	28
3.1.3.1	The gradient operator	29
3.1.4	Numerical schemes	30
3.1.4.1	Central differences	30
3.1.4.2	Lax-Wendroff scheme	30
3.1.4.3	The Two-step Taylor-Galerkin schemes	31
3.1.4.4	Finite element approach	32
3.1.4.5	The time step Δt	35
3.1.5	Artificial viscosity	35
3.1.6	Boundary conditions	35
3.1.7	HPC	36
3.2	YALES2	37

3.2.1	Discretization	37
3.2.1.1	Higher order spatial discretization	38
3.2.2	Numerics for the time advancement	43
3.2.2.1	The fractional step method	43
3.2.2.2	Time integration	44
3.2.3	HPC	45

Mathematical modelling

This chapter deals with the mathematical modeling of fluid mechanics with a focus on the differences between the compressible and the low-Mach number assumptions, as well as their application to LES.

2.1 Basic equations of fluid mechanics

2.1.1 Conservation of mass

Considering the flow of a fluid, the central equations describing its motion are the conservation laws for mass, momentum and energy. Starting with the equation for mass conservation, it can be expressed in its integral form as

$$\frac{\partial}{\partial t} \int_{\Omega} \rho dV = - \int_{\partial\Omega} \mathbf{f}_m \cdot \mathbf{n} dS. \quad (2.1)$$

In Eq. (2.1) Ω represents any subdomain of physical space and $\partial\Omega$ denotes its boundaries. ρ stands for the density, or more precisely mass density. The Right Hand Side (RHS) term is the inner product of the mass flow \mathbf{f}_m with the normalized and outward pointing normal vector \mathbf{n} of the surface $\partial\Omega$. The interpretation of Eq. (2.1) is that the change in time of mass within any subdomain Ω of a fluid flow is due to mass flux across the boundary $\partial\Omega$. Supposing ρ and \mathbf{f}_m are continuously differentiable, the differential and integral operator of the left hand side can be interchanged. Furthermore, applying the divergence theorem to the RHS leads to the following formulation

$$\int_{\Omega} \left(\frac{\partial \rho}{\partial t} + \nabla \cdot \mathbf{f}_m \right) dV = 0. \quad (2.2)$$

Now, assuming that Eq. (2.2) is valid for any subdomain Ω , it can be stated that the integrand will be 0 everywhere and defining $\mathbf{f}_m = (\rho \mathbf{u})$, it can be written as

$$\frac{\partial \rho}{\partial t} + \nabla \cdot (\rho \mathbf{u}) = 0, \quad (2.3)$$

where the term \mathbf{u} is the velocity vector.

2.1.2 Conservation of momentum

By using the same procedure as for the conservation of mass, the integral formulation of the momentum conservation equation (2.4)

$$\frac{\partial}{\partial t} \int_{\Omega} (\rho \mathbf{u}) dV = - \int_{\partial\Omega} ((\rho \mathbf{u}) \circ \mathbf{u}) \cdot \mathbf{n} dS + \int_{\partial\Omega} \boldsymbol{\sigma} \cdot \mathbf{n} dS + \int_{\partial\Omega} g dV \quad (2.4)$$

can be transformed into

$$\frac{\partial(\rho\mathbf{u})}{\partial t} + \nabla \cdot ((\rho\mathbf{u}) \circ \mathbf{u}) + \nabla P = \nabla \cdot \tau + \mathbf{g}. \quad (2.5)$$

In Eqs. (2.4) and (2.5) $(\rho\mathbf{u})$ is the momentum per mass unit. Also comprised in this transformation is the expression of the stress tensor σ as a sum of normal and shear stresses:

$$\sigma = \tau - P\mathcal{I}, \quad (2.6)$$

whith τ being the shear stress tensor and $P\mathcal{I}$ representing the normal stresses due to pressure, where \mathcal{I} is the identity matrix. The last term on the RHS of Eqs. (2.4) and (2.5) takes into account volumetric forces, such as gravity. The conservation equation of momentum is a vector equation.

2.1.3 Conservation of energy

Next, the energy conservation is considered. Defining e to be the total energy per unit mass, the integral formulation holds

$$\begin{aligned} \frac{\partial}{\partial t} \int_{\Omega} e dV = & - \int_{\partial\Omega} \mathbf{u}(e + P) \cdot \mathbf{n} dS + \int_{\partial\Omega} (\tau\mathbf{u}) \cdot \mathbf{n} dS \\ & - \int_{\partial\Omega} \mathbf{q} \cdot \mathbf{n} dS + \int_{\Omega} \mathbf{g} \cdot \mathbf{u} dV + \int_{\Omega} Q dV. \end{aligned} \quad (2.7)$$

Equation (2.7) relates the energy transported by the flow (LHS) to the work done to the fluid by its environment. The newly introduced variables are the heat flux $\mathbf{q} = -k\nabla T$ as well as a certain amount of thermal energy Q , which is added to the fluid. In exactly the same way as for the balance equations of mass and momentum, Eq. (2.7) can be transformed into a partial differential equation (PDE).

2.1.4 The compressible Navier-Stokes equations

The PDEs derived from Eqs. (2.1), (2.4) and (2.7) form the system of conservation equations also known as the **Navier-Stokes equations**:

$$\frac{\partial\rho}{\partial t} + \nabla \cdot (\rho\mathbf{u}) = 0, \quad (2.8)$$

$$\frac{\partial(\rho\mathbf{u})}{\partial t} + \nabla \cdot ((\rho\mathbf{u}) \circ \mathbf{u}) + \nabla P = \nabla \cdot \tau + \mathbf{g}, \quad (2.9)$$

$$\frac{\partial e}{\partial t} + \nabla \cdot (\mathbf{u}(e + P)) = \nabla \cdot (\tau\mathbf{u}) - \nabla \cdot \mathbf{q} + Q. \quad (2.10)$$

In order to be able to solve this system, supplementary information is necessary. Therefore, the equation of state is taken into account, linking the pressure to the other variables and thus closing the system:

$$e = \rho\varepsilon + \frac{1}{2}\rho\mathbf{u}^2, \quad (2.11)$$

where ε denotes the specific energy.

Equation (2.8) to Eq. (2.10) describe the viscous flow of a non-reacting **compressible** fluid. For the case of reacting flows, the contribution of the different species to the balance equations has to be considered. An explicit description of the resulting conservation laws can be found in [Poinsot 2005].

2.1.5 The low-Mach number approach

Flows at a Mach number $Ma \leq 0.3$ are considered incompressible, as pointed out in section 1.4. Therefore, the incompressible Navier-Stokes equations are presented here. They are obtained based on Eqs. (2.8) - (2.10) in the limit for the Mach number tending to zero. The equations in this case are

$$\frac{\partial \mathbf{u}}{\partial t} + (\mathbf{u} \cdot \nabla) \mathbf{u} = -\nabla \frac{1}{\rho} P^* + \nu \Delta \mathbf{u}, \quad (2.12)$$

$$\nabla \cdot \mathbf{u} = 0. \quad (2.13)$$

A description of the derivation of this set of equations is given in appendix A.2. The missing time derivative of the density in Eq. (2.13), which represents the conservation of mass, is responsible for a flow, initiated with spatially constant density, to keep this quantity constant also over time. The momentum equation (2.12) can thus be divided by the mass density. It has to be pointed out that the pressure of the momentum equation (2.12) P^* is a purely hydrodynamic quantity, which ensures the velocity field to be divergence free.

From a mathematical point of view, the system of equations is closed, since two equations are available for two unknowns. Nevertheless, due to the strong coupling of the pressure and the velocity field, no explicit form to determine the pressure is given. By taking the divergence of Eq. (2.12) and applying the divergence free condition of Eq. (2.13) to the resulting terms, the Poisson equation for the pressure is obtained:

$$\Delta P^* = -\rho \nabla \cdot [(\mathbf{u} \cdot \nabla) \mathbf{u}]. \quad (2.14)$$

Equation (2.14) represents an elliptic equation and has to be treated numerically by using an iterative solver. This is one of the issues that section 1.4 was hinting at. The options available with YALES2, in order to resolve Eq. (2.14), are outlined in section 3.2.2.1.

2.1.6 Applicability of the different approaches

Many of today's CFD applications do not exceed the compressibility limit of $Ma = 0.3$ and thus, can be simulated using either the compressible or the incompressible approach. The choice depends on different aspects. Regarding the physics, it is obvious that a flow for which the acoustics are of importance or where shock waves occur are less likely to be treated with the incompressible approach. As stated in section 1.4, this is due to the fact that pressure fluctuations do not occur and hence, the acoustic field is not contained in its equations.

Although this might seem quite restrictive, there is still a wide range of flows for which the low-Mach number approach is interesting. This can be anything from pipe flows up to the flow around a vehicle. Another example is the flow inside an aero-engine combustion chamber as will be considered later on in this work.

Numerical considerations also have to be taken into account, e. g. the number of equations and variables that have to be solved or the nature of the equations at hand. This will be the subject of chapter 3. Prior to this, though, the equations solved in LES will be outlined in the next section.

2.2 The fundamentals of LES

The very beginning of Large-Eddy simulation emerges from meteorological application [Smagorinsky 1963, Lilly 1967, Deardorff 1970]. Although the emphasis lied on meteorology and simple geometry flows for quite a while [Mason 1994, Schumann 1975, Moin 1982], more realistic applications of complex geometries were taken into consideration more recently [Ham 2003, James 2006, Boudier 2007, Boileau 2008, Boudier 2009, Staffelbach 2009]. As pointed out in the introduction, LES is situated between RANS

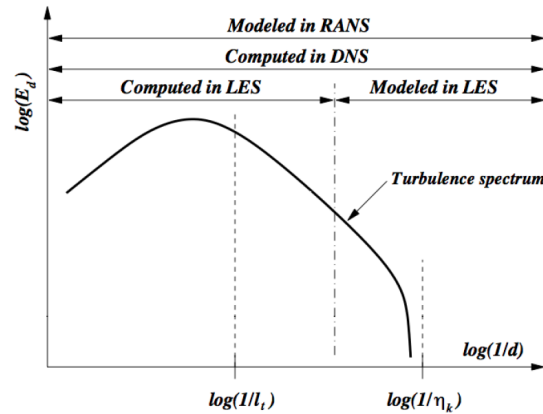


Figure 2.1: *Turbulent kinetic energy spectrum - l_t representing the largest turbulent structures, η_k the smallest (so-called Kolmogorov) scales. Source: [Garcia 2009]*

simulation, in which all turbulent information is modeled, and DNS, resolving the complete length scale spectrum of turbulence. Figure 2.1 illustrates the difference between RANS, LES and DNS using the example of the turbulent kinetic energy spectrum (E_d), which is plotted as a function of the inverse length scale of the turbulent structures.

2.2.1 The LES filtering approach

The cut off between the structures of a turbulent flow that are resolved and the ones, which are modeled, is done by spatially filtering the underlying balance equations. This procedure can be interpreted as the convolution of a quantity of interest ϕ with a low-pass

filter function G [Leonard 1974]. Mathematically this yields:

$$\bar{\phi} = \int_{\Omega} \phi(\mathbf{x}') G(\mathbf{x} - \mathbf{x}', \Delta) d\mathbf{x}', \quad (2.15)$$

where Ω is the entire domain of interest. In general, G is chosen a box filter or a Gaussian filter [Sagaut 2002]. The filtered quantity, denoted using an overbar ($\bar{\cdot}$), represents the resolved turbulent structures (*large eddies*). All structures smaller than the filter width Δ need to be modeled and are described by

$$\phi' = \phi - \bar{\phi}. \quad (2.16)$$

In order to account for density fluctuations when applying filtering to the compressible balance equations, density weighted Favre-filtering [Favre 1969] can be applied, denoted by a tilde over the variable in consideration. By this means, the occurrence of subgrid-scale terms in the mass balance equation is anticipated. A quantity subject to the Favre filter is defined as follows:

$$\tilde{\phi} = \frac{\overline{\rho\phi}}{\bar{\rho}}. \quad (2.17)$$

An important requirement regarding the filter G is, besides the conservation of constants and its linearity, that it commutes with spatial and temporal derivatives. This is the case for homogeneous filters, i. e. with a constant filter width Δ in space. It is obvious that if the filter size is determined by the mesh size, the spatial variation of the grid cells will suspend this condition. It was shown by Ghosal and Moin [Ghosal 1995] that the impact of commuting the operators even for non-homogeneous filters, such as computational grids, can be neglected. Therefore, all the unresolved structures are considered to be those smaller than the grid size, thus *sub-grid scales (SGS)*.

2.2.2 LES equations for the compressible approach

For reasons of readability, the equations are expressed in vectorial notation of the conserved variables:

$$\frac{\partial \bar{\mathbf{w}}}{\partial t} + \nabla \cdot \bar{\mathbf{F}} = \bar{\mathbf{s}}, \quad (2.18)$$

with $\bar{\mathbf{w}} = \left(\bar{\rho}, \bar{\rho}u, \bar{\rho}v, \bar{\rho}w, \bar{\rho}E, \bar{\rho}Y_k \right)^T$ being the state vector and $\bar{\mathbf{s}}$ representing the filtered source terms.

The flux tensor $\bar{\mathbf{F}}$ in Eq. (2.18) consists of three contributions, $\bar{\mathbf{F}}^I$ being the resolved inviscid or convective fluxes, $\bar{\mathbf{F}}^V$ the resolved viscous or diffusive fluxes and $\bar{\mathbf{F}}^t$ the subgrid-scale terms, which have to be modeled. Their definition, and that of the other terms, is given below:

The components of the inviscid terms $\bar{\mathbf{F}}^I$

$$\bar{\mathbf{f}}^I = \begin{pmatrix} \overline{\rho \tilde{u}^2 + P} \\ \overline{\rho \tilde{u} \tilde{v}} \\ \overline{\rho \tilde{u} \tilde{w}} \\ \overline{\rho \tilde{E} \tilde{u} + P u} \\ \overline{\rho_k \tilde{u}} \end{pmatrix}, \bar{\mathbf{g}}^I = \begin{pmatrix} \overline{\rho \tilde{u} \tilde{v}} \\ \overline{\rho \tilde{v}^2 + P} \\ \overline{\rho \tilde{v} \tilde{w}} \\ \overline{\rho \tilde{E} \tilde{v} + P v} \\ \overline{\rho_k \tilde{v}} \end{pmatrix}, \bar{\mathbf{h}}^I = \begin{pmatrix} \overline{\rho \tilde{u} \tilde{w}} \\ \overline{\rho \tilde{v} \tilde{w}} \\ \overline{\rho \tilde{w}^2 + P} \\ \overline{\rho \tilde{E} \tilde{w} + P w} \\ \overline{\rho_k \tilde{w}} \end{pmatrix}. \quad (2.19)$$

The components of the viscous flux tensor $\bar{\mathbf{F}}^V$

$$\bar{\mathbf{f}}^V = \begin{pmatrix} -\overline{\tau_{xx}} \\ -\overline{\tau_{xy}} \\ -\overline{\tau_{xz}} \\ -(\overline{u\tau_{xx}} + \overline{v\tau_{xy}} + \overline{w\tau_{xz}}) + \overline{q_x} \\ \overline{J_{x,k}} \end{pmatrix}, \quad (2.20)$$

$$\bar{\mathbf{g}}^V = \begin{pmatrix} -\overline{\tau_{xy}} \\ -\overline{\tau_{yy}} \\ -\overline{\tau_{yz}} \\ -(\overline{u\tau_{xy}} + \overline{v\tau_{yy}} + \overline{w\tau_{yz}}) + \overline{q_y} \\ \overline{J_{y,k}} \end{pmatrix}, \quad (2.21)$$

$$\bar{\mathbf{h}}^V = \begin{pmatrix} -\overline{\tau_{xz}} \\ -\overline{\tau_{yz}} \\ -\overline{\tau_{zz}} \\ -(\overline{u\tau_{xz}} + \overline{v\tau_{yz}} + \overline{w\tau_{zz}}) + \overline{q_z} \\ \overline{J_{z,k}} \end{pmatrix}. \quad (2.22)$$

The filtered diffusion terms for non-reacting flows are defined as follows ([Poinsot 2005], Chapter 4):

Laminar filtered stress tensor

$$\overline{\tau_{ij}} = 2\mu \overline{\left(S_{ij} - \frac{1}{3} \delta_{ij} S_{ll} \right)} \quad (2.23)$$

$$\approx 2\bar{\mu} \left(\tilde{S}_{ij} - \frac{1}{3} \delta_{ij} \tilde{S}_{ll} \right) \quad (2.24)$$

$$\text{with: } \tilde{S}_{ij} = \frac{1}{2} \left(\frac{\partial \tilde{u}_j}{\partial x_i} + \frac{\partial \tilde{u}_i}{\partial x_j} \right) \text{ and } \bar{\mu} = \mu(\tilde{T})$$

Diffusive species flux

$$\overline{J_{i,k}} = -\rho \overline{\left(D_k \frac{W_k}{W} \frac{\partial X_k}{\partial x_i} - Y_k V_{i,k} \right)} \quad (2.25)$$

$$\approx -\bar{\rho} \overline{\left(\bar{D}_k \frac{W_k}{W} \frac{\partial \tilde{X}_k}{\partial x_i} - \tilde{Y}_k \tilde{V}_{i,k} \right)} \quad (2.26)$$

$$\text{with: } \tilde{V}_{i,k} = \sum_{k=1}^N \bar{D}_k \frac{W_k}{W} \frac{\partial \tilde{X}_k}{\partial x_i} \text{ and } \bar{D}_k \approx \frac{\bar{\mu}}{\rho S c_k} \quad (2.27)$$

Heat flux

$$\bar{q}_i = -\lambda \frac{\partial \bar{T}}{\partial x_i} + \sum_{k=1}^N \overline{J_{i,k} h_{s,k}} \quad (2.28)$$

$$\approx -\bar{\lambda} \frac{\partial \tilde{T}}{\partial x_i} + \sum_{k=1}^N \bar{J}_{i,k} \tilde{h}_{s,k} \quad (2.29)$$

$$\text{with: } \bar{\lambda} \approx \frac{\bar{\mu} \bar{C}_p (\tilde{T})}{Pr}. \quad (2.30)$$

These closure terms imply that the spatial variations of molecular diffusion fluxes are negligible and that a simple gradient assumption is sufficient.

The components of the turbulent SGS flux tensor $\bar{\mathbf{F}}^t$

$$\bar{\mathbf{f}}^t = \begin{pmatrix} -\overline{\tau_{xx}^t} \\ -\overline{\tau_{xy}^t} \\ -\overline{\tau_{xz}^t} \\ \overline{q_x^t} \\ \overline{J_{x,k}^t} \end{pmatrix}, \bar{\mathbf{g}}^t = \begin{pmatrix} -\overline{\tau_{xy}^t} \\ -\overline{\tau_{yy}^t} \\ -\overline{\tau_{yz}^t} \\ \overline{q_y^t} \\ \overline{J_{y,k}^t} \end{pmatrix}, \bar{\mathbf{h}}^t = \begin{pmatrix} -\overline{\tau_{xz}^t} \\ -\overline{\tau_{yz}^t} \\ \overline{q_z^t} \\ \overline{J_{z,k}^t} \end{pmatrix}. \quad (2.31)$$

Again, closure needs to be provided, this time for the subgrid-scales. By this means, the numerical solvability of the system is assured.

Reynolds tensor

$$\overline{\tau_{ij}^t} = -\bar{\rho} (\overline{u_i u_j} - \tilde{u}_i \tilde{u}_j) \quad (2.32)$$

$$= 2\bar{\rho} \nu^t \left(\tilde{S}_{ij} - \frac{1}{3} \delta_{ij} \tilde{S}_{ll} \right) \quad (2.33)$$

$$\text{with: } \tilde{S}_{ij} = \frac{1}{2} \left(\frac{\partial \tilde{u}_i}{\partial x_j} + \frac{\partial \tilde{u}_j}{\partial x_i} \right) - \frac{1}{3} \frac{\partial \tilde{u}_k}{\partial x_k} \delta_{ij} \quad (2.34)$$

ν^t is the so called SGS turbulent viscosity. Its modeling counts among one of the main issues of LES and is presented in Section 2.3.

Diffusive species flux

$$\overline{J_{i,k}}^t = \bar{\rho} \left(\widetilde{u_i Y_k} - \widetilde{u_i} \widetilde{Y_k} \right) \quad (2.35)$$

$$= -\bar{\rho} \left(D_k^t \frac{W_k}{\overline{W}} \frac{\partial \widetilde{X_k}}{\partial x_i} - \widetilde{Y_k} \widetilde{V_{i,k}}^t \right) \quad (2.36)$$

$$\text{with: } \widetilde{V_{i,k}}^t = \sum_{k=1}^N D_k^t \frac{W_k}{\overline{W}} \frac{\partial \widetilde{X_k}}{\partial x_i} \text{ and } D_k^t = \frac{\nu^t}{Sc_k^t} \quad (2.37)$$

Heat flux

$$\overline{q_i}^t = \bar{\rho} \left(\widetilde{u_i E} - \widetilde{u_i} \widetilde{E} \right) \quad (2.38)$$

$$= -\lambda^t \frac{\partial \widetilde{T}}{\partial x_i} + \sum_{k=1}^N \overline{J_{i,k}}^t \widetilde{h_{s,k}} \quad (2.39)$$

$$\text{with: } \lambda^t = \frac{\mu^t \overline{C_p}}{Pr^t} \quad (2.40)$$

2.2.3 The incompressible LES equations

Compared to the compressible case, the system of the incompressible Navier-Stokes equations is much simpler. Again, the filtering procedure of Section 2.2.1 is applied and yields:

$$\nabla \cdot \overline{\mathbf{u}} = 0 \quad (2.41)$$

$$\frac{\partial \overline{\mathbf{u}}}{\partial t} + (\overline{\mathbf{u}} \cdot \nabla) \overline{\mathbf{u}} = -\frac{1}{\rho} \nabla \overline{P^*} + \nu \Delta \overline{\mathbf{u}} \quad (2.42)$$

as well as for the Poisson equation:

$$\Delta \overline{P^*} = -\rho \nabla \cdot [(\overline{\mathbf{u}} \cdot \nabla) \overline{\mathbf{u}}] . \quad (2.43)$$

The mass density ρ is not taken into account in the filtering process due to the conservation of constants of the filter. The term of the convective acceleration in Eq. (2.42) makes a non-linear term appear. Using the decomposition of Eq. (2.16) allows to rewrite this term, following [Leonard 1974]:

$$\overline{\mathbf{u}\mathbf{u}} = \overline{\tau_{ij}}^t + \overline{\mathbf{u}} \overline{\mathbf{u}} . \quad (2.44)$$

leading to this momentum equation:

$$\frac{\partial \overline{\mathbf{u}}}{\partial t} + \nabla \cdot (\overline{\mathbf{u}\mathbf{u}}) = -\frac{1}{\rho} \nabla \overline{P^*} + \nu \Delta (\overline{\mathbf{u}}) - \nabla \cdot \overline{\tau_{ij}}^t . \quad (2.45)$$

The term τ_{ij}^t appearing in Eq. (2.44) can be seen as a combination of interactions between the large turbulent structures, the cross-stresses, describing the interactions of the large and the small scales, and Reynolds-like stresses. This stress tensor corresponds to the one obtained in section 2.2.2, except for the absence of density fluctuations. As for the compressible approach, models for this subgrid stress are required and will be presented in section 2.3.

2.3 Subgrid-scale modeling

The purpose of subgrid-scale modeling is to provide closure for terms, which were introduced into the balance equations by the filtering. When following the theory of Kolmogorov [Kolmogorov 1941], the aim is to withdraw energy from the resolved turbulent structures in order to mimic the forward energy cascade in the unresolved part [Pope 2000, Sagaut 2002]. Such an effect, which is considered to be dissipative only, can be accounted for by introducing a turbulent viscosity, ν^t . Based on the model of [Boussinesq 1877] this can be expressed as follows:

$$\bar{\tau}_{ij}^t - \frac{1}{3}\bar{\tau}_{ll}^t\delta_{ij} = 2\nu^t\bar{S}_{ij}. \quad (2.46)$$

In Eq. (2.46) \bar{S}_{ij} represents the strain rate of the resolved structures.

2.3.1 Smagorinsky model

Smagorinsky presented this model in [Smagorinsky 1963] and is seen as the ancestor of the SGS stress models.

$$\nu^t = (C_S\Delta)^2 \sqrt{2\bar{S}_{ij}\bar{S}_{ij}}, \quad (2.47)$$

with C_S being the Smagorinsky constant and Δ representing the characteristic filter width (usually $\Delta = (\Delta x\Delta y\Delta z)^{\frac{1}{3}}$). Since its publication in the early 1960s it has been applied to various flow problems. Giving the correct amount of dissipation in the case of a homogeneous isotropic turbulence, this model is known to be over predictive as soon as the flow becomes anisotropic, e. g. close to solid boundaries. Values for the Smagorinsky constant can vary depending on the flow configuration and recommendations in literature lie between $0.065 \leq C_S \leq 0.2$ [Ferziger 2002].

2.3.2 Dynamic Smagorinsky model

This model of Germano et al. [Germano 1991] is an evolution of the Smagorinsky model in such a way that C_{SD} is no longer fixed *a priori* but it is evaluated *on the fly*, i. e. during the simulation..

$$\nu^t = (C_{SD}\Delta)^2 \sqrt{2\bar{S}_{ij}\bar{S}_{ij}} \quad (2.48)$$

Equation (2.48) differs from Eq. (2.47) only by the constant C_{SD} . It is based on the Germano identity [Germano 1992] and follows the Lilly procedure [Lilly 1992]:

$$C_{SD}^2 = \frac{1}{2} \frac{L_{ij}M_{ij}}{M_{ij}M_{ij}} \quad (2.49)$$

The tensors of the above equation are defined by:

$$M_{ij} = -\hat{\Delta}^2 < \sqrt{2\bar{S}_{ij}\bar{S}_{ij}} \bar{S}_{ij} > \quad (2.50)$$

$$L_{ij} = < \bar{u}_i > < \bar{u}_j > - < \bar{u}_i\bar{u}_j >, \quad (2.51)$$

where $\widehat{\Delta}$ represents a "test filter", for which the characteristic length is calculated taking the cubic root of the volume constituted by all cells surrounding the cell of interest. To prevent negative values for C_{S_D} and to ensure numerical stability, clipping of the parameter is usually applied.

2.3.3 Wall-Adapting Local Eddy-viscosity (WALE) model

The idea of the WALE model, first presented by Nicoud and Ducros [Nicoud 1999], is to reproduce the proper scaling at the wall of the turbulent viscosity.

$$\nu^t = (C_W \Delta)^2 \frac{\left(s_{ij}^d s_{ij}^d\right)^{\frac{3}{2}}}{\left(\overline{S}_{ij} \overline{S}_{ij}\right)^{\frac{5}{2}} + \left(s_{ij}^d s_{ij}^d\right)^{\frac{5}{4}}} \quad (2.52)$$

$$\text{with: } s_{ij}^d = \frac{1}{2} (\overline{g}_{ij}^2 + \overline{g}_{ji}^2) - \frac{1}{3} \overline{g}_{kk}^2 \delta_{ij}. \quad (2.53)$$

Δ again defines the characteristic filter length, which is the same as for the Smagorinsky model. The parameter $C_W = 0.4929$ is the model constant, \overline{g}_{ij} are the velocity gradients of the resolved scales and s_{ij}^d being the traceless symmetric part of the square of the velocity gradient tensor.

The three *eddy-viscosity models* presented in this section only represent a small variety of what is available. This choice was based on the models used for the simulations presented in parts II and III of this work. For more information on the topic of subgrid-scale modeling the reader is referred to [Sagaut 2002, Piomelli 2010, Pope 2000], just to name a few.

Numerics

Following the outline of the equations in chapter 2, which form the basis of the CFD solvers AVBP and YALES2, this chapter is dedicated to present the numerical concepts that have been implemented.

Both codes use the finite-volume approach [Hirsch 1988], which is based on the discretization of the the conservation laws in their integral form, Eqs. (2.2),(2.4),(2.7). In order to do so, the geometry of the problem at hand has to be divided into a finite number of non-overlapping elements (polygons in 2D, polyhedra in 3D):

$$\Omega = \bigcup_{P_j \in \Omega_h} P_j, \quad (3.1)$$

with P_j standing for the polygons (or polyhedra) of the computational mesh. The finite-volume approach is divided in three main methods, in general *cell-centered*, *vertex-centered* and *cell-vertex*. They differ on how the control-volumes are defined and at which location the variables are stored, see [Lamarque 2007]. Both codes are designed to work on unstructured and hybrid grids. Information on which finite-volume discretization method is used and on the numerical schemes deployed are summarized in the following subsections.

For this section, the following indication is applied:

- $i \in \{1, N_{node}\}$ indicates the global node numbering and nodal quantities.
- $j \in \{1, N_{cell}\}$ denotes the cell number.
- Ω_j refers to values at the CV center.
- $v \in \{1, n_{\Omega_j}^v\}$ enumerates the cell vertices in the local reference of a given cell Ω_j , with $n_{\Omega_j}^v$ being the total number of the cell vertices.
- The index f stands for quantities at the cell faces.

3.1 AVBP

The AVBP code is based on the collaborative work of CERFACS and the Oxford University Computing Laboratory (OUCL, since 2011: Department of Computer Science) [Rudgyard 1995b, Rudgyard 1995a, Schönfeld 1999] and is maintained today by CERFACS and the Institut Francais du Petrol - energies nouvelles (IFP-en). It solves the compressible Navier-Stokes equations in 2D and 3D for unsteady, reactive flows. To

provide high flexibility, this CFD solver is conceived to handle unstructured and hybrid grids, i. e. grids composed of cells of arbitrary type. Furthermore, the code has been ported to a large number of different platforms, from a simple personal computer up to modern HPC systems. For machines of the latter type AVBP has proven to be highly efficient [Staffelbach 2006b]. In this section only an outline of some distinct features of the code are given. A more profound elaboration can be found in [Lamarque 2007].

3.1.1 Spatial discretization

For the AVBP solver the so-called *cell-vertex* discretization is chosen. This method was first presented by Ni [Ni 1982] and later on modified by Hall [Hall 1984]. The particularity of this discretization method is the fact that the solution is not stored at the center of the control volume (CV), on which the conservation laws are solved. This is due to the so-called dual mesh approach. The elements of the primary mesh, which are identical to the actual computational grid, represent the CV. Once the solution is known at the cell center, it is brought to the grid nodes (or cell vertices, hence the method's name), which can be seen as the center of the so-called dual cells, see Fig. 3.1. At this location the conserved variables are stored and then advanced in time.

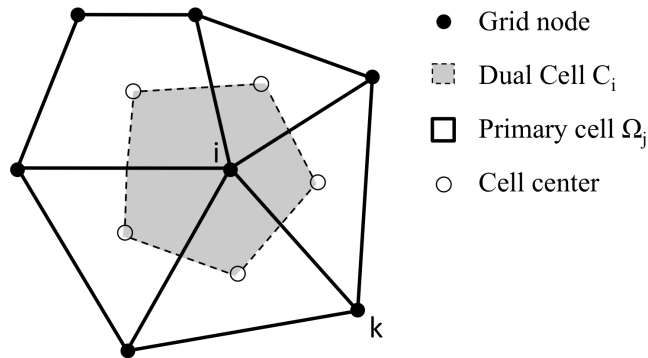


Figure 3.1: *Cell-vertex discretization: the balance equations are integrated on the primary cells, i. e. the mesh elements, whereas the advancement in time of the solution is done for the dual cells.*

The flux over the cell edges (surfaces in 3D), here exemplarily for the edge constituted by the connection of the nodes i and k , is computed using

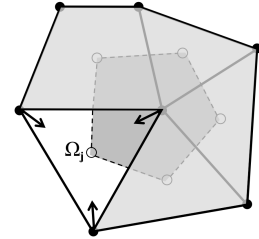
$$\mathcal{F} = \mathcal{F} \left(\frac{\mathbf{U}_i + \mathbf{U}_k}{2} \right) = \frac{1}{2} (\mathcal{F}(\mathbf{U}_i) + \mathcal{F}(\mathbf{U}_k)), \quad (3.2)$$

which can be interpreted as the integration in space of the flux using the trapezoidal rule and thus, supposing that its variation along the cell faces varies linearly. In doing so, a link of the *cell-vertex* method with the finite element method can be established [Morton 1988, Morton 1997], which has been analyzed on various occasions, e. g. [Rudgyard 1993, Roe 1987, Swanson 1991, Süli 1989]. These analyses have shown that, in comparison to the classical *cell-centered* and *vertex-centered* discretization, the *cell-vertex* method achieves a higher precision and is less sensible to mesh distortions.

This outweighs the higher computational cost, which comes with the operations necessary to pass from the primary mesh to the dual mesh, namely:

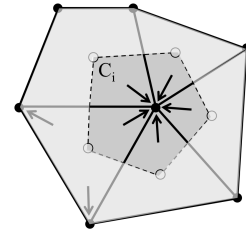
Gather

The information (solution and coordinates) stored at the grid nodes in a global reference is transferred to the vertices of each primary cell, where it is then available in a local temporary array. Now, operators such as the divergence can be calculated for the CV of the cell.



Scatter

The scatter operation consists of retransferring the information from the local temporary arrays of each primal cell to the adjacent grid nodes, and hence back in the global context.



3.1.2 Metrics

The metrics in the framework of the *cell-vertex* discretization are defined for the cells Ω_j . In AVBP these definitions are done for the cell vertices in the following order:

1. The outward pointing surface normals \mathbf{S}_f are computed, which are weighted by the surface area in consideration. When dealing with quadrilateral surfaces, the four vertices are not necessarily in the same plane. If not corrected, this might have a repercussion on the accuracy of the solution, since the linearity is not necessarily preserved anymore. This so-called *linear preserving property* guarantees a convergence behavior of second order on meshes that are sufficiently regular. Hence, surfaces in concern are divided in four triangles, by cutting along the two diagonals, and \mathbf{S}_f is taken to be the mean average of the four resulting surface vectors, see Fig. 3.2.

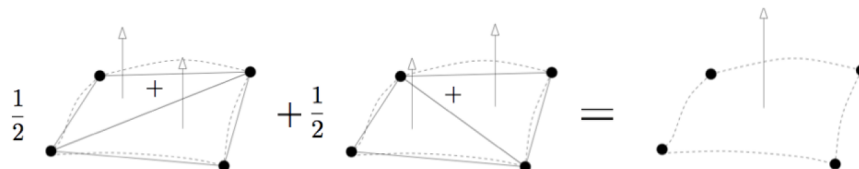


Figure 3.2: Calculation of surface normal for quadrilateral surfaces. [Garcia 2009]

2. In a second step, the normal vectors associated to a cell vertex \mathbf{S}_v are simply defined as the linear combination of normal vectors of adjacent surfaces:

$$\mathbf{S}_v = \sum_{f \in v} -\frac{d}{n_v^f} \mathbf{S}_f \quad (3.3)$$

In AVBP, the convention is that normal vectors \mathbf{S}_v are oriented towards the interior of the element. The term n_v^f represents the number of faces connected to the corresponding vertex v and d is the number of space dimensions of the element. It should be mentioned that, due to the computation of the surface normal vectors, \mathbf{S}_v is also surface area weighted and, hence, its norm is not unitary. Examples for a quadrilateral surface and a linear element are presented in Fig. 3.3. The consistency is verified using: $\sum_{v \in \Omega_c} \mathbf{S}_v = \mathbf{0}$.

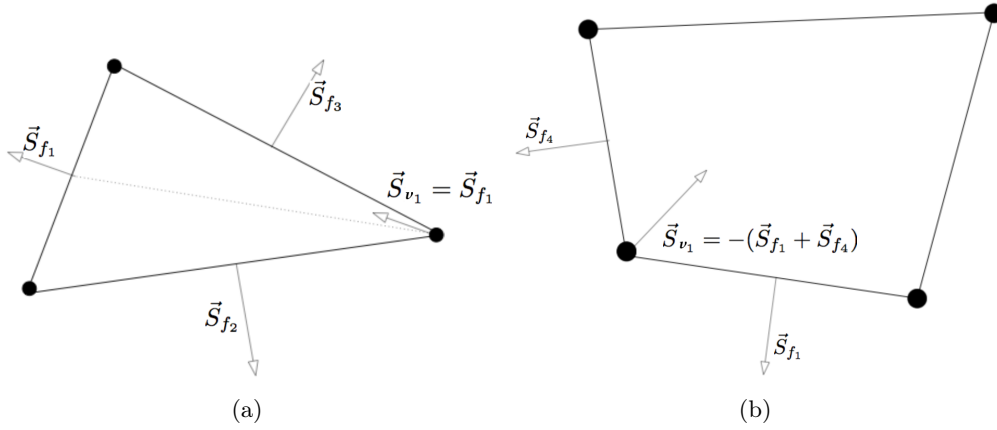


Figure 3.3: a) For a triangle, the vertex normal vector \mathbf{S}_v is the face normal \mathbf{S}_f of the face opposed to the node in consideration. - b) The vertex normal \mathbf{S}_v of a quadrilateral element is calculated as the mean average of the adjacent face normal vectors \mathbf{S}_f . [Lamarque 2007]

3.1.3 Weighted cell residual approach

The following explanations refer to the conservative form of the laminar Navier-Stokes equations of non-reactive flows:

$$\frac{\partial \mathbf{w}}{\partial t} + \nabla \cdot \mathbf{F} = \mathbf{0}. \quad (3.4)$$

Again, \mathbf{w} represents the vector of the conserved variables and \mathbf{F} is the flux tensor, defined as the sum of the inviscid and the diffusive flux $\mathbf{F} = \mathbf{F}^I(\mathbf{w}) + \mathbf{F}^V(\mathbf{w}, \nabla \mathbf{w})$. The so-called **residual** is obtained by approximating the flux divergence of Eq. (3.4) in the CV composed by each cell Ω_j :

$$R_{\Omega_j} = \frac{1}{V_{\Omega_j}} \int_{\partial \Omega_j} \mathbf{F} \cdot \mathbf{n} dS. \quad (3.5)$$

In Eq. (3.5), V_{Ω_j} is the cell volume, $\partial\Omega_j$ stands for its enclosing surface and \mathbf{n} is the corresponding normal vector. With the assumptions and the definitions made in section 3.1.2, the residual R_{Ω_j} at the cell center can be expressed in its discrete form:

$$R_{\Omega_j} = \frac{1}{dV_{\Omega_j}} \sum_{v \in \Omega_j} \mathbf{F}_v \cdot \mathbf{S}_v, \quad (3.6)$$

with \mathbf{F}_v being the nodal approximation of \mathbf{F} . The definition of the divergence operator is consistent if the cell volume V_{Ω_j} is defined as follows:

$$V_{\Omega_j} = \frac{1}{d^2} \sum_{v \in \Omega_j} \mathbf{x}_v \cdot \mathbf{S}_v, \quad \text{with } \nabla \cdot \mathbf{x} = d. \quad (3.7)$$

Finally, the residual at the cell center R_{Ω_j} has to be brought back to the nodes. For this, the cell residuals are distributed from the center of the element to the cell vertices and then scattered back to the global mesh node i , representing the dual cell of Fig. 3.1. This leads to a semi-discrete expression of the temporal derivative of the state variables:

$$\frac{d\mathbf{w}_i}{dt} = -N_i = -\frac{1}{V_i} \sum_{j|\Omega_j \in i} \mathcal{D}_{\Omega_j}^i V_{\Omega_j} R_{\Omega_j}, \quad (3.8)$$

with $\mathcal{D}_{\Omega_j}^i$ being the distribution matrix defining the fraction of the cell residual from the cell Ω_j , which is sent to the grid node i . This weight accorded to every R_{Ω_j} is the reason for the name of the approach. Equation 3.8, in fact, is the mathematical expression of the scatter operation. This semi-discrete formulation then has to be advanced in time. As will be shown in section 3.1.4, the convection schemes in AVBP are defined by the distribution matrix $\mathcal{D}_{\Omega_j}^i$.

3.1.3.1 The gradient operator

The computation of the gradient operator $\nabla \vec{\phi}$ is done in a similar way to the divergence calculation of Eq. (3.6). This is valid, since the gradient can be expressed as follows:

$$\nabla \vec{\phi} = \nabla \cdot (\phi \vec{e}_x) \vec{e}_x + \nabla \cdot (\phi \vec{e}_y) \vec{e}_y + \nabla \cdot (\phi \vec{e}_z) \vec{e}_z, \quad (3.9)$$

where $\vec{e}_{x,y,z}$ being the unit vectors in the three space directions. For the readability, vectors are here denoted using an arrow instead of bold letters. At first, approximations of the gradient within the cells are generated:

$$\left(\frac{\partial \vec{\phi}}{\partial \vec{x}} \right)_{cell} \approx \frac{1}{V_{cell}} \int \int_{\partial\Omega_j} \vec{\phi} \cdot \vec{n} d\vec{S} \quad (3.10)$$

$$= \frac{1}{V_{\Omega_j}} \sum_{v \in \Omega_j} \vec{\phi}_v d\vec{S}_v \quad (3.11)$$

The assumption is made that the gradient of any quantity $\nabla \vec{\phi}$ does not change within a cell Ω_j . Then, the solutions are scattered back to the global mesh nodes:

$$\left(\nabla \vec{\phi} \right)_i = \frac{1}{V_{\Omega_j}} \sum_{j|\Omega_j \in i} V_{\Omega_j} \left(\nabla \vec{\phi} \right)_{\Omega_j} \quad (3.12)$$

3.1.4 Numerical schemes

3.1.4.1 Central differences

When the distribution matrix \mathcal{D}_{Ω_j} of Eq. (3.8) equals the identity matrix \mathcal{I} , a simple central difference scheme is applied to the spatial terms:

$$\mathcal{D}_{\Omega_j}^{k,CD} = \frac{1}{n_v} \mathcal{I} \quad (3.13)$$

As outlined by [Lamarque 2007], this scheme often is coupled to a Runge-Kutta (RK) time integration scheme of higher order (i. e. at least of third order), since the explicit Euler method (equiv. to 1-step RK) and the RK2 scheme are unconditionally unstable when combined with a central spatial scheme [Hirsch 1988]. In AVBP the low storage Runge-Kutta method [Williamson 1980] is implemented, which can be expressed as follows:

$$\begin{aligned} \mathbf{w}^{(0)} &= \mathbf{w}^{(n)} \\ \mathbf{w}^{(1)} &= \mathbf{w}^{(n)} - \gamma_1 \Delta t N^{(1)} \\ \mathbf{w}^{(2)} &= \mathbf{w}^{(n)} - \gamma_2 \Delta t N^{(2)} \\ &\vdots \\ \mathbf{w}^{(n+1)} &= \mathbf{w}^{(n)} - \gamma_M \Delta t N^{(M-1)}. \end{aligned} \quad (3.14)$$

M represents the maximum number of steps, which also is the upper limit for the convergence order attainable and γ_n the coefficient of step n .

3.1.4.2 Lax-Wendroff scheme

The Lax-Wendroff (LW) scheme [Lax 1960, Lax 1964] can be described as a total discretization approach, contrary to the separation of the temporal and spatial method as presented for the central differences. A Taylor series expansion in time of the solution \mathbf{w} up to the third order term forms the basis of the LW scheme, yielding:

$$\mathbf{w}^{(n+1)} = \mathbf{w}^{(n)} + \Delta t \left. \frac{\partial \mathbf{w}}{\partial t} \right|_{t=n} + \frac{1}{2} \Delta t^2 \left. \frac{\partial^2 \mathbf{w}}{\partial t^2} \right|_{t=n} + \mathcal{O}(\Delta t^3), \quad (3.15)$$

with Δt being the time step. The next step consists in replacing the time derivatives with the help of Eq. (3.4), meaning:

$$\left. \frac{\partial \mathbf{w}}{\partial t} \right|_{t=n} = -(\nabla \cdot \mathbf{F})^n. \quad (3.16)$$

In a similar way, the second-order time derivative of Eq. (3.15) can be replaced:

$$\begin{aligned} \frac{\partial^2 \mathbf{w}}{\partial t^2} &= \frac{\partial}{\partial t} \left(\frac{\partial \mathbf{w}}{\partial t} \right) = \frac{\partial}{\partial t} (-\nabla \cdot \mathbf{F}) = \\ &-\nabla \cdot \left(\frac{\partial \mathbf{F}}{\partial t} \right) = -\nabla \cdot \left(\frac{\partial \mathbf{F}}{\partial \mathbf{w}} \frac{\partial \mathbf{w}}{\partial t} \right) = \nabla \cdot (\mathcal{A} \nabla \cdot \mathbf{F}). \end{aligned} \quad (3.17)$$

Finally, Eq. (3.15) can be written as:

$$\frac{\mathbf{w}^{(n+1)} - \mathbf{w}^n}{\Delta t} = -(\nabla \cdot \mathbf{F})^n + \frac{1}{2} \Delta t \nabla \cdot (\mathcal{A} \nabla \cdot \mathbf{F})^n + \mathcal{O}(\Delta t^2) \quad (3.18)$$

Equation (3.18) now represents the semi-discrete formulation of the LW scheme, with \mathcal{A} being the Jacobi matrix. In order to advance the solution in time, this equation has to be integrated. The control volume in this case is the median dual cell \mathbf{C}_i of Fig. 3.1. This leads to the LW scheme of Ni [Ni 1982] and Hall [Hall 1984] for the *cell-vertex* formulation [Giles 1991, Crumpton 1993] and for which the distribution matrix yields:

$$\mathcal{D}_{\Omega_j}^k = \frac{1}{n_v^{\Omega_j}} \left(\mathbf{I} - \frac{\Delta t}{2d} \frac{n_{\Omega_j}^v}{V_{\Omega_j}} \mathcal{A}_{\Omega_j} \cdot \mathbf{S}_{i|\Omega_j} \right). \quad (3.19)$$

$\mathbf{S}_{i|\Omega_j}$ is the normal vector of node i associated with cell Ω_j and $\mathcal{A}_{\Omega_j} = \frac{1}{n_v^{\Omega_j}} \sum_{v \in \Omega_j} \mathcal{A}_v$ is the Jacobi matrix of cell Ω_j , which is, in fact, the mean average of the Jacobi matrices approximated at the vertices v of Ω_j .

3.1.4.3 The Two-step Taylor-Galerkin schemes

Quartapelle and Selmin [Quartapelle 1993] proposed Two-step Taylor-Galerkin (TTG) schemes, which are an extension of the single step Taylor-Galerkin methods proposed by Donea [Donea 1984]. Schemes of this family are at best fourth order accurate in time and, in the context of the *cell-vertex* method of AVBP, third order accurate in space. The basic idea is to combine higher order Taylor series expansion in time with a *finite-element* discretization in space. Colin and Rudgyard contributed the TTGC scheme [Colin 2000b] and presented the following general formulation for the TTG schemes:

$$\tilde{\mathbf{w}}^n = \mathbf{w}^n + \alpha \Delta t \frac{\partial \mathbf{w}^n}{\partial t} + \beta \Delta t^2 \frac{\partial^2 \mathbf{w}^n}{\partial t^2} \quad (3.20)$$

$$\mathbf{w}^{n+1} = \mathbf{w}^n + \Delta t \left(\Theta_1 \frac{\partial \mathbf{w}^n}{\partial t} + \Theta_2 \frac{\partial \tilde{\mathbf{w}}^n}{\partial t} \right) + \Delta t^2 \left(\varepsilon_1 \frac{\partial^2 \mathbf{w}^n}{\partial t^2} + \varepsilon_2 \frac{\partial^2 \tilde{\mathbf{w}}^n}{\partial t^2} \right) \quad (3.21)$$

The first scheme to be described here is the TTGC scheme, which is third order accurate in time. The parameters of Eqs. (3.20) and (3.21) have to be set to the following values, to obtain the scheme's formulation:

$$\alpha = \frac{1}{2} - \gamma, \beta = \frac{1}{6}, \Theta_1 = 0, \Theta_2 = 1, \varepsilon_1 = \gamma, \varepsilon_2 = 0.$$

With these parameters and replacing the time derivatives using the Lax-Wendroff approach from Eqs. (3.16) and (3.17), TTGC yields:

$$\tilde{\mathbf{w}}^n = \mathbf{w}^n - 0.49 \Delta t \nabla \cdot \mathbf{F}^n + \frac{1}{6} \Delta t^2 \nabla \cdot (\mathcal{A} \nabla \cdot \mathbf{F}^n) \quad (3.22)$$

$$\mathbf{w}^n = \mathbf{w}^n - \Delta t \nabla \cdot \tilde{\mathbf{F}}^n + 0.01 \Delta t^2 \nabla \cdot (\mathcal{A} \nabla \cdot \mathbf{F}^n). \quad (3.23)$$

The idea behind the development of TTGC was to obtain a scheme of the TTG family, which would be as little dissipative as possible, especially regarding higher wave numbers

that correspond to the smallest turbulent scales. By this means, the scheme has as little impact as possible on the sub-grid scale modeling and hence is well-suited for LES. The value $\gamma = 0.01$ is a recommendation of Colin and Rudgyard when performing this type of simulations.

Another TTG scheme implemented in AVBP is the so-called TTG4A, developed by Quartapelle and Selmin [Quartapelle 1993, Donea 2003]. This scheme is fourth order accurate in time. TTG4A is the most dissipative of the TTG schemes, but exhibits a preferable dispersive behavior. This scheme can be obtained when inserting the following values into Eqs. (3.20) and (3.21):

$$\alpha = \frac{1}{3}, \beta = \frac{1}{12}, \Theta_1 = 1, \Theta_2 = 0, \varepsilon_1 = 0, \varepsilon_2 = \frac{1}{2},$$

resulting in the equations specified below:

$$\tilde{\mathbf{w}}^n = \mathbf{w}^n - \frac{1}{3}\Delta t \nabla \cdot \mathbf{F}^n + \frac{1}{12}\Delta t^2 \nabla \cdot (\mathcal{A} \nabla \cdot \mathbf{F}^n) \quad (3.24)$$

$$\mathbf{w}^n = \mathbf{w}^n - \Delta t \nabla \cdot \mathbf{F}^n + \frac{1}{2}\Delta t^2 \nabla \cdot (\mathcal{A} \nabla \cdot \tilde{\mathbf{F}}^n) \quad (3.25)$$

3.1.4.4 Finite element approach

The Galerkin method used for the spatial discretization of the TTG schemes will be described in the following for the general Eqs. (3.20) and (3.21). For this, the solution vector as well as the fluxes at the grid nodes, both depending on space and time, are split into linear combinations in which the spatial contribution is replaced by test functions $\phi_i(\mathbf{x})$, yielding:

$$\mathbf{w}(\mathbf{x}, t) = \sum_{i \in N_{node}} \mathbf{w}(t) \phi_i(\mathbf{x}), \quad (3.26)$$

$$\mathbf{F}(\mathbf{x}, t) = \sum_{i \in N_{node}} \mathbf{F}(t) \phi_i(\mathbf{x}). \quad (3.27)$$

Note that, Eq. (3.27) is inconsistent to Eq. (3.26) when considering the non linear equations (3.4). Applying the conventional *finite-element* method, i. e. a separate approximate solution to each non linear term, would computationally be very intensive. Here, Eq. (3.27) represents the so-called *group finite element method*, which constitutes an alternative. This notion was introduced by Fletcher [Fletcher 1991], who has studied the impact of this formulation on the solution's accuracy. He concluded that this approach is applicable, in case the following requirements are met:

- Conservative formulation of the governing equations
- One type of approximation is used for the differential terms in the equations (\mathbf{w} and \mathbf{F} of Eq. (3.4))

It is this method that is implemented in AVBP. The test functions deployed are functions with compact support, meaning:

$$\begin{cases} \phi_i(\mathbf{x}) = 1 & \text{if } \mathbf{x} = \mathbf{x}_i \\ \phi_i(\mathbf{x}) = 0 & \text{else .} \end{cases} \quad (3.28)$$

At first, Eqs. (3.20) and (3.21) are multiplied by a trial function w_j , also with compact support, and are integrated over the domain Ω , leading to:

$$\int_{\Omega} \frac{(\tilde{\mathbf{w}} - \mathbf{w}^n)}{\Delta t} w_j dV = -\alpha L_j(\mathbf{w}^n) + \beta \Delta t LL_j(\mathbf{w}^n), \quad (3.29)$$

$$\int_{\Omega} \frac{(\mathbf{w}^{(n+1)} - \tilde{\mathbf{w}})}{\Delta t} w_j dV = -(\Theta_1 L_j(\mathbf{w}^n) + \Theta_2 L_j(\tilde{\mathbf{w}})) + \Delta t (\varepsilon_1 LL_j(\mathbf{w}^n) + \varepsilon_2 LL_j(\tilde{\mathbf{w}})). \quad (3.30)$$

The definitions for the RHS operators are the following:

$$L_j(\mathbf{w}) = \int_{\Omega} \nabla \cdot \mathbf{F}^n w_j dV \quad (3.31)$$

$$LL_j(\mathbf{w}) = \oint_{\partial\Omega} (\mathcal{A}\nabla \cdot \mathbf{F})^n w_j dS - \int_{\Omega} (\mathcal{A}\nabla \cdot \mathbf{F})^n w_j dV \quad (3.32)$$

The first term in the LL_i operator accounts for the boundary conditions and thus, will have non zero values at the boundaries only. This boundary correction will not be treated explicitly in this document, more information on this topic can be found in [Lamarque 2007]. All further considerations are made for points within the computational domain that are away from the boundaries.

When using triangles (tetrahedra in 3D), the term $\nabla\phi_i$ can be defined as:

$$\nabla\phi_i = -\frac{\mathbf{S}_v}{dV_{\Omega_j}}, \quad (3.33)$$

Eq. (3.33), in combination with Eq. (3.3), expresses the conservativity property of linear finite element methods. Another important relation when using the Galerkin method, i. e. equating the trial function $w_j(\mathbf{x})$ and the test function $\phi_j(\mathbf{x})$, is

$$\int_{\Omega_j} \phi_j(\mathbf{x}) dV = \frac{V_{\Omega_j}}{n_{\Omega_j}^v}. \quad (3.34)$$

Introducing Eqs. (3.26), (3.27), (3.33) and (3.34) into the operators L_j and LL_j allows to rewrite Eqs. (3.35) and (3.36) as follows:

$$\begin{aligned} L_j(\mathbf{w}) &= \sum_{\Omega_j \in \Omega_h} \sum_{i \in \Omega_j} \mathbf{F}_i^n \cdot \int_{\Omega_j} \nabla \phi_i \phi_j dV \\ &= \sum_{\Omega_j \in \Omega_h} \frac{1}{n_{\Omega_j}^v} \mathbf{R}_{\Omega_j} V_{\Omega_j} \end{aligned} \quad (3.35)$$

$$\begin{aligned} LL_j(\mathbf{w}) &= - \sum_{\Omega_j \in \Omega_h} \mathcal{A}_{\Omega_j}^n \sum_{i \in \Omega_j} \int_{\Omega} (\mathbf{F}_i^n \cdot \nabla \phi_i) \phi_j dV \\ &= \frac{1}{d} \sum_{\Omega_j \in \Omega_h} (\mathcal{A}_{\Omega_j} \mathbf{R}_{\Omega_j})^n \cdot \mathbf{S}_v \end{aligned} \quad (3.36)$$

Looking at the left hand side (LHS) of Eqs. (3.29) and (3.30) after these substitutions, the following relations arise:

$$\begin{aligned} \int_{\Omega} \frac{\tilde{\mathbf{w}}_i - \mathbf{w}_i^n}{\Delta t} w_j dV &= \sum_{\Omega_j \in \Omega_h} \sum_{i \in \Omega_j} \int_{\Omega_j} \phi_i \phi_j dV \frac{\tilde{\mathbf{w}}_i - \mathbf{w}_i^n}{\Delta t} \\ &= \mathcal{M}_i \frac{\tilde{\mathbf{w}}_i - \mathbf{w}_i^n}{\Delta t} \end{aligned} \quad (3.37)$$

$$\begin{aligned} \int_{\Omega} \frac{\mathbf{w}_i^{(n+1)} - \tilde{\mathbf{w}}_i^n}{\Delta t} w_j dV &= \sum_{\Omega_j \in \Omega_h} \sum_{i \in \Omega_j} \int_{\Omega_j} \phi_i \phi_j dV \frac{\mathbf{w}_i^{(n+1)} - \tilde{\mathbf{w}}_i^n}{\Delta t} \\ &= \mathcal{M}_i \frac{\mathbf{w}_i^{(n+1)} - \tilde{\mathbf{w}}_i^n}{\Delta t}. \end{aligned} \quad (3.38)$$

The term \mathcal{M}_i is the so-called mass matrix, reading:

$$\mathcal{M}_i = \sum_{\Omega_j \in \Omega_h} \sum_{i \in \Omega_j} \int_{\Omega_j} \phi_i \phi_i dV. \quad (3.39)$$

The mass matrix renders the schemes implicit in space and hence leads to supplemental computational costs for its inversion. This drawback is outweighed, since an implication of the mass matrix is the considerable reduction of the dispersion error of the numerical scheme for a wide range of wave numbers. In AVBP, an iterative Jacobi method is used for the inversion of the mass matrix. Donea [Donea 1984] and also Colin and Rudgyard [Colin 2000b] have shown that already a few steps of the Jacobi method (< 5) allow to improve the solution. Another interpretation of the mass matrix was given by Senoner [Senoner 2010], understanding it as an operator associating the average values in the nodal CV, which are located at the center of mass of the dual cell, to the grid nodes. For irregular meshes, the center of mass of the dual cell and the grid node do not always coincide.

The TTG schemes implemented in the *finite-element* context in AVBP achieve third order accuracy in space, as was shown in [Lamarque 2007]. Theoretically, the order of finite-element schemes is $(2 + 2n)$ with n being the order of the polynomials of the basic

functions (here $n=1$), as was shown by Vichnevetsky and Bowles [Vichnevetsky 1982]. A detailed description and a more complete study of all the numerical schemes at hand in AVBP is given in the work of N. Lamarque [Lamarque 2007].

3.1.4.5 The time step Δt

The advancement of the solution in time is explicit in AVBP. One reason for this is that the implementation of an explicit temporal discretization is straightforward. Furthermore, it is not very expensive in terms of computational cost and also parallelization is less complicated than for implicit methods. However, when using explicit time integration schemes, stability is an issue and the time step Δt is limited in AVBP using the stability conditions for the convective, diffusive and source term operators. In most cases convection is dominant and the time step is limited by the *Courant-Friedrichs-Lewy* (CFL) condition of Eq. (1.3):

$$\Delta t < C_{acoustic} \frac{\min(\Delta x)}{\max|\mathbf{u}| + c}. \quad (3.40)$$

In Eq. (3.40), \mathbf{u} is the convective speed of the flow, c is the speed of sound, Δx represents the mesh size and C is the CFL number. The CFL condition represents a necessary condition and its value, in order to assure stability for the convection problem, depends on the numerical scheme that is used.

3.1.5 Artificial viscosity

The convection operators used in AVBP are centered in space. It is well known that this can lead to the development of high frequency oscillations (so-called wiggles) [Hirsch 1988], which are not physical and therefore have to be removed. One possibility to avoid these instabilities is to add a smoothing term to the equations. This is considered as an artificial viscosity term. An explicit description of the models and the operators used in AVBP can be found in the doctoral thesis of A. Roux [Roux 2010].

3.1.6 Boundary conditions

In internal combustion simulations, predicting the acoustics present in the governing equations is of great importance. An example are the unstable modes of the combustion chamber in jet engines [Schönfeld 1999, Poinso 2005, Staffelbach 2006a]. To capture such effects correctly, the boundary conditions (BC) play an important role. Besides non-characteristic BC, which work directly on the conserved variables, another type of BC in AVBP are the so-called characteristic boundary conditions [Poinso 1992, Granet 2010]. This approach makes use of a wave decomposition, in order to modify the residuals, and represents one of the key features of AVBP, since it enables the general treatment of acoustic boundaries.

3.1.7 HPC

As mentioned in the beginning, AVBP has been developed to take advantage of many-core computer systems. This implies to find adequate solutions for the solver scalability, the partitioning of the simulation domain, the organization of the communications and the impact on the numerical simulations [Gicquel 2011]. Figure 3.4 depicts the speed-up graphs for "strong" scaled problems, i. e. increasing the number of processors while keeping the problem size constant. It becomes obvious that AVBP scales very well on different HPC platforms. The speed-up, which indicates the efficiency of the code to equilibrate the load balancing for the increased number of processors in comparison to the "sequential"¹ simulation, starts to deviate significantly from the linear speed-up for a computation on 12000 processing units and is still at about 92% for 16000 cores. This drop in efficiency can be explained by the number of cells that is treated per core. E. g., for the simulation number 4 of Fig. 3.4, this value is below 3000 cells/core when using 12000 cores. Hence, the communications to advance the simulation become more important than the computational workload of each processor. This clearly shows that

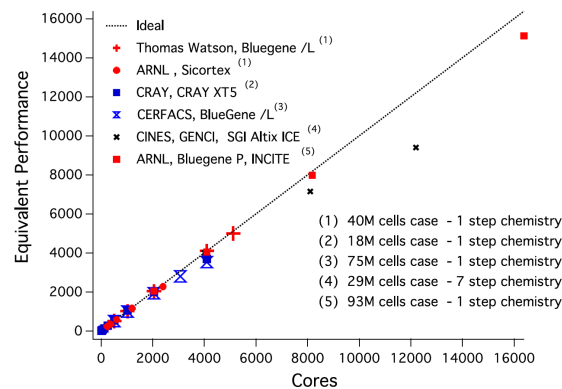


Figure 3.4: *Speed-up (strong scaling) of AVBP for different problem sizes [Gicquel 2011]*

the partitioning algorithm deployed has an impact on the scalability. AVBP allows to choose between different methods for the grid partitioning. An exhaustive study of the different algorithms implemented in AVBP is given in the work of M. Garcia [Garcia 2009].

Note that, AVBP makes use of a second decomposition of the partition transmitted to each computing core. This way, the use of the direct memory (cache) of the processing unit is optimized. As stated in chapter 1 the efficiency of codes now depends more and more on the software engineering than on the hardware (algorithmic efficiency).

¹Since the problem size can exceed the computational power (mainly in terms of memory) for a sequential run, the speed-up can also be obtained by considering a simulation with the smallest number of CPUs possible as reference.

3.2 YALES2

The development of the flow solver YALES2 was started in 2007 by V. Moureau. Today, the code is maintained by CORIA, Rouen (FRANCE). YALES2 is an unstructured, multi-physics solver for a wide range of flow problems capable of handling hybrid meshes [Moureau 2011b]. The initial objective was to create a solver predetermined for simulations on massively parallel systems using several thousands of processors and to manage very large computational grids, which can be composed of up to several billions of mesh elements [Moureau 2011c]. For the present work, only the incompressible solver (`ics`) of YALES2 (r542) is considered.

3.2.1 Discretization

Contrary to AVBP, YALES2 applies the so-called *vertex-centered* method. This approach also counts as a dual mesh approach. The difference regarding the *cell-vertex* discretization consists in the choice of the CV for integrating the balance equations. In the case of the *vertex centered* method, the CV is also the median dual cell (see Fig. 3.1 and 3.5(a)). This reduces the computational cost, since the `gather` and `scatter` operations of the *cell-vertex* method are omitted.

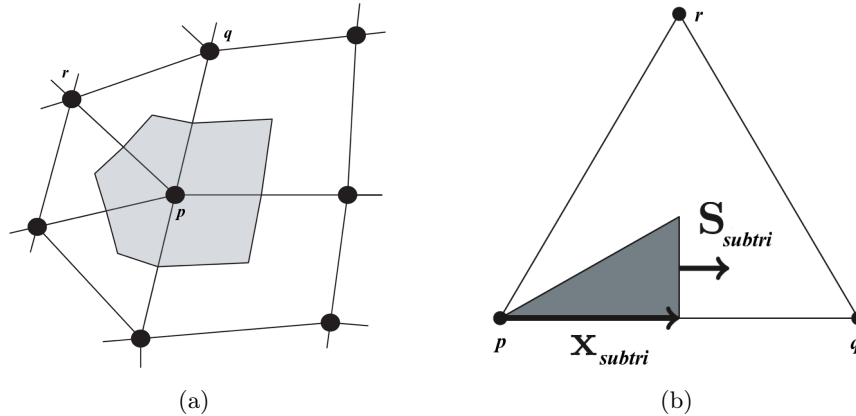


Figure 3.5: a) Definition of the control volume Ω_p (grey shaded area) in YALES2 - b) Construction of the CV by the use of sub-triangles in a 2D mesh. [Vantiegheem 2011]

In the case of YALES2, the CV is defined by a set of sub-triangles. Figure 3.5(b) depicts how these sub-triangles (2D) are defined, namely as the surface delimited by a vertex, the midpoint of an edge that is connected to the vertex and the barycenter of an element face that is adjacent to the vertex as well. The nodal volume is then calculated using:

$$V_{node} = \frac{1}{d} \sum_{subtri} \mathbf{x}_{subtri} \cdot \mathbf{S}_{subtri}, \text{ with: } \sum_{subtri} \mathbf{S}_{subtri} = 0 \quad (3.41)$$

Some of the operators needed for the computation of the Navier-Stokes equations are approximated integrating over the CV surface following the Gauss theorem. In order to do so, the variables need to be known on this surface. For this reason, pairs of nodes are considered, to which then parts of the CV surface are associated. They will be referred to as Π_i from now on. The surface integral then can be obtained by simply summing over the pairs connected to the node of the CV in question. There exist two options to construct stencils based on the pair notion:

- In the sparse stencil, only *physical* pairs are considered, i. e. edges of the cell connecting two nodes.
- For mesh elements other than triangular/tetrahedral ones, the dense stencil also takes into account virtual connected pairs, e. g. nodes connected across the cell by a diagonal.

The normal vector of the face associated to the node pair p, q is denoted $\mathbf{S}_{p,q}$. On irregular meshes, particularly built of quadrilateral elements, the dense stencil assures second-order accuracy of the spatial operators. A detailed description of the spatial discretization in 3D and of the deployed equations can be found in the doctoral thesis of S. Vantieghem [Vantieghem 2011]. With the introduction of the fourth-order spatial discretization scheme the sparse stencil became the default option. This is due to the fact that the additional computational effort for the non-physical node pairs is not compensated by the gain in accuracy.

The above mentioned fourth-order scheme for the spatial discretization will be outlined in section 3.2.1.1. The information provided is based on [Moureau 2011d].

3.2.1.1 Higher order spatial discretization

In section 3.1.4.4 it was mentioned that the mass matrix, occurring within the Galerkin finite-element context of AVBP, can be seen as an operator relating the volume-average values, which are referring to the center of mass (or barycenter) of the CV, to the values at the grid nodes. It is obvious that in unstructured meshes of complex computational domains the grid nodes and the barycenter of the CV do not necessarily have the same position.

The fourth-order spatial discretization of YALES2 is based on the same idea, only in a finite-volume framework. Basically, this approach consists of two steps:

1. Expression of the nodal values as a function of the volume averages calculated at the barycenter of the CV. This is denoted as deconvolution of the finite-volume integration.
2. The resulting expressions of the nodal values are then used to calculate the fluxes between adjacent CV.

The assumption of a smoothly varying top-hat filter in physical space coinciding with the computational mesh is made, in order for the method to be valid. Such a filter is

represented by the average over the CV for a mesh with only small variations in element size throughout the domain and is defined as:

$$\bar{\phi}_{\Omega_p} = \frac{1}{V_p} \int_{\Omega_p} \phi d\Omega, \quad (3.42)$$

here done for grid node p of Fig. 3.5(a), with V_p representing the nodal volume of the dual mesh cell Ω_p .

The first step of the deconvolution consists in expanding Eq. (3.42) in a Taylor series around the grid node at $\mathbf{x} = \mathbf{x}_p$:

$$\begin{aligned} \bar{\phi}_{\Omega_p} &= \frac{1}{V_p} \int_{\Omega_p} \phi_p d\Omega \\ &+ \frac{1}{V_p} \int_{\Omega_p} (x^i - x_p^i) \partial_i \phi_p d\Omega \\ &+ \frac{1}{V_p} \int_{\Omega_p} (x^i - x_p^i) (x^j - x_p^j) \partial_{ij}^2 \phi_p d\Omega. \end{aligned} \quad (3.43)$$

In Eq. (3.43) the term $\partial_i \phi_p$ represents component i of the gradient vector of ϕ and $\partial_{ij}^2 \phi_p$ is the (i, j) component of the Hessian matrix of ϕ . Both operators are calculated at the location of grid node p . Since ϕ_p is constant over Ω_p , this can be expressed as:

$$\bar{\phi}_{\Omega_p} = \phi_p + \bar{\delta x}_p^i (\partial_i \phi_p) + \frac{1}{2} \bar{\delta^2 x}_p^{ij} (\partial_{ij}^2 \phi_p) + \mathcal{O}(\Delta x^3) \quad (3.44)$$

The operators in Eq. (3.44) are:

$$\bar{\delta x}_p^i = \frac{1}{V_p} \int_{\Omega_p} (x^i - x_p^i) d\Omega \quad (3.45)$$

$$\bar{\delta^2 x}_p^{ij} = \frac{1}{V_p} \int_{\Omega_p} (x^i - x_p^i) (x^j - x_p^j) d\Omega \quad (3.46)$$

Using the definition of the barycenter of the CV

$$\mathbf{x}_{\bar{p}} = \bar{\mathbf{x}}_{\Omega_p} = \frac{1}{V_p} \int_{\Omega_p} \mathbf{x} dV, \quad (3.47)$$

Eq. (3.45) can be seen as the i^{th} component of the vector, describing the distance between the grid node and the barycenter of the CV. For the case of an absolutely regular mesh, this vector becomes 0 (see Eq. (3.50)). The second operator, Eq. (3.46), represents a second-order moment tensor.

It is valid to interpret Eq. (3.44) as a continuous filtered field. This allows to apply derivative operators, such that Eq. (3.44) can be inverted and ϕ_p is expressed as a function of $\bar{\phi}_{\Omega_p}$, reading:

$$\phi_p = \bar{\phi}_{\Omega_p} - \bar{\delta x}_p^i \left(\partial_i \bar{\phi}_{\Omega_p} \right) - \left(\frac{1}{2} \bar{\delta^2 x}_p^{ij} - \bar{\delta x}_p^i \bar{\delta x}_p^j \right) \left(\partial_{ij}^2 \bar{\phi}_{\Omega_p} \right) + \mathcal{O}(\Delta x^3) \quad (3.48)$$

When performing the same procedure with respect to the barycenter of the CV at $\mathbf{x} = \mathbf{x}_{\bar{p}}$, the following formulation is obtained:

$$\phi_{\bar{p}} = \bar{\phi}_{\Omega_p} - \bar{\delta x}_{\bar{p}}^i \left(\partial_i \bar{\phi}_{\Omega_p} \right) - \left(\frac{1}{2} \bar{\delta^2 x}_{\bar{p}}^{ij} - \bar{\delta x}_{\bar{p}}^i \bar{\delta x}_{\bar{p}}^j \right) \left(\partial_{ij}^2 \bar{\phi}_{\Omega_p} \right) + \mathcal{O}(\Delta x^3) \quad (3.49)$$

The last equation (3.49) can be simplified, because the operator $\bar{\delta x}_{\bar{p}}^i$ yields:

$$\bar{\delta x}_{\bar{p}}^i = \frac{1}{V_p} \int_{\Omega_p} (x^i - x_{\bar{p}}^i) d\Omega = \mathbf{x}_{\bar{p}}^i - \mathbf{x}_{\bar{p}}^i = 0, \quad (3.50)$$

resulting in

$$\phi_{\bar{p}} = \bar{\phi}_{\Omega_p} - \frac{1}{2} \bar{\delta^2 x}_{\bar{p}}^{ij} \left(\partial_{ij}^2 \bar{\phi}_{\Omega_p} \right) + \mathcal{O}(\Delta x^3) \quad (3.51)$$

The order of the deconvolution is limited to third-order, because this avoids the introduction of derivatives of the order higher than two, which would induce high computational overheads.

In the second step, the deconvolution approach is applied to compute the flux over the CV boundary surface $\partial\Omega_p$. To facilitate the task, this boundary surface is split into pieces with adjacent CVs (e. g. Ω_q , Ω_r , etc.) and the resulting fluxes over these boundary pieces are then summed up.

Considering the nodes p and q of Fig. 3.5(a), both CVs Ω_p and Ω_q share a piece of boundary denoted $\partial\Omega_b$ in the following. The integrated flux over this boundary piece can be defined as:

$$\Psi_{\partial\Omega_b} = \Psi \left(\bar{\phi}_{\partial\Omega_b} \right) \cdot \mathbf{A}_{\partial\Omega_b}, \quad (3.52)$$

with $\mathbf{A}_{\partial\Omega_b}$ being the surface of the boundary piece. The flux is computed using the average value of ϕ at the center of mass of the boundary surface, which depends on the contributions of the adjacent CVs. This value is defined similarly to Eq. (3.42), namely

$$\bar{\phi}_{\partial\Omega_b} = \frac{1}{\mathbf{A}_{\partial\Omega_b}} \int_{\partial\Omega_b} \phi dA. \quad (3.53)$$

The variable ϕ again is evaluated using a Taylor series expansion around the barycenter of Ω_p with respect to the point b , which is the intersection of the boundary surface piece $\partial\Omega_b$ and the midpoint of the edge connecting the nodes p and q :

$$\phi_{\bar{p},\partial\Omega_b} = \phi_{\bar{p}} - \delta x_{\bar{p},b}^i (\nabla_i \phi_{\bar{p}}) - \frac{1}{2} \delta^2 x_{\bar{p},b}^{ij} (\nabla_{ij}^2 \phi_{\bar{p},b}) + \mathcal{O}(\Delta x^3) \quad (3.54)$$

With the help of Eq. (3.51), the value $\phi_{\bar{p},\partial\Omega_b}$ can be transformed into:

$$\phi_{\bar{p},\partial\Omega_b} = \bar{\phi}_{\Omega_p} - \delta x_{\bar{p},b}^i \left(\nabla_i \bar{\phi}_{\Omega_p} \right) - \frac{1}{2} \delta^2 x_{\bar{p},b}^{ij} \left(\nabla_{ij}^2 \bar{\phi}_{\Omega_p,b} \right) + \mathcal{O}(\Delta x^3) \quad (3.55)$$

The newly introduced operators are:

$$\delta x_{\bar{p},b}^i = x_b^i - x_{\bar{p}}^i \quad (3.56)$$

$$\delta^2 x_{\bar{p},b}^{ij} = (x_b^i - x_{\bar{p}}^i) (x_b^j - x_{\bar{p}}^j) = \delta x_{\bar{p},b}^i \delta x_{\bar{p},b}^j \quad (3.57)$$

As aforementioned, the value of ϕ_b depends on the contributions of the CV of grid node p and q . Thus, after having applied the same procedure to the CV Ω_q and after some simplifications, ϕ_b can be written as:

$$\begin{aligned} \phi_b &= \frac{1}{2} (\phi_{b,\Omega_p} + \phi_{b,\Omega_q}) \\ &= \frac{1}{2} (\bar{\phi}_{\Omega_p} + \bar{\phi}_{\Omega_q}) \\ &\quad + \frac{1}{4} (\delta x_{\bar{p},b}^i + \delta x_{\bar{q},b}^i) \nabla_i (\bar{\phi}_{\Omega_p} + \bar{\phi}_{\Omega_q}) \\ &\quad + \frac{1}{8} (\delta^2 x_{\bar{p},b}^{ij} - \bar{\delta}^2 x_{\bar{p}}^{ij} + \delta^2 x_{\bar{q},b}^{ij} - \bar{\delta}^2 x_{\bar{q}}^{ij} - (\delta x_{\bar{p},b}^i - \delta x_{\bar{q},b}^i) \delta x_{\bar{p},q}^j) \nabla_{ij}^2 (\bar{\phi}_{\Omega_p} + \bar{\phi}_{\Omega_q}) \\ &\quad + \mathcal{O}(\Delta x^3) \end{aligned} \quad (3.58)$$

In Eq. (3.58), the following relations can be used

$$\delta x_{\bar{p},b}^i + \delta x_{\bar{q},b}^i = 0, \quad (3.59)$$

$$\delta x_{\bar{p},b}^i - \delta x_{\bar{q},b}^i = x_q^i - x_p^i = \delta x_{\bar{p},q}^i, \quad (3.60)$$

$$\delta x_{\bar{p},b}^i + \delta x_{\bar{q},b}^i = -(\bar{\delta} x_{\bar{p}}^i + \bar{\delta} x_{\bar{q}}^i), \quad (3.61)$$

$$\delta x_{\bar{p},b}^i - \delta x_{\bar{q},b}^i = x_{\bar{p}}^i - x_{\bar{q}}^i = \delta x_{\bar{p},q}^i. \quad (3.62)$$

Finally, the value ϕ_b reads

$$\begin{aligned} \phi_b &= \frac{1}{2} (\bar{\phi}_{\Omega_p} + \bar{\phi}_{\Omega_q}) + \frac{1}{2} (\bar{\delta} x_{\bar{p}}^i + \bar{\delta} x_{\bar{q}}^i) \nabla_i \left(\frac{\bar{\phi}_{\Omega_p} + \bar{\phi}_{\Omega_q}}{2} \right) \\ &\quad + \frac{1}{2} \left(\frac{\delta x_{\bar{p},b}^i \delta x_{\bar{q},b}^j + \delta x_{\bar{q},b}^i \delta x_{\bar{p},b}^j}{2} - \frac{\bar{\delta}^2 x_{\bar{p}}^{ij} + \bar{\delta}^2 x_{\bar{q}}^{ij}}{2} \right) \nabla_{ij}^2 \left(\frac{\bar{\phi}_{\Omega_p} + \bar{\phi}_{\Omega_q}}{2} \right) \\ &\quad + \mathcal{O}(\Delta x^3) \end{aligned} \quad (3.63)$$

Equation (3.63) represents the approximation of the quantity ϕ at the CV surface as a function of the average values of the adjacent CVs Ω_p and Ω_q . Coming back to the assumption of the smoothly varying filter, this means that the distance between the mesh node and the corresponding barycenter of the CV is very small. Mathematically, this can be expressed by introducing $\bar{\delta} x_{\bar{p}}^i \approx \varepsilon \delta x_{\bar{p},b}^i$ and $\bar{\delta} x_{\bar{q}}^i \approx \varepsilon \delta x_{\bar{q},b}^i$. The parameter ε is an indicator for the mesh quality and in the case of a quasi-homogeneous mesh, it is $|\varepsilon| \ll 1$. In the case of a regular mesh, its value is 0, since the barycenter and the mesh

node coincide. Introducing ε into Eq. (3.63), one obtains:

$$\begin{aligned} \phi_b = & \frac{(\bar{\phi}_{\Omega_p} + \bar{\phi}_{\Omega_q})}{2} + \frac{1}{2} \left(\frac{\delta^2 x_{p,q}^{ij}}{4} + \frac{\overline{\delta^2 x_p^{ij}} + \overline{\delta^2 x_q^{ij}}}{2} \right) \nabla_i^2 \left(\frac{\bar{\phi}_{\Omega_p} + \bar{\phi}_{\Omega_q}}{2} \right) \\ & - \left(\frac{\overline{\delta x_p^i} + \overline{\delta x_q^i}}{2} \right) \nabla_{ij}^2 (\bar{\phi}_{\Omega_p} + \bar{\phi}_{\Omega_q}) + \mathcal{O}(\varepsilon^2 \Delta x^2) + \mathcal{O}(\Delta x^3) \end{aligned} \quad (3.64)$$

As mentioned at the beginning of this description for the higher order spatial discretization, this scheme is fourth-order accurate. More precisely, this is true for regular grids and reduces to a third-order accurate scheme on meshes, for which the assumption $|\varepsilon| \ll 1$ is valid. To provide proof, Eq. (3.64) will be written for a regular, one dimensional mesh. First, $\phi_b = \phi_{(i+\frac{1}{2})}$ will be presented. The gradient operator is a first order, forward difference for ϕ_{Ω_p} and a backward difference for ϕ_{Ω_q} , respectively. Same is applied to the diffusion term, i. e. a forward/backward difference for the second-order derivative. Only the operators for ϕ_{Ω_p} are presented here:

$$\nabla_i \bar{\phi}_{\Omega_p} = \frac{\bar{\phi}_{(i+1)} - \bar{\phi}_i}{\Delta x} + \mathcal{O}(\Delta x^2), \quad (3.65)$$

$$\nabla_{ij}^2 \bar{\phi}_{\Omega_p} = \frac{\bar{\phi}_{(i+2)} - 2\bar{\phi}_{(i+1)} + \bar{\phi}_i}{\Delta x^2} + \mathcal{O}(\Delta x). \quad (3.66)$$

The operators in Eq. (3.64) are:

$$\delta^2 x_{p,q}^{11} = \Delta x, \quad (3.67)$$

$$\overline{\delta^2 x_p^{11}} = \frac{1}{V_p} \int_{\Omega_p} (x^i - x_p^i) (x^j - x_p^j) d\Omega = \frac{\Delta x}{12} \text{ (same for } \bar{q}), \quad (3.68)$$

$$\overline{\delta x_p^1} = \overline{\delta x_q^1} = 0 \quad (3.69)$$

By this, one obtains

$$\bar{\phi}_{(i+\frac{1}{2})} = \frac{-\bar{\phi}_{(i+2)} + 7\bar{\phi}_{(i+1)} + 7\bar{\phi}_i - \bar{\phi}_{(i-1)}}{12} \quad (3.70)$$

and

$$\bar{\phi}_{(i-\frac{1}{2})} = \frac{-\bar{\phi}_{(i+1)} + 7\bar{\phi}_i + 7\bar{\phi}_{(i-1)} - \bar{\phi}_{(i-2)}}{12}. \quad (3.71)$$

Building the scalar gradient by combining Eqs. (3.70) and (3.71) gives the classical fourth-order finite-difference centered scheme:

$$\nabla \phi|_i = \frac{\bar{\phi}_{i+\frac{1}{2}} - \bar{\phi}_{i-\frac{1}{2}}}{\Delta x} = \frac{-\bar{\phi}_{(i+2)} + 8\bar{\phi}_{(i+1)} - 8\bar{\phi}_{(i-1)} + \bar{\phi}_{(i-2)}}{12\Delta x} \quad (3.72)$$

3.2.2 Numerics for the time advancement

When trying to advance the solution of the incompressible NS equations in time, one issue is the absence of a derivative with respect to time in the mass conservation equation. The incompressibility constraint, i. e. Eq. (2.41), can rather be interpreted as a kinematic constraint on the velocity field. It implicitly couples pressure and velocity, since the pressure can be seen as a variable needed to enforce continuity. One approach to circumvent this difficulty are the so-called fractional-step methods, which will be outlined in the following.

3.2.2.1 The fractional step method

The basic idea of fractional step methods is to separate the pressure gradient from the other terms in the momentum equation (2.42). It is used for the projection of the velocity field onto a divergence-free field by introducing an intermediate velocity u^{star} . The original formulation was presented by Chorin [Chorin 1968] and is based on the Helmholtz-Hodge decomposition of vector fields. Today, these methods are very popular and it exists a wide variety.

In YALES2, a slightly modified version is implemented, which uses corrections of the boundary conditions for the fractional step method [Kim 1985, Vantiegheem 2011]:

1. Based on the known velocity field \mathbf{u}^n a first intermediate velocity field $\hat{\mathbf{u}}$ is calculated, including a pressure gradient term at $t = t_{n-\frac{1}{2}}$:

$$\frac{\hat{\mathbf{u}} - \mathbf{u}^n}{\Delta t} = -\mathbf{u}^n \cdot \nabla \mathbf{u}^n + \nu \nabla^2 \mathbf{u}^n - \nabla P^{(n-\frac{1}{2})}, \quad (3.73)$$

with the BC $\hat{\mathbf{u}}|_{\partial \Omega_c} = \mathbf{u}^{n+1}|_{\partial \Omega_c}$.

2. In order for the actual intermediate velocity field \mathbf{u}^* of the fractional step method to satisfy the corrected BC, which assures second-order accuracy in time, the 'old' pressure gradient is removed from $\hat{\mathbf{u}}$.

$$\frac{\mathbf{u}^* - \hat{\mathbf{u}}}{\Delta t} = \nabla P^{(n-\frac{1}{2})} \quad (3.74)$$

3. With \mathbf{u}^* known, the irrotational part can be defined as:

$$\frac{\mathbf{u}^{(n+1)} - \mathbf{u}^*}{\Delta t} = -\nabla P^{(n+\frac{1}{2})}. \quad (3.75)$$

Taking the divergence of Eq. (3.75) and taking into account the incompressibility constraint $\nabla \cdot \mathbf{u}^{(n+1)} = 0$, this results in the Poisson equation:

$$\nabla \cdot \frac{\mathbf{u}^*}{\Delta t} = \nabla \cdot \nabla P^{(n+\frac{1}{2})} \quad (3.76)$$

Preventing the introduction of an error term by taking into account the 'old' pressure at $t = t_{(n-\frac{1}{2})}$ in an additional step largely compensates the supplementary computational costs.

In order to solve the elliptic equation (3.76), YALES2 disposes of the following iterative solvers:

- Preconditioned Conjugated Gradient (PCG)
- Bi-Conjugate Gradient stabilized (BiCGstab)
- Deflated PCG
- Deflated BiCGstab(2)

In the course of this work, the DPCG [Saad 1999] solver is used, with a convergence criterion $\varepsilon = 1 \cdot 10^{-8}$. For more detailed information on iterative solvers the reader is asked to consider specialized literature, e. g. [Saad 2003, Trefethen 1997].

3.2.2.2 Time integration

To advance the solution in time, YALES2 disposes of explicit as well as implicit time integration schemes. Contrary to an explicit time advancement, which only uses known values at $t = t_n$, implicit schemes also depend on the unknown quantities at $t = t_{(n+1)}$. The resulting system of equations is rather large and requires some computational effort. This drawback can be outweighed by the higher stability that these schemes provide, allowing larger time steps (i. e. $C > 1$).

Implicit methods

The implicit method implemented in YALES2 is called the Θ family of methods (e. g. [Donea 2003]). This scheme reads

$$\frac{\mathbf{u}^{(n+1)} - \mathbf{u}^n}{\Delta t} = \Theta \frac{\partial \mathbf{u}^{(n+1)}}{\partial t} + (1 - \Theta) \frac{\partial \mathbf{u}^n}{\partial t} + \mathcal{O}\left(\left(\frac{1}{2} - \Theta\right) \Delta t, \Delta t^2\right) \quad (3.77)$$

and allows to switch between different implicit schemes depending on the value for Θ , except for $\Theta = 0$ (i. e. Euler method). Commonly used schemes are the implicit (or backward) Euler ($\Theta = 1$) or the Crank-Nicolson scheme ($\Theta = \frac{1}{2}$). As can be seen from the error term, these schemes are at most second-order accurate in time (for the case of the Crank-Nicolson scheme). Note that the Crank-Nicolson scheme is unconditionally stable [Hirsch 1988, Munz 2006], contrary to the widely used explicit Runge-Kutta schemes.

When using the Crank-Nicolson scheme in YALES2, the right hand side of Eq. (3.77) is predicted using a second-order Adams-Bashforth method (see e. g. [Donea 2003]), which, according to [Vantieghem 2011], avoids the use for non-linear equation solvers and hence, reduces the computational effort needed considerably.

Explicit methods

A more interesting method for the temporal integration is the numerical scheme denoted *TRK4* (a.k.a. *TFV4A* in the context of YALES2). This time integration scheme is fourth-order accurate and allows to adjust the in-built diffusion by modification of a parameter. Since its implementation in the cell-vertex framework is part of the present work, a detailed description as well as its analysis is presented in chapter 4.

3.2.3 HPC

YALES2, just like AVBP, was designed from the very beginning to benefit of massively parallel architectures. As can be seen in Fig. 3.6 the code YALES2 performs also very well on super-computers.

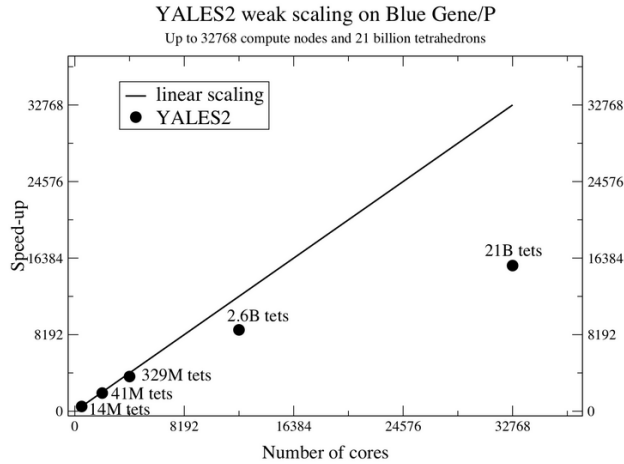


Figure 3.6: *Speed-up (weak scaling) of YALES2 on an IBM BlueGene/P computer [Moureau 2011a]*

Different to the previous section, where the speed-up of AVBP for strong scaling was presented, the speed-up graph of YALES2 depicts the behavior of the solver on up to 32768 processors for a weak scaled test case. Weak scaling means to test the software performance for an increasing number of processors while, at the same time, increasing the problem size, i. e. in this case the number of mesh elements. This is done because YALES2 is capable of refining the computational grids automatically. The algorithm deployed for the homogeneous mesh refinement [Rivara 1984] is conceived to prevent the mesh from deteriorating by conserving the skewness of the elements. Combining the mesh refinement with the HPC capability of the code forms the basis of the approach to tend towards DNS of complex problems and industrial applications [Moureau 2011c, Moureau 2010a]. To obtain such a performance on HPC architectures, YALES2 also applies the methodology of a double domain decomposition. Besides the interest of optimizing the cache memory usage, this approach provides a coarse mesh formed by the cell groups, which is used to precondition the Poisson solver [Moureau 2011b]. The algorithm for the primary domain partitioning is based on the METIS algorithm [Karypis 1995].

Part II

Tunable time integration scheme for the LES

With regard to the comparison of the compressible and incompressible approaches in part III, the idea was to align the CFD solvers AVBP and YALES2 concerning the numerical schemes and hence, eliminate one possible source for differences impacting the results. For this reason, the objective was to determine the mathematical properties of the time integration scheme TRK4 of YALES2, adapt the scheme to the *cell-vertex* method of AVBP and compare its performance to already established schemes of the compressible solver.

4	Numerical schemes for LES	51
4.1	The Two-step Runge-Kutta family of schemes	51
4.2	Development of the TRK schemes	52
4.3	Implementation of the TRK schemes in AVBP	53
4.4	Mathematical properties of the newly developed schemes	55
4.4.1	The second order scheme TRK2	56
4.4.2	The fourth order scheme TRK4	58
4.4.3	Temporal order measurements	62
4.4.4	Scalar step advection	62
4.4.5	Dissipation measurements in a turbulent flow	63
4.5	Application of TRK4 in the cell-vertex formulation to complex test-cases .	66
4.5.1	Turbine blade in two dimensions	66
4.5.2	Full 3D LES of turbine blade	68
4.5.3	Full 3D LES of a reactive flow in PRECCINSTA	72
4.5.3.1	Computational cost of TRK4	72
4.6	Conclusions	77

Numerical schemes for LES

4.1 The Two-step Runge-Kutta family of schemes

In LES, more precisely in explicit LES [Sagaut 2002], the continuity of the decaying energy spectrum beyond the resolved scales (see Fig. 2.1) is mimicked by the sub-grid scale models, some of which are presented in section 2.3. These models achieve this forward energy cascade by adding a viscous-like term to the balance equations. In order not to overshadow the turbulent viscosity of the SGS models and thus, falsify the representation of the energy cascade, high order time integration schemes with low-diffusion properties are preferred for this type of simulations. Their development is a recurring issue for CFD solvers.

A widely used family of schemes are the Runge-Kutta (RK) methods. Schemes of the RK family are based on the work of C. Runge [Runge 1895] and W. Kutta [Kutta 1901]. The low-storage version of the RK schemes [Williamson 1980], that was presented in Eqs. (3.14), is often used, since its implementation is rather straight forward and an integration of third order of accuracy or higher can be achieved easily.

The CFD solvers AVBP and YALES2 are based on central space discretizations (see sections 3.1 and 3.2), which are oscillatory by nature [Hirsch 1988]. Their application is justified though, because of their property to preserve the initial dispersion of the physics. As a consequence, when combining RK methods with these discretizations in space, the resulting schemes can become unstable, as in the case of the one-step RK1 (simple Euler step) and the two-step RK2 scheme. Alternatively, stabilizing measures have to be taken, which is the case for higher order RK schemes. It is thus necessary to add a distinct amount of numerical diffusion to overcome this problem. In general, two strategies are possible:

1. Adding artificial viscosity or applying high-wave number filters
2. Numerical viscosity built-in to the time and space discretization

Approach 1 is the most common, for the simple reason that it is easy to realize. Meanwhile, numerous sensors for various fields of application have been developed. Examples for such a sensor are [Cook 2004], which is implemented in YALES2, or the sensors of AVBP (see [Roux 2010]). A drawback of this methodology, however, is the fact that an analysis of the resulting numerical scheme, in terms of linear stability, is extremely difficult. Furthermore, it is almost impossible to predict the amount of artificial viscosity added.

The second option reveals to be less straight-forward. Examples are the TTGC scheme [Colin 2000b] of AVBP or [Berland 007, Bogey 004]. Contrary to the artificial

viscosity approach, a linear stability analysis can be performed and thus, the amount and type of numerical diffusion added can be assessed *a priori*.

Thus, the idea for the development of the Two-step Runge-Kutta (TRK) family of schemes was to design a simple time integration scheme providing a large region of stability (in terms of the CFL condition) and the possibility to adjust the incorporated numerical diffusion.

4.2 Development of the TRK schemes

The following considerations are based on the scalar transport equation

$$\frac{\partial \phi}{\partial t} + v \cdot \nabla \phi = 0, \quad (4.1)$$

with v being the convective velocity, which is supposed to be constant.

The Eqs. (3.14) can be rewritten in a more generalized form using $\mathcal{C}(\phi, v)$, which represents the discretized spatial operator and will be specified later:

$$\begin{aligned} \phi^{(1)} &= \phi^n - \gamma_{(1)} \Delta t \mathcal{C}(\phi^n, v), \\ \phi^{(2)} &= \phi^n - \gamma_{(2)} \Delta t \mathcal{C}(\phi^{(1)}, v), \\ &\vdots \\ \phi^{(n+1)} &= \phi^n - \gamma_{(k)} \Delta t \mathcal{C}(\phi^{(k-1)}, v). \end{aligned} \quad (4.2)$$

For the TRK schemes it is necessary to combine each two steps of the RK scheme. This way, the RK2 scheme can be expressed as:

$$\phi^{(n+1)} = \phi^n - \Delta t \mathcal{C}(\phi^n, v) + \frac{1}{2} \Delta t^2 \mathcal{C}^2(\phi^n, v) \quad (4.3)$$

and the RK4 scheme yields:

$$\phi^{(2)} = \phi^n - \frac{1}{3} \Delta t \mathcal{C}(\phi^n, v) + \frac{1}{12} \Delta t^2 \mathcal{C}^2(\phi^n, v), \quad (4.4)$$

$$\phi^{(n+1)} = \phi^n - \Delta t \mathcal{C}(\phi^n, v) + \frac{1}{2} \Delta t^2 \mathcal{C}^2(\phi^2, v). \quad (4.5)$$

In Eqs. (4.3), (4.4) and (4.5), the term \mathcal{C}^2 stands for the twice applied convective operator:

$$\mathcal{C}^2(\phi, v) = \mathcal{C} \circ \mathcal{C}(\phi, v) = v \cdot \nabla (v \cdot \nabla \phi). \quad (4.6)$$

The RK approach can be summarized as the sequential application of the spatial discretization and then of the temporal discretization to the governing equations.

Contrary to this is the approach of P. Lax and B. Wendroff, that is presented in section 3.1.4.2 and for which the order of this sequential application is inverted. Using again the operator notation introduced in the beginning of this section, the second order LW scheme yields:

$$\phi^{(n+1)} = \phi^n - \Delta t \mathcal{C}(\phi^n, v) + \frac{1}{2} \Delta t^2 \mathcal{D}(\phi^n, v). \quad (4.7)$$

Another LW type scheme that was presented in the course of this work is the TTG4A scheme. In operator notation, this scheme reads:

$$\phi^{(2)} = \phi^n - \frac{1}{3}\Delta t\mathcal{C}(\phi^n, v) + \frac{1}{12}\Delta t^2\mathcal{D}(\phi^n, v) \quad (4.8)$$

$$\phi^{(n+1)} = \phi^n - \Delta t\mathcal{C}(\phi^n, v) + \frac{1}{2}\Delta t^2\mathcal{D}(\phi^2, v) \quad (4.9)$$

The newly appearing operator \mathcal{D} represents the discretization operator of the classical LW diffusion term. As can be noticed, the RK schemes and the LW type schemes only differ in this term. This resemblance is at the basis of the TRK schemes. By combining the RK scheme and the corresponding LW type scheme linearly, the second order scheme TRK2 results in:

$$\phi^{(n+1)} = \phi^n - \alpha\Delta t\mathcal{C}(\phi^n, v) + (1 - \alpha)\frac{1}{2}\Delta t^2\mathcal{C}^2(\phi^n, v) + \alpha\frac{1}{2}\Delta t^2\mathcal{D}(\phi^n, v), \quad (4.10)$$

and for the fourth order method, named TRK4, the following equations are obtained:

$$\phi^{(2)} = \phi^n - \alpha\frac{1}{3}\Delta t\mathcal{C}(\phi^n, v) + (1 - \alpha)\frac{1}{12}\Delta t^2\mathcal{C}^2(\phi^n, v) + \alpha\frac{1}{12}\Delta t^2\mathcal{D}(\phi^n, v), \quad (4.11)$$

$$\phi^{(n+1)} = \phi^n - \alpha\Delta t\mathcal{C}(\phi^n, v) + (1 - \alpha)\frac{1}{2}\Delta t^2\mathcal{C}^2(\phi^2, v) + \alpha\frac{1}{2}\Delta t^2\mathcal{D}(\phi^2, v). \quad (4.12)$$

It has to be pointed out that the operator \mathcal{D} differs from the corresponding term \mathcal{C}^2 , depending on the method used for the discretization. Considering the example of section 4.4.1, it can be noticed that the operator of the RK scheme (Eq. (4.16)) uses a wider stencil than the operator of Eq. (4.17), i. e. 5 adjacent points for \mathcal{C}^2 instead of only 3 for the operator \mathcal{D} . This difference in the stencil width, illustrated in Fig. 4.2, renders the LW type schemes more diffusive especially for higher frequencies. The parameter α allows to adjust the impact of the different diffusive terms. For $\alpha = 0$, the RK scheme is recovered, whereas $\alpha = 1$ leads to the LW type scheme.

4.3 Implementation of the TRK schemes in AVBP

One objective of this work was to implement the fourth order scheme of the TRK family in the cell-vertex framework of AVBP and compare it to other schemes already at hand. It is clearly of advantage that the schemes, which form the basis of TRK4, namely RK4 and TTG4A, already exist in the solver. At this point we will consider the schemes in their finite-volume formulation, which is second order accurate in space. Concerning the TTG4A scheme this can be interpreted as finite-element method using a lumped mass matrix [Hirsch 1988]. In the section 4.2 it is pointed out that the particularity of the TRK schemes comes from the linear combination of two different discretizations of the diffusive terms. For AVBP this means, in return, to evaluate the Lax-Wendroff type diffusion term \mathcal{D} on a 2Δ wide stencil, whereas \mathcal{C}^2 , based on the RK scheme, uses a 4Δ stencil.

Structured solvers use grids, in which the position of the adjacent grid nodes to a point in consideration are easily identified by adding ± 1 to the indices in each direction,

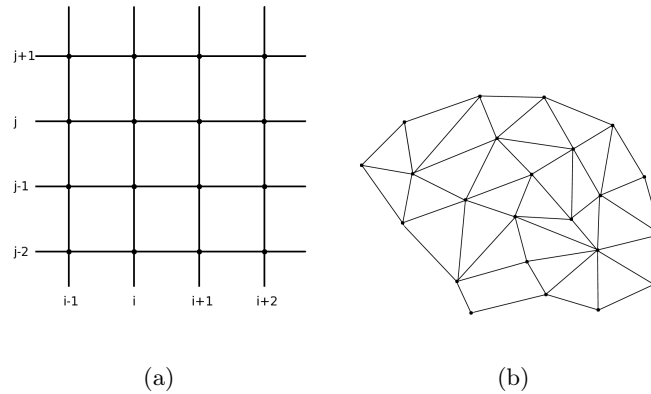


Figure 4.1: a) Example for a structured grid. Grid points (in 2D) are identified by the indices (i, j) , which are numbered consecutively. - b) In an unstructured grid the node numbering is specified explicitly.

see Fig. 4.1(a). AVBP, on the contrary, is an unstructured code. The organization of the grid is not intrinsic at all and is specified explicitly. Although, this grid type implicates additional computational cost, it is extremely flexible concerning its adaption to complex geometries and thus, very well suited for the *finite-volume* and *finite-element* approach. An example is presented in Fig. 4.1(b). One drawback is that the width of the stencil used by the numerical schemes can not be modified this easily and usually compact stencils are used.

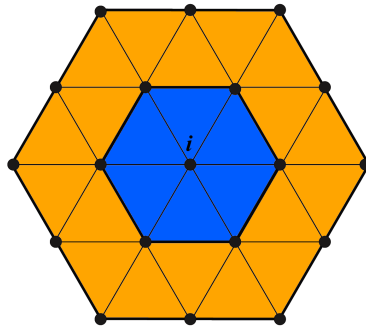


Figure 4.2: Grid elements considered by the 2Δ (red) and the 4Δ (blue + orange) stencil of AVBP.

The basic stencil in AVBP is obtained during a *gather-scatter* operation and encloses the cells directly connected to the grid node in consideration, i. e. the blue surface in Fig. 4.2. Transposed to 1D, this is equivalent to a 2Δ wide stencil. This compact stencil is used for all spatial operators of the convective schemes. Generally speaking, a 4Δ wide stencil can be obtained by applying the *gather-scatter* operation twice, which leads to enclosing the cells marked orange in Fig. 4.2. Since the TTG4A scheme is already implemented in AVBP, its diffusive terms will be multiplied by a factor α . In order to

obtain the TRK4 scheme of Eqs. (4.11) and (4.12), only the term containing \mathcal{C}^2 has to be added. The procedure to compute this diffusive operator term on the 4Δ stencil in AVBP is presented below:

1. After the conservative variables are gathered on the vertices of each cell, the flux divergence is computed, as presented in section 3.1.3, within the elements of the primal mesh. The result is then redistributed to the global grid nodes using the scatter operation, see Eq. (3.8). In addition, the distribution matrix of the central differences of Eq. (3.13) is applied, leading to:

$$(\nabla \cdot \mathbf{F})|_i = -\frac{1}{V_i} \sum_{j|\Omega_j \in i} \frac{1}{n_v} \mathcal{I} V_{\Omega_j} R_{\Omega_j} \quad (4.13)$$

2. Next, the nodal flux divergence of step 1 again is gathered to the vertices of the primal cells. At the vertices the product of the flux divergence and the Jacobian is computed. Although the same approach of Eq. (3.17) is used for its computation, this Jacobian is based on the nodal primitive variables in order to be consistent with the nodal flux divergence. Hence, the Jacobian matrix \mathcal{A}_i is considered to be constant for the nodal volume and not for the CV of the primal cell:

$$\mathcal{A}_i (\nabla \cdot \mathbf{F})|_i \quad (4.14)$$

3. The final step, before scattering the diffusive term back to the global nodes, is to compute the divergence of Eq. (4.14) for each mesh element using again Eq. (3.6). Furthermore, the different factors, such as $(1 - \alpha)$ or Δt^2 , are applied to the result:

$$\frac{1}{\Delta t^2} (1 - \alpha) \mathcal{C}^2 = \frac{1}{V_i} \sum_{j|\Omega_j \in i} \frac{1}{n_v} \mathcal{I} V_{\Omega_j} \left(\frac{1}{dV_{\Omega_j}} \sum_{v \in \Omega_j} \mathcal{A}_v (\nabla \cdot \mathbf{F})|_v \cdot \mathbf{S}_v \right) \quad (4.15)$$

4.4 Mathematical properties of the newly developed schemes

In this section a closer look is taken regarding the new schemes' properties. To facilitate the task, this will be presented in more detail for the TRK2 scheme, before giving the results for TRK4. The investigated properties are the consistency of the scheme and its stability. If the TRK schemes prove to be consistent, i. e. the truncation error tends to zero for $\Delta t, \Delta x \rightarrow 0$, and if the stability analysis shows, that errors occurring in the course of the numerical solution process are not amplified, they can be seen as convergent. This property, indicating that the solution of the discretized problem tends towards the continuous problem for $\Delta t, \Delta x \rightarrow 0$, is drawn from the *Lax equivalence theorem* [Lax 1956], stating that given a properly posed linear initial value problem and a finite difference approximation to it that satisfies the consistency condition, stability is the necessary and sufficient condition for convergence.

4.4.1 The second order scheme TRK2

Spatial operators

For all following analyses only one space dimension and a uniform mesh of constant step width Δ are considered. Thus, the convective and diffusive operators \mathcal{C} and \mathcal{D} of Eq. (4.10) are replaced, using second order, centered discretization operators in space:

$$\mathcal{C}_{2nd} = \frac{\left((\phi^n v)_{(i+1)} - (\phi^n v)_{(i-1)} \right)}{2\Delta x} \Rightarrow \mathcal{C}_{2nd}^2 = \frac{\left((\phi^n v)_{(i+2)} - 2(\phi^n v)_i + (\phi^n v)_{(i-2)} \right)}{4\Delta x^2}, \quad (4.16)$$

and

$$\mathcal{D}_{2nd} = \frac{\left((\phi^n v)_{(i+1)} - 2(\phi^n v)_i + (\phi^n v)_{(i-1)} \right)}{\Delta x^2}. \quad (4.17)$$

It is at this point that the different nature of the three operators becomes obvious due to the varying stencils, which are used for the approximations, i. e. a classical $2\Delta x$ stencil for the second order diffusive operator \mathcal{D}_{2nd} and a $4\Delta x$ stencil for the operator \mathcal{C}_{2nd}^2 .

Consistency analysis

The consistency analysis permits to estimate the diffusion introduced by a numerical scheme with the help of the modified equation. This approach was first presented by Warming and Hyett [Warming 1974]. In fact, the modified equation analysis consists of determining the actual difference equations solved by the numerical scheme, resulting from the application of a specific spatial and temporal discretization. This equation is the sum of the original differential equation and a truncation error ε , caused by the discretization. It is this error term that gives an idea of the amount and the type of the implicit diffusion. For Eq. (4.1) the model equation yields:

$$\frac{\partial \phi}{\partial t} + v \frac{\partial \phi}{\partial x} = \varepsilon \quad (4.18)$$

The error term ε in the modified equation indicates an implicit diffusion mainly of the dissipative type, when the order of the leading term is even. On the contrary, if the order of the leading derivative in the error term is odd, the scheme dominantly introduces dispersion. Applying this approach to the scheme TRK, the truncation error reads:

$$\varepsilon_{TRK2,2nd} = -\frac{v\Delta x}{6} (1 - C^2) \frac{\partial^3 \phi}{\partial x^3} - \frac{v^2 \Delta x^2 \Delta t}{8} (\alpha - C^2) \frac{\partial^4 \phi}{\partial x^4} + \mathcal{O}(\Delta x^5). \quad (4.19)$$

Equation (4.19) confirms the claim, to design a scheme with adjustable dissipation, since the parameter α of the TRK scheme only acts on the even derivative term but not on the leading error term.

Linear stability and modified wave number analysis

The *von Neumann* analysis is based on the assumption that in general stability problems are rarely caused by BC (existing exceptions are not relevant here). By ignoring them, the analysis of a numerical scheme is simplified. Detailed explanations can be found in [Hirsch 1988, Ferziger 2002, Lamarque 2007]. Nevertheless, the basic idea will be outlined here.

Supposing a one-dimensional domain of unity length with periodic BC. This allows to express the solutions in form of a Fourier series at time $t = t_n$. Following, the example of a mono-dimensional, monochromatic signal is considered:

$$\phi = \sum_{p \in \mathbb{Z}} A_p \exp \left(I \frac{2\pi}{p\Delta x} x \right) \quad (4.20)$$

with p representing the number of points in the signal, A_p the amplitude and $I = \sqrt{-1}$ the imaginary number. The idea of the stability analysis is to investigate the evolution of the signal due to the discrete scheme in the course of time, i. e. from the instant t_n to $t_{(n+1)} = t + \Delta t$:

$$\phi^n = A_p^n \exp \left(I \frac{2\pi}{p\Delta x} x \right) \quad (4.21)$$

$$\phi^{(n+1)} = A_p^{(n+1)} \exp \left(I \frac{2\pi}{p\Delta x} x \right) \quad (4.22)$$

In the ideal case, the transport of ϕ is exact and the solution after one time step Δt will be advanced by the distance $v\Delta t$. Mathematically, this can be translated as:

$$\phi^{(n+1)} = A_p^n \exp \left(I \frac{2\pi}{p\Delta x} (x - v\Delta t) \right) \quad (4.23)$$

$$= \phi^n \exp(-Ik(C)), \quad (4.24)$$

with $k = \frac{2\pi}{p}$ being the non-dimensionalized wave number. In order to take account for the dissipation and dispersion introduced by the discretization, Eq. (4.24) has to be adjusted and thus, reads:

$$\phi^{(n+1)} = \phi^n G \exp(-Ik'(C)). \quad (4.25)$$

In Eq. (4.25) G represents the norm of the amplitude ratio of the signals before and after the advancement in time and k' is the modified wave number. These quantities can be expressed as:

$$G = \left| \frac{A_p^{(n+1)}}{A_p^n} \right|, \quad -\sin((C)k') = \mathcal{I} \left(\frac{1}{G} \frac{A_p^{(n+1)}}{A_p^n} \right) \quad (4.26)$$

G is thus an indicator for the dissipation a discretization introduces to a numerical scheme. This one is considered stable in the sense of the von Neumann analysis, when

the amplitude ratio G is less than unity for all wave numbers. Furthermore, the modified wave number describes the shift in frequency of the solution, due to the discretization. The closer k' is to the wave number k , the less dispersive the scheme.

Applying this approach to the TRK2 scheme yields:

$$\frac{A_p^{(n+1)}}{A_p^n} = 1 - (C) I \sin\left(\frac{2\pi}{p}\right) - 2\alpha (C^2) \sin^2\left(\frac{\pi}{p}\right) - \frac{(1-\alpha)}{2} (C^2) \sin^2\left(\frac{2\pi}{p}\right) \quad (4.27)$$

It can be noticed that G of Eq. (4.27) is a function of the CFL number C , which that way determines whether the scheme is stable or not. In Fig. 4.3, the CFL limit as a function of the parameter α is plotted (denoted TRK2 - DF2). The values recovered for the extreme values, $C_{\alpha=0} = 0$ (RK2) and $C_{\alpha=1} = 1$ (LW), are consistent with theory.

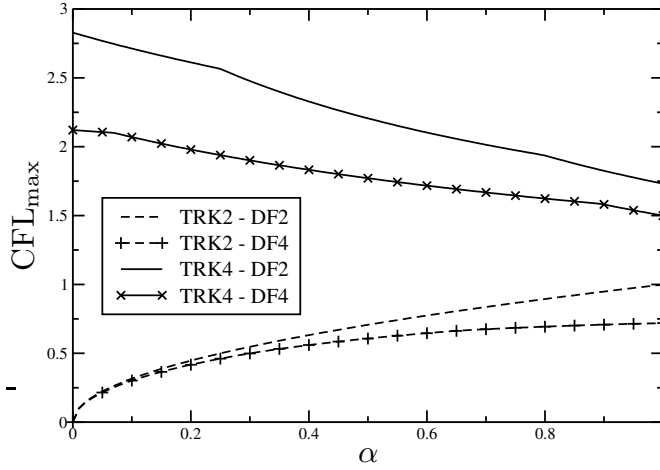
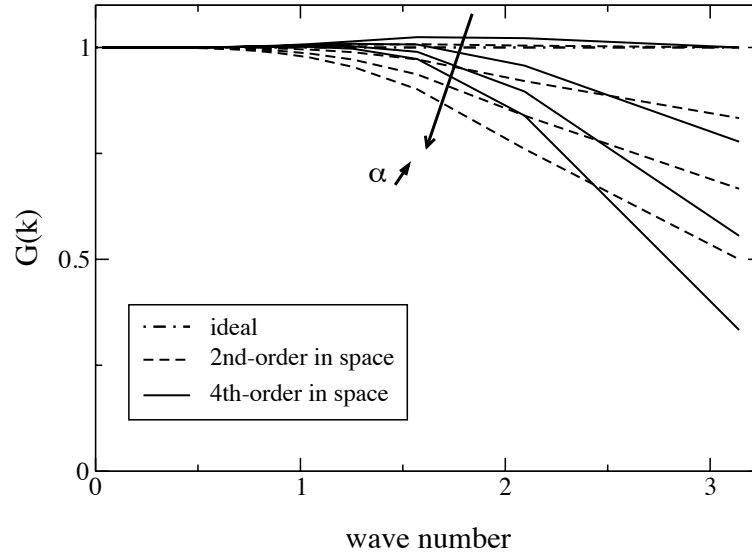


Figure 4.3: Maximum CFL numbers as a function of α for the TRK2 and TRK4 schemes using second (DF2) and fourth order (DF4) finite differences for the discretization in space.

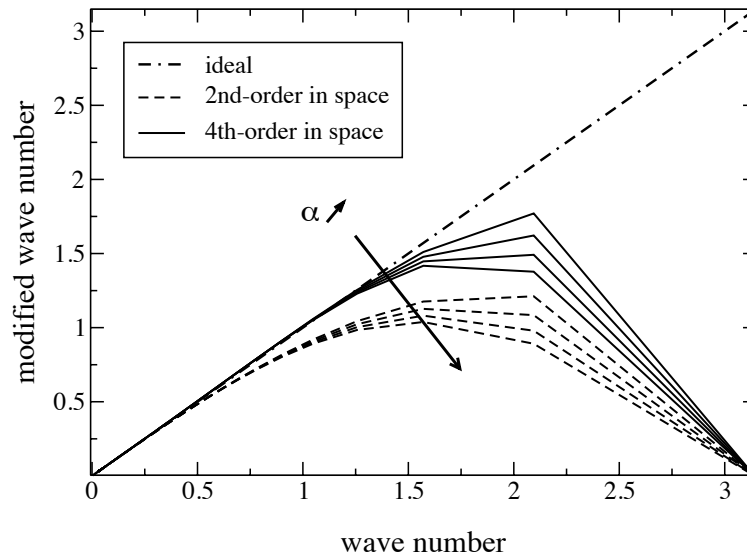
Exemplarily for a value of $C = 0.5$, the graphs in Fig. 4.4 present a) the amplitude ratio G and b) the modified wave number k' as functions of the wave number k for various α of the TRK2 scheme using the second order centered spatial discretization. The graphs for the fourth order centered spatial discretization were evaluated numerically.

4.4.2 The fourth order scheme TRK4

As noted in [Ferziger 2002] it is best to apply discretizations of equivalent order to spatial terms as well as to temporal ones. When considering unstructured codes, e. g. AVBP, it might not always be feasible to construct larger stencils for the spatial operators. Therefore, the TRK4 scheme will be analyzed for the second order centered operators of section 4.4.1.



(a)



(b)

Figure 4.4: a) Growth rate of TRK2 schemes with two space integrations and four different values of α : 0, 1/3, 2/3 and 1. The CFL number is equal to 0.5. - b) Modified wave number of TRK2 schemes with two space integrations and four different values of α : 0, 1/3, 2/3 and 1. The CFL number is equal to 0.5.

The truncation error of the consistency analysis reads in this case:

$$\varepsilon_{TRK4,2nd} = -\frac{v\Delta x^2}{6} \frac{\partial^3 \phi}{\partial x^3} - \frac{v^2 \Delta x^3}{8} (C) \alpha \frac{\partial^4 \phi}{\partial x^4} + \mathcal{O}(\Delta x^5) \quad (4.28)$$

Like in the case for the TRK2 scheme, the parameter α only modifies the even derivative terms in Eq. (4.28) and thus, allows to control the dissipation implied in the scheme. Following, the amplification ratio for the above mentioned combination results in:

$$\begin{aligned} \frac{\tilde{A}_p}{A_p^n} &= 1 - \frac{1}{3} (C) I \sin\left(\frac{2\pi}{p}\right) \\ &+ \frac{\alpha}{6} (C^2) \sin^2\left(\frac{\pi}{p}\right) - \frac{(1-\alpha)}{12} (C^2) \sin^2\left(\frac{2\pi}{p}\right) \end{aligned} \quad (4.29)$$

$$\begin{aligned} \frac{A_p^{(n+1)}}{A_p^n} &= 1 - (C) I \sin\left(\frac{2\pi}{p}\right) \\ &+ \left(\frac{\tilde{A}_p}{A_p^n}\right) \left(\frac{\alpha}{6} (C^2) \sin^2\left(\frac{\pi}{p}\right) - \frac{(1-\alpha)}{12} (C^2) \sin^2\left(\frac{2\pi}{p}\right)\right) \end{aligned} \quad (4.30)$$

As for the TRK2 scheme, the *CFL* limits are presented in Fig. 4.3 (denoted TRK4-DF2). The growth rate G and the modified wave number k' for the TRK4 scheme are plotted in Fig. 4.5.

Finally, the best-case scenario of a temporal and spatial discretization using the same order of accuracy is presented to complement this analysis. Using the 4th order centered spatial operators

$$C_{4th} = \frac{-(\phi^n v)_{i+2} + 8(\phi^n v)_{i+1} - 8(\phi^n v)_{i-1} + (\phi^n v)_{i-2}}{12\Delta x} \quad (4.31)$$

and

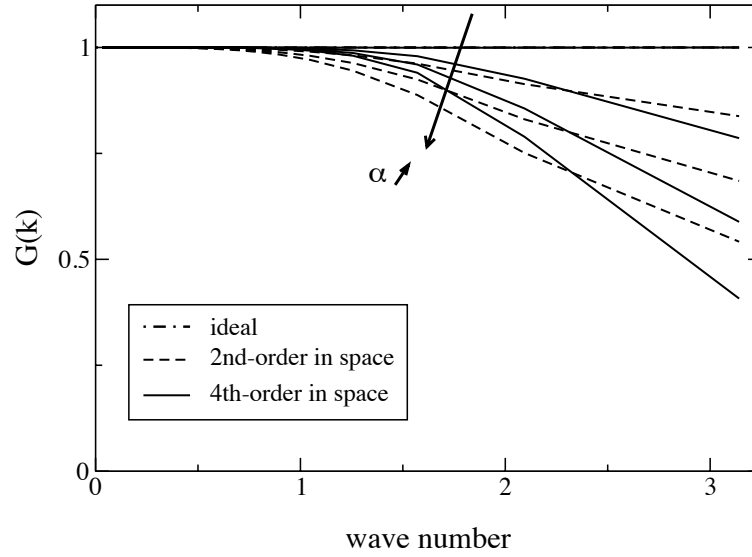
$$D_{4th} = \frac{-(\phi^n v)_{i+2} + 16(\phi^n v)_{i+1} - 30(\phi^n v)_i + 16(\phi^n v)_{i-1} - (\phi^n v)_{i-2}}{12\Delta x^2}, \quad (4.32)$$

the consistency analysis for this combination of TRK4 and the 4th order spatial operator leads to

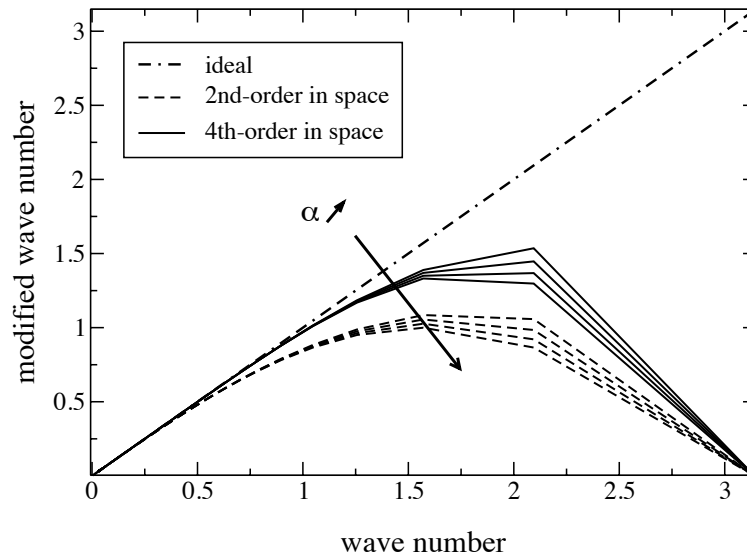
$$\varepsilon_{TRK4,4th} = \frac{v\Delta x^4}{120} (C^4 + 4) \frac{\partial^5 \phi}{\partial x^5} - \frac{v^2 C \Delta x^5}{144} (C^4 + 4\alpha) \frac{\partial^6 \phi}{\partial x^6} + \mathcal{O}(\Delta x^7). \quad (4.33)$$

As remarked for the earlier schemes, the result shows once more that the parameter α allows to adjust particularly the implicit dissipation of the scheme.

The RK4 schemes are conditionally stable with a maximum CFL greater than two [Hirsch 1988] and will be obtained for $\alpha = 0$. For $\alpha = 1$, the TTG4A scheme is obtained, i.e. evaluated at 1 [Quartapelle 1993]. The TRK4 appears to be promising because of their high maximum CFL number that may compensate their higher cost due to the additional steps. The amplification ratios for the fourth order spatial operators in combination with TRK2 and TRK4 will not be shown here, but can be obtained, e.g., with the help of computer algebra systems. The results presented in Figs. 4.3 to 4.5 have been obtained numerically.



(a)



(b)

Figure 4.5: a) Growth rate of TRK4 schemes with two space integrations and four different values of α : 0, 1/3, 2/3 and 1. The CFL number is equal to 0.5. - b) Modified wave number of TRK4 schemes with two space integrations and four different values of α : 0, 1/3, 2/3 and 1. The CFL number is equal to 0.5.

4.4.3 Temporal order measurements

For the measurements of the temporal order of TRK4 a simple 1D code was used. This code convected a Gaussian pulse within a computational domain on a regular, structured mesh. In order to obtain results that do not depend on the spatial errors due to the numerics nor to the spatial discretization, the spatial operators of Eq. (4.11) and Eq. (4.12) were chosen as centered finite difference of 10^{th} order of accuracy [Sari 2010]. The grid resolution used is $\Delta x = 1.25 \cdot 10^{-4}$ m for a computational length of $L = 0.2$ m. The results are plotted in Fig. 4.6 and they confirm what is to be expected from theory.

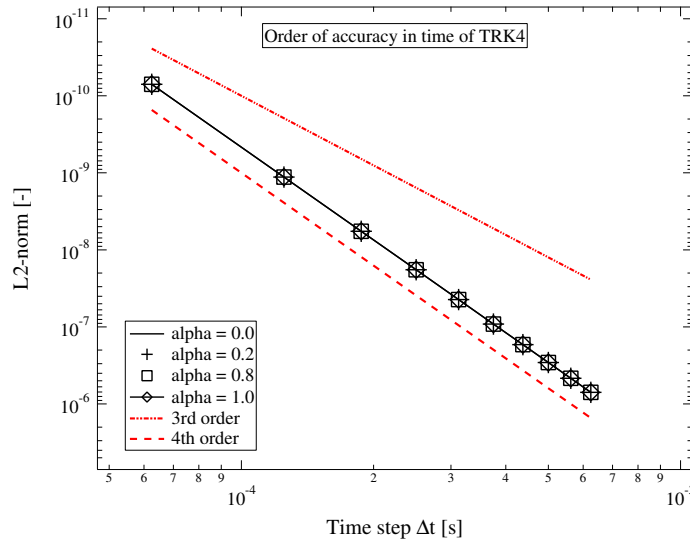


Figure 4.6: Order of accuracy in time of TRK4 for varying values of the parameter α .

4.4.4 Scalar step advection

To assess the numerical diffusion and dispersion at all wave numbers, the TRK time integration may be applied to a simple transport equation of a scalar ϕ with a step:

$$\frac{\partial \phi}{\partial t} + \mathbf{v} \cdot \nabla \phi = 0, \quad (4.34)$$

where the velocity \mathbf{v} is constant and $\phi(t = 0, \mathbf{x})$ is a Heaviside function. The computational domain is chosen sufficiently large to avoid any spurious effects from the boundary treatment. This step function is transported at $C = 1$ for 100 time steps with the TRK4 time integration and with the classical fourth order finite-difference scheme. The number of cells used to discretize the computational domain is $N = 1000$, resulting in a regular mesh with a cell size of $\Delta x = 5 \cdot 10^{-3}$ m. The results for different values of α are presented in Fig. 4.7. The influence of this parameter is rather important on the high wave-number oscillations, as stated in section 4.2. For the present test case the oscillations especially in the wake (i. e. to the left) of the gradient are partially damped when

$\alpha \geq 0.5$, while the position and the slope of the computed gradient at $\phi = 0.5$ is not affected by the variation of α , as expected from the theoretical developments presented before.

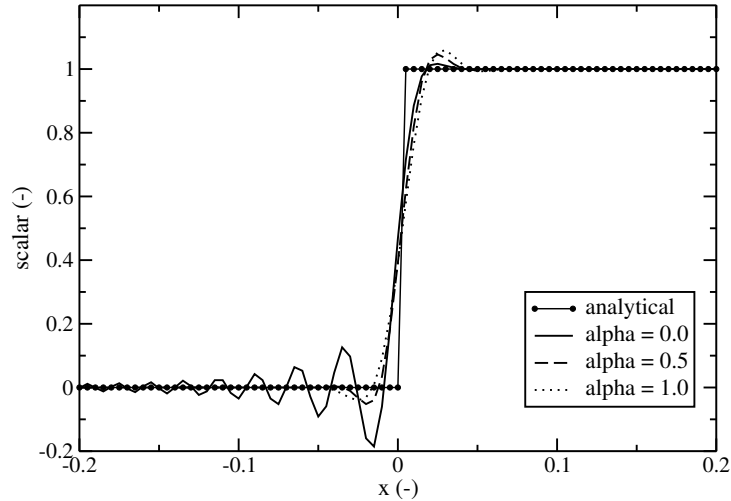


Figure 4.7: Advection of a scalar step with TRK4 for varying values of the parameter α .

4.4.5 Dissipation measurements in a turbulent flow

Since the TRK time integration has been designed for transport equations, it is a good candidate for the computation of turbulent flows. In this section, the TRK4 scheme is assessed for the simulation of Homogeneous Isotropic Turbulence (HIT) at moderate Reynolds number. Two series of computations are carried out: Direct Numerical Simulations (DNS) on a 256^3 mesh, and Large-Eddy Simulations (LES) on a 64^3 with a dynamic Smagorinsky model [Lilly 1992]. In these computations, the turbulent flow is initialized with a Passot-Pouquet spectrum [Passot 1987] that has a turbulent Reynolds number $Re_t = 608$ and a Reynolds number based on the Taylor scale of $Re_\lambda = 95$. This initial field is illustrated in Fig. 4.8, which presents the turbulent scales plotted with iso-contours of the Q-criterion [Jeong 1995].

Once initialized, the simulation is performed with YALES2 without any additional external forcing, since the characteristics of the test case suit the incompressible solver. This freely decaying turbulence is analyzed from two angles: the resolved kinetic energy decay and the kinetic energy spectra. The results are presented in the following for the extreme values of α , for reasons of better legibility. Figure 4.9 shows, that the decay of the resolved kinetic energy for a DNS and LES is comparable for extreme values of the parameter α , thus confirming that the amount of numerical diffusion remains moderate. Regarding the kinetic energy spectra, the DNS again gives similar results for $\alpha = 0$ and $\alpha = 1$, see Fig. 4.10. This is slightly different for LES, as shown in Fig. 4.11. Indeed, the spectral content close to the cut-off frequency is larger in LES than in DNS and the built-in numerical diffusion of the TRK4 scheme makes a difference. When $\alpha = 1$, the

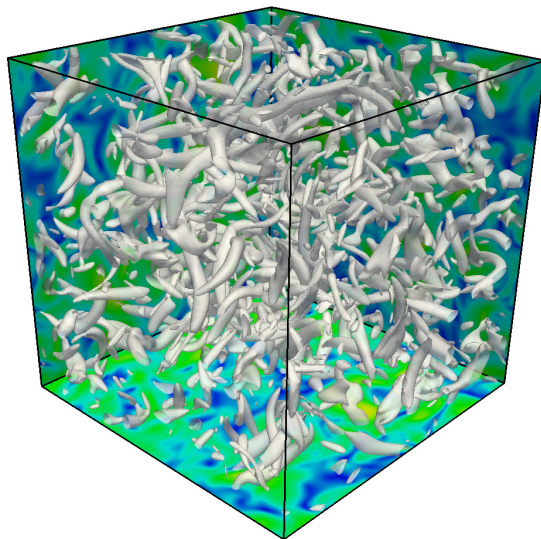


Figure 4.8: *Initial field of Homogeneous Isotropic Turbulence on the DNS mesh.*

high-wave number scales, that are resolved with two points at the cut-off to four points at half the cut-off, are slightly dissipated, while the large scales are unaffected. From these results, this TRK time integration may be applied to more complex flows with a broad spectrum of turbulent scales.

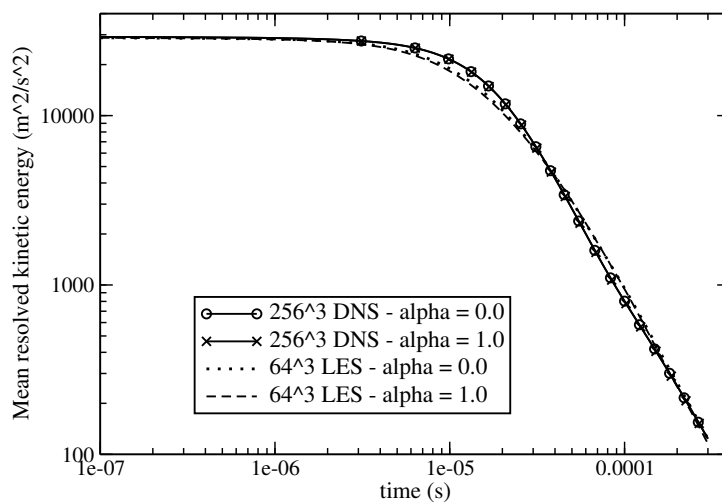


Figure 4.9: *Mean resolved kinetic energy decrease in DNS and LES with TRK₄ for two values of the parameter α .*

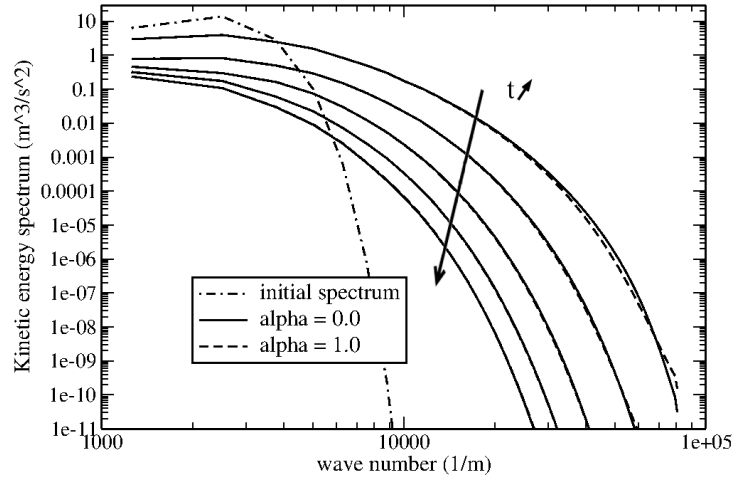


Figure 4.10: *Direct Numerical Simulation of Homogeneous Isotropic Turbulence on a 256^3 mesh with TRK4 for two values of the parameter α plotted for different instants in time t .*

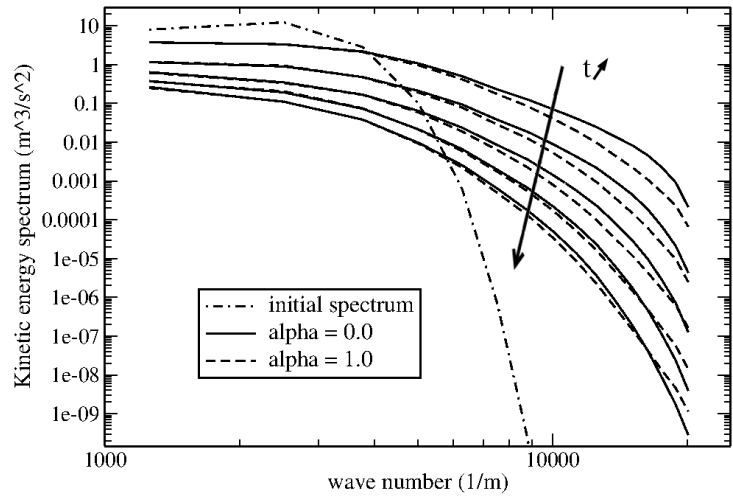


Figure 4.11: *Large-Eddy Simulation of Homogeneous Isotropic Turbulence on a 64^3 mesh with TRK4 for two values of the parameter α plotted for different instants in time t .*

Re [-]	$2.8 \cdot 10^6$
CFL [-]	0.7
T_{tot} (at the inlet) [K]	280
P_{tot} (at the inlet) [mbar]	1400
M_{iso} (at the outlet) [-]	0.79

Table 4.1: *Initial conditions for the 2D turbine blade computation.*

4.5 Application of TRK4 in the cell-vertex formulation to complex test-cases

4.5.1 Turbine blade in two dimensions

At first, the flow around the cross-section of a turbine blade is simulated. To get an idea of the flow properties, the characteristics of the simulation are summarized in Tab. 4.1. For more details on the test case, the reader is referred to Granet et al. [Granet 2010]. More information on the experimental configuration itself can be found in Sieverding et al. [Sieverding 2003, Sieverding 2004]. The mesh used for this simulation is unstructured and constructed from about 96,000 triangle-shaped cells, see Fig. 4.12.

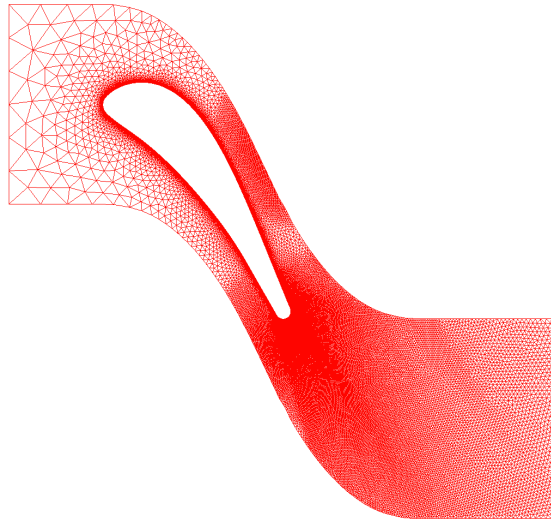


Figure 4.12: *Unstructured mesh used for the simulation of the turbine blade*

The boundary conditions for the top and bottom boundaries are set periodic. At the inlet boundary on the left, the total pressure and total temperature are imposed. For the outlet boundary condition, a NSCBC type pressure outlet [Granet 2010] is set to maintain a certain pressure in order to be consistent with the experiment.

Considering the Mach number indicated in Tab. 4.1, this test case clearly is compressible. Thus, AVBP is used for the computations. The cell-vertex finite-volume method in

AVBP is 2^{nd} order accurate in space, as pointed out in section 4.3. Hence, the simulations using the TRK4 scheme will be compared not only to the experiments but also to computations performed with the Lax-Wendroff scheme. Figure 4.13 presents a map of the averaged flow Mach number around the blade. This first and qualitative comparison between LW and TRK4 shows reasonable results. For both schemes the vortex shedding in the wake of the blade is very similar, only slight differences concerning the strength and the location of the vortices are noticeable.

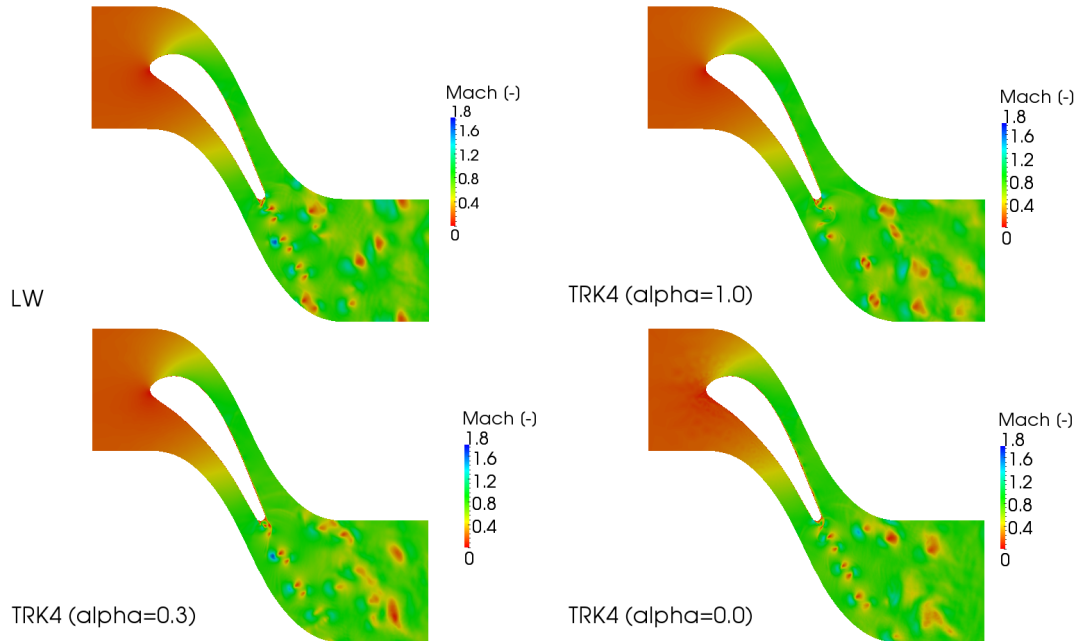


Figure 4.13: Comparison of TRK4 computations using different values for the parameter α with a simulation conducted using LW. This first quantitative evaluation shows good agreement between the different simulations, although an influence of the tuning parameter can be observed.

To confirm these observations, a more quantitative evaluation of the simulation will be given in the following. For this, the distribution of the isentropic Mach number on the blade surface is evaluated from the average solution. The obtained graphs have then been compared to experimental data provided by Sieverding et al. in [Sieverding 2003, Sieverding 2004]. As Fig. 4.14(a) clearly shows, the distribution of the isentropic Mach number obtained with AVBP superpose almost perfectly the experimental data. In the region of the trailing edge an absence of experimental results for this quantity can be noticed, which is mainly due to the high sensibility of the flow in this area. Hence, the pressure distribution normalized by the inlet pressure has been examined, for which more reliable data around the trailing edge is available. The graphs presented in Fig. 4.14(b) depict the disparities in more details. This graph clearly shows a different behavior between LW and TRK4 for various α , which can be attributed to the modified diffusion added by the scheme. LW and TRK4 for $\alpha = 1.0$ (corresponding to mass-lumped

TTG4A [Quartapelle 1993]) are more dissipative by construction and therefore, the minimum value of the pressure at the trailing edge is the smallest. In contrast, the graph for $\alpha = 0.0$ (corresponding to RK4 [Sengupta 2004]) gives the highest value at this position. It can be pointed out that only for $\alpha = 0.3$ the left lateral peak can be reproduced more accurately. Although the results are not perfect, each one is conform with the theoretical understanding of the behavior of the schemes presented in the preceding sections.

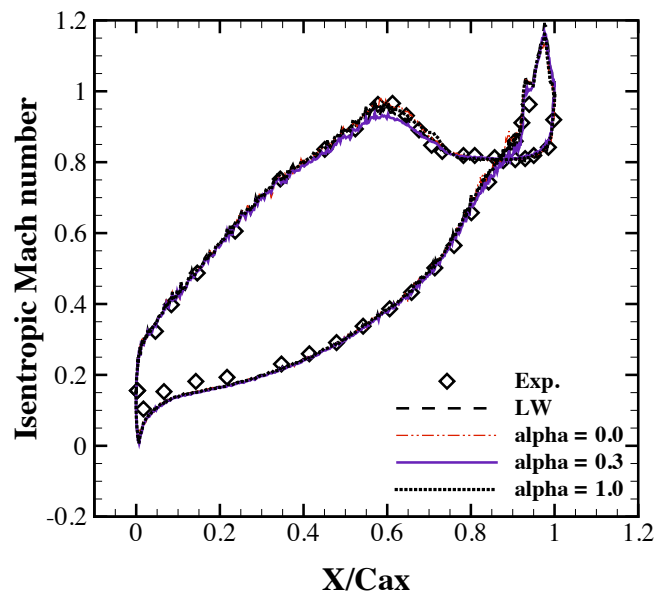
A final comparison consists of plotting the velocity profiles of the boundary layer on the pressure and the suction side of the blade close to the trailing edge. Like for the other evaluations, the results outlined in Figs. 4.15(a) and 4.15(b) highlight the impact of the tunable diffusion of the TRK4 scheme, in particular for the profile of the boundary layer at the trailing edge for the suction side. The difference of the numerical simulation compared to the experimental data is due to the fact that the boundary layer is not resolved by the mesh. This is a known drawback of LES, for which the meshes in general are too coarse when treating wall bounded flows, as will be pointed out in chapter 6.

4.5.2 Full 3D LES of turbine blade

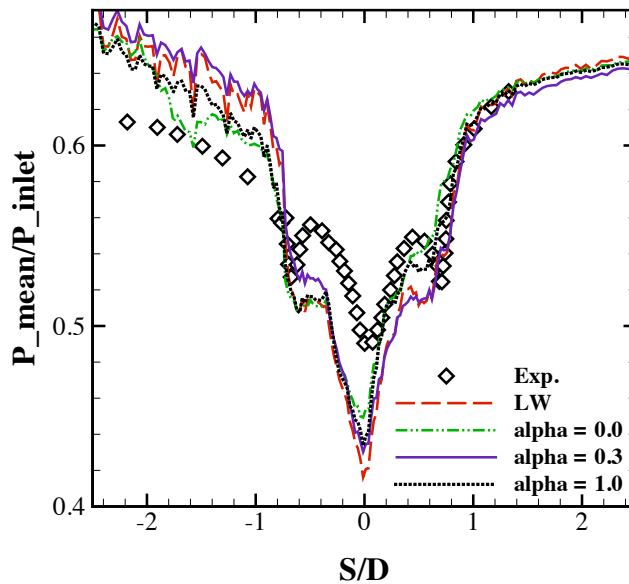
In a second test the scheme TRK4 is used to conduct a full LES of a complex geometry. The test case of the turbine blade of Sieverding et al. [Sieverding 2003, Sieverding 2004] is employed again. The simulation is based on the configuration of Léonard et al. [Léonard 2010] and the basic informations of the flow field are identical to those given in Tab. 4.1. The mesh is unstructured and built of approximately 1,900,000 tetrahedral cells. Following the configuration of Léonard et al. [Léonard 2010], the Smagorinsky model [Smagorinsky 1963] is utilized with a constant of 0.09. Figure 4.16 represents the Q-criterion [Jeong 1995] ($Q = 7.5 \cdot 10^8 \frac{1}{s^2}$) of the instantaneous flow field after 20ms physical time. In the zoom on the trailing edge (left hand side of this figure), turbulent structures separating from the blade are clearly visible. While convected downstream in the wake, dissipation is reducing their strength and only the bigger coherent vortical structures remain visible.

Furthermore, as already done for the 2D version of the test case, the mean pressure distribution around the trailing edge is used to analyze the simulation, Fig. 4.17. It can be noted that for this complex 3D test case, the parameter α becomes more important and the intermediate value of $\alpha = 0.3$ clearly helps improving the prediction quality. It is for this value only, that the lateral peaks of the distribution are properly reproduced.

One argument for LES is its capability to not only reproduce averaged solutions, but also to obtain informations on the instantaneous flow field. Figures 4.18 and 4.19 show the pressure fluctuations recorded with two probes situated on the trailing edge circle, the first one positioned on the suction side and the latter one on the pressure side. In part a) of these figures, the measurement data is compared to the LW and the TTGC [Colin 2000b] scheme of AVBP, which are considered as reference schemes, and part b) compares the solutions obtained with TRK4 to the experimental data. The TTGC scheme, which is third order accurate in space and time, is giving good results, whereas LW displays a dispersive and dissipative behavior. The TRK4 results again depend strongly on the value of α . It is highly probable, that the perturbation of the pressure

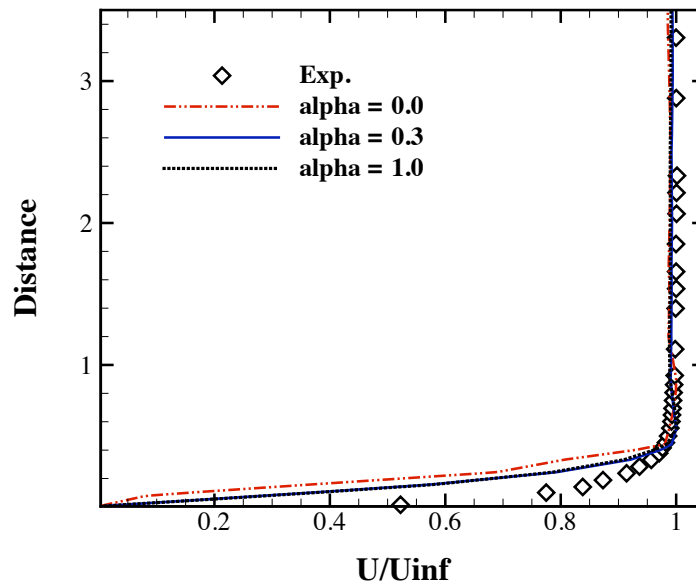


(a)

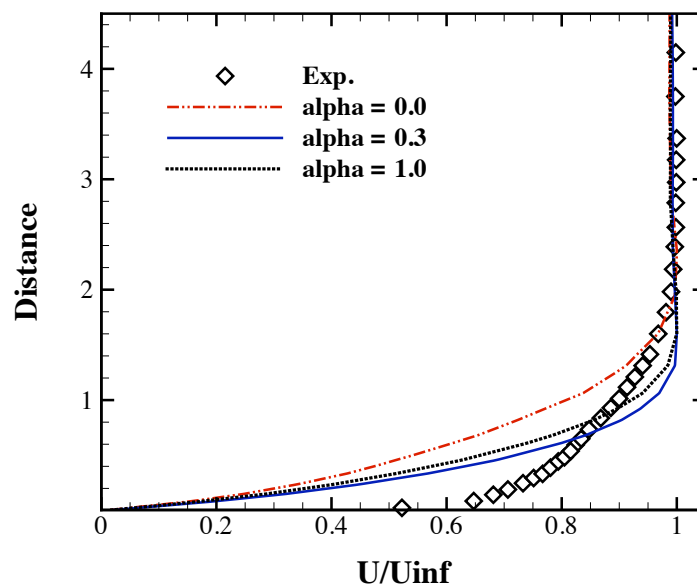


(b)

Figure 4.14: a) Distribution of the isentropic Mach number around the airfoil. The presented schemes are in good accordance with the experimental results. - b) Distribution of the Pressure (made dimensionless by the inlet pressure) around the airfoil. [here: Zoom on the coordinates for which experimental data was available]



(a) Velocity profile of the boundary layer at the trailing edge for the pressure side



(b) Velocity profile of the boundary layer at the trailing edge for the suction side

Figure 4.15: *Graphs of the boundary layer velocity profiles. The results for the suction side show at best the influence, which can be taken on the computation by variation of the parameter α .*

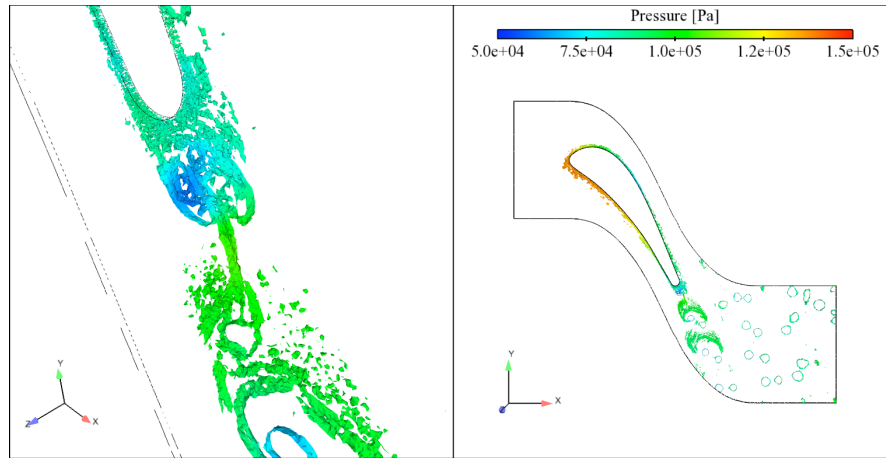


Figure 4.16: Q criterion for the 3D LES ($\alpha = 0.3$) of the turbine blade colored by the pressure. Right: side view of the configuration showing the development of the vortical structures around the profile and in the wake. - Left: Zoom on the area around the trailing edge.

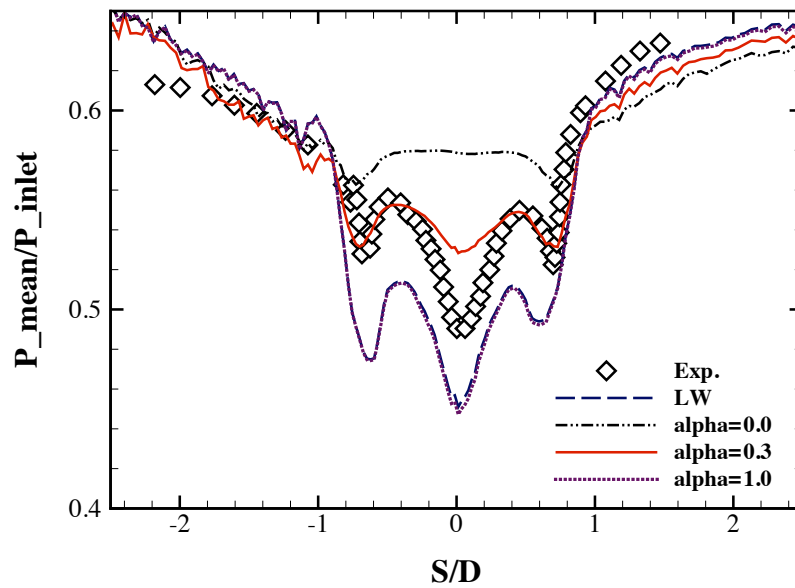


Figure 4.17: Comparison of the mean pressure (normalized by the inlet pressure) for the 3D test case. The influence of the parameter α on the diffusion of the scheme is clearly visible. In this particular case, a value of 0.3 gives results that are very close to the experimental data.

signal, which can be observed for $\alpha = 0.0$, is due to the small amount of numerical diffusion added to the simulation. When changing to $\alpha = 1.0$, some peaks are delayed, just as it was pointed out for the LW scheme. For $\alpha = 0.3$, as already seen for other test cases, the results obtained are very satisfying. The peaks superpose the frequency of the experiments. Compared to TTGC, TRK4 is one order of accuracy lower in space, which is seen as explanation for the incapability of TRK4 to reproduce the amplitude of the measurements.

4.5.3 Full 3D LES of a reactive flow in PRECCINSTA

Finally, the scheme TRK4 has been used to compute the PRECCINSTA burner configuration [Roux 2005]. The results presented in this paper correspond to a premixed simulation of a methane/air-mixture. A 2-step mechanism of B. Franzelli and E. Riber [Franzelli 2010] is used to model the chemistry in combination with a Pre-Exponential Adjustment (PEA) to predict the laminar flame speed more accurately. The computation was done solving the transport equations for 6 species (CH₄, O₂, H₂O, CO₂, CO, N₂). Figure 4.20 shows a cross section of the used geometry.

The mesh consists of about 20 million tetrahedral cells. For this LES the WALE model [Nicoud 1999] has been chosen for the sub-grid scales and for the turbulent flame closure the thickened flame approach [Colin 2000a] was used in order to keep a reasonable number of cells for its resolution. The simulation has been conducted for $C = 0.7$.

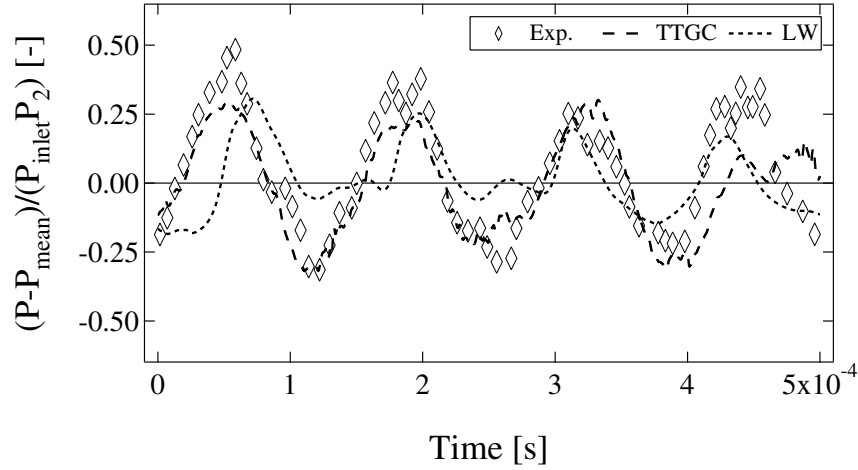
In Figs. 4.21(a) and 4.21(b), the averaged temperature and the RMS values of the temperature for different positions downstream of the swirler are displayed, obtained using TRK4 with an $\alpha = 0.2$ and compared to the scheme TTG4A [Quartapelle 1993] of AVBP. Both graphs show a good agreement, not only between the numerical simulations but also compared to the experimental data. The deviation of the simulations from the experiments for bigger radial distances can be explained by the fact, that the wall boundary conditions are adiabatic and no thermal losses are taken into account.

4.5.3.1 Computational cost of TRK4

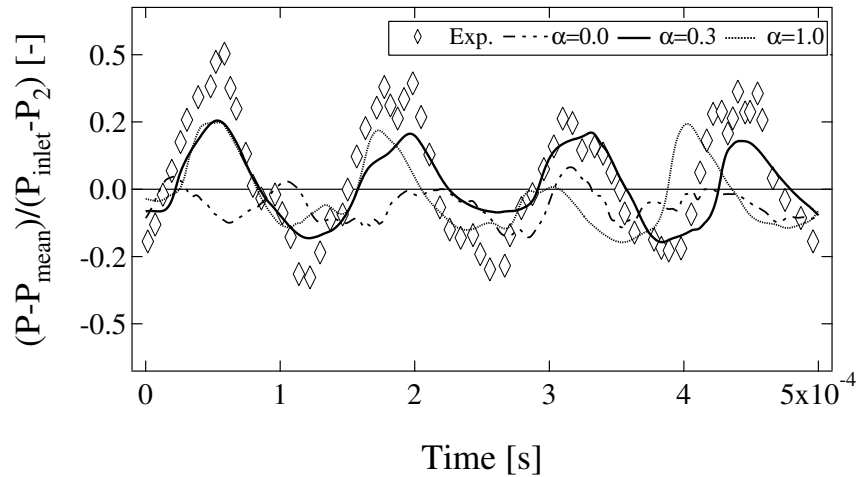
Concerning the simulations performed using the AVBP code, the TRK4 scheme has been compared to the LW, RK4 and the TTG4A scheme regarding the precision of the reproduced solution. Another interesting aspect, especially when talking about massively parallel computations, is the computational cost generated by the scheme. To compare these schemes, Eq. (4.35) has been deployed

$$Cost = \frac{Total\ simulation\ time}{physical\ time\ simulated \cdot number\ of\ processors} \quad (4.35)$$

and the results are presented in Tab. 4.2. The LW scheme was taken as reference. The values obtained for the schemes LW, RK4 and TTG4A match those indicated by Lamarque in [Lamarque 2007]. The reason for TRK4 to be as time consuming as TTG4A is that for every step of the scheme two diffusive terms on two different stencils have to be computed.

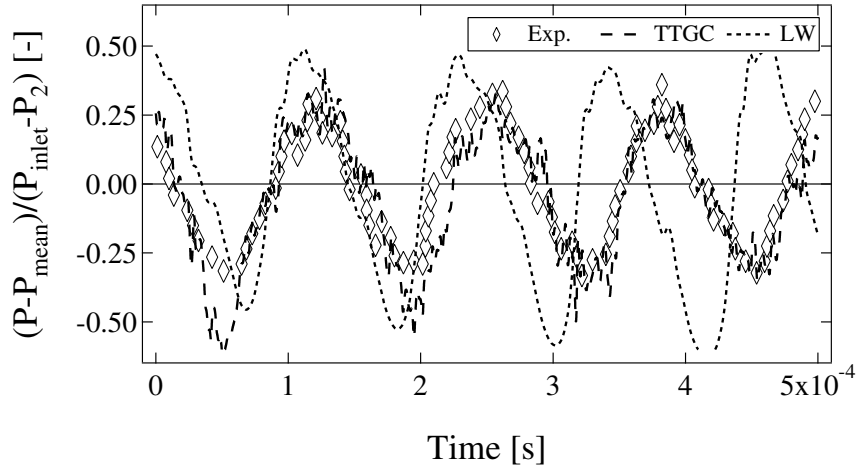


(a) Comparison of the experimental measurements to the established numerical schemes TTGC and LW of AVBP.

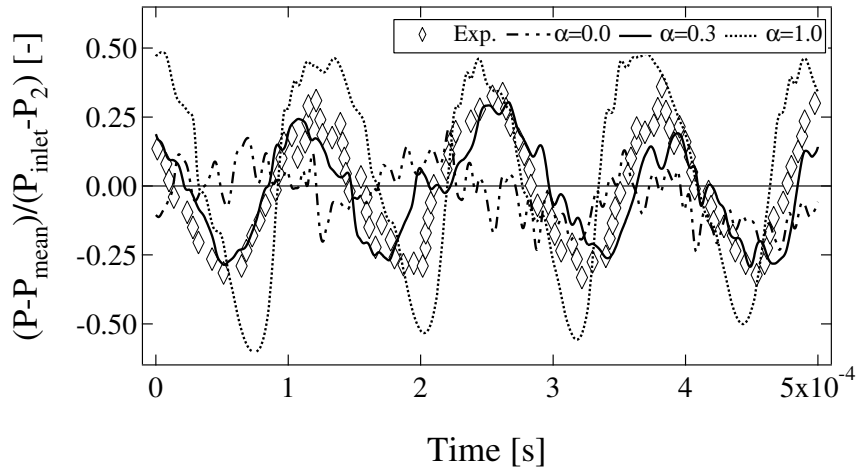


(b) Comparison of the experimental measurements to the TRK4 scheme.

Figure 4.18: Comparison of the pressure fluctuations (normalized by the pressure difference between the inlet and the outlet) for a probe on the suction side situated on the trailing edge circle. TRK4 for $\alpha = 0.3$ is showing a good agreement compared to the experimental measurements. Only the peaks of the signal are more damped than for the TTGC simulation. An explanation for this could be due to the lower spatial resolution of the TRK4 scheme (2nd order) compared to TTGC (3rd order).



(a) Comparison of the experimental measurements to the established numerical schemes TTGC and LW of AVBP.



(b) Comparison of the experimental measurements to the TRK4 scheme.

Figure 4.19: Comparison of the pressure fluctuations (normalized by the pressure difference between the inlet and the outlet) for a probe on the pressure side situated on the trailing edge circle. TRK4 for $\alpha = 0.3$ is showing a good agreement compared to the experimental measurements. The difference to the TTGC scheme for this probe is rather negligible.

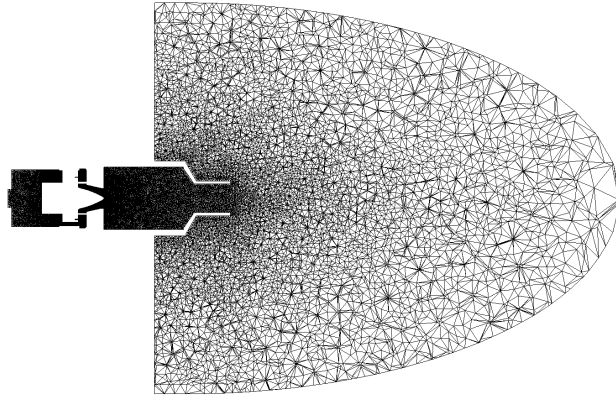
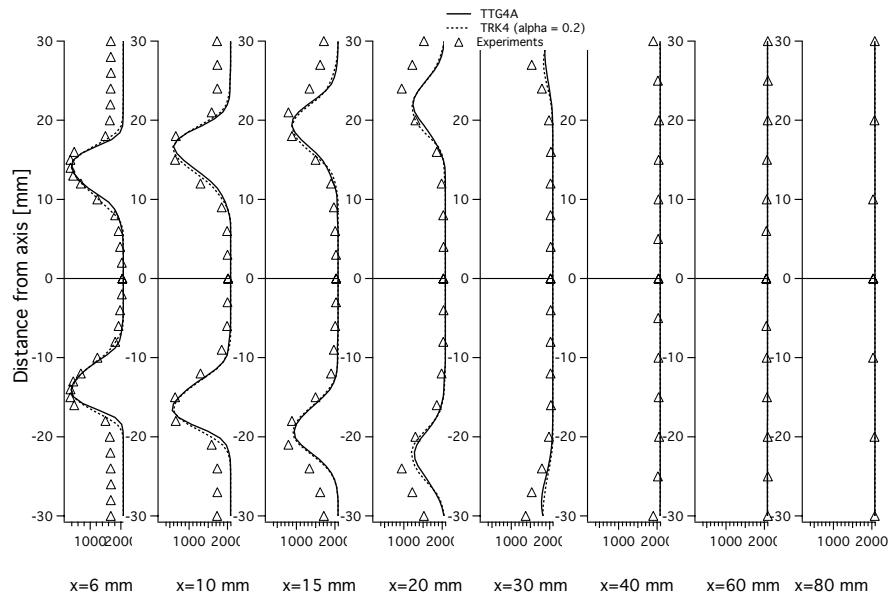


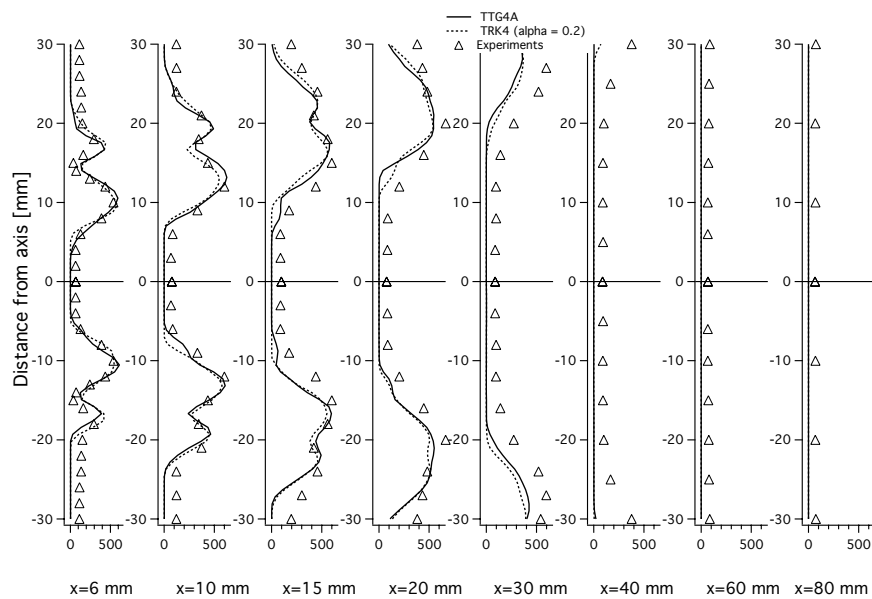
Figure 4.20: *Cross section of the PRECCINSTA geometry.*

Scheme	Cost
LW	1
TTG4A	1.82
RK4	2.66
TRK4	1.97

Table 4.2: *Computational cost of the different schemes deployed when using AVBP. LW was taken as reference. The high value for the TRK4 scheme can be explained due to the computation of two diffusive terms at each step of the scheme.*



(a)



(b)

Figure 4.21: a) Profiles of the temperature along cuts for different positions downstream of the PRECCINSTA burner. The simulations are in good agreement with each other and also with the experiments. Higher values towards the walls of the combustion chamber in the simulations are due to boundary conditions. - b) RMS profiles of the temperature along cuts at different positions downstream of the PRECCINSTA burner. The simulations are in good agreement with each other and also with the experiments.

4.6 Conclusions

This chapter presented a new family of explicit schemes for hyperbolic equations with incorporated tunable diffusion, called TRK schemes. Derived for a simple 1D transport equation, it is shown that these schemes present a linear combination of Runge-Kutta and Lax-Wendroff type schemes, which are blended using the parameter α . Their development to second- and fourth-order accuracy, namely the schemes TRK2 and TRK4, has been explained in detail. Following, the schemes were analyzed using a consistency analysis as well as a Von Neumann analysis. The spatial discretization that are coupled to the new time integration schemes are classical second- and fourth-order central spatial discretizations. The implementation of the fourth-order scheme TRK4 into the LES solver AVBP is described.

The theoretical part is followed by a series of numerical experiments and validations for LES applications, e.g. the flow around a turbine blade and the combustion simulation in the swirled flow of the PRECCINSTA burner. In particular, the TRK4 scheme is of interest regarding the LES approach, since its properties shown by the consistency and stability analysis are at no point inferior to what is at the basis of this scheme, i.e. standard RK and LW-type schemes, but with the addition of giving the possibility to adjust the diffusion implied in the scheme. Being fourth-order accurate in time, as shown by the numerical experiments, the LES simulations were performed in combination with a fourth-order spatial discretization in the case of YALES2 and a second-order spatial discretization when AVBP was used. Nevertheless, TRK4 was capable of reproducing equivalent results even in comparison to the TTG4A scheme, which is also fourth-order accurate in time and third order accurate in space. Even for a complicated simulation as the reactive test case of the PRECCINSTA burner, TRK4 showed good agreement compared to the experiments and TTG4A.

Concerning the choice of the parameter α , it has to be pointed out that the optimal value depends on the test case at hand. As can be observed from the convection of the passive scalar, a value of $\alpha = 1.0$ is recommended. For most other simulations a value within the range of $0.2 \leq \alpha \leq 0.3$ has turned out to give the best results. Nevertheless, certain test cases might show the need to diverge from this empirical result.

Nevertheless, the objective to benefit of numerical schemes with identical diffusive behavior for the direct comparison of AVBP and YALES2 was not reached. Although TRK4 performed better than LW, the strong dissipation due to the second-order spatial discretization of AVBP is not desirable. This is clearly a disadvantage when compared to the TTG schemes of AVBP.

Part III

Comparison of the compressible and the incompressible approach to LES

This section is dedicated to the comparison of the two approaches implemented in the CFD solvers AVBP and YALES2, which have been presented earlier in part I. The test cases are chosen to evaluate both the accuracy of the numerics implemented and the performance of the codes, in particular when tending towards HPC. In order to obtain meaningful results, the test cases are performed using the same characteristics (boundary condition, SGS model, numerical schemes, ...) wherever possible. If no identical setting is available, the best option possible is then taken.

Chapter 5 mainly responds to the question of the numerical accuracy of the schemes implemented, whereas in chapter 6 both solvers are compared regarding the physical content computed for a realistic configuration.

5	Basic test cases	83
5.1	Convection of a vortex	83
5.1.1	2D vortex	84
5.1.2	3D vortex benchmark	85
6	Application to a realistic configuration	93
6.1	The test case of the KIAI burner	93
6.1.1	Numerical setup	94
6.1.2	General flow characteristics	97
6.1.2.1	Swirl	97
6.1.3	Mean flow quantities analysis	98
6.1.3.1	Qualitative assessment	98
6.1.3.2	Quantitative analysis	100
6.1.4	Instantaneous results	105
6.1.4.1	Qualitative considerations	105
6.1.4.2	Spectral analysis	106
6.1.5	The effect of refining the mesh	122
6.1.6	Performance	131
6.1.6.1	Benchmark of AVBP and YALES2 for the one-burner configuration	131
6.1.6.2	Convergence behavior of the solvers	133
6.1.7	Conclusions	134

Basic test cases

5.1 Convection of a vortex

As already stated before, the quality of LES relies to a large extent on the numerical schemes. In order not to overshadow the dissipation of the turbulent structures of the subgrid-scale models, the use of low-dissipation and low-dispersion schemes is recommended for explicit LES. A simple way to examine the impact of the numerical schemes on these structures is the convection of a 2D vortex. More precisely, the transport of an isentropic vortex is chosen, since its analytical solution is known, i. e. the stream function:

$$\Psi(x, y) = \Gamma_0 \cdot \exp\left(-\frac{(x - x_0)^2 + (y - y_0)^2}{2R^2}\right). \quad (5.1)$$

In Eq. (5.1), Γ_0 is the vortex strength, (x_0, y_0) represents the location of the vortex center and R the radius of the vortex. The velocity and the vorticity distribution induced by Eq. (5.1) is obtained by applying the velocity stream function relationship:

$$u = \frac{\partial \Psi}{\partial y}, \quad v = -\frac{\partial \Psi}{\partial x}, \quad \omega = \frac{\partial v}{\partial x} - \frac{\partial u}{\partial y}, \quad (5.2)$$

leading to the following expressions:

$$u = -\frac{\Gamma_0}{R^2} (y - y_0) \cdot \exp\left(-\frac{(x - x_0)^2 + (y - y_0)^2}{2R^2}\right), \quad (5.3)$$

$$v = \frac{\Gamma_0}{R^2} (x - x_0) \cdot \exp\left(-\frac{(x - x_0)^2 + (y - y_0)^2}{2R^2}\right), \quad (5.4)$$

$$\omega = \frac{\Gamma_0}{R^2} \left(2 - \frac{(x - x_0)^2 + (y - y_0)^2}{2R^2}\right) \cdot \exp\left(-\frac{(x - x_0)^2 + (y - y_0)^2}{2R^2}\right). \quad (5.5)$$

Within the vortex, the maximum for the velocity magnitude is found at a distance $r = R$ from the center of the vortex and is defined as $U_{max} = \sqrt{u_{max}^2 + v_{max}^2}$. The convection of the vortex is achieved by adding a uniform velocity U_0 in positive x-direction to the flow field. The initial field of the simulation is generated using the parameters of Table 5.1. The values are chosen to obtain an initial solution at a global Mach number of $Ma = 0.1$. The value for the maximum velocity is defined to be $U_{max} = 0.04 \cdot U_0$ and for the radius of the vortex the following relation was determined $R = \frac{L}{20}$. By this means, an interaction of the initial vortex with the boundaries is avoided, since a vortical structure defined by

ρ_0 $\left[\frac{\text{kg}}{\text{m}^3}\right]$	T_0 [K]	P_0 [Pa]	U_0 $\left[\frac{\text{m}}{\text{s}}\right]$
1.17170407	300	101300	35

Table 5.1: Parameters to generate initial solution of the vortex.

Eq. (5.1) has a near zero total circulation for $r > 2R$ [Poinsot 2005]. However, the value of the velocities are truncated to zero for $r > 4R$. One reason for this is to avoid the impact of the vortex on itself, since periodic boundary conditions are set in all directions.

Regarding the computational domain, two different simulations are conducted. The first one is a quadratic 2D domain with a characteristic length of $L = 0.3112\text{m}$. It is discretized using 80×80 rectangular mesh elements. This configuration is dedicated to the above mentioned evaluation of the numerical scheme. The second set-up is based on the 2D simulation. The computational domain is extruded in the third dimension, again with an edge length of $L = 0.3112\text{m}$ and divided into 80 elements. The objective of the 3D simulation is to obtain a first idea of the performance of AVBP and YALES2. In both cases, the origin of (x, y, z) is situated in the center of the computational domain. Based on these informations the characteristics of the vortex are summarized in Table 5.2.

U_{max} $\left[\frac{\text{m}}{\text{s}}\right]$	Γ $\left[\frac{\text{m}^2}{\text{s}}\right]$
1.4	3.59157

Table 5.2: Characteristics of the initial vortex.

These computations have been set to obtain 40 vortex cycles. At first sight, the distance covered by the vortex is rather long, much longer than the average distance of a vortex in a turbulent flow before dissipation would have broken up the structure into smaller ones. Nevertheless, this leads to a more coherent picture of the scheme's behavior than when looking at the solution after one turnover. Furthermore, for the 3D benchmark this approach allows to obtain significant results, since the time of the system needed to set up the simulation becomes negligible compared to the real simulation time. All simulations were performed on the IBM iDataplex of CERFACS (a.k.a. OCTOPUS), using up to eight computing nodes. Each node is composed of two quad core Intel Xeon "Nehalem" processors with a peak performance of 42.72 GFlops each and 24GB RAM per node.

Table 5.3 summarizes the numerics deployed for both solvers. The idea is to deploy the best numerical setup at hand for the simulations.

5.1.1 2D vortex

For the comparison of the simulations two different quantities are evaluated. The first is the stream wise velocity distribution induced by the vortex ($u - U_0$), plotted for the entire computational domain in Figs. 5.1, 5.2 and 5.3. It provides a first qualitative

	AVBP	YALES2
Numerical scheme	TTGC (3^{rd} order in space and time)	TRK4 (4^{th} order) time integration scheme) + 4^{th} order finite-volume spatial scheme
CFL number	0.7 (acoustic)	0.3 (convective)

Table 5.3: Numerical setup deployed for the simulations in two and three dimension of the convected vortex.

notion of the solution produced by the code. Secondly, the transverse velocity is plotted along a line probe for $y = 0$ in Fig. 5.4. Here, effects can be pointed out quantitatively.

When looking at the results in Fig. 5.1, obtained using AVBP, the vortex appears unchanged. This is true regarding the intensity as well as for its position. This observation is confirmed by Fig. 5.4 - a) and b). The loss in transverse velocity is less than 10%.

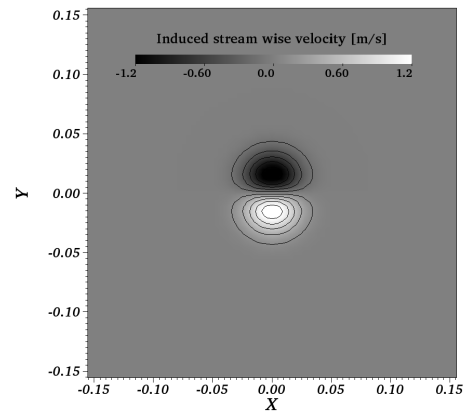
In comparison, the results of YALES2 show a much more diffusive behavior, although the numerical schemes of YALES2 are of higher order than those of AVBP. The induced stream wise velocity for the YALES2 run with $\alpha = 1.0$ is presented in Fig. 5.2. For this setting, which corresponds to the *finite-volume* formulation of TTG4A, mainly dissipation can be observed. The vortex is situated at the center of the domain during the complete simulation. But for the induced stream wise velocity the plots become more smudgy and the number of the iso-lines decreases. Looking at the transverse velocity of this simulation in Fig. 5.4 - c), this loss can be quantified to a reduction of the velocity down to 30% of the initial value.

Setting $\alpha = 0.2$ reduces the dissipation but, at the same time, adds more dispersion to the results, see Fig. 5.3. An indication for this are the wave-like patterns in the wake of the vortex. For the induced stream wise velocity the larger number of iso-lines compared to the run with $\alpha = 1.0$ indicate the smaller dissipation, while simultaneously the vortex shape deteriorates and changes its position and orientation due to the augmented dispersion. This latter observation explains, why in Fig. 5.4 (d) the graphs show that the amplitude of the transverse velocity increases again between the cycles 30 and 40, since the line probe does not pass necessarily through the vortex center.

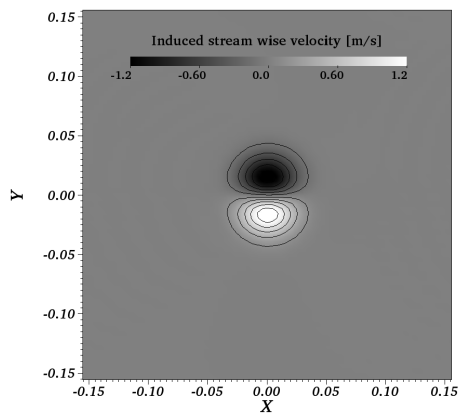
In the case of AVBP, this test confirms the experiences made so far with the scheme TTGC, namely the very small dissipation as well as the low dispersion due to the use of a mass matrix, as pointed out in 3.1. Contrary to this, the results of YALES2 can be explained by taking a look at the modified equation presented in 3.2. It seems that the dissipation introduced for $\alpha = 1.0$ is able to dispose of the leading error term, which is of dispersive character. By reducing the value of α , this leading error term is no longer counterbalanced.

5.1.2 3D vortex benchmark

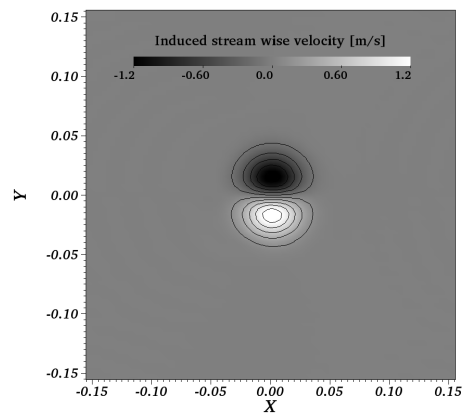
An idea of the performance of the codes AVBP and YALES2 is obtained by the 3D simulation of the convected vortex. Four simulations for different Mach numbers, namely



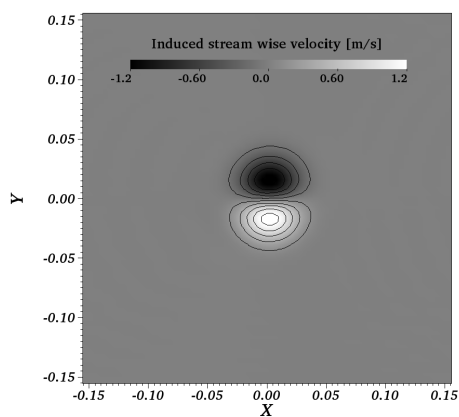
(a)



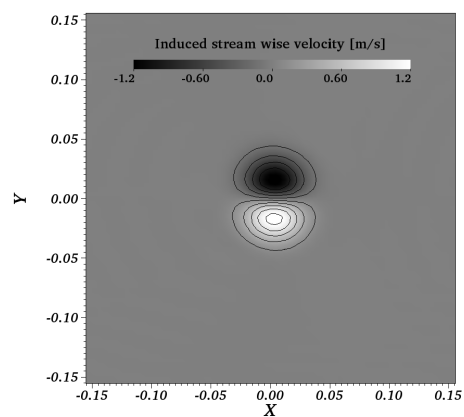
(b)



(c)



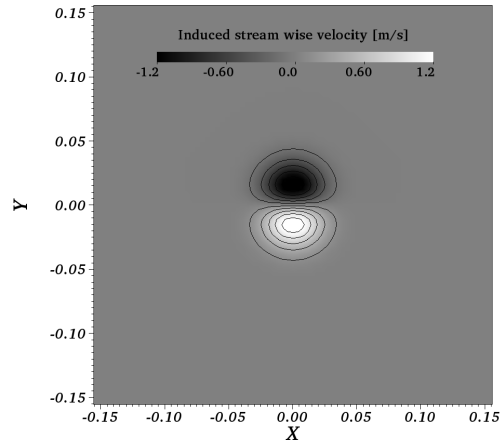
(d)



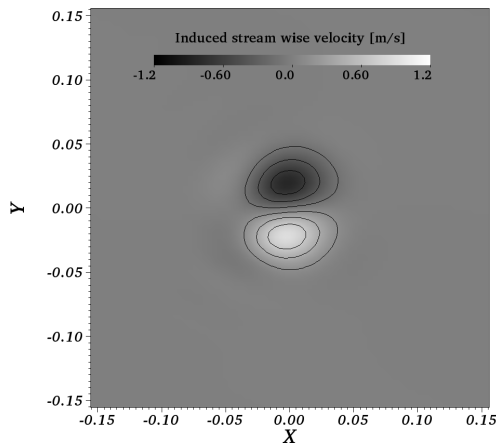
(e)

Figure 5.1: Evolution of the vortex for AVBP (TTGC, $C = 0.7$) at different instances illustrated for the induced stream wise velocity $u - U_0$.

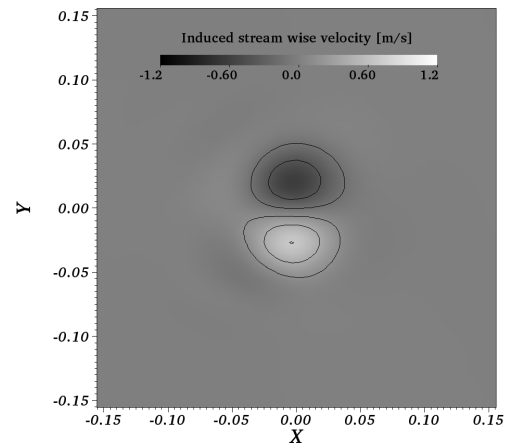
a) initial solution - b) $t = 10 \frac{L}{U_0}$ - c) $t = 20 \frac{L}{U_0}$ - d) $t = 30 \frac{L}{U_0}$ - e) $t = 40 \frac{L}{U_0}$



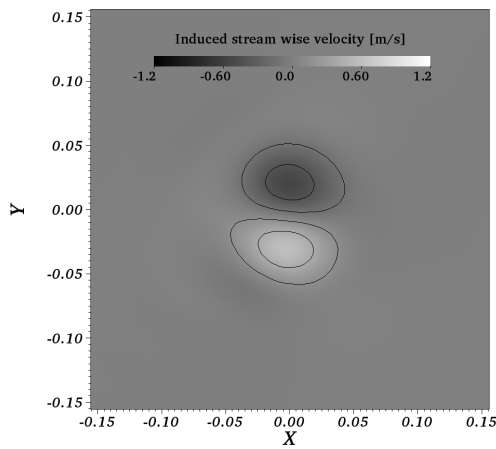
(a)



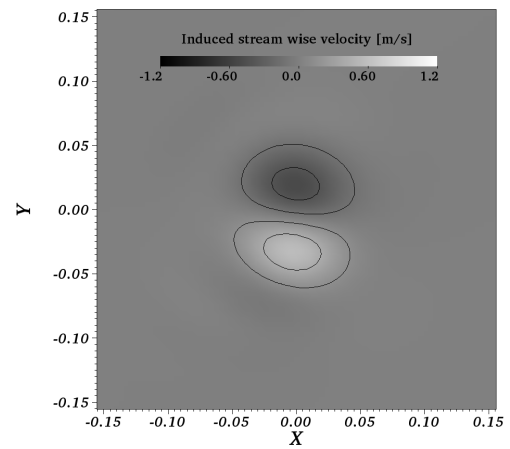
(b)



(c)



(d)



(e)

Figure 5.2: Evolution of the vortex for YALES2 (TRK4, $C = 0.3$, $\alpha = 1.0$) at different instances illustrated for the induced stream wise velocity $u - U_0$.

a) initial solution - b) $t = 10 \frac{L}{U_0}$ - c) $t = 20 \frac{L}{U_0}$ - d) $t = 30 \frac{L}{U_0}$ - e) $t = 40 \frac{L}{U_0}$

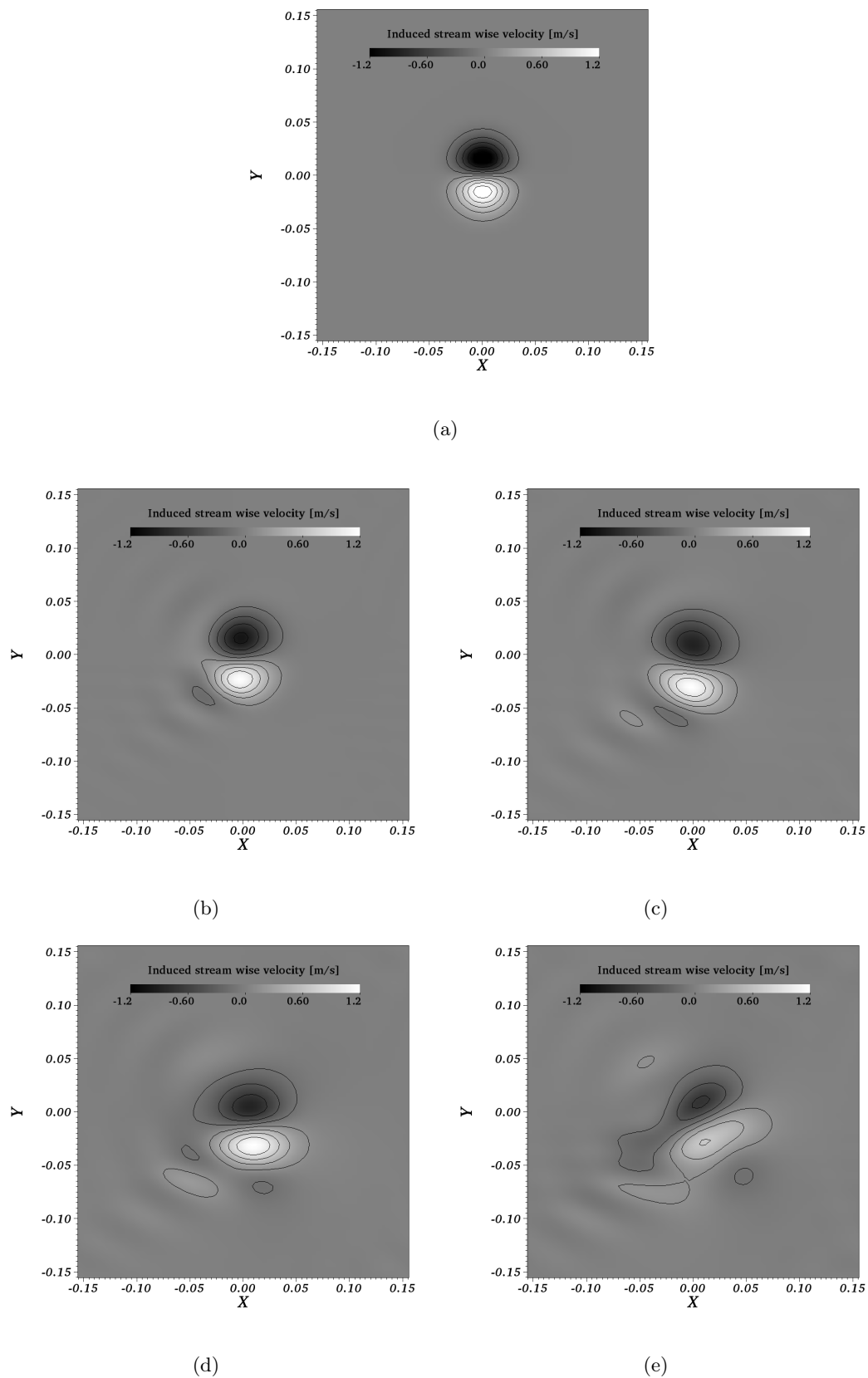


Figure 5.3: Evolution of the vortex for YALES2 (TRK4, $C = 0.3$, $\alpha = 0.2$) at different instances illustrated for the induced stream wise velocity $u - U_0$.
 a) initial solution - b) $t = 10 \frac{L}{U_0}$ - c) $t = 20 \frac{L}{U_0}$ - d) $t = 30 \frac{L}{U_0}$ - e) $t = 40 \frac{L}{U_0}$

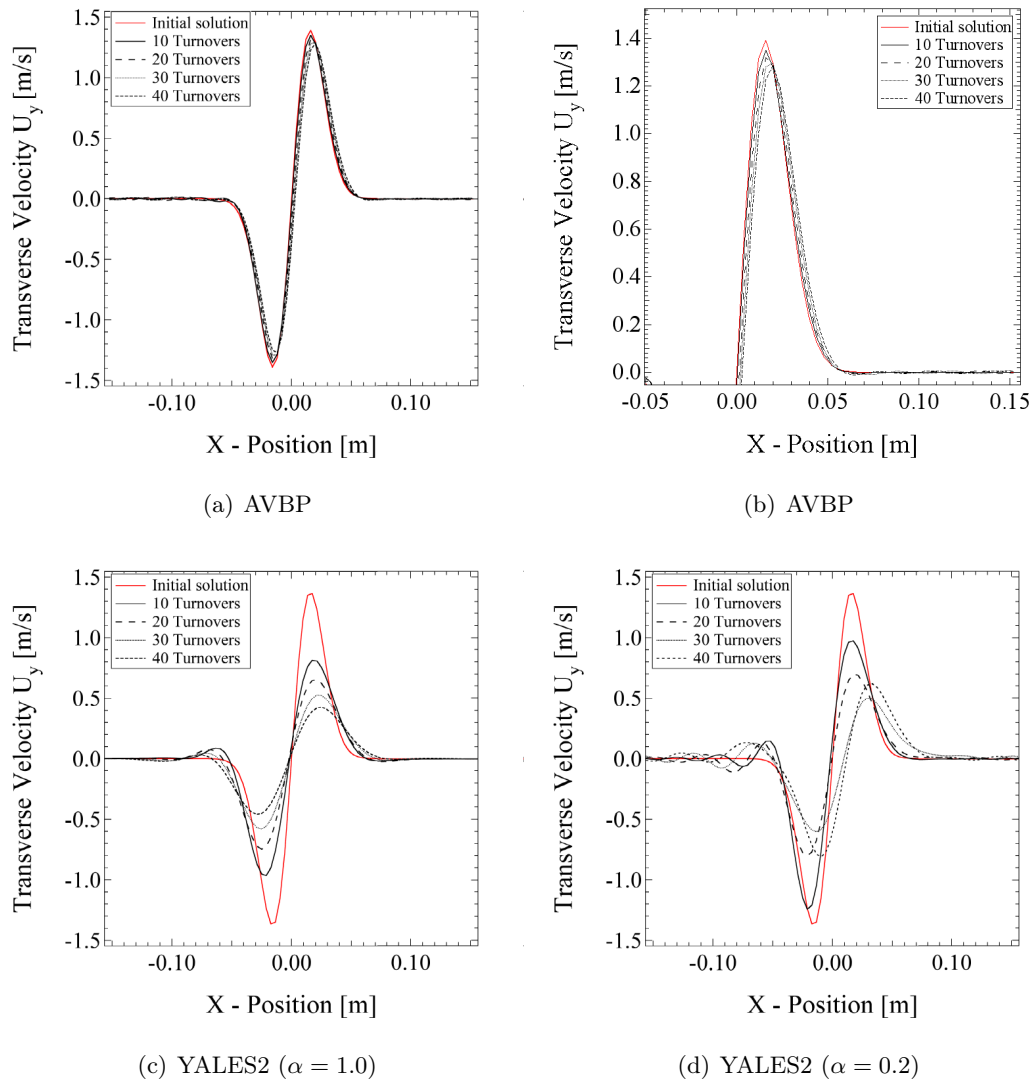


Figure 5.4: Comparison of the transversal velocity along a line probe for $y = 0$. Graph (b) presents a zoom on the AVBP solution (a), since the solutions are very close to each other.

$Ma = 0.01, 0.1, 0.2, 0.3$, have been conducted on a regular grid composed of 512000 rectangular elements. The first quantity of interest is the simulation time. As explained earlier, it is expected that the time needed for one simulation of the compressible solver will reduce for increasing Mach numbers, whereas the changes for YALES2 should be negligible. This is confirmed by the present comparison and the result is presented in Fig. 5.5.

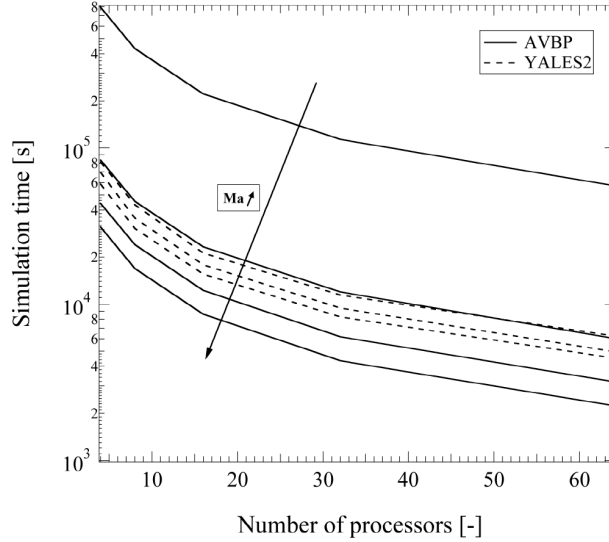


Figure 5.5: The simulation time of the compressible solver AVBP decreases when the Mach number increases, which corresponds perfectly to theory. The same can be stated for YALES2, for which the simulation time is independent of the Mach number. Graphs represent $Ma = 0.3, 0.2, 0.1, 0.01$.

Although the simulation time is already a good indicator on how a solver performs, more meaningful quantities are necessary to assess their behavior properly. One quantity is the parallel speedup, which represents the parallel efficiency of a program. It is defined as follows:

$$S(p) = \frac{t_{ref}}{t_p}. \quad (5.6)$$

In Eq. (5.6), t_p is the time needed for a program to run on a certain number of processors p , t_{ref} is the time needed by the same program on a reference number of processors (usually $p_{ref} = 1$, if a sequential run is feasible) and $S(p)$ is the resulting speedup in simulation time that is induced to the increased processor number. The ideal case is *linear speedup*, for which $S(p) = p$. In general, the speedup $S(p)$ is mainly influenced by the following two aspects:

- By increasing the number of processors used to solve a problem not only the computational resources increase, but also the number of communications between the

distributed tasks. The less the number of interchanges between two processors to exchange results, the better the speedup. It is one of the key issues when performing massively parallel computations.

- A very important role is played by the architectures used for the simulations, more precisely the kind and the location of the memory available. In general, a distinction can be made between the *cache* memory (very fast - close to the processor) and the standard memory *RAM* (for **R**andom **A**ccess **M**emory). By increasing the number of processors, the global amount of *cache* memory increases as well. In return, the simulation time reduces and this can even lead to *super-scalar* behavior of the program for a certain processor number, which fits to the problem at hand.

To determine the speedup of a code, two different approaches are available. The first measures the *weak scaling* that consists of increasing the problem size at the same time as the number of processors is augmented. Usually, this is achieved by refining the mesh. Alternative to this is the *strong scaling*, for which only the number of processors is increased, while the problem size is kept constant. This latter approach is used throughout this part of the work, since it is, in fact, an imitation of the procedural method used for simulations on high performance computers. For the 3D test case of the convected vortex both codes show similar behavior which is also very close to linear speedup, see Fig. 5.6. Nevertheless, this is just a first result, since the size of the test case is rather small.

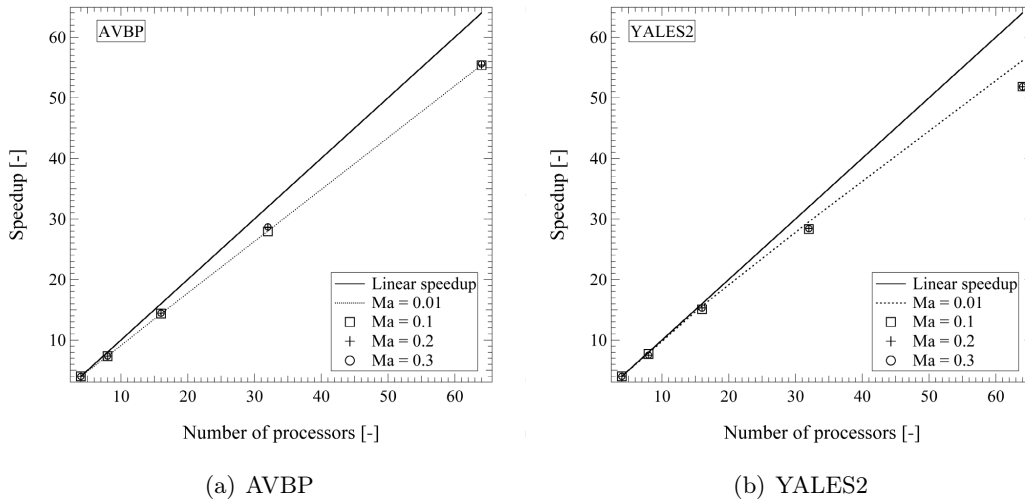


Figure 5.6: Speedup of AVBP and YALES2 for the test case of the 3D isentropic vortex on 512000 mesh elements.

A second quantity, that is significant even if the problem size is rather small, is the

efficiency, denoted $E(p)$. The formula used to calculate this criterion is:

$$E(p) = \frac{t_p}{(N_{iter} N_{node})}, \quad (5.7)$$

where N_{iter} stands for the total number of iterations conducted throughout the simulation and N_{node} is the number of mesh nodes. Physically speaking, this can be seen as the time needed to do a single iteration per node using p processors. Multiplying the efficiency by the number of processors p results in the *reduced efficiency*, denoted $RE(p)$ in the following. This quantity is very convenient, since its value becomes constant when the speedup of a code is linear. The unit of both, the efficiency as well as reduced efficiency, is $[\mu s]$.

The graphs for the reduced efficiency of AVBP and YALES2 in Fig. 5.7 correspond to the results presented in Fig. 5.6. Although for the low Mach numbers the simulations performed using YALES2 are faster, $RE(p)$ reveals that one iteration for this solver takes 3 to 4 times longer than AVBP. This is mainly due to the resolution of the Poisson equation, which is solved implicitly. Conversely, a gain in simulation time, which is linked to the incompressible formulation, is only achieved if

$$\Delta t_{convective} \geq 4 \times \Delta t_{acoustic}.$$

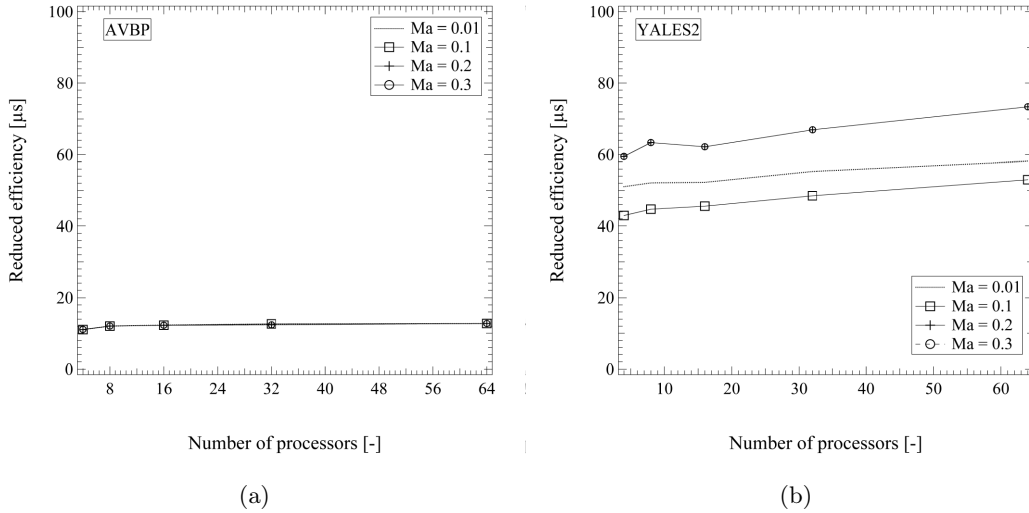


Figure 5.7: Reduced efficiency of both codes for the test case of the 3D isentropic vortex on 512000 mesh elements. The values for YALES2 are higher, because at each iteration the inversion of the Poisson equation is quite costly.

Application to a realistic configuration

The test cases presented in chapter 5 allow to point out characteristics for distinct properties of a solver, e. g. that of the numerical schemes implemented. In this chapter, the CFD solvers are evaluated for the simulation of an industrial burner. At first, the comparison regarding the solution and the performance of AVBP and YALES2 is presented. Subsequently, the feature of automatic mesh refinement of YALES2 is analyzed.

6.1 The test case of the KIAI burner

The aim of European project **KIAI** (short for *Knowledge for Ignition, Acoustics and Instabilities*) is to provide insight into unsteady phenomena occurring especially in aero engines. This knowledge is then intended to allow the development of CFD tools, helping to reduce the emission of pollutants by next generation engines. Amongst the 18 partners working together in this project, CERFACS is involved in performing LES of this configuration. Furthermore, the research center CORIA Rouen (FRANCE) is conducting experimental studies in order to provide data, which will be used to validate the LES. Hence, this one-burner configuration was chosen to serve as the test case, for which a detailed comparison and a quality assessment of the solvers AVBP and YALES2 will be presented for the non-reacting case. The simulations done using AVBP are realized in collaboration with D. Barré (Ph.D. student at CERFACS).

The burner in question is composed of the following four components:

- **Plenum** - serving to tranquilize the flow before entering the injection system. A grid placed in the lower part of the plenum destroys the large structures of the flow.
- **Swirl injection system** - it consists of two admissions, see schematic in Fig. 6.1(b). In the center a tube ($d = 4\text{mm}$) acts as fuel injector, which is surrounded by a radial air swirler ($D_{ext} = 20\text{mm}$). This air swirler is built of 9 or 18 channels, respectively, which are inclined by 45° . By this means, flows at different swirl numbers can be obtained. For the simulations presented in the following, the 18 channel setup was used, see Fig. 6.1(c). The complete injection system is presented in Fig. 6.1(d).
- **Combustion chamber** - its cross section is squared with an edge length of 100mm, assuring a symmetric flow field, and its length is 260mm. Synthetic quartz is used

to provide an optical access of $228 \times 78\text{mm}$ on at least three sides of the chamber, allowing to perform diagnostics such as PIV, PLIF, see Fig. 6.1(a)

- **Convergent exhaust** - to avoid negative mean axial velocities.

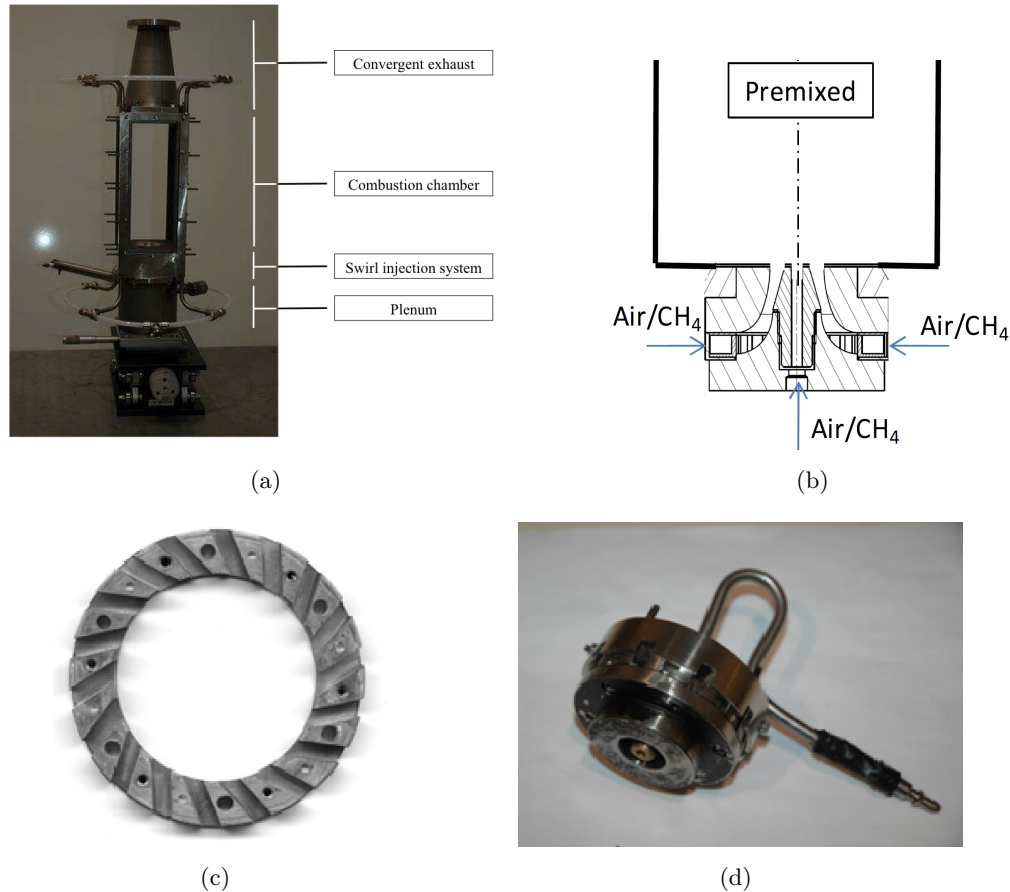


Figure 6.1: a) Photo of the full combustion chamber used for the experiments at CO-RIA Rouen. b) Burner configuration that is used for the comparisons. c) Picture of the air swirler. d) The complete injection system. - All images courtesy of B. Renou [Renou 2010]

The working point of this configuration is summarized in Table 6.1 and corresponds to the fully premixed burner presented in Fig. 6.1(b). The indicated equivalence ratio for the swirler $\phi_{Swirler}$ is equal to the total equivalence ration ϕ_{total} . During the cold flow simulations temperature was at $T = 298\text{K}$ and the pressure in the combustion chamber was the ambient pressure $P = 101325\text{Pa}$.

6.1.1 Numerical setup

In order to obtain significant results for this comparison, it is assured to keep the numerical setup identical wherever possible. The model of the geometry used for the mesh

$m_{fuel,Swirler}$ [$\frac{g}{s}$]	$m_{fuel,Injector}$ [$\frac{g}{s}$]	$m_{Air,Swirler}$ [$\frac{g}{s}$]	$m_{Air,Injector}$ [$\frac{g}{s}$]	$\phi_{Injector}$ [-]	$\phi_{Swirler}$ [-]
0.218	0.010	5.03	0.227	0.76	0.75

Table 6.1: Flow conditions for the experiments

generation is presented in Fig. 6.2. The grid placed in the plenum, in order to tranquilize the flow upstream of the swirler, is not taken into account in the simulations.

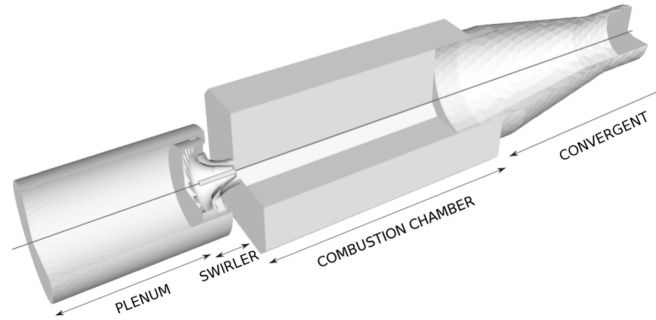


Figure 6.2: CAD model of the burner geometry

The basic mesh is created by David Barré using CENTAUR Soft (v9.0). It is an unstructured mesh composed entirely of tetrahedral elements. This mesh serves mainly for the direct comparison between AVBP and YALES2 and is depicted in Fig. 6.3. Table 6.2 summarizes the mesh's characteristics.

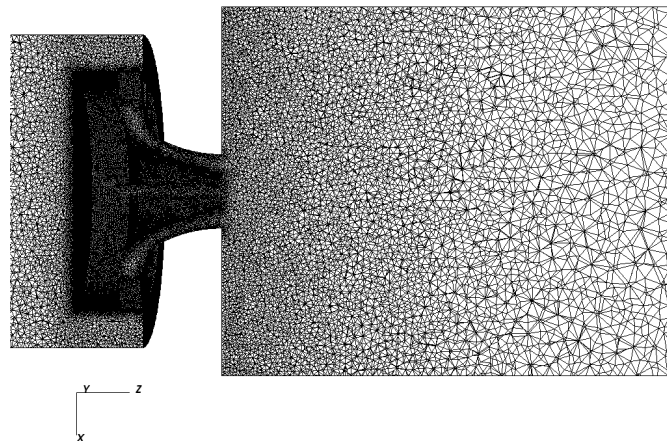


Figure 6.3: Cut through the basic mesh. Composed of about 4.3 million tetrahedral elements, this mesh is comparable to those used in industry for similar applications.

	<i>basic mesh</i>
Number of tetrahedras	4301471
Number of nodes	837311
Total cell volume	$3.922 \cdot 10^{-3} \text{m}^3$

Table 6.2: *Meshes used for the comparison of YALES2 with AVBP*

In Table 6.3, the choices concerning the numerical methods and the boundary conditions deployed for the simulations are summarized. Concerning the numerical scheme as well as for the SGS model, the codes do not provide exactly the same options and hence, these parameters are set as recommended in such cases.

For AVBP, this means the use of the Two-step Taylor Galerkin scheme TTGC, which is detailed in section 3.1.4.3 and is the recommendation for turbulent flows due to its diffusive characteristics. Furthermore, the WALE model is chosen as explained in section 2.3, because this SGS model is particularly suited for wall bounded flows as encountered in this configuration.

In the case of YALES2, the numerical scheme used in general is the TRK4 time integration, which is detailed in part II, combined with a spatial discretization that is fourth order accurate (see chapter 3.2.1.1). Concerning the SGS model, the dynamic Smagorinsky model is the most sophisticated model at hand in YALES2. Due to the automatic adjustment of the Smagorinsky constant, see section 2.3, this model is also fitting for this kind of simulations.

	AVBP	YALES2
Numerical scheme	TTGC	TFV4A ($\alpha = 0.2$)
CFL	0.7 (acoustic)	1.5 (convective)
SGS - Model	WALE	Dynamic Smagorinsky
Boundary	Boundary condition	supplementary informations
Inlet swirler	INLET	$\dot{m} = 5.248 \cdot 10^{-3} \frac{\text{kg}}{\text{s}}$
Inlet jet	INLET	$\dot{m} = 0.2371 \cdot 10^{-3} \frac{\text{kg}}{\text{s}}$
Outlet	PRESSURE OUTLET	101325Pa
Central injection tube	adiabatic slip wall	-
Combustion chamber	adiabatic no-slip wall	-
Swirler	adiabatic no-slip wall	-
Exhaust cone	adiabatic no-slip wall	-

Table 6.3: *Upper part - Numerical methods used for the simulations; lower part - boundary conditions*

Since the simulation is conducted for a non-reacting flow, both solvers are run using the single species *Air*. The mean density of the gas mixture is $\bar{\rho} = 1.14 \frac{\text{kg}}{\text{m}^3}$.

6.1.2 General flow characteristics

To give a general description of the flow field, at first the flow-through time for the investigated setup and Reynolds number at the injection are indicated.

- The flow-through time is the ratio of the total mass within the system and the mass flow rate of injected air and is calculated as follows:

$$T_{Flow-through} = \rho \frac{V_{tot}}{\dot{m}_{Air}} = 1.14 \frac{\text{kg}}{\text{m}^3} \frac{0.00392176 \text{m}^3}{0.005248 \frac{\text{kg}}{\text{s}}} = 0.85191 \text{s}$$

- The Reynolds number at the injection plane of the combustion chamber is

$$Re = \frac{U_{Swirler} D_{ext}}{\nu},$$

where the velocity at the swirler is computed by $U_{Swirler} = \sqrt{\frac{\Delta P}{\rho}}$. This leads to the following values for the Reynolds number:

$$\textbf{Experiments: } U_{Swirler} = 22.48 \frac{\text{m}}{\text{s}} \Rightarrow Re_{Swirler} \approx 25028$$

- The Mach number at the injection for the present configuration is

$$Ma = \frac{U_{Swirler}}{c} = 0.064,$$

with the speed of sound, for which a value of $c \approx 352.2 \frac{\text{m}}{\text{s}}$ is found.

6.1.2.1 Swirl

The flow that is to be observed is swirled. At present, the use of swirled flows in combustion devices is very common, e. g. in gas turbine combustors (be it for jet engines or power generation), internal combustion engines or refinery burners [Syred 2006]. It represents one important technique towards low-polluting combustion.

The acceptance of swirl-stabilized combustion is mainly due to the fact that it is simple to implement regarding the construction of combustor systems, i. e. no additional parts, which could impact the flow field, have to be introduced. Moreover, its mechanism was studied profoundly and is well documented. As explained in [Gupta 1985, Syred 2006], the stabilization mechanism is mainly based on the formation of a Central Recirculation Zone (CRZ) due to the breakdown of a highly-swirled flow. The CRZ is responsible for the upstream transport of hot gases and unburned chemical species back to the flame root. It is in fact the interaction of heat and active chemical species in regions with low velocities, which is responsible for the improved flame stability.

Whether a CRZ occurs or not can be evaluated using the so-called swirl number. This dimensionless quantity is based on the ratio of the angular momentum flux in axial direction and the axial flux of the axial momentum multiplied by the corresponding nozzle radius. The results presented in the following have been obtained using Eq. (6.1).

It should be pointed out, that the pressure integral term for the axial momentum flux has been neglected, as proposed by Sheen et al. in [Sheen 1996].

$$S = \frac{\int_0^R UW r^2 dr}{R \cdot \int_0^R U^2 dr} \quad (6.1)$$

The velocities U and W are the mean velocities in axial and tangential direction. Usually, for swirl numbers larger than $0.6 - 0.7$ a *Precessing Vortex Core* (PVC) in combination with a *Central Recirculation Zone* (CRZ) and an *External Recirculation Zone* (ERZ) (in the case of confined flows) occur [Syred 2006]. This limit is the *critical swirl number* S_c . Table 6.4 presents the swirl numbers calculated for the AVBP and YALES2 results for different downstream positions. These results show a good agreement between the

Position $\frac{z}{D}$	S_{AVBP}	S_{YALES2}	Re
0	0.78	0.80	25028
0.2	0.77	0.77	38860

Table 6.4: Swirl numbers for different planes normal to the flow direction. Swirl number preliminarily obtained for the experiments $S_{xp} = 0.9$ [Renou 2010].

two codes and both solvers are within a 10% deviation compared to the experiments, for which S was evaluated at the injection. Furthermore, the swirl numbers obtained lie above the aforementioned critical swirl number range and hence, privileges the creation of a CRZ in combination with a PVC.

6.1.3 Mean flow quantities analysis

6.1.3.1 Qualitative assessment

Figures 6.4 - 6.6 present the pseudo-color plots of the time averaged velocity components for a plane at $y = 0$. The time average of a quantity $\phi(\mathbf{x}, t)$ is obtained using

$$\langle \phi(\mathbf{x}, t) \rangle = \frac{1}{T_{av}} \sum_{n=1}^{N_{sol}} \phi(\mathbf{x}, t^n) \Delta t_{av} \quad (6.2)$$

with Δt_{av} being the time between two snapshots, N_{sol} representing the total number of instantaneous solutions available and T_{av} is the period, over which averaging is done. In the present case $T_{av} = 0.035s$, starting from a converged solution at $t = 2.274s$. Referring to the evaluation of the swirl number in section 6.1.2.1, Fig. 6.6 clearly shows the CRZ occurring in both simulations, as well as the indication of the ERZ, which are expected in a confined flow. Moreover, Fig. 6.5 is an indicator for the swirl-character of the flow.

At first sight the flows reproduced by AVBP as well as by YALES2 are very similar. The most striking difference is the expansion of the iso-lines for the tangential and the axial velocities predicted by both solvers. Nevertheless, these differences as well as the disagreement in the opening angle of the injection or the penetration length of the vortical structure are considered small.

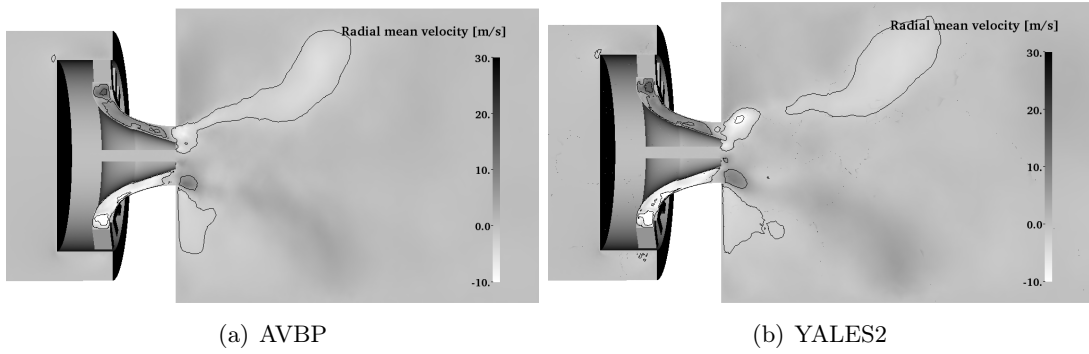


Figure 6.4: Sectional drawing for the plane at $y=0$. Pseudocolor and iso-lines of radial mean velocity for $-10 \frac{m}{s} \leq \langle u_x \rangle \leq 30 \frac{m}{s}$.

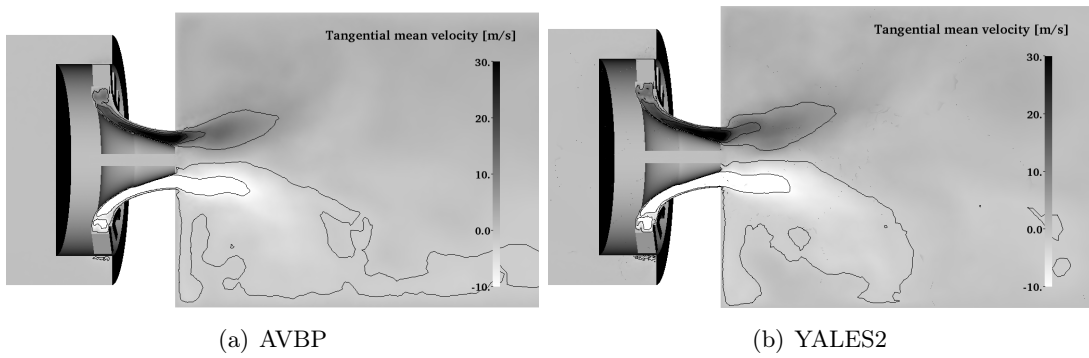


Figure 6.5: Sectional drawing for the plane at $y=0$. Pseudocolor and iso-lines of tangential mean velocity for $-10 \frac{m}{s} \leq \langle u_y \rangle \leq 30 \frac{m}{s}$.

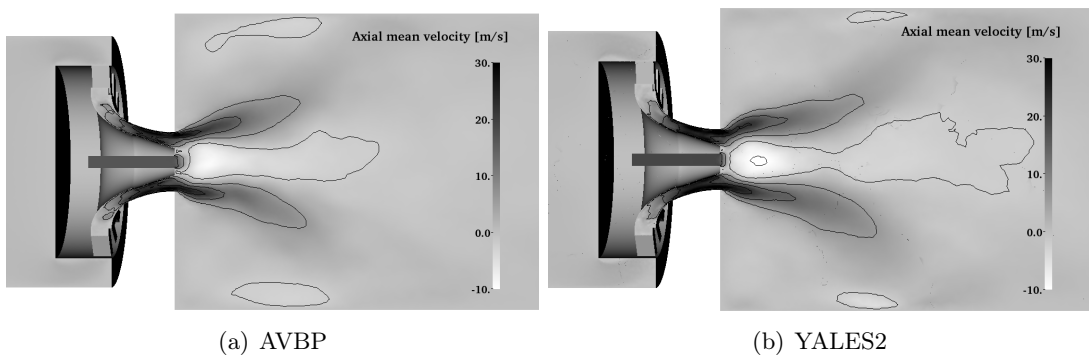


Figure 6.6: Sectional drawing for the plane at $y=0$. Pseudocolor and iso-lines of mean axial velocity for $-10 \frac{m}{s} \leq \langle u_z \rangle \leq 30 \frac{m}{s}$.

Another quantity of interest are the fluctuations, which are computed using the following relation:

$$\mathbf{w}_{RMS}(\mathbf{x}, t) = \sqrt{\langle \mathbf{w}(\mathbf{x}, t)^2 \rangle - \langle \mathbf{w}(\mathbf{x}, t) \rangle^2} \quad (6.3)$$

Using the velocity fluctuations to determine the fluctuating kinetic energy ($\frac{1}{2}\mathbf{u}_{RMS}\mathbf{u}_{RMS}$) allows to visualize regions of high turbulent activity. For the present test case this is illustrated in Fig. 6.7. The high levels of this quantity, occurring at the location of the jet and enclosing the CRZ, can be interpreted as an indication of the PVC. Once more, AVBP and YALES2 give very similar results.

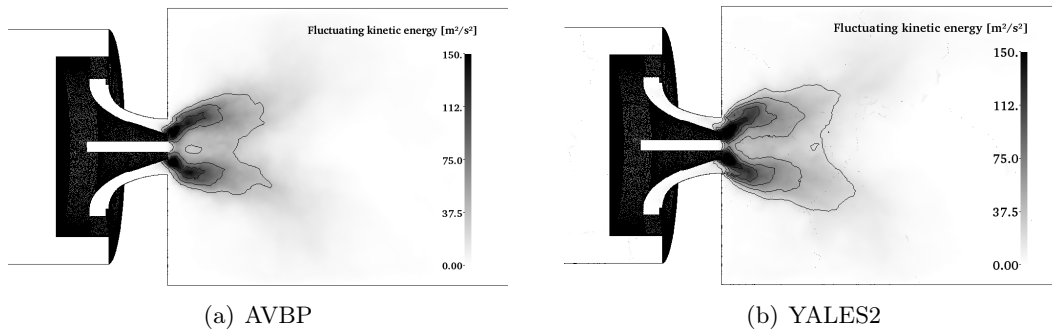


Figure 6.7: Sectional drawing for the plane at $y=0$. Pseudocolor and iso-lines of the fluctuating kinetic energy.

6.1.3.2 Quantitative analysis

Mean flow

In order to obtain a more precise idea of the agreement achieved between the two codes, the profiles of the mean velocity components along several line probes are compared. The position at which the profiles are located is presented in Fig. 6.8(a). The results of the numerical simulations are compared to the experimental results in addition. Figures 6.9 to 6.11 present the the results obtained. Data of the simulated flow fields was extracted for 300 equidistant points along the line probes. For the tangential velocity component only the comparison between the two CFD solvers is performed, due to the lack of experimental data.

At first glance the results are very encouraging regarding the direct comparison of AVBP and YALES2. The good accordance found for the qualitative assessment of both codes is now validated quantitatively. Only smaller differences occur in form of slight over- or underestimations. For the overall result, though, it can be stated that both solvers reproduce the same mean flow field.

Regarding the swirled flow and the phenomena this implies, the profiles for the tangential mean velocity of Fig. 6.11 clearly reveal its swirled nature. Taking a closer look at the high level of the tangential mean velocity the flow can be considered as highly swirled.

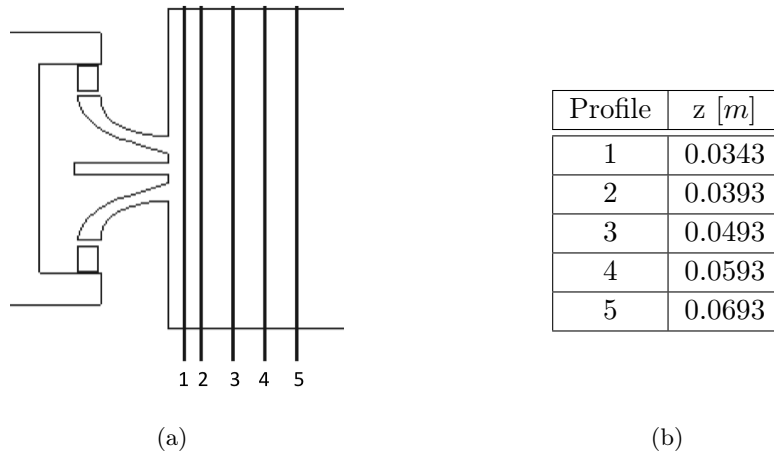


Figure 6.8: (a) Position of the line probes, for which the mean velocity components are plotted. - (b) Coordinate in axial direction for the placement of the 1D profiles.

Moreover, the axial mean velocity, presented in Fig. 6.10 brings out the appearance of the CRZ, which is surrounded by the jet of the injection. Hence, the conclusions drawn from the qualitative assessment of the mean flow are confirmed.

This first impression is further confirmed by the agreement of the numerical solutions with the experimental measurements, which is very good as well. The opening angle of the injection, the penetration length of the jet as well as flow structures, e. g. the CRZ, are well predicted by either solver.

Fluctuating quantities

For the line probes 1-5, presented in Fig. 6.8(a), the velocity fluctuations have been extracted. The results of AVBP and YALES2 are presented in Figs. 6.12 - 6.14 and are compared to the experimental data, wherever available.

Regarding the level predicted by the numerical simulations and the experiments, the results show a good agreement. Solely the profiles of the radial and the axial velocity for $z = 0.0343\text{m}$ and the axial velocity fluctuation at $z = 0.0393\text{m}$ are overestimated by both solvers. Since the graphs of AVBP and YALES2 are superposed for these coordinates, it is supposed that the difference between experiments and simulations are due to a disparity of the boundary conditions. As pointed out in Table 6.3, adiabatic slip-wall is set to the region of the central injection. This measure is necessary in order to obtain the correct velocity distribution at the exit of the central tube.

Taking a closer look at the graph ($z = 0.0343\text{m}$) of Fig. 6.14 reveals a rather important divergence of the two codes. AVBP presents two distinct peaks at each side of the axis line, whereas YALES2 just slightly gives a hint to their existence.

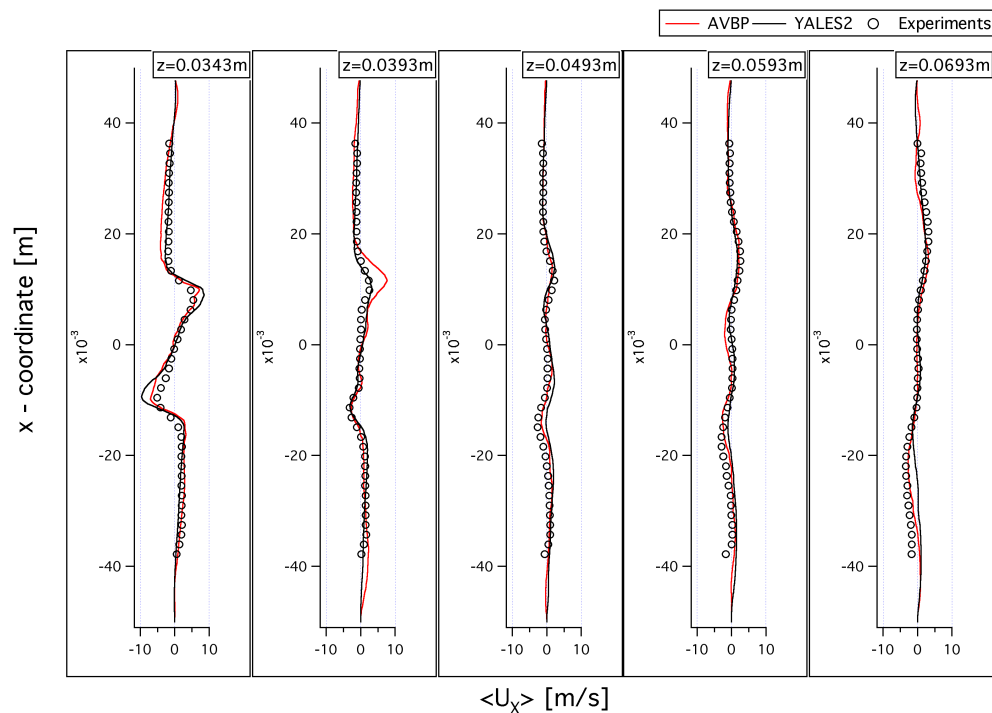


Figure 6.9: Mean profiles of the radial velocity $\langle u_x \rangle$.

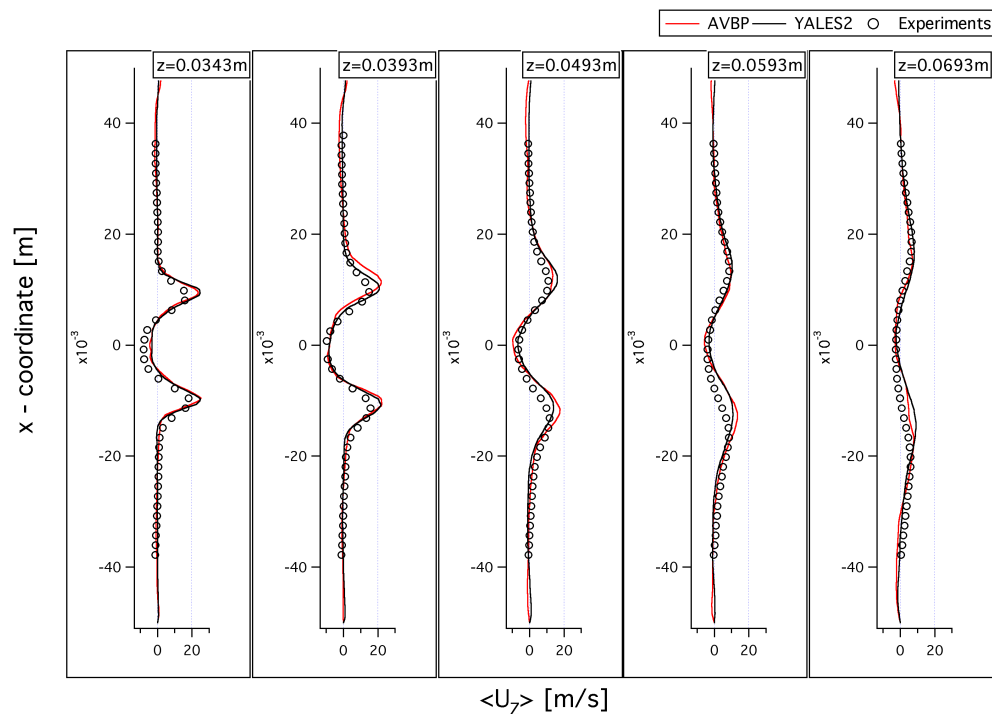


Figure 6.10: Mean profiles of the axial velocity $\langle u_z \rangle$.

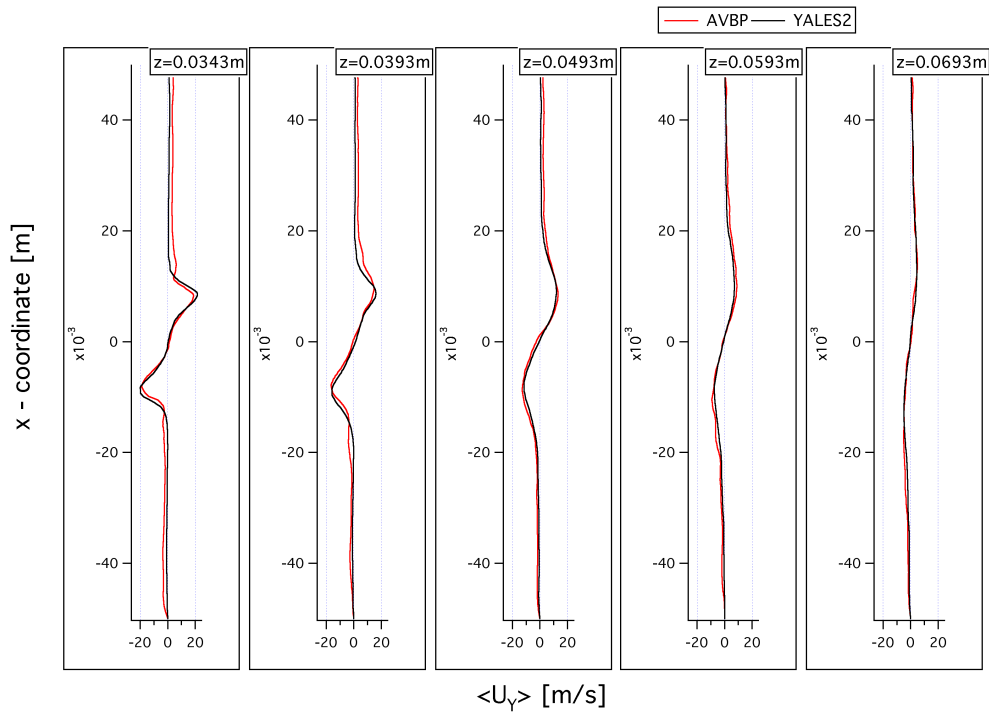


Figure 6.11: Mean profiles of the tangential velocity $\langle u_y \rangle$.

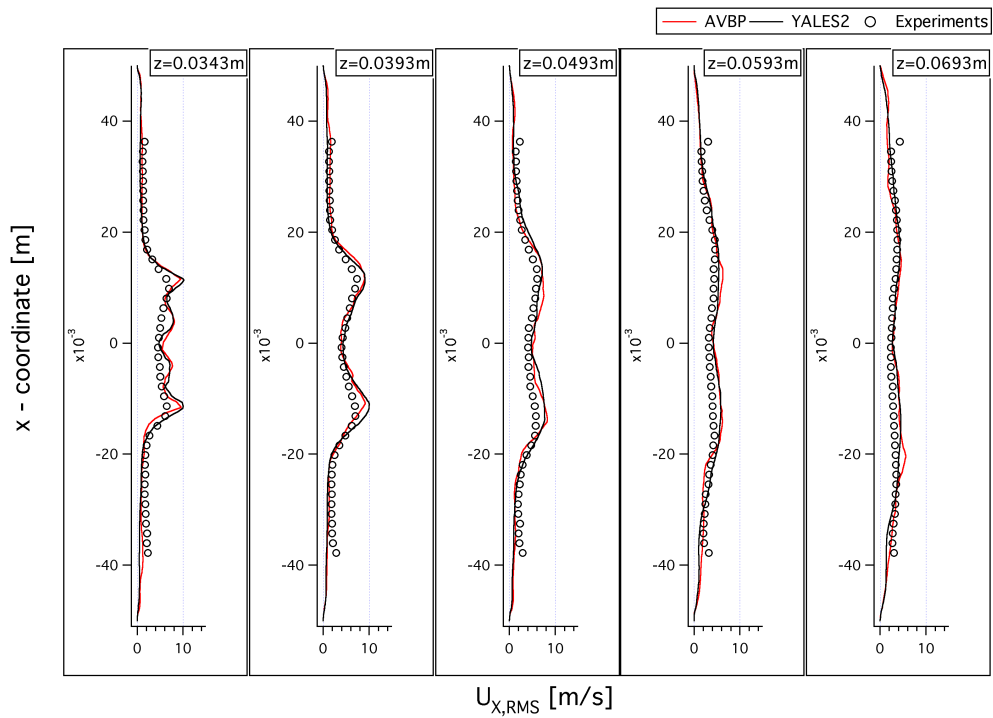


Figure 6.12: Profiles of the radial velocity fluctuations $u_{x,RMS}$.

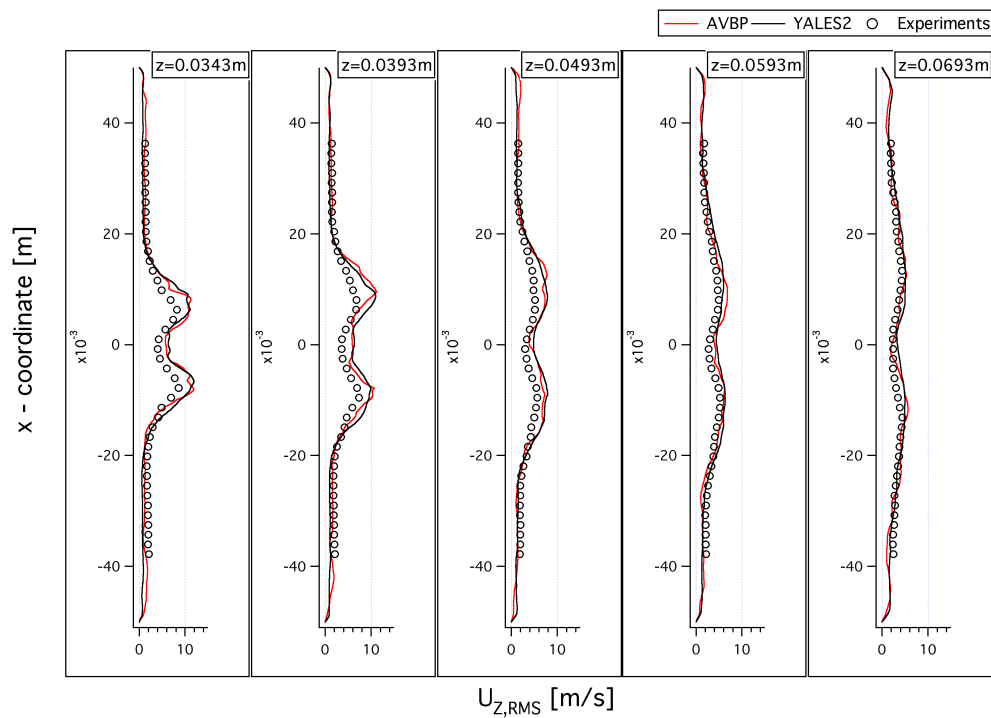


Figure 6.13: Profiles of the axial velocity fluctuations $u_{z,RMS}$.

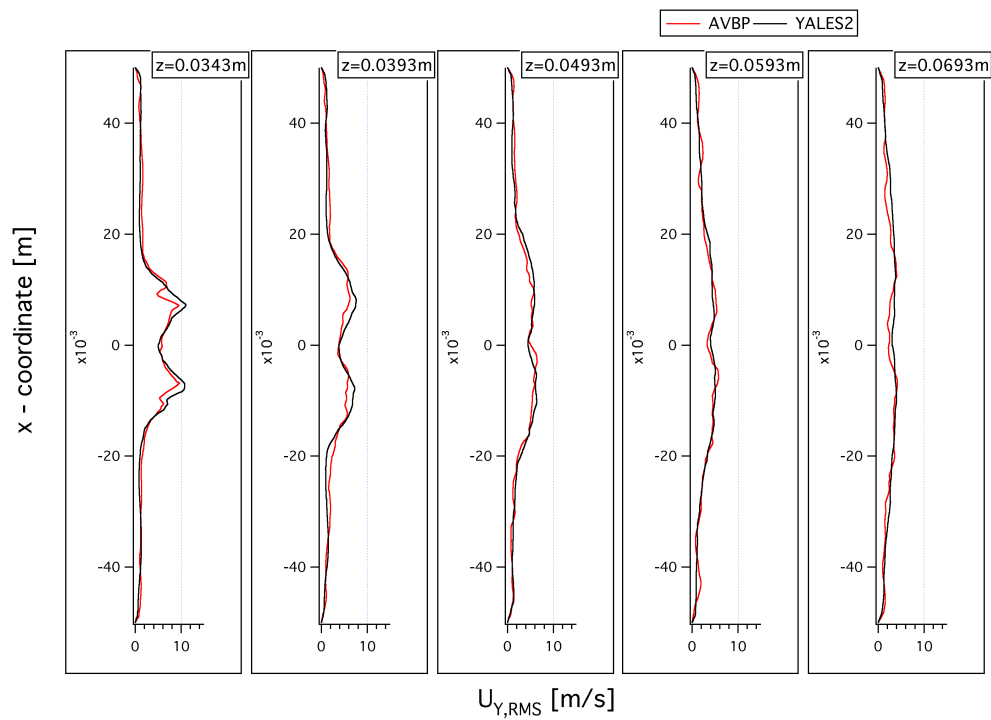


Figure 6.14: Profiles of the tangential velocity fluctuations $u_{y,RMS}$.

6.1.4 Instantaneous results

6.1.4.1 Qualitative considerations

As for the mean flow, the first analysis of the instantaneous flow field given by AVBP and YALES2 is the comparison of pseudo-color plots close to the injection. First of all, the Figs. 6.15 - 6.17 clearly illustrate the turbulent flow originating from the injector. Regarding these plots, the same observations of flow phenomena can be made as it was done for the mean velocity plots, i. e. the recirculation zones, the expansion of the flow field into the combustion chamber and the swirled nature of the flow. Again, the results obtained for AVBP and YALES2 seem very similar.

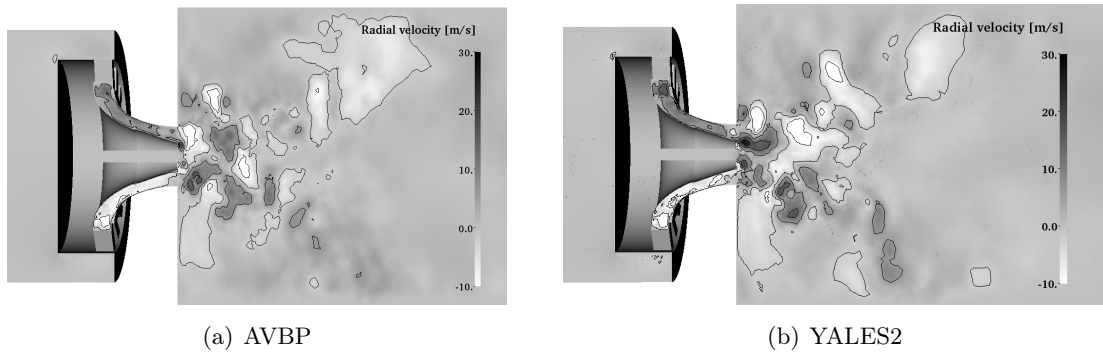


Figure 6.15: Sectional drawing for the plane at $y=0$. Pseudocolor and iso-lines of the radial velocity for $-10 \frac{m}{s} \leq u_x \leq 30 \frac{m}{s}$.

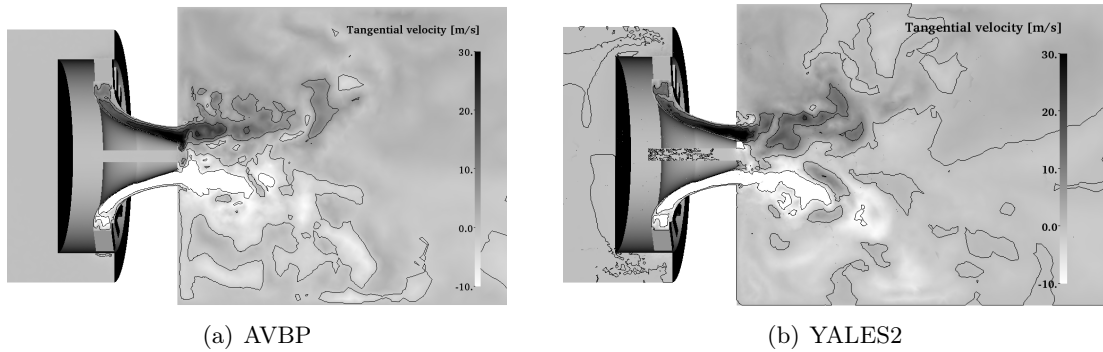


Figure 6.16: Sectional drawing for the plane at $y=0$. Pseudocolor and iso-lines of the tangential velocity for $-10 \frac{m}{s} \leq u_y \leq 30 \frac{m}{s}$.

So far, the existence of the PVC is based on theory and on plots of mean and fluctuating quantities. One approach to visualize such vortical structures is the Q-criterion [Hussain 1995]. The basic idea is to split the velocity gradient into:

$$\nabla \mathbf{u} = \mathbf{\Omega} + \mathbf{S}. \quad (6.4)$$

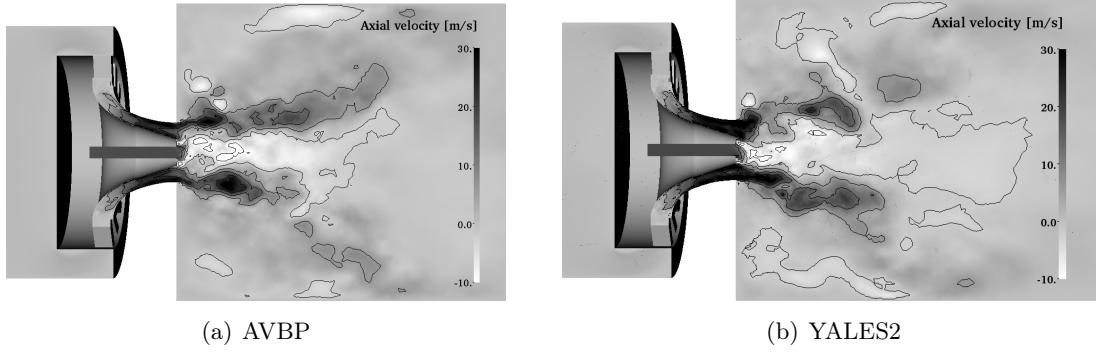


Figure 6.17: Sectional drawing for the plane at $y=0$. Pseudocolor and iso-lines of the axial velocity for $-10 \frac{m}{s} \leq u_z \leq 30 \frac{m}{s}$.

Ω , the vorticity tensor, and the rate-of-strain tensor \mathbf{S} are defined as

$$\Omega = \frac{1}{2} \left[\nabla \mathbf{u} - (\nabla \mathbf{u})^T \right]. \quad (6.5)$$

$$\mathbf{S} = \frac{1}{2} \left[\nabla \mathbf{u} + (\nabla \mathbf{u})^T \right], \quad (6.6)$$

As defined in [Hunt 1988], a vortex is a region in space, for which

$$Q = \frac{1}{2} \left[|\mathbf{Q}|^2 - |\mathbf{S}|^2 \right] > 0, \quad (6.7)$$

i. e. regions where rotation dominates strain in the flow. Figure 6.18 presents two different snapshots for AVBP and YALES2 illustrating the so-called fingers of the PVC. As can be noticed, the number of the fingers of the PVC can vary, not only between two different solvers, but also within a simulation in the course of time.

6.1.4.2 Spectral analysis

In order to clearly identify the phenomena occurring in the swirler a spectral analysis of the flow field is performed. First, the spectral tools in use are presented. Then, the results are put into perspective.

The acoustic solver AVSP

AVSP is the in-house acoustic solver of CERFACS [Nottin 2000, Benoit 2005, Nicoud 2007, Sensiau 2008, Gullaud 2010, Silva 2010, Wieczorek 2010]. It is based on the AVBP solver and thus, inherits such features as the ability to treat unstructured meshes and run in parallel. Since the prediction of low and medium frequency instabilities does not require highly refined meshes, it is possible to treat even complex three-dimensional geometries at reasonable computational costs.

For a given mean flow, AVSP solves the Helmholtz equation (6.8), with \bar{c} being the local mean flow velocity (usually obtained through an AVBP simulation) and p' representing

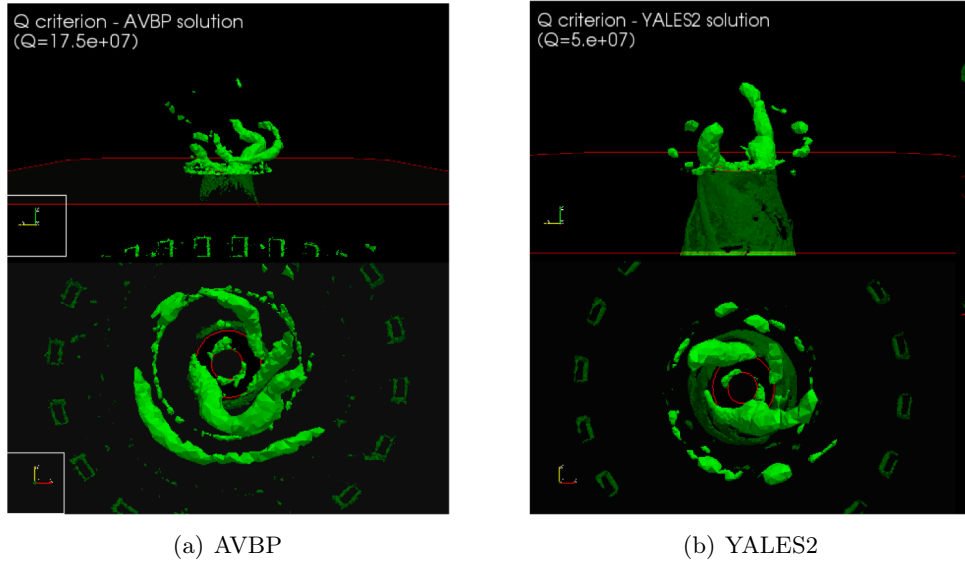


Figure 6.18: Iso-surface of the Q -criterion visualizing the PVC. For AVBP, it is composed of 3 fingers, in the case of YALES2 of 2. The number of the finger like structures varied during the simulation.

the acoustic pressure fluctuation. The solution produced by the acoustic solver consists of two information: First, the eigenfrequency ω of the investigated geometry and, second, the spatial structure of the associated eigenmode in form of the pressure fluctuation field, both solutions of:

$$\nabla \cdot (\bar{c}^2 \nabla p') + \omega^2 p' = 0 \quad (6.8)$$

This approach implies a certain number of assumptions, which are

- Low-Mach number flow,
- negligible volumetric forces,
- linear acoustics regime, i. e. only considering small acoustic fluctuations and
- constant mean pressure P_0 in the whole configuration.

The following boundary conditions are available in AVSP:

1. Zero acoustic pressure boundary
2. Zero acoustic speed boundary
3. Specified admittance boundary
4. Multiperforated plates

In the present case only the boundaries for $p' = 0$ and $u' = 0$ are used. This choice is seen applicable mainly due to the low Mach number.

The frequencies of the acoustic modes identified by AVSP are compared to Fast-Fourier Transformation (FFT) of pressure fluctuations recorded at different locations in the flow field, in order to give insight into the differences between the compressible and incompressible approach.

The Proper Orthogonal Decomposition method (POD)

A second approach to perform a spatio-temporal analysis is the Proper Orthogonal Decomposition method. The basic idea for this method relies on the work of Karhunen [Karhunen 1946] and Loève [Loève 1945], who presented an approach to reproduce a stochastic process by linear combinations of orthogonal functions. Lumley [Lumley 1967] was the first to introduce the POD¹ method for turbulent flow analysis. The results presented in this section were obtained applying the so-called *snapshot* POD [Sirovich 1987], which can be seen as a discrete version of the classical method. Since the POD has been elaborated many times in literature [Berkoöz 1993, Holmes 1996, Chatterjee 2000, Pope 2000, Huang 2006, Wolf 2010, Roux 2008], only the principle is recalled briefly. Based on the sequence of a discrete number N_{sol} of snapshots at different instants $t_n = t_1..t_N$, the flow quantity $\phi(\mathbf{x}, t^n)$ is approximated using the Galerkin approximation

$$\phi(\mathbf{x}, t^n) = \sum_{i=0}^M a_i(t^n) \phi_i(\mathbf{x}), \quad (6.9)$$

with a_i being one of the $M = N_{sol}$ temporal amplitude coefficients and ϕ_i representing the corresponding basis function. Note that the time step between two snapshots t_n and t_{n+1} should be constant for the complete set of snapshots. Furthermore, the choice of this time step size determines the maximum frequencies resolved by the POD following the *Nyquist-Shannon sampling theorem* [Shannon 1949].

The POD now reconstructs the snapshots according to Eq. (6.9) such that Eq. (6.10) is optimized (i. e. minimization of the orthogonal projection error ε_k) for k orthogonal basis functions, with $k \leq N_{sol}$.

$$\varepsilon_k = \int_{\Omega} \int_T \left(\phi(\mathbf{x}, t^n) - \sum_{i=0}^k a_i(t^n) \phi_i(\mathbf{x}) \right)^2 dt dV, \quad (6.10)$$

The first mode ϕ_0 represents the temporal average of the snapshot sequence with the coefficient $a_0 = 1$, allowing to focus the analysis on the fluctuating quantities $\phi' = \phi - \phi_0$. Finding the optimum for Eq. 6.10 then leads to the task of solving the eigenvalue problem

$$\mathbf{C} \mathbf{a}^i = \lambda^i \mathbf{a}^i. \quad (6.11)$$

The correlation matrix \mathbf{C} of Eq. 6.11 is composed of the inner product of the quantity of interest at different instants t_n . The eigenvectors \mathbf{a}^i found for each mode i are composed

¹This denomination is mainly established in the field of fluid mechanics

of the amplitude coefficients a_i and are sorted by the corresponding eigenvalue λ^i , which gives evidence about the intensity of the mode.

Since the POD is also applied to incompressible simulations, the flow velocity is the variable of interest. Thus, the inner product, which is used to obtain the correlation matrix \mathbf{C} , represents the kinetic energy.

The eigenvectors \mathbf{a}_i allow to reconstruct the temporal evolution (and frequency content) of each mode, which then is compared to FFT of flow velocity signals probed throughout the computational domain. Furthermore, the representation $\phi_i(\mathbf{x})$ allows to determine the form in physical space of the mode i . A POD tool is available in the solver YALES2 and was used in the course of this work.

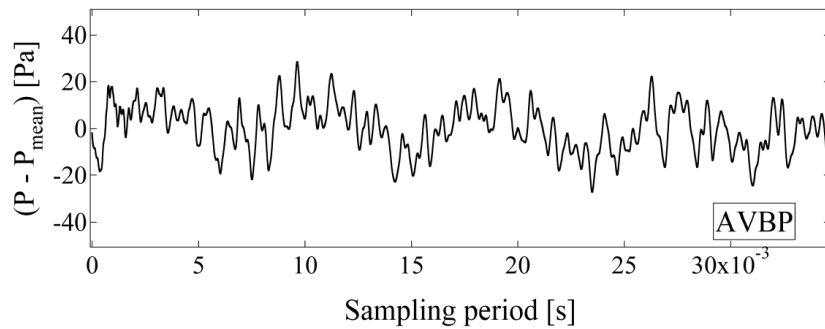
Results of the Fast Fourier Transformation (FFT) analysis of the flow

In a first attempt, FFT spectra at different probe locations are presented, in order to obtain an idea of the frequencies present within the flow field. Based on this information, the utilities AVBP and the POD method will be used to identify the nature of the modes in consideration, so whether these modes are attributed to the PVC or to acoustics. Before starting with the presentation and interpretation of the results, some characteristics concerning the solutions at hand are summarized in Table 6.5:

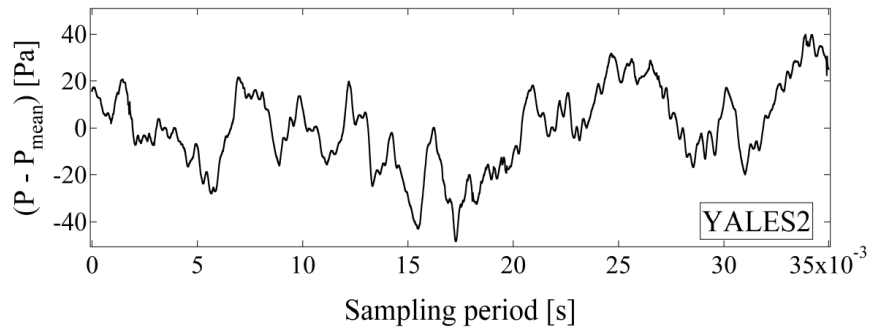
	AVBP	YALES2
Physical time simulated	35ms	
Spectral resolution	28.57Hz	
Sampling rate probes	59159Hz	58554Hz

Table 6.5: Information necessary for the following considerations concerning data acquisition during the simulations with AVBP and YALES2.

Fourier transformation is based on the assumption that the signal is of infinite length, or at least periodic, and that this signal can be described as a sum of harmonic waves of different frequency content and phase. Since it is not possible to achieve such a signal in real life, compromises have to be met. Hence, to guarantee a certain level of quality a signal should be stationary, i. e. the first central moments do not vary with time [Kunt 1981]. In the present work this will be evaluated for the mean and RMS values of the pressure signal recorded for probe 98, see Fig. 6.25. Although restricted to probe 98, similar results are obtained for probes throughout the computational domain. The raw data of this probe, normalized by the mean pressure value of the signal, is presented in Fig. (6.19) for the two solvers. Already at this stage the high content of low frequencies in the signal produced by YALES2 is noticeable and it can be expected to be recovered in the results of the FFT. In order to judge the stationarity, the 35ms signals are divided into four parts of 9ms duration. The central moment of order zero and one, i. e. the mean and the RMS values, are examined on each of the 0.9ms samples. The result for the mean values is plotted in Fig. 6.20. For the signal computed by YALES2 the mean value shows strong variations compared to what is obtained for AVBP, differing

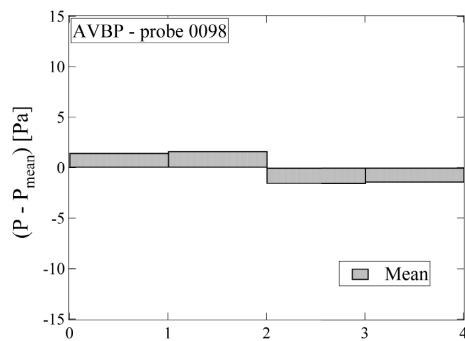


(a) AVBP

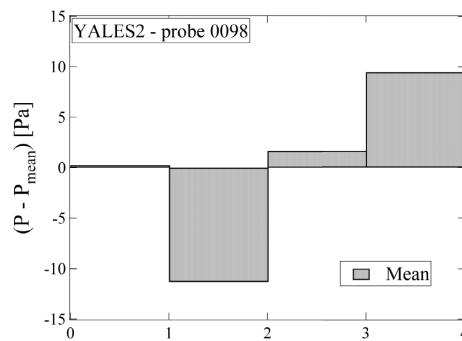


(b) YALES2

Figure 6.19: Pressure signal recorded by probe 98. The signal produced by YALES2 (b) shows a higher content of low frequencies than the one of AVBP (a).



(a) AVBP



(b) YALES2

Figure 6.20: Comparison of the mean value evolution for the pressure signal of probe 98. For this comparison the signal of 35ms is divided in four sub signals of 9ms. Variations of the mean value are one indication for possible bias in the low frequency representation of the FFT. (a) AVBP - (b) YALES2

by one order of magnitude. It shall be recalled at this point that the solutions of both simulations are converged, see Fig. 6.52. The same behavior is discovered for the RMS values of the same signal, see Fig. 6.21. Note that the global RMS value is higher in YALES2 compared to AVBP.

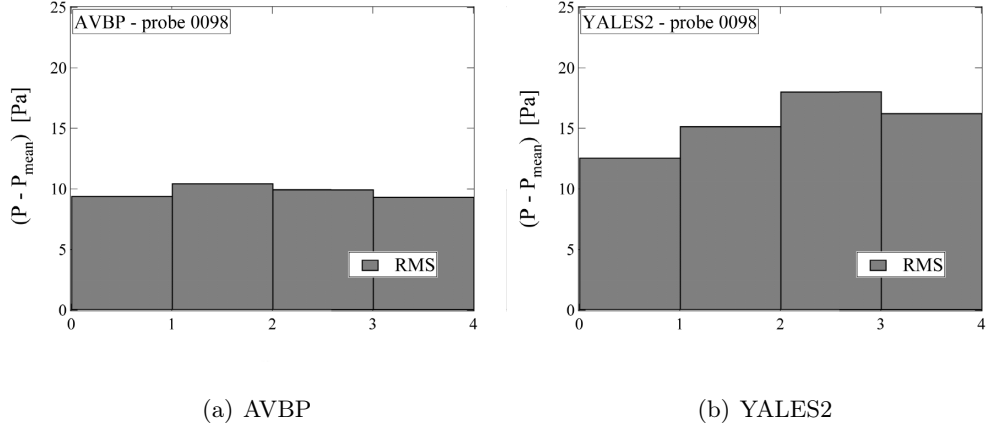


Figure 6.21: Evolution of the RMS values for the pressure signal of probe 98. For this comparison the signal of 35ms is divided in four sub signals of 9ms. YALES2 exhibits stronger variations than AVBP. (a) AVBP - (b) YALES2

Concerning the general accuracy of the FFT results for the simulation of the KIAI test case a consequence of these strong temporal variations for the zeroth and first central moment is the introduction of a bias in the low frequency band in particular. This has to be kept in mind for any further interpretation.

The signal recorded by probe 72 at the exit of the nozzle (see location in Fig. 6.22) is subjected to a FFT on pressure and the velocity components. The results are presented in Figs. 6.23 and 6.24 (only the radial velocity component is considered, since the spectra of the other two components do not add any extra information). In both cases the codes give similar spectra. The main peaks occur around 650Hz, 1200Hz and 2000Hz. In addition, a peak at around 125Hz is found in the spectrum of AVBP. At first glance this peak could represent the acoustics contained in the compressible formulation of AVBP, but so far this hypothesis has to be verified. Furthermore, Fig. 6.23(b) exhibits rising amplitudes when approaching the very low frequencies from 200Hz down to 0Hz. This certainly is, at least in parts, due to the before presented analyses of the signal properties.

Based on the frequencies at approximately 650Hz and 1200Hz identified with the help of the spectral analysis, the Strouhal numbers for these peaks are calculated. The Strouhal number is defined by:

$$St = \frac{D_{ext}f}{U_{Swirler}}, \quad (6.12)$$

with f the frequency of the PVC, D_{ext} the exterior diameter of the swirler exit and $U_{Swirler}$ the stream velocity of the flow entering the combustion chamber. The values

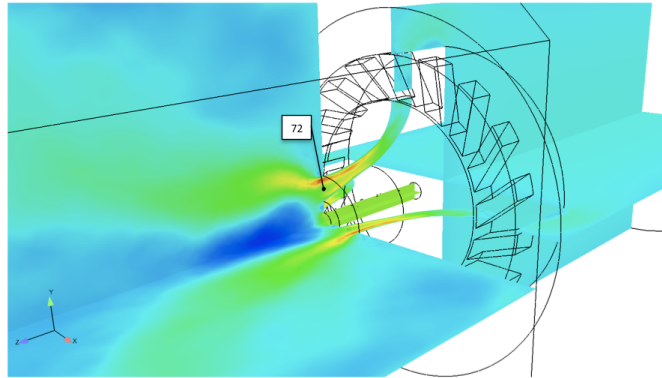


Figure 6.22: Probe 72 is situated in the injection plane in the nozzle exit.

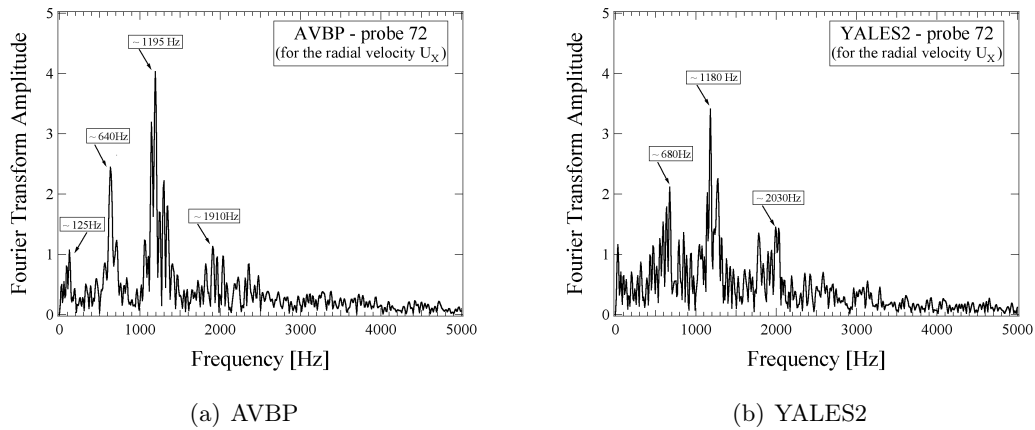


Figure 6.23: FFT amplitude of the radial velocity signal recorded at probe 72.

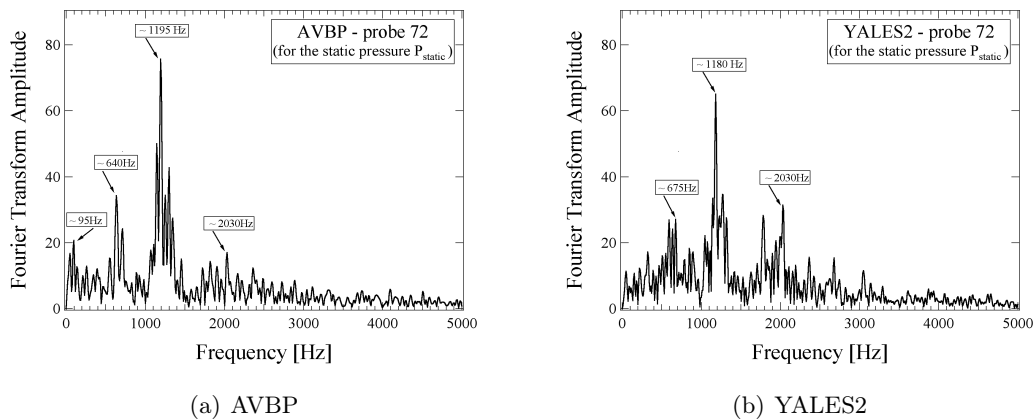


Figure 6.24: FFT amplitude of the static pressure signal recorded at probe 72.

obtained for the Strouhal number are summarized in Table 6.6.

Frequency [Hz]	640/680	1180/1195
St [-]	0.427-0.453	0.787 - 0.797

Table 6.6: *Strouhal numbers for the frequency ranges identified using FFT.*

Regarding the Strouhal numbers given in the literature, e. g. [Syred 2006], the values usually found for a PVC are in the range of the result of $St \approx 0.8$ presented in Table 6.6 for the second frequency of 1200Hz. It is this frequency then, which is considered the main frequency of the PVC. The occurrence of the other frequencies explains what is hinted at in Fig. 6.18, namely the emergence and disappearance of the finger like structures of the PVC during the simulation.

Next, the nature of the low frequency peak spotted in the AVBP spectrum is examined. Due to the position of probe 72 it is rather difficult to unambiguously identify hydrodynamic from acoustic modes. Therefore, a second set of probes is investigated using FFT. This time, probes 47, 98 and 164, are situated farther away from the PVC in the combustion chamber as well as in the plenum. Their positions are given in Fig. 6.25. Since the main interest with these probes are the acoustic modes, only the static pressure fluctuations are analyzed.

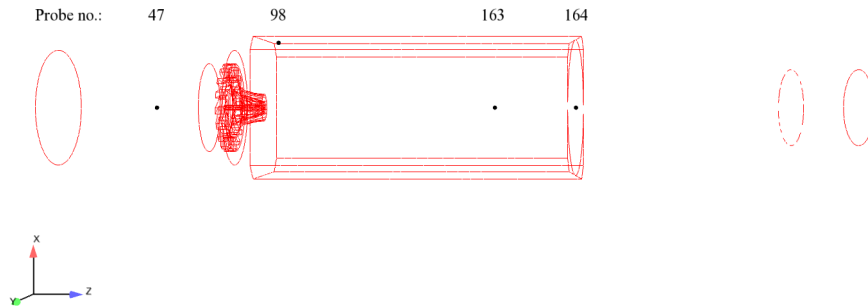


Figure 6.25: *Position of the probes located outside of the PVC, in order to identify frequencies of acoustic modes.*

First of all, the YALES2 spectra for the probes placed in the combustion chamber, see graphs (b) of Figs. 6.27 and 6.28, do resemble one another. This is consistent with the elliptic nature of the incompressible NS equations, since these results imply that the information of flow field variations is transmitted throughout the computational domain almost instantly (see section 1.4). Furthermore, the increased intensity in the YALES2 spectra for decreasing frequencies is partly attributed to the variations of the first central moments of the underlying signal.

Secondly, the spectra of AVBP and YALES2 plotted in Figs. 6.26 - 6.28 present a shift of the high amplitudes towards the low frequencies. In the case of AVBP, three peaks so far not identified as being due to hydrodynamics are found within the combustion chamber at frequencies around 125Hz, 580Hz and 865Hz. These three frequencies are supposedly acoustic modes in the chamber and will be studied in more detail in the next

paragraph. The plenum, represented by probe 47 only reveals a peak around 30Hz. This very low frequency found in the plenum is not conclusive, given the spectral resolution presented in Table 6.5.

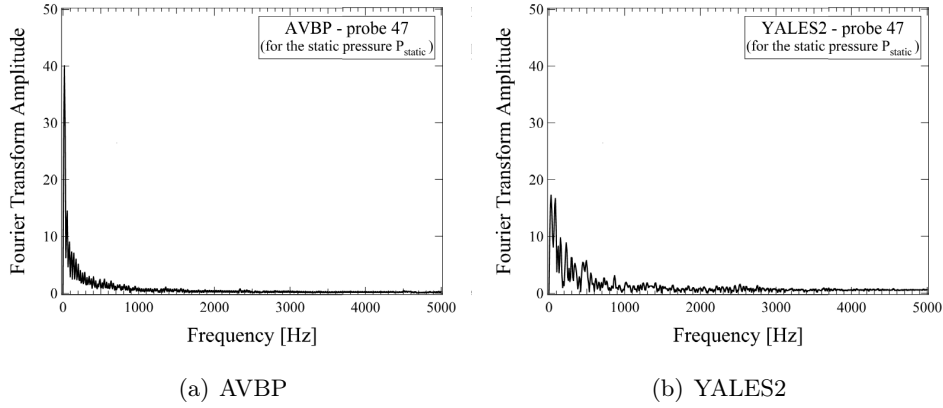


Figure 6.26: *FFT of the static pressure fluctuations for probe 47. a) AVBP - b) YALES2*

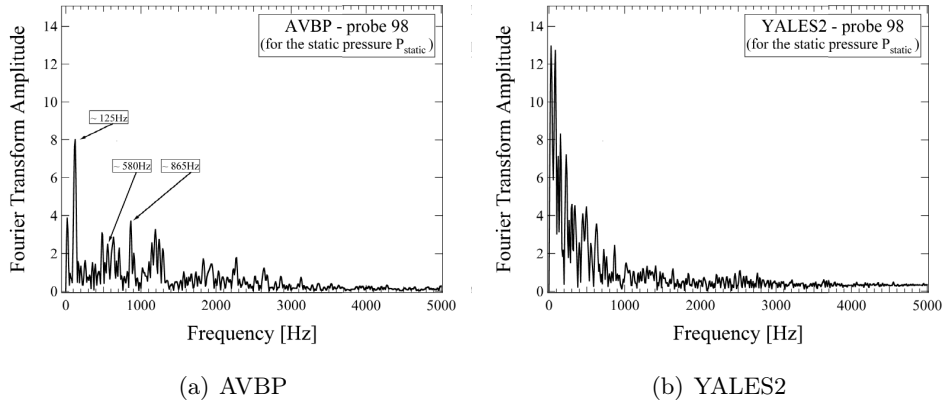


Figure 6.27: *FFT of the static pressure fluctuations for probe 98. a) AVBP - b) YALES2*

The acoustic field solution of AVSP

In Table 6.7, the eigenfrequencies of the identified acoustic modes that can occur in the KIAI configuration are listed and are now being compared to the results presented in the preceding paragraph. With regard to this, one needs to note that the peaks obtained from the FFT for the probes 47, 98 and 164 are also solutions of the acoustic solver.

Again considering probe 98, the acoustic modes corresponding to the peaks identified in

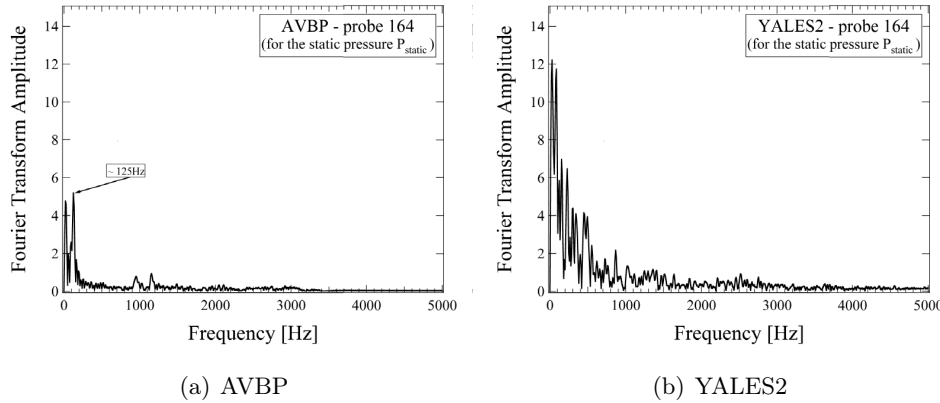


Figure 6.28: *FFT of the static pressure fluctuations for probe 164. a) AVBP - b) YALES2*

Mode [-]	Frequency [Hz]
0	28
2	150.53
12,13	580
18,19	650
34	865.66

Table 6.7: *Acoustic modes and corresponding frequencies as a result of the AVSP simulation.*

this spectra are the modes 2, 12/13 and 34 given by AVSP. The spatial representation (in terms of the acoustic pressure) is presented in Fig. 6.29 and 6.31. Note that the "0" acoustic mode found by AVSP cannot be identified with absolute certainty in the AVBP LES because its frequency is too close to the spectral resolution of the solution.

Another option to evaluate the presence of acoustics in a given configuration is by oversaturating the pseudo-color plot of the pressure RMS issued by LES, see Fig. 6.30.

The now visible structures in Fig. 6.30(a) bear resemblance with the modes 12 and 13 calculated by AVSP, by which the acoustics present in AVBP could be demonstrated. Furthermore, the lack of structures resembling the AVSP solution in Fig. 6.30(b) is consistent with the assumption that acoustics are not present in the incompressible simulation.

The frequency of the eigenmode visualized in Fig. 6.30(a), which coincides with mode 12/13 of the acoustic solution, is $f \approx 580\text{Hz}$. This does not mean of course that the rest of the eigenmodes is not present, but rather that in terms of visibility this acoustic mode is more easily spotted. Moreover, the acoustic modes 18 and 19, which are in fact exactly at one of the PVC frequencies, are seen as an indicator for the coupling of the fluid with acoustics. They are plotted in Fig. 6.29.

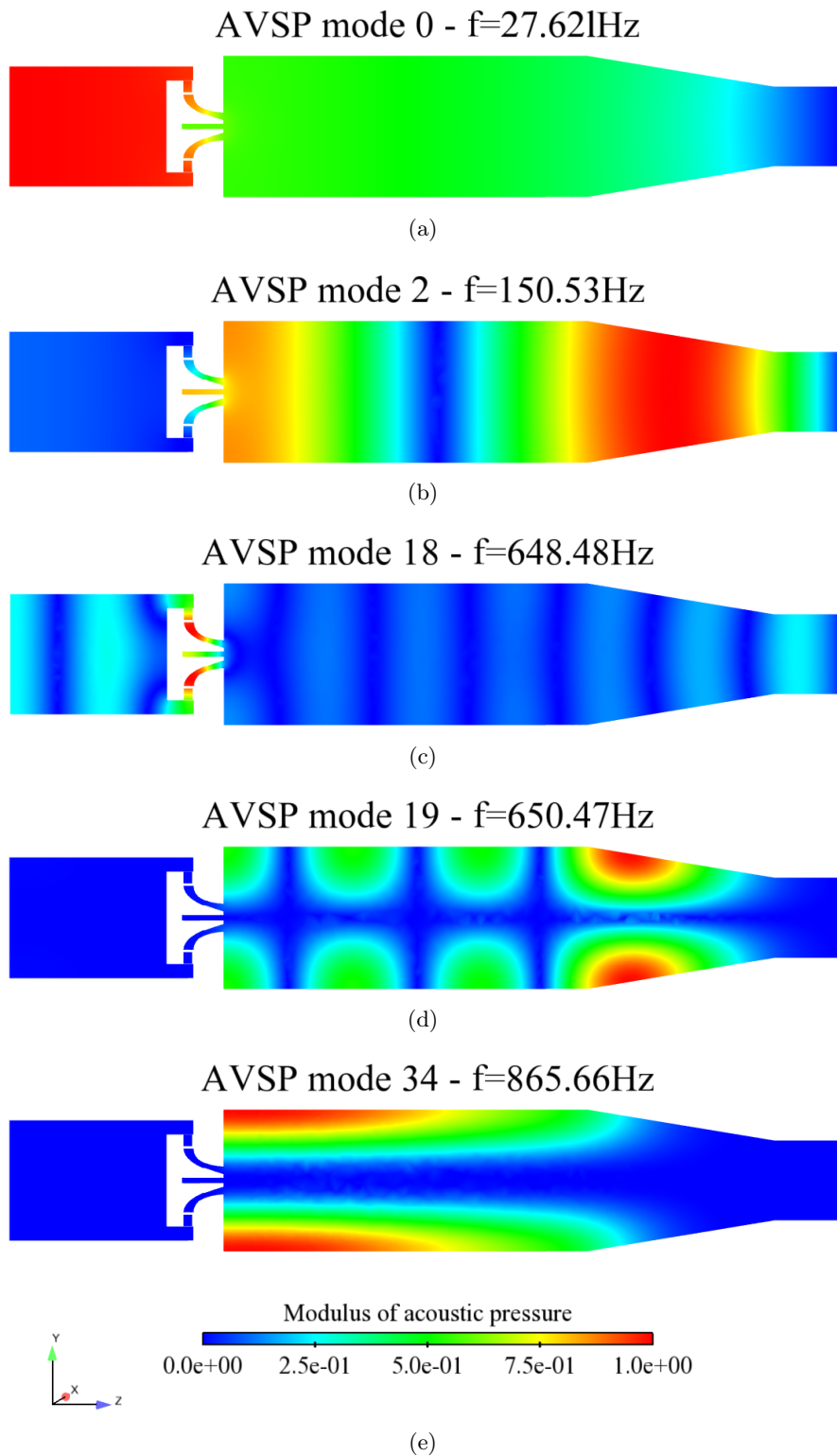


Figure 6.29: The spatial structures of the acoustic eigenmodes 2 and 34 correspond to the frequencies identified in the FFT spectrum of probe 98. Mode 18 and 19 are seen as an indication for the coupling of the fluid with acoustics.

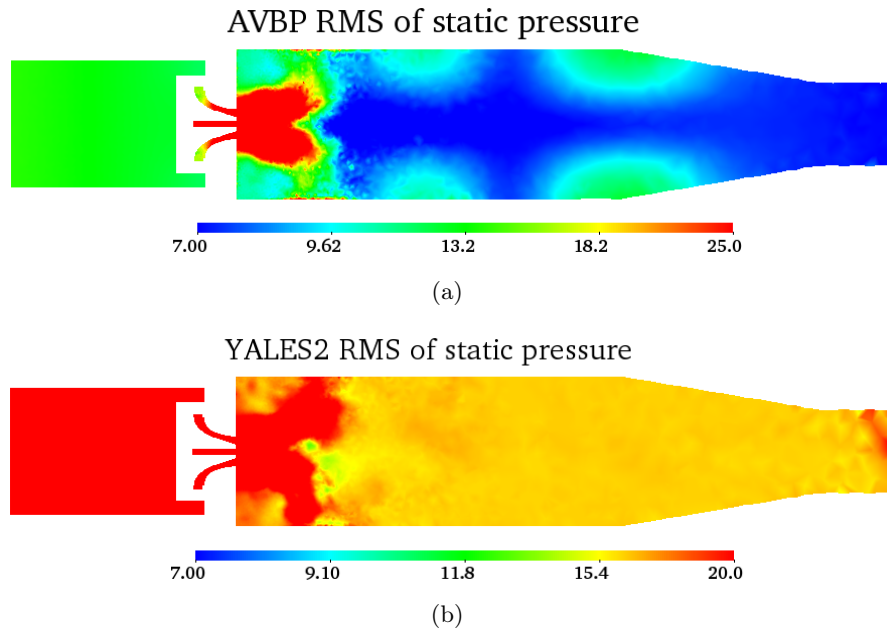


Figure 6.30: Comparison of the pressure RMS of AVBP (a) and YALES2 (b) represented in oversaturated pseudo-color plots using a logarithmic scale. Structures resembling the acoustic eigenmodes 12 and 13 can be found in the plot of the AVBP solution but not for YALES2.

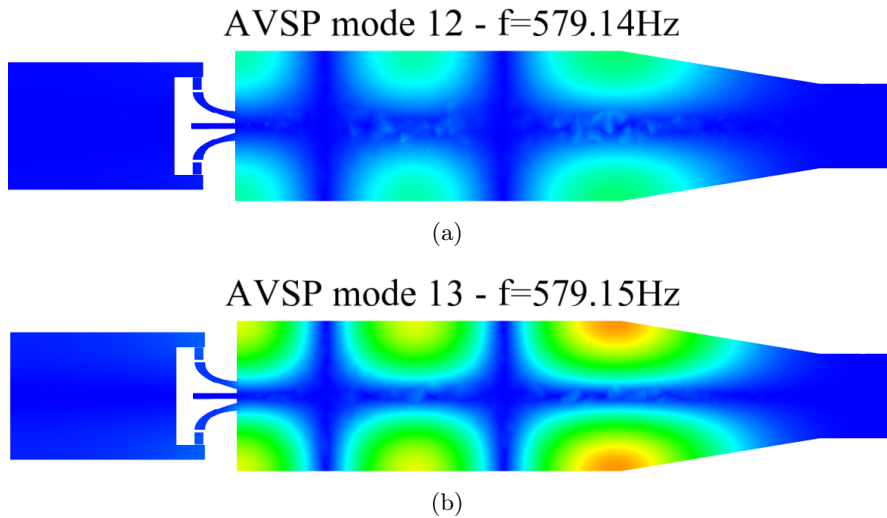


Figure 6.31: The spatial structures of the acoustic eigenmodes 12 and 13 resemble the mode represented in the AVBP pressure RMS in Fig. 6.30(a). Both eigenmodes correspond to one frequency identified in the FFT spectrum of probe 98.

Evaluation using the Proper Orthogonal Decomposition (POD) approach

Finally, the POD method is used to determine the PVC. Its frequencies identified with the POD method are compared to the ones found by the FFT. In addition, the intensity of the hydrodynamic structures of AVBP and YALES2 are quantified, due to the ordering of the eigenvalues. For this analysis $N_{sol} = 200$ snapshots are gathered during the physical time simulated and at a sampling rate indicated in Table 6.5. The quantity analyzed are the velocity fluctuations.

As explained, one result obtained by the POD are the eigenvalues of the different modes, also referred to as energies. Since in the present diagnostics the velocity is the quantity of interest, these eigenvalues are indeed related to the fluid's kinetic energy [Chatterjee 2000]. They are organized beginning with the most energetic mode. Figure 6.32 presents the energy levels of the first 100 modes found for AVBP and YALES2. The difference between the energy levels is overall rather small, indicating that the overall level of kinetic energy in the flow field for both solutions is similar. This is confirmed by the plot of the kinetic energy over time, see Fig. 6.52.

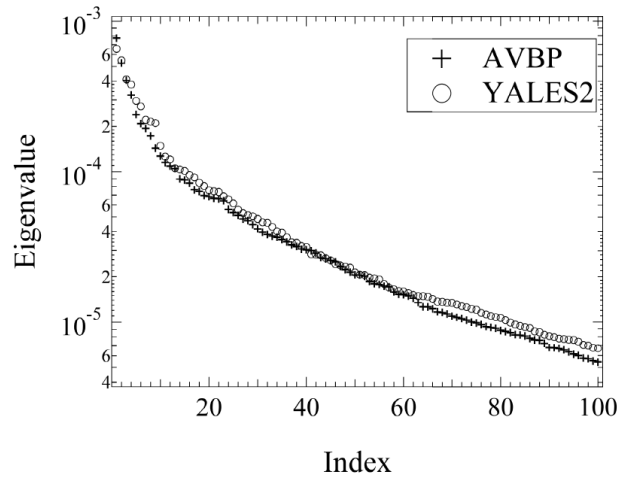


Figure 6.32: Energy level of the first hundred eigenvalues given by the POD analysis of the velocity fluctuations for AVBP and YALES2.

At first, the peak frequencies of the POD eigenmodes, which are obtained by subjecting the eigenvectors A^i of Eq. (6.11) to a FFT, are compared to the frequencies found for the FFT of the probe 72. The corresponding modes are listed in Table 6.8. In order to link the extracted frequencies of probe 72 to the modes identified using POD, the spatial representation $\phi(\mathbf{x})$ of the POD is analyzed, whether the structure of the PVC is visible or not.

For the first frequency of $f \approx 650\text{Hz}$, Figs. 6.33 and 6.34 compare the structure in the flow field of the corresponding modes. Although three different eigenmodes at the same frequency are found, this proves that this frequency is not only acoustic, but also linked

Strongest Frequency of the PVC [Hz]	Mode _{AVBP}	Mode _{YALES2}
~ 650	18,50	15
~ 1200	21	21

Table 6.8: *Frequencies of the POD modes of AVBP and YALES2 attributed to the PVC.*

to the PVC, as it was assumed in the preceding paragraph. Fig. 6.33 particularly reveals the presence of the vortical structures in form of iso-surfaces of the velocity magnitude. This result is consistent with the plots of the axial velocity component of the eigenmode, shown in Fig. 6.34.

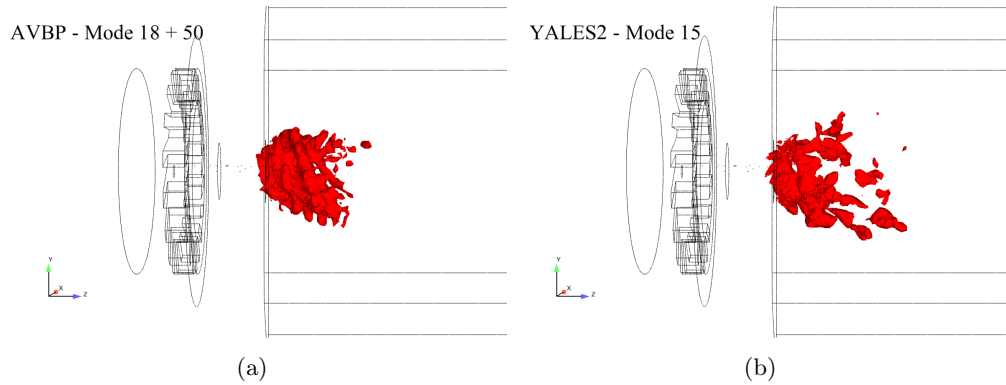
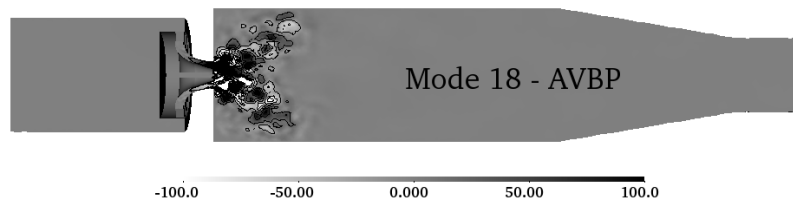
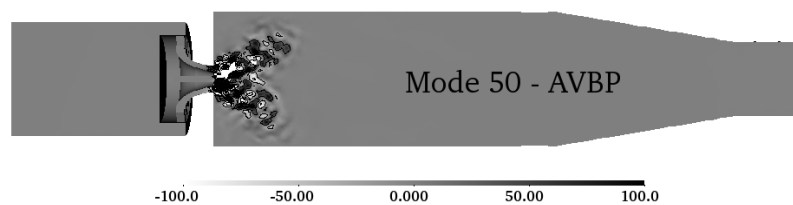


Figure 6.33: *Comparison of the iso-contour for the velocity magnitude of (a) AVBP (eigenmodes 18 and 50 are combined) and (b) of YALES2 (eigenmode 15). The structure of the PVC is clearly visible.*

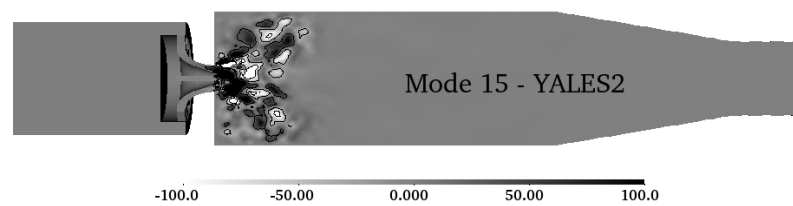
Concerning the frequency of $f \approx 1200\text{Hz}$, the snapshots of mode 21 as well as their iso-contours for the velocity magnitude are compared in Figs. 6.35 and 6.36. For this second frequency, which was classified as the main PVC frequency using the swirl number, the accordance of the iso-contour is particularly good, even more since the exact same iso-values are used ($U_{iso,21} = 350 \frac{\text{m}}{\text{s}}$).



(a)



(b)



(c)

Figure 6.34: Spatial structures for the axial component of the velocity magnitude of the eigenmodes 18 (a) and 50 (b) of AVBP (iso-value: $320 \frac{m}{s}$) as well as of eigenmode 15 (c) of YALES2 (iso-value: $200 \frac{m}{s}$). These modes are identified for the frequency of approximately 650Hz of the PVC. The different iso-values refer to the difference in the energy level between the modes.

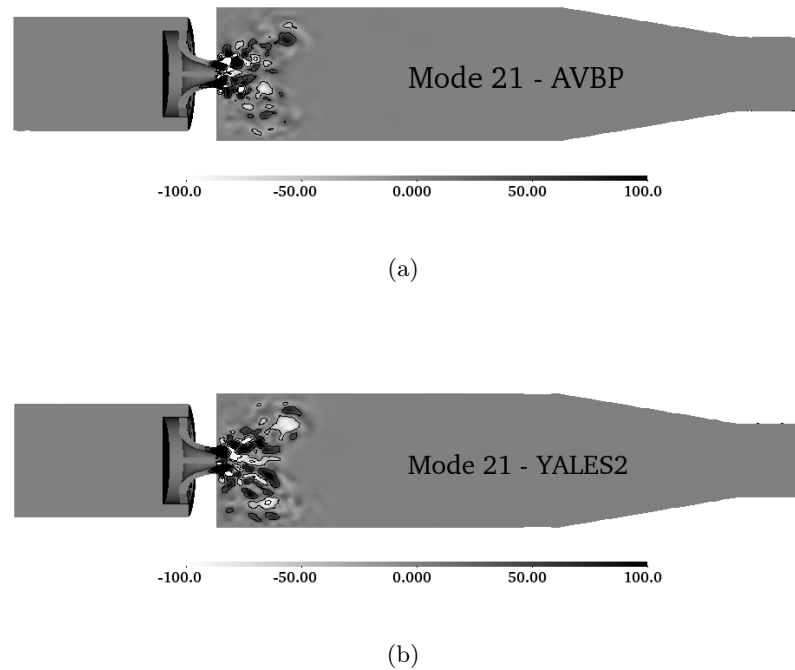


Figure 6.35: Spatial structures for the axial component of the velocity magnitude of the Eigenmodes 21 of AVBP (a) and YALES2 (b). These modes are identified for the frequency of approximately 1200Hz, which is attributed to the PVC.

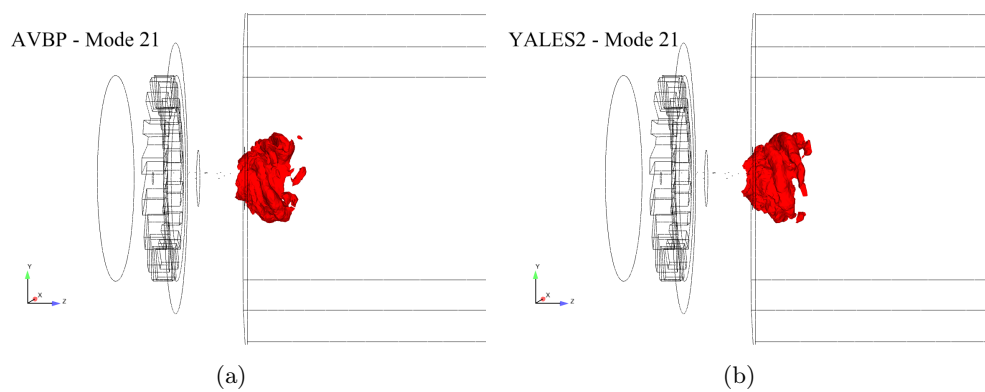


Figure 6.36: Spatial structures for the velocity magnitude of the Eigenmodes 21 of AVBP (a) and YALES2 (b). These modes are identified for the frequency of approximately 1200Hz, which is attributed to the PVC.

To conclude on this section, it is confirmed that acoustic information is only present in the solution provided by AVBP. By comparison of the FFT spectra to the solution of the AVSP solver, the acoustic modes have clearly been identified. In addition, the consideration of pressure RMS plots of AVBP and YALES2 is consistent with theory, stating that the incompressible equations do not account for acoustics. At this point it shall be highlighted that the higher constant RMS values of YALES2 in Fig. 6.21(b) are in accordance with Fig. 6.30(b). Again, this is due to the incompressible approach (see 1.4), which propagates pressure fluctuations instantaneously up- and downstream, leading to variations in the RMS of the pressure term. Taking into account the role of the pressure term within the incompressible NS equations, it is expected to find this behavior whenever performing incompressible simulations of unsteady turbulent flows. These fluctuations of the RMS values could be an explanation for the higher amplitudes of the lower frequencies in the FFT.

Regarding the PVC, two statements can be made. First, the intensity in terms of kinetic energy is similar for AVBP and YALES2. This is clear when considering the eigenvalues calculated using POD. Second, the characteristic frequencies of the PVC, which are important also in terms of kinetic energy, have been identified.

Having established that the main structures of the flow are reproduced similarly by AVBP and YALES2, the prediction of the pressure loss by either code is evaluated.

6.1.5 The effect of refining the mesh

For applications, such as the KIAI burner, one very important quantity for their development is the pressure drop occurring across the swirler, since pressure losses can impact the performance of the device. Whereas measurements are feasible for rather simple systems such as the combustor studied here, this still is one of the main issues when performing LES. The pressure drop is defined as follows:

$$\Delta P = P_{tot,2} - P_{tot,1}, \quad (6.13)$$

with $P_{tot,1}$ and $P_{tot,2}$ being the total pressure upstream and downstream of the swirler respectively. Depending on the approach, the total pressure has to be calculated differently, namely using Eq. (6.14) based on Bernoulli, which is applicable in the case of incompressible flow, and Eq. (6.15), derived for the isentropic process of bringing the fluid to stagnation.

$$P_{tot,incomp} = P_{stat} + \frac{1}{2}\rho [u_x^2 + u_y^2 + u_z^2] \quad (6.14)$$

$$P_{tot,comp} = P_{stat} \left(1 + \frac{\gamma - 1}{2} Ma^2 \right)^{\frac{\gamma}{\gamma - 1}} \quad (6.15)$$

One of the main issues impacting on the pressure loss prediction is a rather poor resolution of the velocity gradients at the wall, which clearly depends on the computational mesh. It becomes obvious that in a swirler, e. g., the result of imposing a poor estimate of the linear losses (wall friction) as well as a wrong flow behavior in the main stream has a rather strong impact.

Often in LES the sub-grid scales are modeled as isotropic structures due to the construction of the SGS models. Conversely, this assumption of isotropic structures becomes less accurate the closer the flow approaches a wall [Robinson 1991]. Considering the boundary layer as composed of two regions, it can be distinguished between the outer layer and the wall layer. In the latter strong velocity gradients can occur as well as significant production and dissipation of turbulence [Piomelli 2010]. To distinguish between the different near wall regions, *wall units* are used, which are dimensionless quantities denoted by a superscript +, e. g. y^+ of Eq. (6.16) represents the dimensionless wall distance in viscous lengths and is defined as

$$y^+ = \frac{u_\tau y}{\nu}, \quad (6.16)$$

where $u_\tau = \sqrt{\frac{\tau_{wall}}{\rho}}$ being the so-called friction velocity. Equation (6.16) resembles a Reynolds number and can thus be seen as an indicator for the relevance of viscosity and turbulence when approaching the wall [Pope 2000]. The inner layer is usually considered for $y^+ < 50$ [Pope 2000]. Reproducing the flow accurately in this region is anything but evident and moreover, can become very expensive.

Two main numerical strategies can be derived to improve the pressure drop estimate. One is the application of wall-law boundary conditions, in order to reproduce more accurately the boundary layer flow in the different sub-layers. Alternatively, the sufficient refinement of the grid in the near wall region would theoretically lead to the same result as the wall-law, provided that the SGS model has the desired behavior. But even with the increasing computational power, mainly in form of massively parallel machines, the latter option remains difficult to achieve, especially for complex configurations. The reason for this is that the number of solvers able to handle such huge meshes is rather limited. YALES2 is one of the solvers capable of doing so (see Fig. 3.6) because of the option to automatically refine the mesh, see section 3.2.3.

This section presents an evaluation of the impact on the pressure loss prediction due to a higher resolution of the near wall region in LES of a complex geometry. For this reason, the simulation performed so far was repeated using different meshes. Table 6.9 summarizes the properties of the computational grids, which are all composed of tetrahedral elements. The non-dimensional wall distance is used here to give an idea at what level the different meshes resolve the wall boundary layer. Mesh 1 was a first attempt to obtain an idea of the flow field in general and thus, it is very coarse. Since no mesh refinement algorithm is implemented in AVBP, mesh 3 was created explicitly. Although composed of less cells and giving a higher y^+ , it has to be kept in mind that the mesh refinement was done locally in consideration of the flow topology, contrary to the homogeneous refinement in the computational domain by YALES2.

In a first step the impact of refining the mesh on the flow field is evaluated for the mean and fluctuating quantities. The results for the axial mean velocity profiles of AVBP are presented in Figs. 6.38 and 6.39, the ones for YALES2 in Figs. 6.40 as well as in Fig. 6.41. Here, already an influence is noticeable close to the central injection. Using no-slip wall boundary conditions with a low mesh resolution leads to an overestimation resulting in a peak not occurring in the experimental data. Increasing the resolution

Mesh number	1	2	3	4	5
Number of elements	2M	4.3M	24M	35M	275M
y^+	~ 60	~ 30	~ 20	~ 15	~ 8

Table 6.9: Basic characteristics of the meshes used. Mesh 4 and 5 represent the automated refinement levels provided by YALES2 based on mesh 2. Mesh 3 was generated explicitly for this comparison.

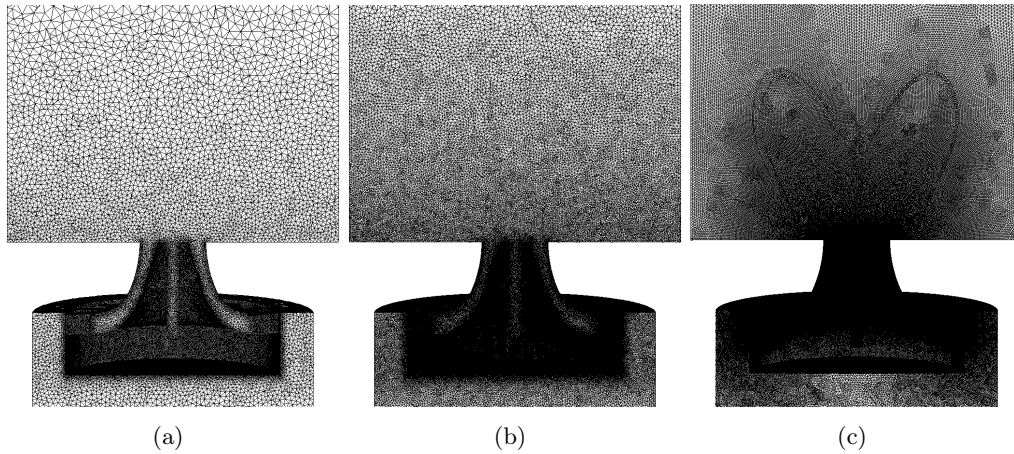


Figure 6.37: Evolution of the mesh refinement: a) basis mesh (4.3M cells) - b) first refinement level (35M cells) - c) second refinement level (275M cells).

corrects the velocity magnitude in this region. When looking at the radial mean velocity and RMS obtained with YALES2 (Figs. 6.42 and 6.43), important differences due to the mesh resolution only occur for the velocity fluctuations. This observation is also valid for AVBP, see Figs. 6.44 and 6.45. For the simulation using the mesh composed of 274M cells no quantity related to the mean flow field could be extracted, since the total time of $T_{av} = 35ms$ was not reached.

In order to give a visual impression other than in form of 1D graphs, the different levels of the mesh refinement are depicted exemplarily for the meshes 2, 4 and 5 of YALES2 in Figs. 6.37(a) - 6.37(c). Furthermore, a snapshot of the axial velocity is plotted for the meshes 2, 4 and 5, see Fig. 6.46. The level of details regarding the resolved flow structures increases noticeably.

The evolution of the total pressure along the centerline in axial direction for AVBP and YALES2 is presented in Fig. 6.47 and the absolute values are indicated in Table 6.10. The difference regarding the absolute values of the total pressure reproduced by YALES2 is simply due to the post-processing. To recalculate this quantity, the reference pressure was used, which is not exact but enhances the readability of the graph. This is valid, since the absolute pressure values are of no importance for the incompressible approach. Taking into account the results of the comparison between AVBP and YALES2 so far,

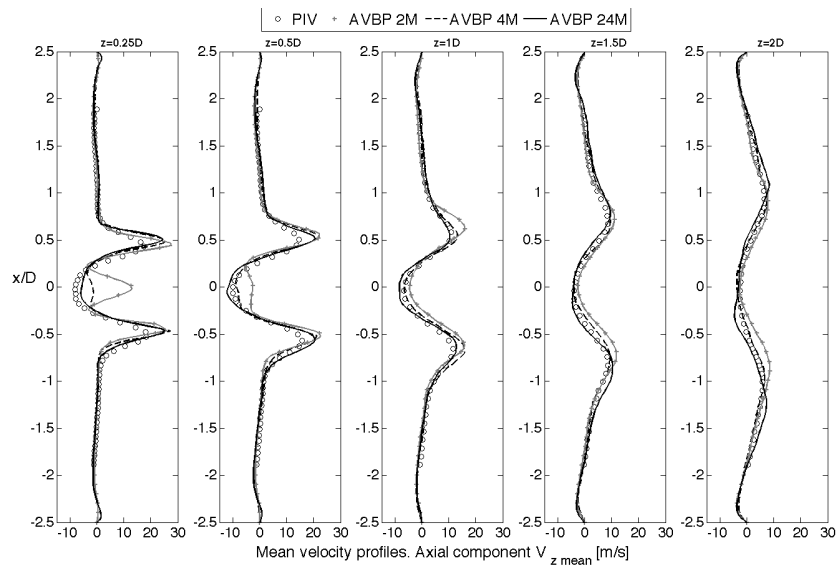


Figure 6.38: Profiles of the axial mean velocity for the meshes 1, 2 and 3 obtained using AVBP. Source: [Barré 2011]

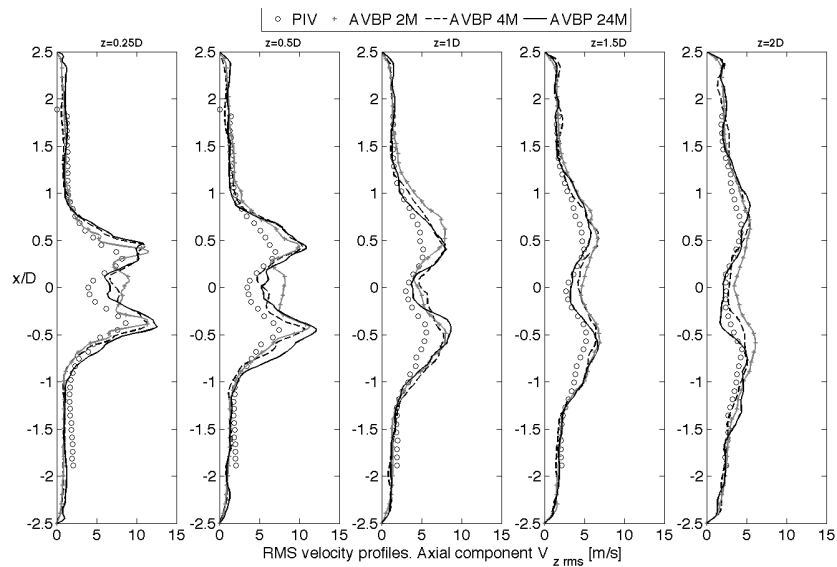


Figure 6.39: Profiles of the axial velocity fluctuations for the meshes 1, 2 and 3 obtained using AVBP. Source: [Barré 2011]

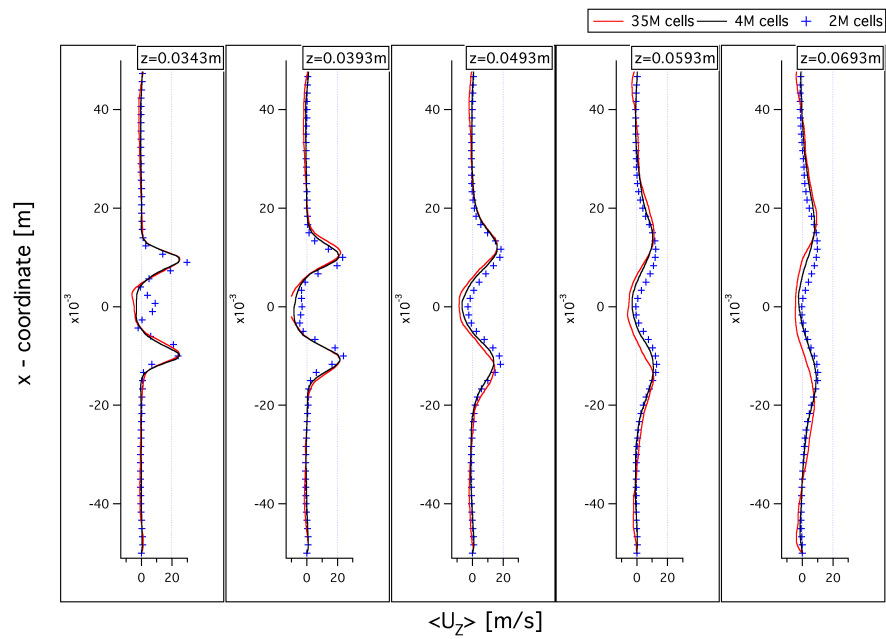


Figure 6.40: Profiles of the axial mean velocity for the meshes 1, 2 and 4 obtained using YALES2.

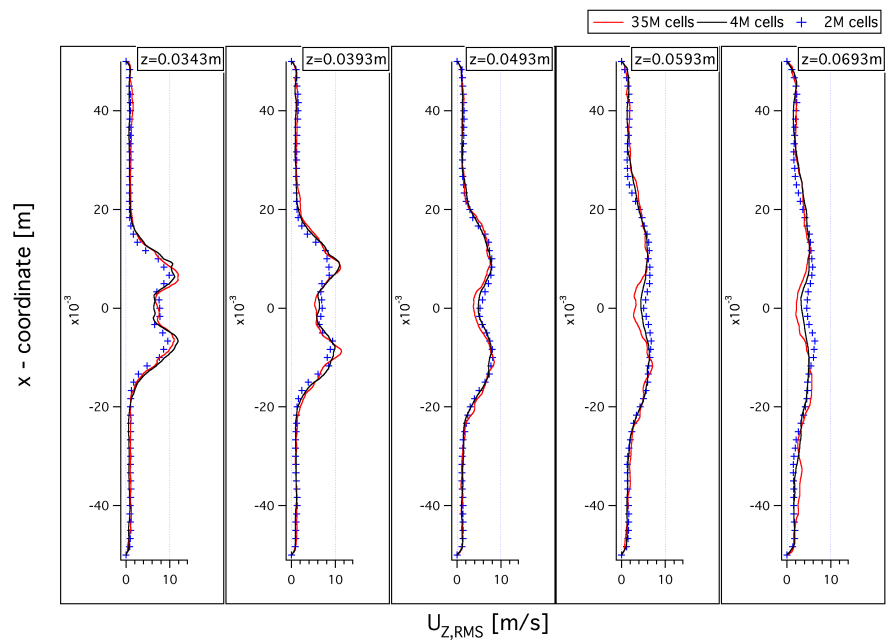


Figure 6.41: Profiles of the axial velocity fluctuations for the meshes 1, 2 and 4 obtained using YALES2.

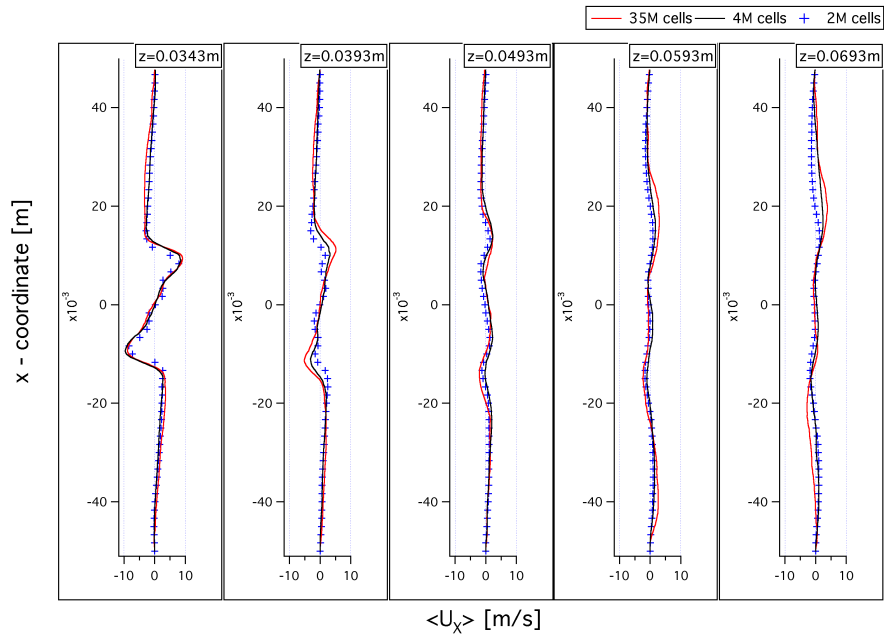


Figure 6.42: Profiles of the radial mean velocity for the meshes 1, 2 and 4 obtained using YALES2.

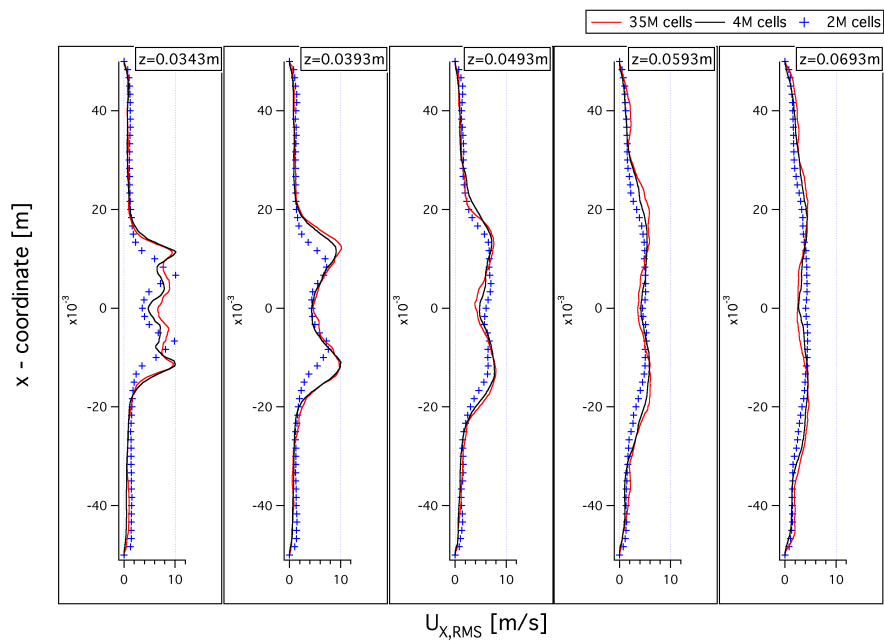


Figure 6.43: Profiles of the radial velocity fluctuations for the meshes 1, 2 and 4 obtained using YALES2.

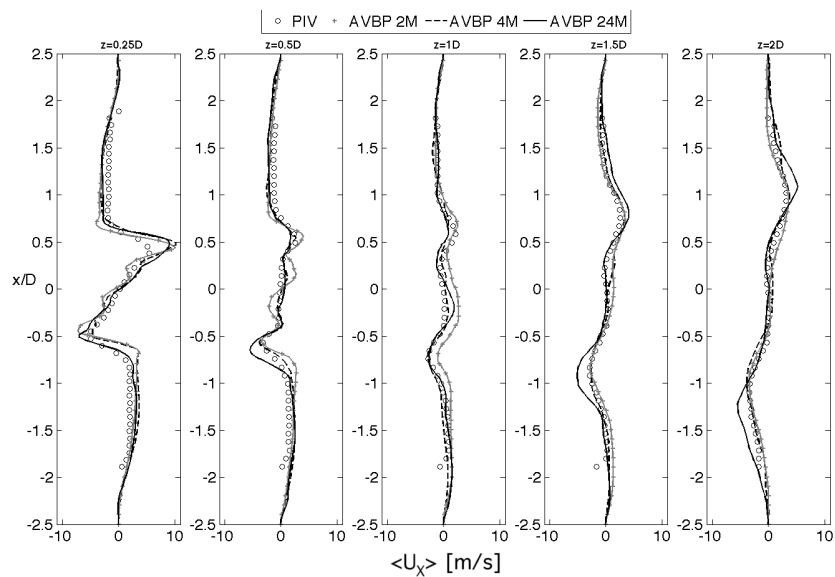


Figure 6.44: Profiles of the radial mean velocity for the meshes 1, 2 and 3 obtained using AVBP. Source: [Barré 2011]

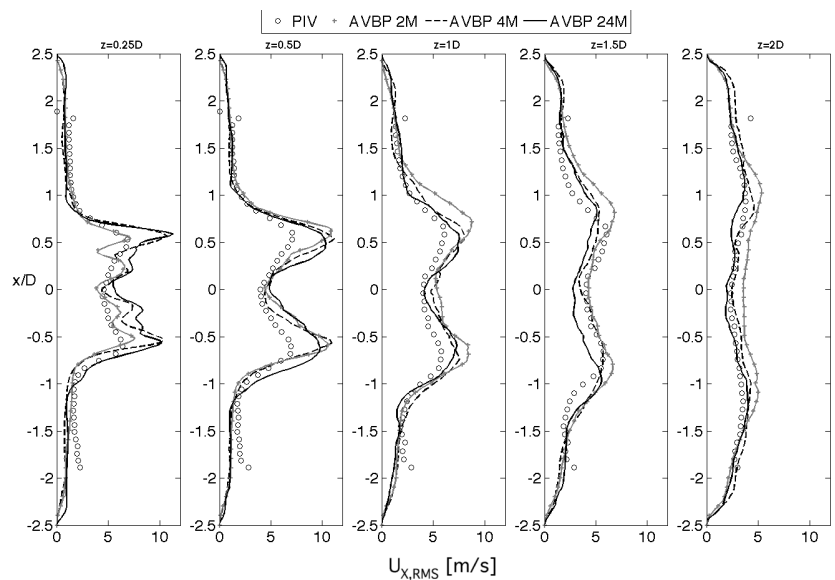


Figure 6.45: Profiles of the radial velocity fluctuations for the meshes 1, 2 and 3 obtained using AVBP. Source: [Barré 2011]

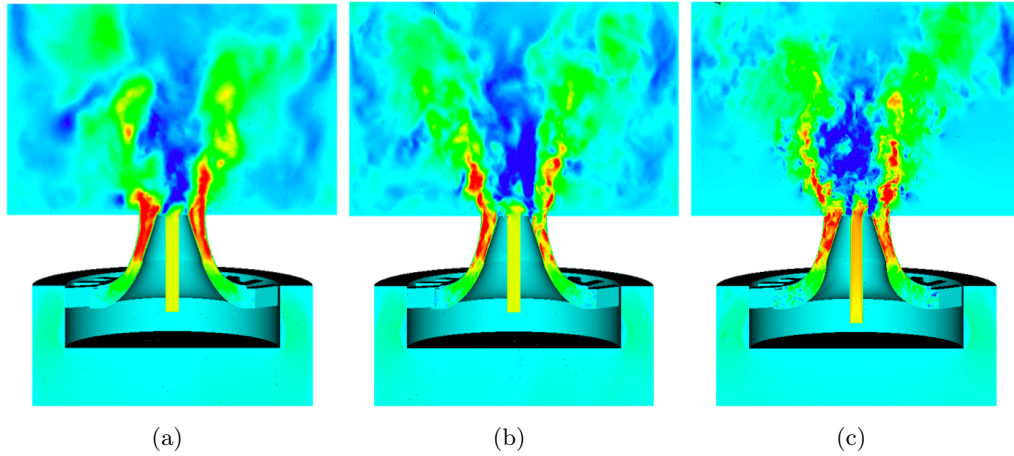


Figure 6.46: Evolution of the solution due to mesh refinement - presented here the axial velocity: a) basis mesh (4.3M cells) - b) first refinement level (35M cells) - c) second refinement level (275M cells).

it is not surprising that the pressure loss calculated by either code is not too far from the other. Compared to the experimental results, the relative error is extremely large. Overestimating by about 100% for the very coarse mesh 1, the solvers reduce this value within their predictions down to approximately 50-55%. Overall, AVBP's prediction of the pressure loss is slightly more accurate but still far from delivering proper results.

Despite these results, the overall tendency of an increasing accuracy is clearly visible², see Fig. 6.48. This graph also shows the level of precision resulting when applying wall law boundary conditions to the simulations, instead of wall no-slip boundaries.

The question remains, whether the benefit of the gain in accuracy by refining the mesh outweighs the effort that has to be raised. This question is linked to the secondment at Turboméca, Bordes (FRANCE) mentioned in section 1.5 and the results obtained are used to give a first evaluation on this topic.

Table 6.11 summarizes the simulation times and the memory needed for the different simulations presented within this section. The basic mesh and the first refinement level were computed using TITANE (Bull Novascale R422 - 1596 nodes consisting of two Intel Xeon 5570 [$4 \times 2.93GHz$] processors and 3GB/core of memory), a super-computer installed at CEA, France. The last mesh refinement was conducted on JADE (SGI Altix Ice 8200 - 2880 nodes consisting of two Intel Quad-Core E5472 or X5560 processors and 30GB or 34GB memory, respectively), a computer of CINES - Montpellier, FRANCE.

A conclusion regarding the mesh refinement has to be drawn considering two different points of view. The first one is the need of industry to obtain reliable data without investing too much into one single run. It is obvious that in this case, the mesh refinement is not yet a tool for the daily use in the industrial processes, since in the majority of cases neither the time needed to perform such a simulation nor the infrastructure to acceptably

²Moureau *et al.* presented similar conclusions in [Moureau 2010b], obtaining a relative error in the pressure drop estimate of 31.2% (48M tets) and 22% (380M tets)

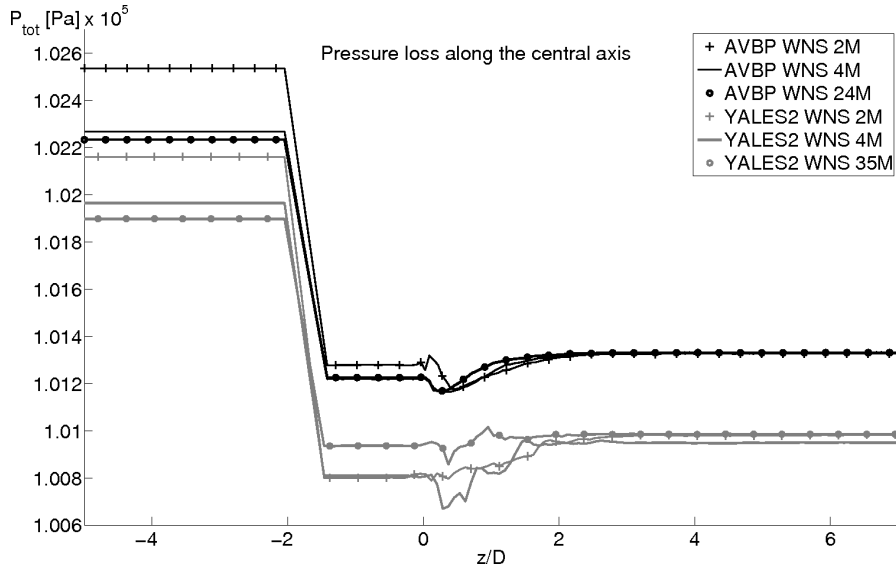


Figure 6.47: Relative pressure drop obtained for the simulation using AVBP and YALES2 on the on the different meshes. In comparison, the experimental measurements yielded a $\Delta P = 594$ Pa.

Mesh	ΔP_{AVBP} [Pa]	Relative error	ΔP_{YALES2} [Pa]	Relative error
1	1220	105%	1200	102%
2	945	59%	1010	70%
3	900	51%	—	—
4	—	—	915	54%

Table 6.10: The pressure drop values for the different meshes and the corresponding relative error of the prediction compared to the results obtained in the experiments.

Refinement level	Mesh	# of processors	Simulation time [s]	Disk space [GB]
0	2	72	3248	1.5
1	4	128	56295	8.9
2	5	4096	301224	125

Table 6.11: Summary of the simulation time and the memory requirements for the simulations of the refined meshes in comparison to the basic mesh.

store or even post-process the data is at hand. With regard to [Moureau 2010b] though, this method might become applicable with further increase in computing power. Until then, a deployable alternative is the wall-law boundary conditions, since the additional computational costs, depending on which wall law condition is applied, are outweighed by the large reduction in the relative error of the pressure loss prediction.

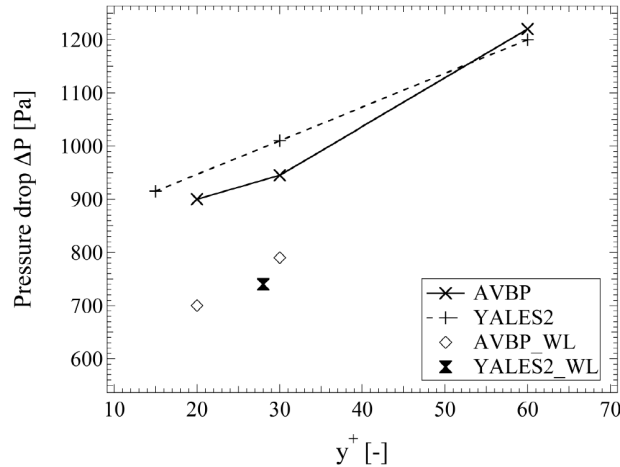


Figure 6.48: Evolution of the predicted pressure loss of AVBP and YALES2 as a function of the dimensionless wall distance y^+ .

Second, from a researcher’s point of view, the application of the mesh refinement algorithm opens up new possibilities to study flow phenomena in more detail, see e. g. the accuracy that can be achieved in the instantaneous solution of Fig. 6.46. As already proposed by Moureau et al. [Moureau 2011d, Moureau 2010a], this represents one approach to DNS of realistic configurations. Additionally, most HPC-centers are, in first place, created for scientific projects and not to provide computational power to industry.

6.1.6 Performance

Both codes have been subjected to an evaluation of their performance on parallel machines. The machine utilized for these tests is CORAIL. One node of the HP cluster is composed of 2 AMD MagnyCours (2.2GHz) processors possessing 12 cores each and giving a peak performance of 211GFlops per node. Each node is equipped with 32GB or memory.

A particularity of AVBP is that the simulations, presented in this section, have been carried out in *cryogenic* mode. This technique is applied to accelerate the computation of non-reactive transient simulations by artificially increasing the Mach number and hence, the time step. In order to conserve the momentum and the kinetic energy during the simulation, the only possibility to influence the Mach number is by decreasing the temperature (hence the name *cryogenic*). For the presented simulations, the speed of sound was decreased by a factor 4.

6.1.6.1 Benchmark of AVBP and YALES2 for the one-burner configuration

Before taking a closer look at the convergence velocity, the overall performance of the solvers is evaluated. The benchmarks presented in this section are based on a simulation of 3ms physical time on the basic mesh 2 of approximately 4.3 million cells. This is

estimated to be sufficient in order to retrieve significant information on the performance of both solvers. Fig. 6.49 presents the simulation time for different numbers of processors. When looking at the ratio of the time needed by AVBP and the simulation time of YALES2, a factor between 6 and 9 is recovered (see Table 6.12). Not using the *cryogenic* mode of AVBP, these ratios increase to approximately 24 to 36.

# of processors	24	48	72	96	120
$\frac{T_{AVBP}}{T_{YALES2}}$	8.74	8.06	7.22	6.92	5.97

Table 6.12: Ratio of simulation times for AVBP and YALES2.

Another distinctive feature is that the simulation time of YALES2 compared to the one of AVBP is constant for more than 48 processors. This is not only due to the large difference in the magnitudes of the simulation time in the same graph, but can also be explained with Fig. 6.50, which plots the speedup of both codes. In the same manner as done in chapter 5, only strong scaling is considered, i. e. an increase in the number of processors for a constant problem size.

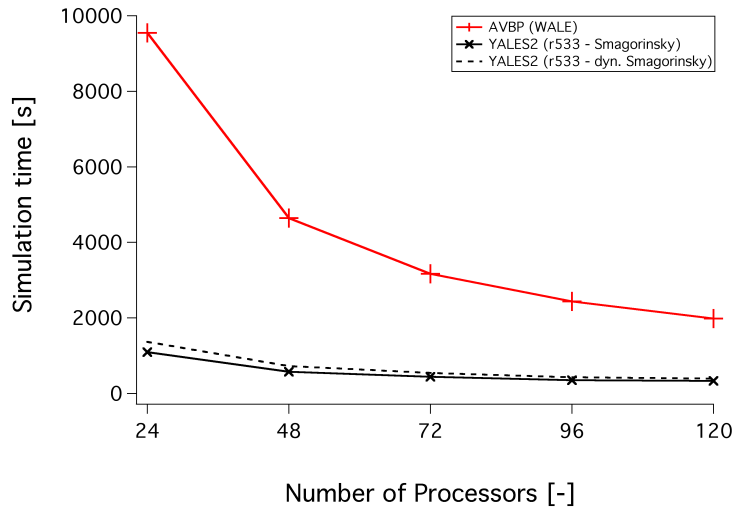


Figure 6.49: Simulation time of AVBP and YALES2 needed to compute 3ms of physical time on the coarse mesh 2.

As can be seen in this graph, the speedup of AVBP stays close to the linear speedup, meaning that by using twice as many processors, the solution is obtained in approximately half of the time. The speedup of YALES2, on the other hand, deviates noticeably from the linear speedup when using more than 48 processors. Hence, the simulation time is reduced by a factor considerably smaller than 2. Furthermore, it can be observed that the graph of YALES2 becomes saturated rather quickly when increasing the number of processors. For one, this can be explained considering the ratio *number of cells / nodes*, which is necessary to run the code efficient on parallel machines. The estimated values

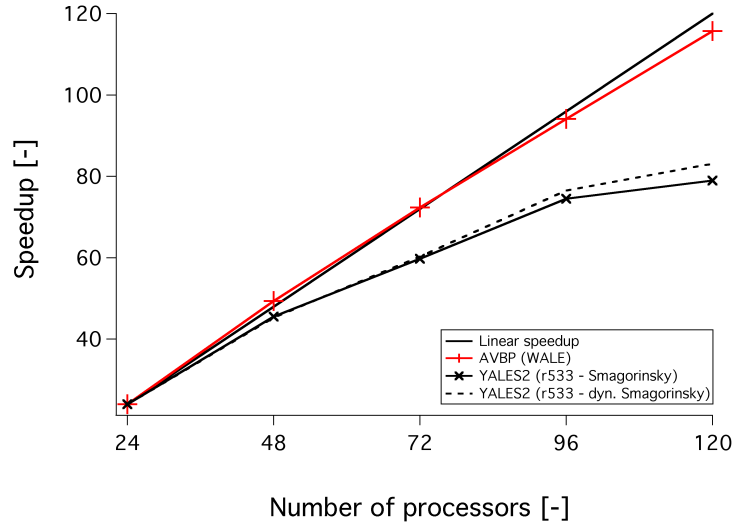


Figure 6.50: Speedup of both codes obtained for simulations using mesh 2 in comparison to the linear speedup

for both codes are given in Table 6.13. The large factor between both solvers mainly comes from the fact that the incompressible solver of YALES2 treats a smaller number of variables. In addition, Amdahl's law [Amdahl 1967] might also play a role. It states

AVBP	YALES2 (r533)
$8000 \frac{\text{nodes}}{\text{processor}}$	$70000 \frac{\text{cells}}{\text{processor}}$

Table 6.13: Estimated values in order to run each code efficiently.

that an algorithm is only scalable up to a certain point, which is determined by the parts of the algorithm that cannot be run but sequentially. A more detailed description is given in [Gourdain 2009a].

Finally, the reduced efficiency is plotted in Fig. 6.51. For the configuration of the KIAI burner the ratio between AVBP and YALES2 is a bit smaller than for the benchmark of the convected vortex. For the combustor, the incompressible solver will be faster than the compressible, as soon as the convective timestep is 2 to 3 times higher than the acoustic one. Another influence might derive from the elements used for the simulations. The mesh of the KIAI simulation is composed of tetrahedra uniquely contrary to the mesh used for the vortex, which was built from hexahedra.

6.1.6.2 Convergence behavior of the solvers

The graphs of the convergence for AVBP and YALES2 in this section represent simulations done on the coarse mesh 1. Both computations have been initiated for the flow to be at rest in the configuration. The AVBP results are obtained for a simulation of 0.3s

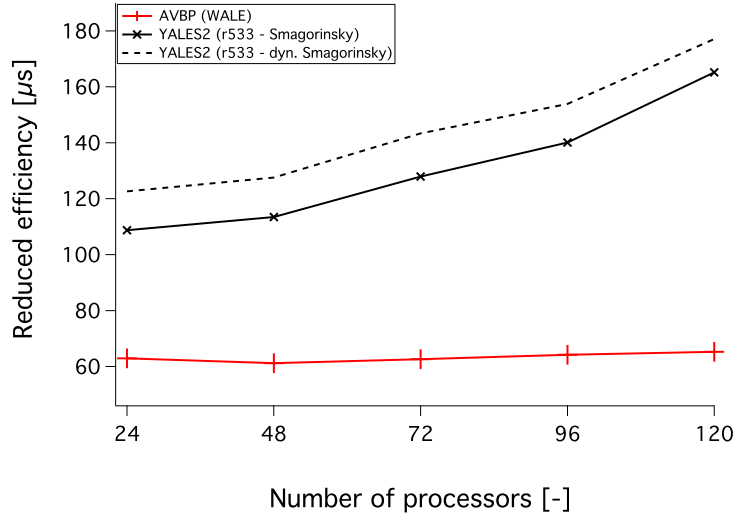


Figure 6.51: Reduced efficiency of AVBP and YALES2 for simulations using mesh 2.

using 64 processors of CORAIL, whereas YALES2 was using 48 processing units. In the case of AVBP the development of the kinetic energy over time is considered one principal convergence criterion. Since the energy equation is solved by AVBP, the mean of this quantity is calculated based on the conservative variables computed during the simulation. In the case of YALES2, the mean average of the kinetic energy is calculated using the L_2 -norm of the velocity. Figure 6.52 presents these graphs for both codes plotted against the physical time of the simulation. The difference in the kinetic energy levels of both solvers corresponds to the value of the density and is due to the conservative formulation of AVBP. This graph confirms that the physics in both simulations evolve at the same rate, indicating that the choice of the compressible or incompressible approach does not impact the development of the flow but the computational efforts needed.

Looking at the same criterion plotted against the number of iterations, see Fig. 6.53, the impact of the larger time-step of the incompressible solver is clearly visible. But keeping in mind the higher price for one iteration using YALES2, as was seen in Figs. 5.7 and 6.51 presenting the reduced efficiency, this must not necessarily mean that the code will attain convergence in a faster time. For the present simulations, the time needed on one processor to obtain a converged solution, i. e. the CPU cost, is presented in Fig. 6.54. The impression obtained for the convergence regarding the number of iterations needed is thus confirmed. For the KIAI burner simulations using CORAIL of CERFACS, the CPU cost for the YALES2 simulation is nine times smaller than for the one done using AVBP.

6.1.7 Conclusions

In part III of the present work, the compressible and the incompressible approach are investigated. This is done using the AVBP code for the compressible computations and

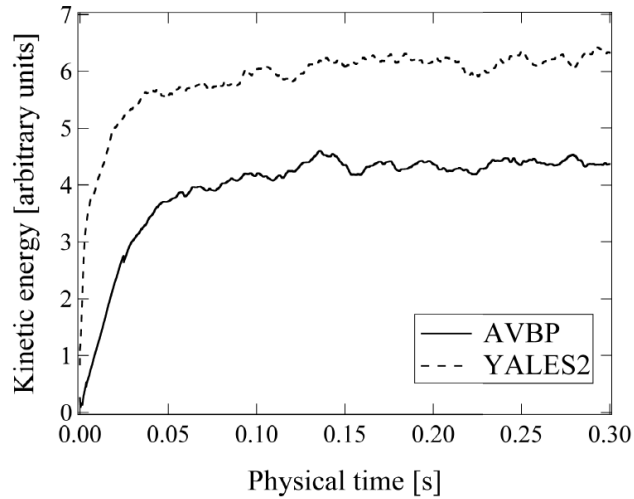


Figure 6.52: Convergence of AVBP and YALES2 determined by the development of the kinetic energy throughout the domain plotted over physical time. This can be interpreted as a confirmation that the physics evolve similarly in both simulations.

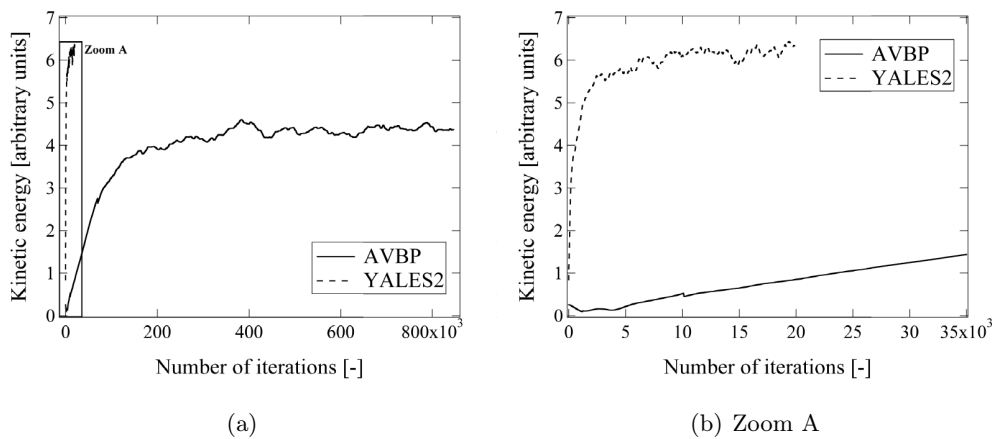


Figure 6.53: Convergence of AVBP and YALES2 determined by the development of the kinetic energy throughout the domain plotted over the number of iterations needed.

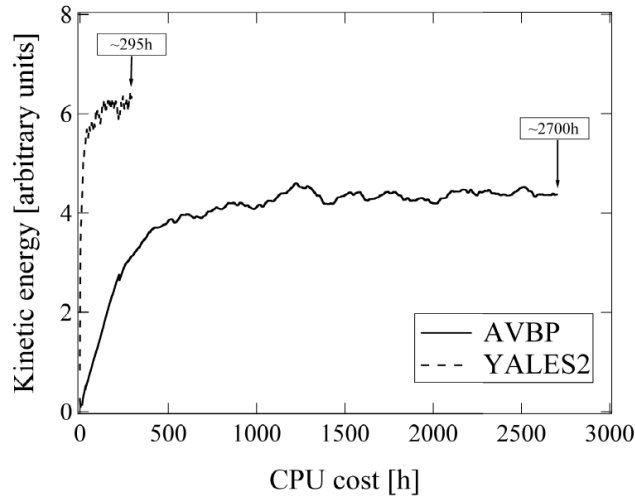


Figure 6.54: Computational cost of AVBP and YALES2. In this case, YALES2 reduces the CPU cost by a factor 9.

the incompressible solver YALES2. Both codes are used to perform simulations of different complexity, of which one is an industrial single-burner configuration, and are then compared in terms of the solver’s performance as well as in terms of accuracy of the produced results.

For the basic test case of the convected vortex, the differences between both solvers are huge. The setup revealed a diffusive (mainly dissipative) behavior of YALES2, even for fourth-order accurate schemes in time and space. Nevertheless, for the complex test case of the KIAI burner, the flow fields reproduced by either code are very similar. Spectral analysis using FFT and the POD method allowed to identify similar energy levels regarding the reproduction of the PVC in both cases. Furthermore, using the acoustic solver AVSP permitted to point out the differences for the acoustics in the solutions of both solvers due to the compressible and the incompressible approaches. Another difference observed are higher RMS values of the pressure for YALES2, see Figs. 6.21 and 6.30. Following, the pressure loss predictions is investigated and the approach using mesh refinement is evaluated and compared to the impact of wall law boundary conditions.

Finally, AVBP and YALES2 are benchmarked in terms of parallelization and also convergence velocity. YALES2 returned results faster than AVBP, as is expected taking into account the time-step size of either solver. The evaluation of the convergence velocity shows that YALES2 reduces significantly the CPU cost for the presented simulations. However, AVBP is more efficient in terms of parallelism for the presented computations.

Part IV

Conclusions and Perspectives

Conclusion and Perspectives

7.1 Conclusions

The present thesis contributes to the field of Large-Eddy Simulation (LES), more precisely to the numerical approaches preferable for this type of simulation. It is the objective to extend and to evaluate the existing methods that are used ultimately for the flow prediction within industrial applications, such as aero-engines. In this respect, the two main focal points are

1. the stability and accuracy of computations and
2. the reduction of simulation time.

Of course, the accuracy of the produced results is a recurring issue for both items. This list also roughly reflects the structure inherent to this document.

In part I the mathematical basics of Computational Fluid Dynamics (CFD) and of LES have been recalled for both, the compressible and the low-Mach number approach. Furthermore, the two state-of-the-art CFD solvers were presented, namely AVBP, which is based on the compressible formulation, and YALES2, which provides the incompressible solver utilized. Their description comprises the discretization of the conservation laws in space and time as well as the approaches deployed to cope with the increasing number of computing nodes on massively parallel architectures.

Part II was dedicated to respond to the first item listed above. The stability in computational simulations is an important factor in many ways. Stability of a numerical scheme is one of the two characteristics ensuring convergence. Of course, rendering a scheme more stable does not allow to reduce the accuracy of the scheme in terms of the produced results. This is a task which becomes rather difficult when combining these demands with the claim for codes, which are capable of taking advantage of modern High Performance (HPC) architectures.

An option is presented in form of a newly developed explicit, high-order family of schemes for time-integration. These schemes, denoted TRK (Two-step Runge-Kutta) schemes, are based on the combination of Runge-Kutta (RK) schemes with Lax-Wendroff (LW) type schemes. The interest is due to the properties of both the RK schemes, which are very little diffusive, and, contrary to that, the LW type schemes. Furthermore, both families of schemes are widely used, especially for their higher-order versions, such as the RK4 or TTG4A. Summing up these qualities by a linear combination, a family of schemes is obtained that provides the same order of accuracy as the schemes, on which it is based. In addition, a parameter allows to adjust the amount of numerical diffusion

added to the simulation by the numerical scheme.

Beginning with the derivation of the scheme for the 1D case for second- and fourth-order accuracy, the mathematical properties and a consistency analysis are presented. Moreover, the implementation of the fourth-order scheme, named TRK4, into AVBP is outlined. Finally, its applicability even to complex geometries and reacting flows is proven on the basis of flow simulation results.

Subsequently, part III refers to the second item, the reduction of simulation time. Different strategies are thinkable to accelerate CFD solvers. Regarding compressible codes, one example is the so-called *cryogenic* approach that consists in increasing artificially the Mach number of a simulation, in order to augment the time step. Of course, a solver adapted to low-Mach number flows, which is the case for many engineering applications, presents an interesting alternative. On this account, a comparison is presented regarding not only the performance achieved with either approach but also a detailed analysis is given in terms of the result's accuracy. The first test case, a convected 2D vortex, is chosen to evaluate the impact of the numerical schemes for each solver. Then the swirled one-burner configuration of the KIAI project of the European Commission is simulated and the results are compared between both codes and with the experimental measurements additionally:

- Although, the numerical setup of YALES2 showed diffusive behavior for the vortex convection compared to AVBP, both solvers returned very similar and also encouraging solutions for the KIAI burner, since they are in very good agreement to the experimental data. The analysis is considering the qualitative and quantitative evaluation of fluctuating and mean quantities, including characteristics such as the swirl number or the prediction of the pressure drop over the swirler. In addition, the results are subjected to a spectral analysis in order to determine the Precessing Vortex Core (PVC) in detail. The spectral analysis allowed to reveal the acoustics contained in the solution of the compressible solver as well as the characteristic frequencies and energy levels of the PVC.
- Concerning the performances of AVBP and YALES2, the results obtained for non-reacting flows are consistent with theory. Due to the acoustics inherent to the compressible equations, AVBP is forced to adapt the time step using stability criteria, mainly the Courant-Friedrichs-Lewy (CFL) condition. Assuming the validity of the incompressible equations for the flow problem in consideration, YALES2 can benefit from the fact that the acoustic field is not present in these conservation laws. Thus, an acceleration of a factor 6 to 36 was recovered, depending on the test configuration in question and the numerical setup of the solver, e. g. using an option such as *cryogenic*.
- A final issue of this comparison is the built-in mesh refinement algorithm of YALES2. It allows the code to homogeneously refine an existing and rather coarse mesh, if certain criteria are met. The influence of the mesh refinement is analyzed especially on the pressure drop prediction within the one-burner configuration. While

the mesh refinement seems interesting for scientific applications, due to the increase in spatial resolution that can be achieved, and for which it has already been used, this option is less applicable from an industrial point of view, since simulations become very expensive and the handling of the solutions requires an adapted infrastructure. For the specific problem of pressure loss predictions and for the configuration considered, a wall law model seems to be the only acceptable approach in term of prediction accuracy and associated computational cost.

7.2 Perspectives

Regarding the time-integration scheme of part II, the results are encouraging, but the implementation in AVBP suffers clearly from the low order of accuracy in space, which is in fact of second-order. To reduce especially the dispersive error, an implementation of the TRK4 scheme in the *finite-element* framework of AVBP was attempted. But applying the mass matrix to the diffusive terms coming from the RK4 scheme turned out problematic for non-linear problems. In this case, no proper formulation was found to factor out the mass matrix, which for the Galerkin-RK4 scheme is applied in every step, without causing an immense growth in memory consumption and simulation time. Hence, the transformation of the TRK4 scheme in AVBP to the *finite-element* formalism is proposed.

Part III showed that the incompressible approach allows to achieve a gain in simulation time without being penalized regarding the quality of the solution. As for pressure drop predictions, mesh quality has not been directly addressed in this work although it is now accepted that too large changes in local grid characteristic size has a great impact on the predictions.

Another interesting issue concerns the performance of the incompressible solver in comparison to the compressible approach. In the present work this question is answered for non-reacting flows only. This evaluation has to be repeated for reacting flows. The interest lies in excluding an impact on the physics, since the characteristics of the flow field are less preferable for numerical simulations, e. g. containing a larger length scale spectrum, steeper gradients and the modeling of chemical reactions.

Explanations for incompressible flow

A.1 Influence of the Mach number on compressibility

The following explanations are based on the generalized Bernoulli equation

$$\int \frac{dp}{\rho} + \frac{u^2}{2} = \text{const.}, \quad (\text{A.1})$$

which, expressed in its differential form, yields

$$\frac{dp}{\rho} + u \cdot du = 0. \quad (\text{A.2})$$

In Eq. (A.2), the first term can be expanded, giving

$$\frac{dp}{\rho} = \left(\frac{dp}{d\rho} \right) \cdot \frac{d\rho}{\rho}. \quad (\text{A.3})$$

When considering small perturbations, their propagation velocity, which in fact is the speed of sound, is defined as

$$c^2|_{s=\text{const.}} = \frac{dp}{d\rho}. \quad (\text{A.4})$$

Combining Eq. (A.2), (A.3) and (A.4) one obtains:

$$\frac{d\rho}{\rho} = -\frac{u}{c^2} \cdot du = -Ma^2 \cdot \frac{du}{u}. \quad (\text{A.5})$$

Equation (A.5) links the relative change in density to the square of the Mach number. It is generally accepted that for $Ma^2 \leq 0.1$, i. e. $Ma \leq 0.3$, a flow can be seen as incompressible.

A.2 Derivation of the incompressible conservation equations

Based on the compressible Navies-Stokes equations (2.8),(2.9) and (2.10), different approaches can be used to develop the mathematical model for incompressible flows. One very popular way is to follow the physical explanation for flows within the incompressible limit presented in section 1.4, i. e. to consider the mass density as constant. Applying this assumption to the continuity equation (2.8) and the momentum equation (2.9), one obtains the incompressible conservation equations (2.12) and (2.13). Despite the correct set of equations, this approach can be misleading on the true nature of the pressure term occurring, as pointed out by [Meister 2002]. In order to reveal the hydrodynamic role taken by the pressure term in the incompressible limit (see section 2.1.5), the development of the incompressible Navier-Stokes equations is recalled here using an asymptotic expansion in powers of the global Mach number M_∞ following [Klainerman 1982].

At first, the Eqs. (2.8) - (2.10) are non-dimensionalized using reference values for length, mass density, flow velocity, pressure and energy:

$$x = x_\infty \cdot x^*, \quad (\text{A.6})$$

$$\rho = \rho_\infty \cdot \rho^*, \quad (\text{A.7})$$

$$\mathbf{u} = \mathbf{u}_\infty \cdot \mathbf{u}^*, \quad (\text{A.8})$$

$$P = \rho_\infty c_\infty^2 \cdot P^*. \quad (\text{A.9})$$

$$E = c_\infty^2 \cdot E^*. \quad (\text{A.10})$$

The quantities with the index ∞ represent the reference value and the superscript $*$ stands for the non-dimensionalized values. With the help of the Eqs. A.6 - A.10, the Navier-Stokes equations yield:

$$\frac{\partial \rho^*}{\partial t} + \nabla \cdot (\rho^* \mathbf{u}^*) = 0, \quad (\text{A.11})$$

$$\frac{\partial (\rho^* \mathbf{u}^*)}{\partial t} + \nabla \cdot ((\rho^* \mathbf{u}^*) \circ \mathbf{u}^*) = -\frac{1}{M_\infty^2} \nabla P^* + \frac{1}{Re} \nabla \cdot \tau^*, \quad (\text{A.12})$$

$$\begin{aligned} \frac{\partial P^*}{\partial t} + \mathbf{u}^* \cdot \nabla P^* + \gamma P^* \nabla \cdot \mathbf{u}^* &= \frac{(\gamma - 1)}{RePr} \nabla \cdot \mathbf{q}^* \\ &+ \frac{M_\infty^2 (\gamma - 1)}{Re} (\nabla \cdot (\tau^* \mathbf{u}^* - \mathbf{u}^* \nabla \cdot \tau^*)). \end{aligned} \quad (\text{A.13})$$

This transformation makes appear the Reynolds number Re , the Prandtl number Pr and the Mach number M_∞ . The latter one is defined as:

$$M_\infty = \frac{\mathbf{u}_\infty}{c_\infty}, \quad (\text{A.14})$$

with $c_\infty = \sqrt{(\gamma p)/\rho}$ being the reference speed of sound. Furthermore, the equation of state (2.11) reads in its non-dimensionalized form:

$$P^* = \rho^* (\gamma - 1) \left(E^* - \frac{1}{2} M_\infty^2 \mathbf{u} \right). \quad (\text{A.15})$$

The most important observation is the appearance of the factor $(M_\infty)^{-2}$ in Eq. (A.12), leading to a singularity when the Mach number reaches $M_\infty = 0$. With this it becomes obvious that the physical interpretation of the pressure has to change from a thermodynamic variable towards an "incompressible" one. This behavior cannot be explained when deriving the incompressible conservation equations only based on the assumption $\rho = \text{const.}$

For simplicity reasons, the viscous terms and the heat flux in Eqs. (A.11) - (A.13) are neglected in the following. In order to acquire a better understanding, the non-dimensionalized quantities mass density, pressure, velocity and energy are developed in asymptotic expansions as expressed in the following:

$$\rho^* = \rho^{*(0)} + M_\infty \rho^{*(1)} + M_\infty^2 \rho^{*(2)} + \mathcal{O}(M^2) , \quad (\text{A.16})$$

$$\mathbf{u}^* = \mathbf{u}^{*(0)} + M_\infty \mathbf{u}^{*(1)} + M_\infty^2 \mathbf{u}^{*(2)} + \mathcal{O}(M^2) . \quad (\text{A.17})$$

$$P^* = P^{*(0)} + M_\infty P^{*(1)} + M_\infty^2 P^{*(2)} + \mathcal{O}(M^2) , \quad (\text{A.18})$$

$$\mathbf{E}^* = \mathbf{E}^{*(0)} + M_\infty \mathbf{E}^{*(1)} + M_\infty^2 \mathbf{E}^{*(2)} + \mathcal{O}(M^2) . \quad (\text{A.19})$$

In case of the pressure, the term $P^{*(0)}$ is considered the thermodynamic or background pressure, $P^{*(1)}$ represents acoustic perturbations and $P^{*(2)}$ is interpreted as a hydrodynamic quantity. Inserting the relations (A.16) - (A.19) into Eqs. (A.11) - (A.13) and considering the global Mach number tending towards $M_\infty \rightarrow 0$ leads to the following conclusions:

1. The velocity divergence can be defined with the help of the continuity equation (A.11):

$$\nabla \cdot \mathbf{u}^{*(0)} = -\frac{1}{\rho_0} \frac{D\rho_0}{Dt} .$$

2. The pressure gradient term in Eq. (A.12) requires the background pressure to be constant in space in order to prevent singular behavior of the momentum equation due to the factor $(M_\infty)^{-2}$, i. e.:

$$\nabla P^{*(0)} = 0 .$$

3. For the same reason acoustic perturbations must not occur in space:

$$\nabla P^{*(1)} = 0 .$$

4. The equation of state (A.15) yields:

$$P^{*(0)} = \rho^{*(0)} (\gamma - 1) E^{*(0)} .$$

Points 2 and 3 of this list clearly show that the role of the pressure term in the momentum equation for the incompressible limit changes into a hydrodynamic variable. The equation of state in point 4 indicates that, if the thermodynamic pressure and the energy do not vary in space and time, density will be constant. As a consequence, the velocity divergence given in point 1 will be zero. These considerations then lead to the incompressible Navier-Stokes equations (2.12) and (2.13).

Application of the TRK4 time integration in AVBP to the KIAI burner

A condition for the comparison of the compressible and the incompressible approach, presented in part III, is to choose the best option available without violating the assumption to keep the setup equivalent wherever possible. For the choice of the numerical scheme this clearly leads to the use of one of the TTG schemes, in this case TTG4A (see section 3). Nevertheless, this test case is also used to show the applicability of the newly introduced TRK4 scheme for such configurations. The comparison is restricted to the mean flow field and the results are presented in comparison to the TTG4A solutions as well as the experimental data.

In the case of TTG4A artificial viscosity based on the Colin sensor [CERFACS 2009] is applied. Conversely to this, for the TRK4 simulations no artificial viscosity was added. It has to be kept in mind, though, that TRK4 in AVBP is more dissipative compared to the TTG schemes because it uses the classical second-order stencil in space of the cell-vertex discretization, see part II. The parameter to adjust the incorporated numerical viscosity of this scheme is set to $\alpha = 0.8$.

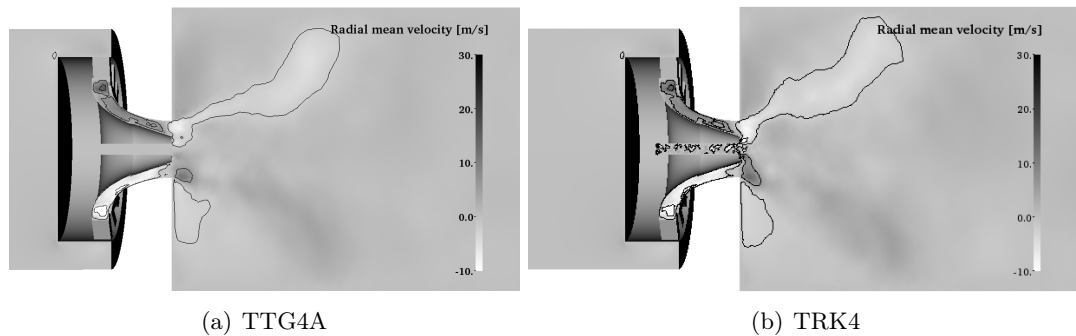


Figure B.1: Sectional drawing for the plane at $y=0$. Pseudocolor and iso-lines of radial mean velocity for $-10 \frac{m}{s} \leq \langle u_x \rangle \leq 30 \frac{m}{s}$.

The mean flow field, which is presented in Figs. B.1 - B.2, of the one-burner configuration is very similar for both schemes for the combustion chamber. In the case of TRK4 radial and tangential contributions occur in the central injection, which are due to the smaller amount of numerical viscosity added to the simulation and the properties of the scheme

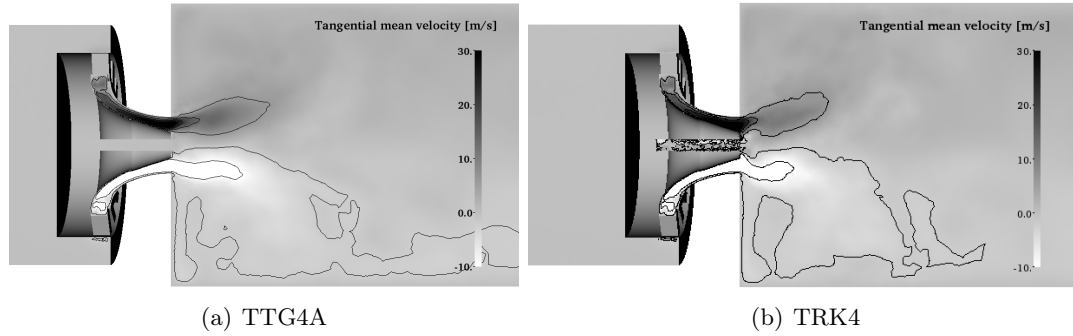


Figure B.2: Sectional drawing for the plane at $y=0$. Pseudocolor and iso-lines of tangential mean velocity for $-10 \frac{m}{s} \leq \langle u_y \rangle \leq 30 \frac{m}{s}$.

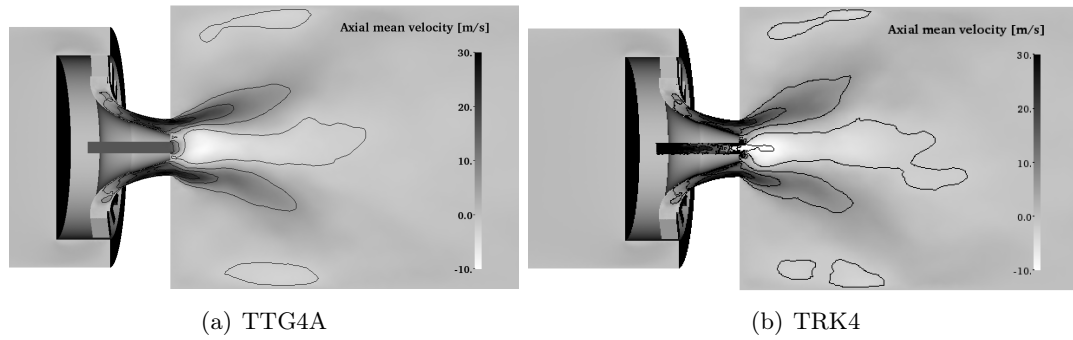


Figure B.3: Sectional drawing for the plane at $y=0$. Pseudocolor and iso-lines of mean axial velocity for $-10 \frac{m}{s} \leq \langle u_z \rangle \leq 30 \frac{m}{s}$.

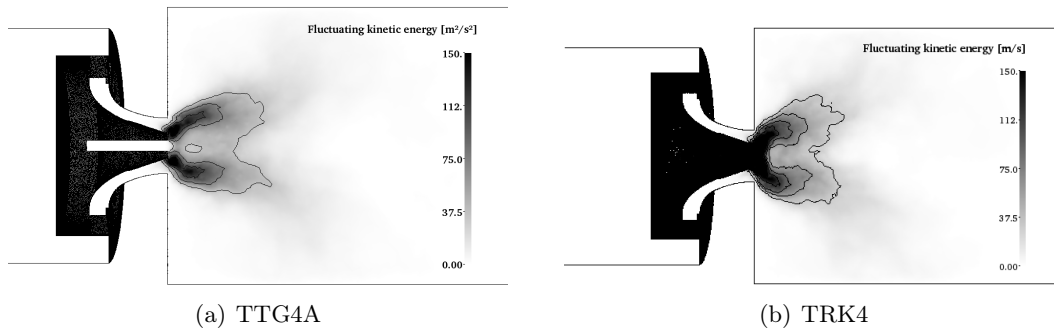


Figure B.4: Sectional drawing for the plane at $y=0$. Pseudocolor and iso-lines of the fluctuating kinetic energy.

in AVBP. The fluctuating kinetic energy is plotted in Fig. (B.4) and reveals much larger differences, mainly for the central injection. The observations made for the snapshots of the mean quantities are verified by the profiles of the mean and the RMS values in Figs. B.7 - B.10.

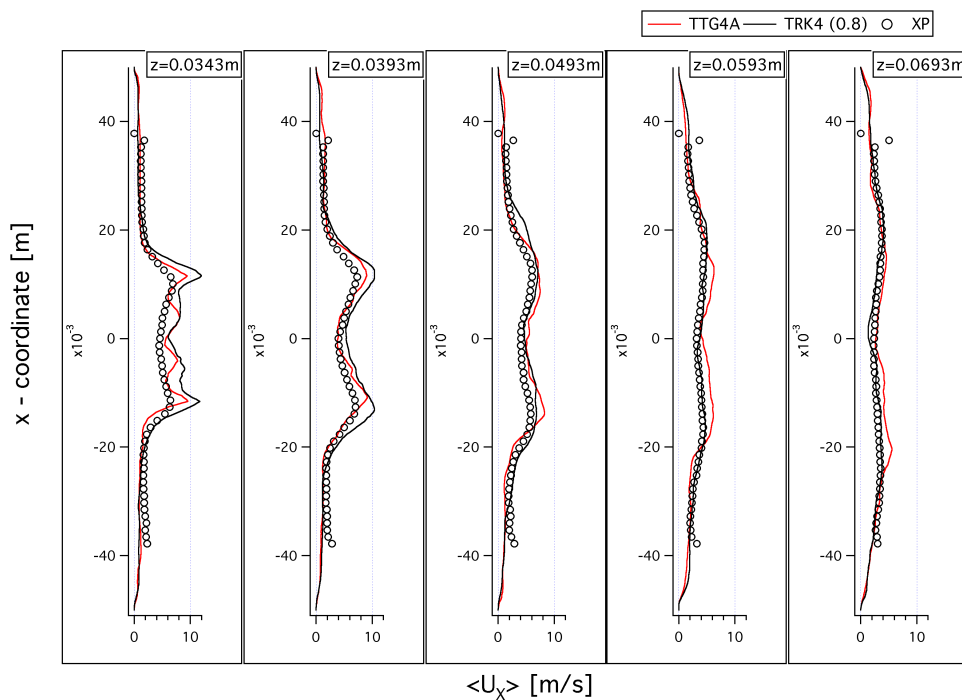


Figure B.5: Mean profiles of the radial velocity $\langle u_x \rangle$.

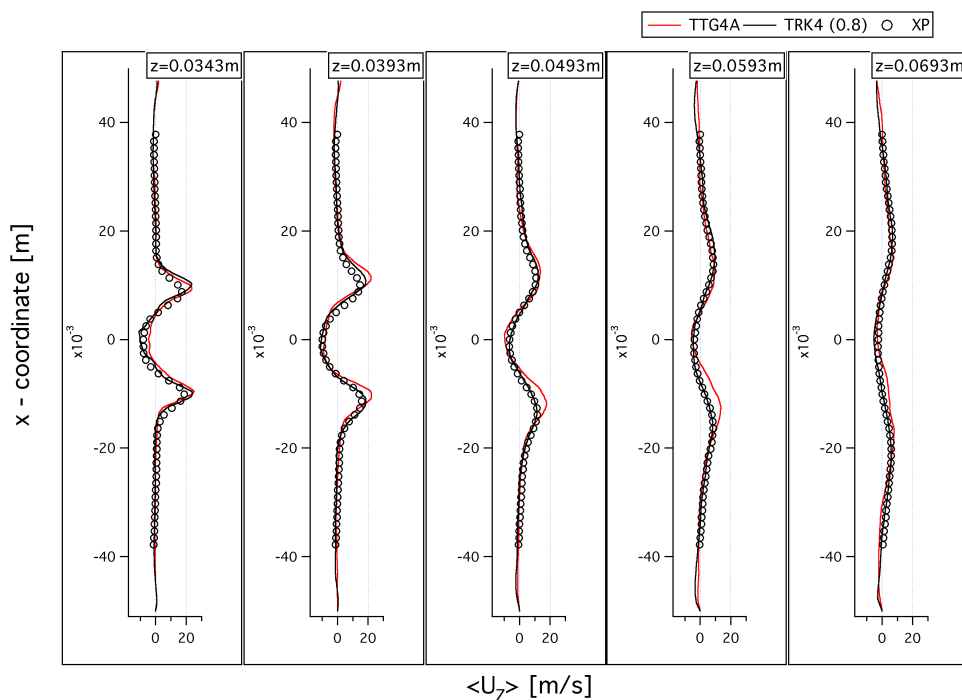


Figure B.6: Mean profiles of the axial velocity $\langle u_z \rangle$.

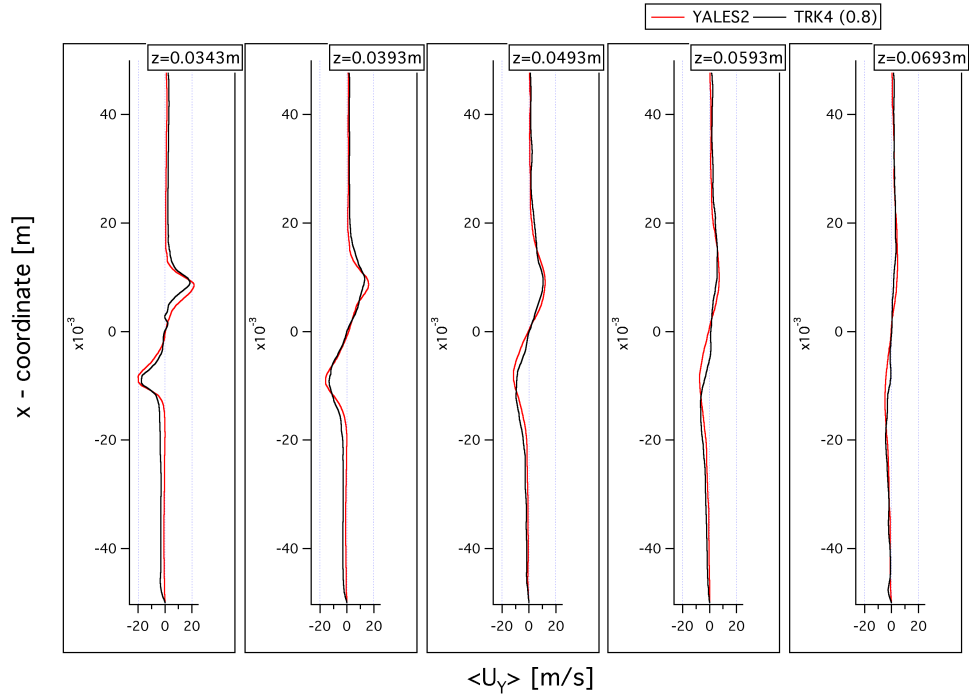


Figure B.7: Mean profiles of the tangential velocity $\langle u_y \rangle$.

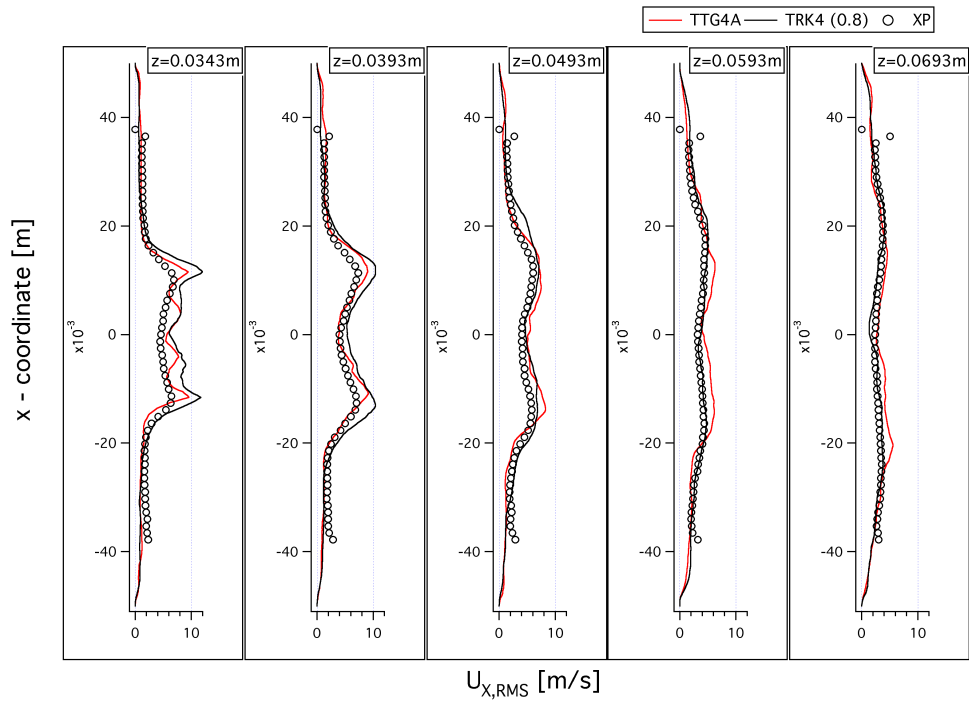


Figure B.8: Profiles of the radial velocity fluctuations $u_{x,RMS}$.

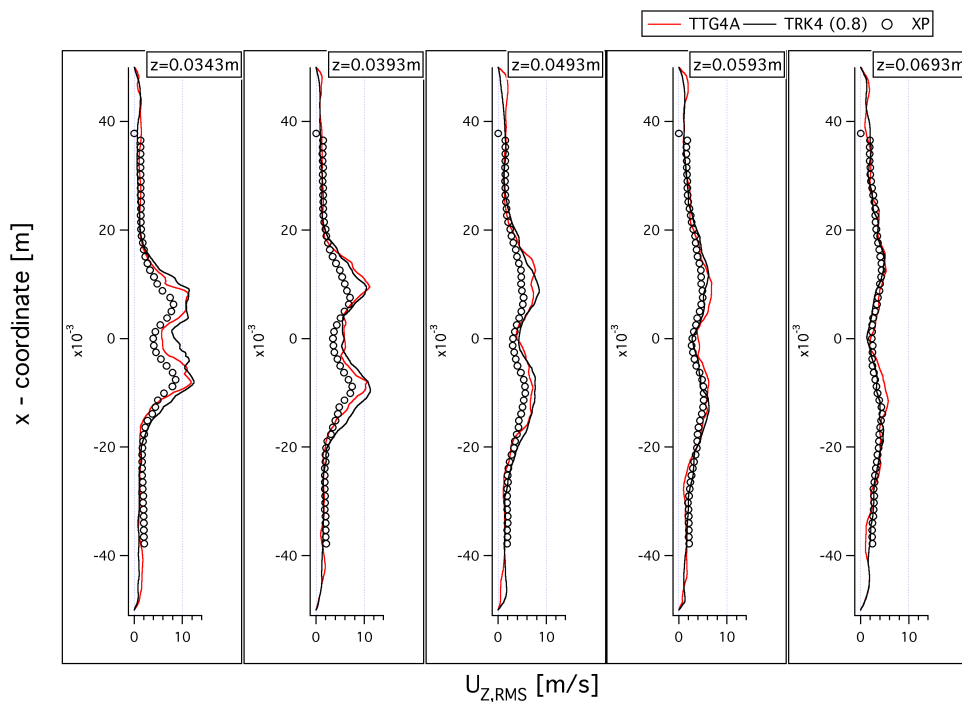


Figure B.9: Profiles of the axial velocity fluctuations $u_{z,RMS}$.

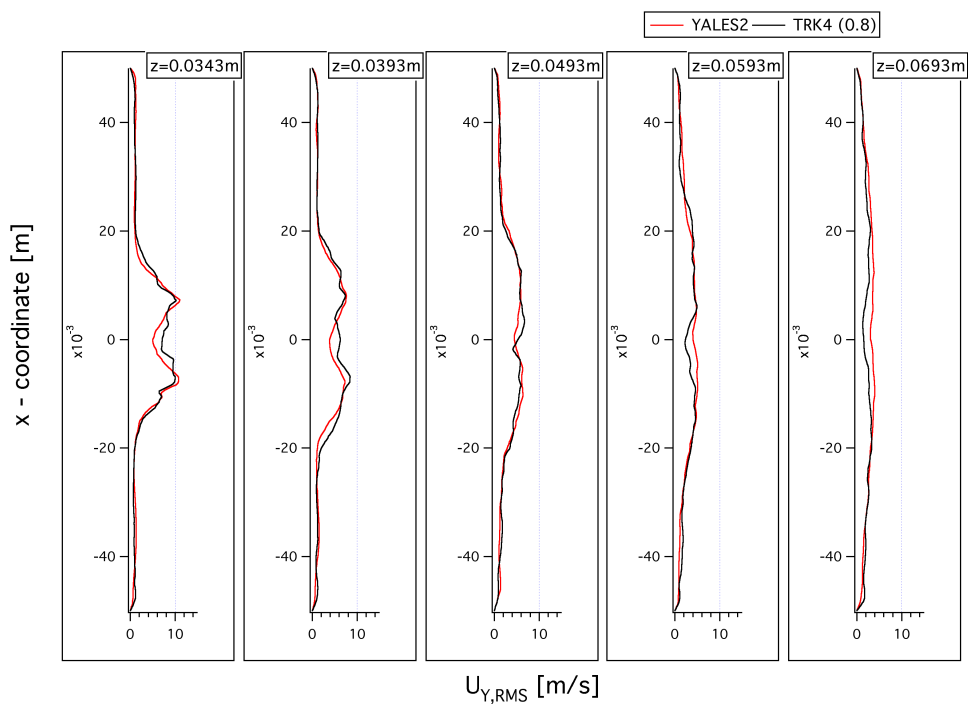


Figure B.10: Profiles of the tangential velocity fluctuations $u_{y,RMS}$.

Bibliography

- [Amaya 2010] J. Amaya, E. Collado, B. Cuenot and T. Poinsot. *Coupling LES, radiation and structure in gas turbine simulations*. In NASA Ames/Stanford Univ. Center for Turbulence Research, editeur, Proc. of the Summer Program , volume in press, 2010. (Cited on page 4.)
- [Amdahl 1967] Gene M. Amdahl. *Validity of the single processor approach to achieving large scale computing capabilities*. In Proceedings of the April 18-20, 1967, spring joint computer conference, AFIPS '67 (Spring), pages 483–485, New York, NY, USA, 1967. ACM. (Cited on page 133.)
- [Barré 2011] D. Barré, M. Kraushaar, G. Staffelbach, V. Moureau and L.Y.M. Gicquel. *Compressible and incompressible LES of a swirl experimental burner*. 3rd INCA Colloquium, 2011. (Cited on pages 125 and 128.)
- [Benoit 2005] L. Benoit. *Prédiction des instabilités thermo-acoustiques dans les turbines à gaz*. Phd thesis, University Montpellier II, 2005. (Cited on page 106.)
- [Berkooz 1993] G. Berkooz, P. Holmes and J. L. Lumley. *The proper orthogonal decomposition in the analysis of turbulent flows*. Annual Review of Fluid Mechanics, vol. 25, pages 539–575, 1993. (Cited on page 108.)
- [Berland 007] Julien Berland, Christophe Bogey, Olivier Marsden and Christophe Bailly. *High-order, low dispersive and low dissipative explicit schemes for multiple-scale and boundary problems*. Journal of Computational Physics, vol. 224, no. 2, pages 637–662, JUN 10 2007. (Cited on page 51.)
- [Bogey 004] C Bogey and C Bailly. *A family of low dispersive and low dissipative explicit schemes for flow and noise computations*. Journal of Computational Physics, vol. 194, no. 1, pages 194–214, FEB 10 2004. (Cited on page 51.)
- [Boileau 2008] M. Boileau, G. Staffelbach, B. Cuenot, T. Poinsot and C. Bérat. *LES of an ignition sequence in a gas turbine engine*. Combust. Flame , vol. 154, no. 1-2, pages 2–22, 2008. (Cited on pages 3 and 18.)
- [Boudier 2007] G. Boudier, L. Y. M. Gicquel, T. Poinsot, D. Bissières and C. Bérat. *Comparison of LES, RANS and Experiments in an Aeronautical Gas Turbine Combustion Chamber*. Proc. Combust. Inst. , vol. 31, pages 3075–3082, 2007. (Cited on page 18.)
- [Boudier 2009] G. Boudier, N. Lamarque, G. Staffelbach, L.Y.M. Gicquel and T. Poinsot. *Thermo-acoustic stability of a helicopter gas turbine combustor using large-eddy simulations*. Int. Journal Aeroacoustics, vol. 8, no. 1, pages 69–94, 2009. (Cited on page 18.)

- [Boussinesq 1877] J. Boussinesq. *Essai sur la théorie des eaux courantes*. 26ème éd. Acad. Sci. Paris, 1877. (Cited on page 23.)
- [CERFACS 2009] CERFACS. *AVBP Handbook* - http://cerfacs.fr/~avbp/AVBP_V5.X/HANDBOOK. CERFACS, 2009. (Cited on page 147.)
- [Chatterjee 2000] Anindya Chatterjee. *An introduction to the proper orthogonal decomposition*. Current Science, vol. 78, no. 7, pages 808–817, 2000. (Cited on pages 108 and 118.)
- [Chorin 1968] A. J. Chorin. *Numerical solution of the Navier-Stokes equations*. Mathematics of Computation, vol. 22, no. 104, pages 745–762, 1968. (Cited on page 43.)
- [Colin 2000a] O. Colin, F. Ducros, D. Veynante and T. Poinso. *A thickened flame model for large eddy simulations of turbulent premixed combustion*. Phys. Fluids , vol. 12, no. 7, pages 1843–1863, 2000. (Cited on page 72.)
- [Colin 2000b] O. Colin and M. Rudgyard. *Development of high-order Taylor-Galerkin schemes for unsteady calculations*. J. Comput. Phys. , vol. 162, no. 2, pages 338–371, 2000. (Cited on pages 31, 34, 51 and 68.)
- [Cook 2004] A.W. Cook and W.H. Cabot. *A high-wavenumber viscosity for high-resolution numerical methods*. Journal of Computational Physics, vol. 195, no. 2, pages 594–601, 2004. (Cited on page 51.)
- [Crumpton 1993] P. I. Crumpton, J. A. Mackenzie and K. W. Morton. *Cell vertex algorithms for the compressible Navier-Stokes equations*. J. Comput. Phys. , vol. 109, pages 1–15, 1993. (Cited on page 31.)
- [Deardorff 1970] J. Deardorff. *A numerical study of three-dimensional turbulent channel flow at large Reynolds numbers*. J. Fluid Mech. , vol. 41, pages 453–480, 1970. (Cited on page 18.)
- [Donea 1984] J. Donea. *Taylor-Galerkin Method for Convective Transport Problems*. Int. J. Numer. Meth. Fluids , vol. 20, no. 1, pages 101–119, 1984. (Cited on pages 31 and 34.)
- [Donea 2003] J. Donea and A. Huerta. *Finite Element Methods for Flow Problems*. Wiley, 2003. (Cited on pages 32 and 44.)
- [Dongarra 1988] Jack Dongarra. *The LINPACK Benchmark: An Explanation*. In Proceedings of the 1st International Conference on Supercomputing, pages 456–474, London, UK, 1988. Springer-Verlag. (Cited on page 5.)
- [Favre 1969] A. Favre. *Statistical equations of turbulent gases*. In Problems of hydrodynamics and continuum mechanics, pages 231–266. SIAM, Philadelphia, 1969. (Cited on page 19.)

- [Ferziger 2002] J. H. Ferziger and M. Perić. Computational methods for fluid dynamics. Springer, 3rd édition, 2002. (Cited on pages 23, 57 and 58.)
- [Fletcher 1991] C. A. J. Fletcher. Computational techniques for fluid dynamics, volume 1. Springer, 2nd édition, 1991. (Cited on page 32.)
- [Franzelli 2010] B. Franzelli, E. Riber, M. Sanjosé and T. Poinsot. *A two-step chemical scheme for kerosene-air premixed flames*. Combustion and Flame, vol. 157, no. 7, pages 1364–1373, 2010. (Cited on page 72.)
- [Franzelli 2011] Benedetta Franzelli. *Impact of the chemical description on Direct Numerical Simulation and Large-Eddy Simulation of turbulent combustion in industrial aero-engines*. PhD thesis, Université de Toulouse, France - MeGeP Dynamique des Fluides, 2011. (Cited on page 4.)
- [Garcia 2009] Marta Garcia. *Développement et validation du formalisme Euler-Lagrange dans un solveur parallèle et non-structuré pour la simulation aux grandes échelles*. PhD thesis, INP Toulouse, 2009. (Cited on pages 18, 27 and 36.)
- [Germano 1991] M. Germano, U. Piomelli, P. Moin and W. Cabot. *A dynamic subgrid-scale eddy viscosity model*. Phys. Fluids , vol. 3, no. 7, pages 1760–1765, 1991. (Cited on page 23.)
- [Germano 1992] M. Germano. *Turbulence: the filtering approach*. J. Fluid Mech. , vol. 238, pages 325–336, 1992. (Cited on page 23.)
- [Ghosal 1995] S. Ghosal and P. Moin. *The basic equations for the large eddy simulation of turbulent flows in complex geometry*. J. Comput. Phys. , vol. 118, pages 24 – 37, 1995. (Cited on page 19.)
- [Gicquel 2011] L.Y.M. Gicquel, N. Gourdain, J.-F. Boussuge, H. Deniau, G. Staffelbach, P. Wolf and T. Poinsot. *High performance parallel computing of flows in complex geometries*. Comptes Rendus de l'Académie des Sciences - Mathématiques, vol. 339, pages 104–124, 2011. (Cited on pages 7 and 36.)
- [Giles 1991] M. Giles. *UNSFLO: A Numerical Method for Unsteady Inviscid Flow in Turbomachinery*. Tech. Rep. GTL 205, MIT - Gas Turbine Laboratory, 1991. (Cited on page 31.)
- [Gourdain 2009a] N Gourdain, L Gicquel, M Montagnac, O Vermorel, M Gazaix, G Staffelbach, M Garcia, JF Boussuge and T Poinsot. *High performance parallel computing of flows in complex geometries: I. Methods*. Comput. Sci. Disc., vol. 2, page 015003, 2009. (Cited on pages 7 and 133.)
- [Gourdain 2009b] N Gourdain, L Gicquel, M Montagnac, O Vermorel, M Gazaix, G Staffelbach, M Garcia, JF Boussuge and T Poinsot. *High performance parallel computing of flows in complex geometries: II - applications*. Comput. Sci. Disc., vol. 2, page 015004, 2009. (Cited on page 7.)

- [Granet 2010] V. Granet, O. Vermorel, T. Leonard, L. Gicquel, and T. Poinso. *Comparison of Nonreflecting Outlet Boundary Conditions for Compressible Solvers on Unstructured Grids*. AIAA Journal , vol. 48, no. 10, pages 2348–2364, 2010. (Cited on pages 35 and 66.)
- [Gullaude 2010] E. Gullaude. *Impact des plaques multiperforées sur l'acoustique des chambres de combustion aéronautiques*. PhD thesis, Université Montpellier II - DOCTORALE ISS: Spécialité Mathématiques et Modélisation, 2010. (Cited on page 106.)
- [Gupta 1985] A. K. Gupta, D. G. Lilley and Nick Syred. *Swirl Flows*. ABACUS Press, Cambridge, USA, 1985. (Cited on page 97.)
- [Hall 1984] M.G. Hall. *Cell vertex multigrid solution of the Euler equations for transonic flow past aerofoils*. Rapport technique, Royal Aerospace Establishment, 1984. NLnum2. (Cited on pages 26 and 31.)
- [Ham 2003] F. Ham, S. V. Apte, G. Iaccarino, X. Wu, M. Herrmann, G. Constantinescu, K. Mahesh and P. Moin. *Unstructured LES of reacting multiphase flows in realistic gas turbine combustors*. In Annual Research Briefs , pages 139–160. Center for Turbulence Research, NASA Ames/Stanford Univ., 2003. (Cited on page 18.)
- [Hirsch 1988] C. Hirsch. Numerical computation of internal and external flows. John Wiley, New York, 1988. (Cited on pages 25, 30, 35, 44, 51, 53, 57 and 60.)
- [Holmes 1996] P. Holmes, J.L. Lumley and G. Berkooz. Turbulence, coherent structures, dynamical systems and symmetry. Cambridge Monographs on Mechanics. Cambridge University Press, 1996. (Cited on page 108.)
- [Huang 2006] Y. Huang, S. Wang and V. Yang. *Systematic analysis of lean-premixed swirl-stabilized combustion*. AIAA Journal , vol. 44, no. 724-740, 2006. (Cited on page 108.)
- [Hunt 1988] J. C. R. Hunt, A. A. Wray and P. Moin. *Eddies, streams, and convergence zones in turbulent flows*. In Proc. of the Summer Program , pages 193–208. Center for Turbulence Research, NASA Ames/Stanford Univ., 1988. (Cited on page 106.)
- [Hussain 1995] F. Hussain and J. Jeong. *On the identification of a vortex*. J. Fluid Mech. , vol. 285, pages 69–94, 1995. (Cited on page 105.)
- [James 2006] S. James, J. Zhu and M. Anand. *Large eddy simulation as a design tool for gas turbine combustion systems*. AIAA Journal , vol. 44, pages 674–686, 2006. (Cited on page 18.)
- [Jeong 1995] J. Jeong and F. Hussain. *On the identification of a vortex*. Journal of Fluid Mechanics, vol. 285, pages 69–94, 1995. (Cited on pages 63 and 68.)

- [Karhunen 1946] K. Karhunen. *Zur Spektraltheorie stochastischer Prozesse*. Annales Academiae Scientiarum Fennicae A, vol. 37, 1946. (Cited on page 108.)
- [Karypis 1995] George Karypis and Vipin Kumar. *METIS - Unstructured Graph Partitioning and Sparse Matrix Ordering System, Version 2.0*. Rapport technique, University of Minnesota, Department of Computer Science, 1995. (Cited on page 45.)
- [Keyes 1997] David E. Keyes, Dinesh K. Kaushik, Barry and F. Smith. *Prospects for CFD on Petaflops Systems*. In CFD Review, pages 1079–1096. Wiley, 1997. (Cited on page 6.)
- [Kim 1985] J. Kim and P. Moin. *Application of a fractional-step method to incompressible Navier-Stokes equations*. J. Comput. Phys. , vol. 59, no. 2, pages 308–323, 1985. (Cited on page 43.)
- [Klainerman 1982] Sergiu Klainerman and Andrew Majda. *Compressible and incompressible fluids*. Communications on Pure and Applied Mathematics, vol. 35, no. 5, pages 629–651, 1982. (Cited on page 144.)
- [Kolmogorov 1941] A. N. Kolmogorov. *The local structure of turbulence in incompressible viscous fluid for very large Reynolds numbers*. C. R. Acad. Sci. , USSR, vol. 30, page 301, 1941. (Cited on page 23.)
- [Kunt 1981] M. Kunt. *Traitement numérique des signaux*. Traité d'électricité, d'électronique et d'électrotechnique. Dunod, 1981. (Cited on page 109.)
- [Kutta 1901] W. Kutta. *Beitrag zur näherungsweise Integration totaler Differentialgleichungen (German)*. Z. Math. Phys., vol. 46, pages 435–453, 1901. (Cited on page 51.)
- [Lamarque 2007] N. Lamarque. *Schémas numériques et conditions limites pour la simulation aux grandes échelles de la combustion diphasique dans les foyers d'hélicoptère*. Phd thesis, INP Toulouse, 2007. (Cited on pages 25, 26, 28, 30, 33, 34, 35, 57 and 72.)
- [Launder 1972] B.E. Launder and D.B. Spalding. *Mathematical models of turbulence*. Academic Press, 1972. (Cited on page 3.)
- [Lax 1956] P. D. Lax and R. D. Richtmyer. *Survey of the stability of linear finite difference equations*. Communications on Pure and Applied Mathematics, vol. 9, no. 2, pages 267–293, 1956. (Cited on page 55.)
- [Lax 1960] P. D. Lax and B. Wendroff. *Systems of conservation laws*. Commun. Pure Appl. Math. , vol. 13, pages 217–237, 1960. (Cited on page 30.)
- [Lax 1964] P. D. Lax and B. Wendroff. *Difference schemes for hyperbolic equations with high order of accuracy*. Commun. Pure Appl. Math. , vol. 17, pages 381–398, 1964. (Cited on page 30.)

- [Leonard 1974] A. Leonard. *Energy cascade in large eddy simulations of turbulent fluid flows*. Adv. Geophys., vol. 18, no. A, pages 237–248, 1974. (Cited on pages 19 and 22.)
- [Leonard 1995] A. Leonard. *Direct numerical simulation*. In T. Gatski, editeur, Turbulence and its Simulations, 1995. (Cited on page 3.)
- [Léonard 2010] T. Léonard, F. Duchaine, N. Gourdain and L.Y.M. Gicquel. *Steady/Unsteady Reynolds Averaged Navier-Stokes and Large Eddy Simulations of a turbine blade at high subsonic outlet Mach number*. In Proceedings of the ASME TURBO EXPO 2010 Gas Turbine Technical Congress & Exposit, Glasgow, UK, 2010. (Cited on page 68.)
- [Lilly 1967] D. K. Lilly. *The representation of small-scale turbulence in numerical simulation experiments*. In Proceedings of the IBM Scientific Computing Symposium on Environmental Sciences, Yorktown Heights, USA, 1967. (Cited on page 18.)
- [Lilly 1992] D. K. Lilly. *A proposed modification of the germano sub-grid closure method*. Phys. Fluids , vol. 4, no. 3, pages 633–635, 1992. (Cited on pages 23 and 63.)
- [Loève 1945] M. M. Loève. *Functions aleatoire de second ordre*. Comptes Rendus de l’Académie des Sciences, vol. 220, 1945. (Cited on page 108.)
- [Lumley 1967] J. L. Lumley. *The Structure of Inhomogeneous Turbulent Flows*. In A. M. Yaglom and V. I. Tatarski, editeurs, Atmospheric turbulence and radio propagation, pages 166–178. Nauka, Moscow, 1967. (Cited on page 108.)
- [Mason 1994] P. J. Mason. *Large-eddy simulation: a critical review of the technique*. Quarterly Journal of the Royal Meteorology Society, vol. 120 (A), no. 515, pages 1–26, 1994. (Cited on page 18.)
- [Medic 2006] G. Medic, G. Kalitzin, D. You, M. Herrmann, F. Ham, E. van der Weide, H. Pitsch and J. Alonso. *Integrated RANS/LES computations of turbulent flow through a turbofan jet engine*. In Annual Research Briefs , pages 275–285. Center for Turbulence Research, NASA Ames/Stanford Univ., 2006. (Cited on page 4.)
- [Meister 2002] A. Meister and J. Struckmeier. *Hyperbolic partial differential equations: theory, numerics and applications*. Vieweg, 2002. (Cited on pages 7 and 144.)
- [Moin 1982] P. Moin and J. Kim. *Numerical investigation of turbulent channel flow*. J. Fluid Mech. , vol. 118, pages 341–377, 1982. (Cited on page 18.)
- [Moore 1965] Gordon E. Moore. *Cramming more components onto integrated circuits*. Electronics, vol. 38, no. 8, April 1965. (Cited on page 5.)
- [Morton 1988] K.W. Morton. *Finite Volume and Finite Element Methods for the Steady Euler Equations of Gas Dynamics*. In The Mathematics of Finite Elements and Applications VI : MAFELAP 1987, pages 353–378. J.R. Whiteman, 1988. NLnum2. (Cited on page 26.)

- [Morton 1997] K. W. Morton, M. Stynes and E. Süli. *Analysis of a cell-vertex finite volume method for convection-diffusion problems*. Math. Comp. , vol. 66, no. 220, pages 1389–1406, 1997. (Cited on page 26.)
- [Moureau 2010a] V. Moureau, P. Domingo, L. Vervisch and D. Veynante. *DNS analysis of a $Re=40000$ swirl burner*. In NASA Ames/Stanford Univ. Center for Turbulence Research, editeur, Proc. of the Summer Program , volume in press, 2010. (Cited on pages 45 and 131.)
- [Moureau 2010b] V. Moureau, J. P. Frenillot, G. Cabot, B. Renou, A. Vandell, M. Boukhalfa, G. Lartigue, G. Ribert, P. Domingo and L. Vervisch. Rapport sur les calculs d’allumage de la configuration expérimentale du projet KIAI. Livrable de la thèse CIFRE Snecma de J.P Frenillot, 2010. (Cited on pages 129 and 130.)
- [Moureau 2011a] V. Moureau. *YALES2 Public Page*, 2011. (Cited on page 45.)
- [Moureau 2011b] V. Moureau, P. Domingo and L. Vervisch. *Design of a massively parallel CFD code for complex geometries*. Comptes Rendus Mécanique, vol. 339, no. 2-3, pages 141–148, 2011. (Cited on pages 37 and 45.)
- [Moureau 2011c] V. Moureau, P. Domingo and L. Vervisch. *From Large-Eddy Simulation to Direct Numerical Simulation of a lean premixed swirl flame: Filtered laminar flame-PDF modeling*. Combustion and Flame, vol. 158, no. 7, pages 1340 – 1357, 2011. (Cited on pages 37 and 45.)
- [Moureau 2011d] V. Moureau and G. Lartigue. *Private Communication*, August 2011. (Cited on pages 38 and 131.)
- [Munz 2006] Claus-Dieter Munz and Thomas Westermann. Numerische Behandlung gewöhnlicher und partieller Differenzialgleichungen. Springer Berlin Heidelberg, 2006. (Cited on page 44.)
- [Ni 1982] R.-H. Ni. *A multiple grid scheme for solving the Euler equations*. Am. Inst. Aeronaut. Astronaut. J. , vol. 20, pages 1565–1571, 1982. (Cited on pages 26 and 31.)
- [Nicoud 1999] F. Nicoud and F. Ducros. *Subgrid-scale stress modelling based on the square of the velocity gradient*. Flow, Turb. and Combustion , vol. 62, no. 3, pages 183–200, 1999. (Cited on pages 24 and 72.)
- [Nicoud 2007] F. Nicoud, L. Benoit, C. Sensiau and T. Poinso. *Acoustic modes in combustors with complex impedances and multidimensional active flames*. AIAA Journal , vol. 45, pages 426–441, 2007. (Cited on page 106.)
- [Nottin 2000] C. Nottin. *Large Eddy Simulation of combustion instabilities*. Phd thesis, Ecole Centrale Paris, 2000. (Cited on page 106.)

- [Passot 1987] T. Passot and A. Pouquet. *Numerical simulation of compressible homogeneous flows in the turbulent regime*. J. Fluid Mech. , vol. 181, pages 441–466, 1987. (Cited on page 63.)
- [Piomelli 2010] U. Piomelli. *Large-eddy simulation of turbulent flows. Part 1: Introduction*. In VKI Lecture Series 2010-04, 2010. (Cited on pages 24 and 123.)
- [Poinsot 1992] T. Poinsot and S. Lele. *Boundary conditions for direct simulations of compressible viscous flows*. J. Comput. Phys. , vol. 101, no. 1, pages 104–129, 1992. (Cited on page 35.)
- [Poinsot 2005] T. Poinsot and D. Veynante. *Theoretical and numerical combustion*. R.T. Edwards, 2nd edition, 2005. (Cited on pages 17, 20, 35 and 84.)
- [Pope 2000] S. B. Pope. *Turbulent flows*. Cambridge University Press, 2000. (Cited on pages 23, 24, 108 and 123.)
- [Pope 2002] S. B. Pope. *Stochastic Lagrangian models of velocity in homogeneous turbulent shear flow*. Phys. Fluids , vol. 14, no. 5, pages 1696–1702, 2002. (Cited on page 3.)
- [Quartapelle 1993] L. Quartapelle and V. Selmin. *High-order Taylor-Galerkin methods for non-linear multidimensional problems.*, 1993. (Cited on pages 31, 32, 60, 68 and 72.)
- [Renou 2010] B. Renou. *Deliverable D4.5.1: Report on preliminary experimental results concerning the one injector configuration*. Rapport technique, CORIA, Rouen, 2010. (Cited on pages 94 and 98.)
- [Rivara 1984] Maria-Cecilia Rivara. *Mesh Refinement Processes Based on the Generalized Bisection of Simplices*. SIAM J. Numer. Anal. , vol. 21, no. 6, pages 604–613, 1984. (Cited on page 45.)
- [Robinson 1991] S.K. Robinson. *Coherent Motions in the Turbulent Boundary Layer*. Ann. Rev. Fluid Mech. , vol. 23, pages 601–639, 1991. (Cited on page 123.)
- [Roe 1987] P. L. Roe. *Error Estimates for Cell-Vertex Solutions of the Compressible Euler Equations*. Rapport technique ICASE Report No.87-6, NASA Langley Research Center, 1987. (Cited on page 26.)
- [Roux 2005] S. Roux, G. Lartigue, T. Poinsot, U. Meier and C. Bérat. *Studies of mean and unsteady flow in a swirled combustor using experiments, acoustic analysis and Large Eddy Simulations*. Combust. Flame , vol. 141, pages 40–54, 2005. (Cited on page 72.)
- [Roux 2008] S. Roux, M. Cazalens and T. Poinsot. *Influence of Outlet Boundary Condition for Large Eddy Simulation of Combustion Instabilities in Gas Turbine*. J. Prop. Power , vol. 24, no. 3, pages 541–546, 2008. (Cited on page 108.)

- [Roux 2010] A. Roux, L. Y. M. Gicquel, S. Reichstadt, N. Bertier, G. Staffelbach, F. Vuillot and T. Poinso. *Analysis of unsteady reacting flows and impact of chemistry description in Large Eddy Simulations of side-dump ramjet combustors*. Combust. Flame , vol. 157, pages 176–191, 2010. (Cited on pages 35 and 51.)
- [Rudgyard 1993] M. Rudgyard. *Multidimensional wave decompositions for the Euler equations*. In Von Karman Institute for Fluid Dynamics, editeur, Lectures Series 1993-04, volume 1993-04. Von Karman Institute for Fluid Dynamics, 1993. (Cited on page 26.)
- [Rudgyard 1995a] M. Rudgyard. *Integrated Preprocessing Tools for Unstructured Parallel CFD Applications*. Rapport technique TR/CFD/95/08, CERFACS, 1995. (Cited on page 25.)
- [Rudgyard 1995b] M. Rudgyard, T. Schoenfeld, R. Struijs, G. Audemar and P. Leyland. *A Modular Approach for Computational Fluid Dynamics*. Rapport technique TR/CFD/95/07, CERFACS, 1995. (Cited on page 25.)
- [Runge 1895] C. Runge. *Über die numerische Auflösung von Differentialgleichungen (German)*. Math. Ann., vol. 46, no. 2, pages 167–178, 1895. (Cited on page 51.)
- [Saad 1999] Y. Saad, M. Yeung, J. Erhel and F. Guyomarc’h. *A Deflated Version of the Conjugate Gradient Algorithm*. SIAM J. Sci. Comput., vol. 21, pages 1909–1926, December 1999. (Cited on page 44.)
- [Saad 2003] Y. Saad. *Iterative methods for sparse linear systems*. Society for Industrial and Applied Mathematics, Philadelphia, PA, USA, 2nd édition, 2003. (Cited on page 44.)
- [Sagaut 2002] P. Sagaut. *Large eddy simulation for incompressible flows*. Springer, 2002. (Cited on pages 3, 19, 23, 24 and 51.)
- [Sari 2010] Murat Sari, Gürhan Gürarlan and Asuman Zeytinoğlu. *High-order finite difference schemes for the solution of the generalized Burgers–Fisher equation*. International Journal for Numerical Methods in Biomedical Engineering, 2010. (Cited on page 62.)
- [Schönfeld 1999] T. Schönfeld and M. Rudgyard. *Steady and Unsteady Flows Simulations Using the Hybrid Flow Solver AVBP*. AIAA Journal , vol. 37, no. 11, pages 1378–1385, 1999. (Cited on pages 25 and 35.)
- [Schumann 1975] U. Schumann. *Subgrid scale model for finite difference simulations of turbulent flows in plane channels and annuli*. J. Comput. Phys. , vol. 18, pages 376–404, 1975. (Cited on page 18.)
- [Sengupta 2004] T. K. Sengupta. *Fundamentals of computational fluid dynamics*. Universities Press, Hyderabad (India), 2004. (Cited on page 68.)

- [Senoner 2010] J.-M. Senoner. *Simulation aux grandes échelles de l'écoulement diphasique évaporant dans un brûleur aéronautique par une approche Euler-Lagrange*. PhD thesis, INP Toulouse, 2010. (Cited on page 34.)
- [Sensiau 2008] C. Sensiau. *Simulations numériques des instabilités thermoacoustiques dans les chambres de combustion aéronautiques - TH/CFD/08/127*. PhD thesis, Université de Montpellier II, - Institut de Mathématiques et de Modélisation de Montpellier, France, 2008. (Cited on page 106.)
- [Shannon 1949] C. E. Shannon. *Communication in the Presence of Noise*. Proceedings of the IRE, vol. 37, no. 1, pages 10–21, January 1949. (Cited on page 108.)
- [Sheen 1996] H. J. Sheen and W. J. Chen and. *Correlation of Swirl Number for a Radial-Type Swirl Generator*. Experimental Thermal and Fluid Science, vol. 12, no. 4, pages 444–451, 1996. (Cited on page 98.)
- [Sieverding 2003] C. Sieverding, H. Richard and J.-M. Dese. *Turbine Blade Trailing Edge Flow Characteristics at High Subsonic Outlet Mach Number*. Journal of Turbomachinery, vol. 125, pages 298–309, April 2003. (Cited on pages 66, 67 and 68.)
- [Sieverding 2004] C. Sieverding, D. Ottolia, C. Bagnera, A. Comadoro, J.-F. Brouckaert and J.-M. Dese. *Unsteady turbine blade wake characteristics*. Journal of Turbomachinery, vol. 126, pages 551–559, October 2004. (Cited on pages 66, 67 and 68.)
- [Silva 2010] C. Silva. *Etude numérique du bruit de combustion dans les turbines à gaz*. PhD thesis, Université Montpellier II - DOCTORALE ISS: Spécialité Mathématiques et Modélisation, 2010. (Cited on page 106.)
- [Sirovich 1987] L. Sirovich. *Turbulence and the Dynamics of Coherent Structures, Part I: Coherent Structures*. Quarterly of Appl. Math., vol. XLV, pages 561–571, 1987. (Cited on page 108.)
- [Smagorinsky 1963] J. Smagorinsky. *General circulation experiments with the primitive equations: 1. The basic experiment*. Mon. Weather Rev. , vol. 91, pages 99–164, 1963. (Cited on pages 18, 23 and 68.)
- [Staffelbach 2006a] G. Staffelbach. *Simulation aux grandes échelles des instabilités de combustion dans les configurations multi-brûleurs*. Phd thesis, INP Toulouse, 2006. (Cited on page 35.)
- [Staffelbach 2006b] G. Staffelbach, L. Gicquel and T. Poinsot. *Highly parallel Large Eddy Simulations of multiburner configurations in industrial gas turbines*. In Springer, editeur, Lecture Notes in Computational Science and Engineering - Complex effects in Large Eddy Simulation, volume 56, pages 326–336, 2006. (Cited on page 26.)

- [Staffelbach 2009] G. Staffelbach, L.Y.M. Gicquel, G. Boudier and T. Poinso. *Large Eddy Simulation of self-excited azimuthal modes in annular combustors*. Proc. Combust. Inst. , vol. 32, pages 2909–2916, 2009. (Cited on page 18.)
- [Subcommittee on Exascale Computing 2010] Subcommittee on Exascale Computing. *Opportunities and Challenges of Exascale Computing - Summary Report of the Advanced Scientific Computing Advisory Committee (ASCAC) Subcommittee*. Rapport technique, Department of Energy, 2010. (Cited on pages 1 and 4.)
- [Süli 1989] E. Süli. *Finite volume methods on distorted meshes: stability, accuracy, adaptivity*. Rapport technique NA89/6, Oxford University Computing Laboratory, 1989. (Cited on page 26.)
- [Swanson 1991] R.C. Swanson and R. Radespiel. *Cell Centered and Cell Vertex Multigrid Schemes for the Navier-Stokes*. Am. Inst. Aeronaut. Astronaut. J. , vol. 29, pages 697–703, 1991. NLnum2. (Cited on page 26.)
- [Syred 2006] N. Syred. *A review of oscillation mechanisms and the role of the precessing vortex core in swirl combustion systems*. Prog. Energy Comb. Sci. , vol. 32, no. 2, pages 93–161, 2006. (Cited on pages 97, 98 and 113.)
- [Trefethen 1997] L. N. Trefethen and D. Bau. Numerical linear algebra. Society for Industrial and Applied Mathematics SIAM., Philadelphia, United States of America, 1997. (Cited on page 44.)
- [Vantiegheem 2011] Stijn Vantiegheem. *Numerical simulations of quasi-static magnetohydrodynamics using an unstructured finite volume solver: development and applications*. PhD thesis, Université Libre de Bruxelles, 2011. (Cited on pages 37, 38, 43 and 44.)
- [Vichnevetsky 1982] Robert Vichnevetsky and John B. Bowles. Fourier analysis of numerical approximations of hyperbolic equations. Society for Industrial and Applied Mathematics, Philadelphia, PA, 1982. (Cited on page 35.)
- [Warming 1974] R F Warming and B J Hyett. *The modified equation approach to the stability and accuracy analysis of finite-difference methods*. Journal of Computational Physics, vol. 14, no. 2, pages 159–179, 1974. (Cited on page 56.)
- [Wieczorek 2010] K. Wieczorek. *Numerical study of mach number effects on combustion instability*. PhD thesis, Université Montpellier II - ECOLE DOCTORALE ISS - Mathématiques et Modélisation, 2010. (Cited on page 106.)
- [Williamson 1980] J. H. Williamson. *Low-storage Runge-Kutta schemes*. J. Comput. Phys. , vol. 35, no. 1, pages 48–56, March 1980. (Cited on pages 30 and 51.)
- [Wolf 2010] P. Wolf, G. Staffelbach, R. Balakrishnan, A. Roux and T. Poinso. *Azimuthal instabilities in annular combustion chambers*. In NASA Ames/Stanford Univ. Center for Turbulence Research, editeur, Proc. of the Summer Program , pages 259–269, 2010. (Cited on page 108.)

